Influence of some bioactive molecules on the structure and phase behavior of lipid membranes

by

Sreeja Sasidharan

A thesis submitted to the Jawaharlal Nehru University

for the degree of

Doctor of Philosophy

Raman Research Institute

Bangalore 560080

India

March 2020

Dedicated to my parents

DECLARATION

I hereby declare that this thesis is composed independently by me at Raman Research Institute, Bangalore under the supervision of Prof. V. A. Raghunathan. The subject matter presented in this thesis has not previously formed the basis of the award of any degree, diploma, associateship, fellowship or any other similar title. I also declare that I have run it through the **Turnitin** plagiarism software.

Prof. V. A. Raghunathan
Raman Research Institute
Bangalore 560080 INDIA

Sreeja Sasidharan

CERTIFICATE

This is to certify that the thesis entitled **Influence of some bioactive molecules on the structure and phase behaviour of lipid membranes** submitted by Sreeja Sasidharan for the award of degree DOCTOR OF PHILOSOPHY of Jawaharlal Nehru University is her original work. This has not been published or submitted to any other university for any other degree or diploma.

Prof. R. Subrahmanyan
Director
Raman Research Institute
Bangalore 560080 INDIA

Prof. V. A. Raghunathan
(Thesis Supervisor)

Acknowledgements

I would like to express my sincere gratitude towards my supervisor Prof. V. A. Raghunathan, for giving me the chance to work with him. Without his excellent guidance and constant encouragement, this thesis would not have happened. I always felt proud that I am his student. Professionally and personally, I consider him as a great role model to follow. His immense patience, incredible knowledge, and humble nature always inspired me personally. He is one of the excellent teachers so far I met in my academic time chart. I feel blessed for being his student.

Yashodhan being a wonderful teacher and excellent scientist, always tune us to think scientifically. Thanks to him for all the unique classes and discussions.

I would like to thank Pramod and Yashodhan for chairing my academic committee. Their critical analysis and thoughtful suggestions made the way for many interesting results in this thesis.

Thanks to Prathibha, Madhusudhana, Ranjini, Arun, Gautam, Sayatan for all the interactions I have. They have always been accommodating and encouraging.

I would like to thank Sanjib, Urbasi, Andal, Reji, Shiv, Tarun, Hema for all the courses they have given at RRI.

My sincere thanks to Namboothiri sir, Jaceentha madam and Thomas sir from Nirmala College and Harish Kumar sir, Nirmala madam from IIT Madras. I especially am grateful to Namboothiri sir, for believing me more than I believe in myself.

Sr. Jency Therese deserves a special place in my heart for molding me who I am now. Her constant encouragement and excellent classes have motivated me a lot for learning during my school time.

I would like to remember and thank all my teachers whose efforts made me who l am.

Thanks to all faculties at RRI, whose inspiring talks and discussions gave me the daily dose of motivation.

RRI is blessed with the technical staffs who are ready to work for the students whenever it is needed. I am extremely thankful Mr. Yatheendran, without his help in SEM, AFM, and confocal microscopy, much of the chapters were not possible. Mr. Dhason was very

helpful with AFM measurements, as well as in teaching me the technique. The temperature-controlled chamber made by Mr. Mani is used for confocal microscopy measurements. Thanks a lot for his careful work creating the chamber. Ms. Serene was always ready to help with any biological questions and protocols. Thanks to her for all the help. I would also like to thank Mr. Srinivas and Mr. Ishaq for their support.

The lab is an ideal place to work if one gets lab members like Meera, Madhukar, Anindya, Surya, Shabeeb, Ayush and Santhosh. Thanks to Meera for being the perfect senior, Madhukar for his extreme patience in teaching me x-ray techniques and sample preparation, Anindya for being the nicest junior and all his help in the lab, Surya for all the help and learning adventures during the initial years, Shabeeb for teaching me multilayer fluorescence imaging and all academic and literature discussions, Ayush for many engaging discussions and his ready to help nature, Santhosh for his help during my comprehensive project. I would like to thank all my seniors, whose theses I was constantly referring to, especially RK, for all the wonderful discussions.

I would like to thank Vasudha madam for patiently listening to all my complaints and worries. She is a family away from family.

Friends are the ones who make life easy going in the toughest of a tough situation. I am extremely lucky that I found a lot of friends in RRI.

I was always an intruder in to this batchmate trio of Meera, Karam, and Priyanka. I had a wonderful time with them. I can not thank Meera enough for her support, care, encouragement, and for being a shoulder to cry on. For me, she is a friend, elder sister who I believe more than myself. I will always be grateful to her. I would like to express my sincere gratitude to Karam for her excellent suggestions and decisions whenever I was confused. Priyanka for all the never-ending discussions.

I would like to thank Madhukar, Swami, Mari, Jagadeesh, Asha, Chandan, Sushil, Niranjan. They are accommodating and always been a friend in need, especially Madhukar, for all the musical discussions and accompanying me for concerts. Special thanks to JK for all the beautiful classes he has taken.

I am happy to have Sanjay, Santanu, Amit, Alkesh, Ashutosh, Janakee, Deepshika, Varun, Saurabh, Aswath as batchmates. Thanks to them for all the wonderful time during the coursework and especially Sanjay and Santanu, for being best buddies.

Juniors like Adwaith, Arsalan, Irla, Nishant, Saichand, Nancy, Bhagyalakshmi, Arun, Hemanth, Shilpa always made every day better. Thanks to Adwaith, Arsalan, Irla, and Nishant for all the care they showed during my hospital days. Thanks to Nancy for the help with

fluorescence measurements.

I would like to thank all the SCM students for the excellent discussions I have with them. Thanks to Sumanth, Chandu, Palak, Sourabh, Vishnu, Ashish, Tonmoy, Ritwika, Rajkumar, Sukhweer, Swarnak, Deepak, Subhadeep for the time they spent with me. Special thanks to Chandu, Tonmoy, Riddhika, Sumant, and Sourabh for their help in different experiments.

Thanks to Nidhin, Sarayoo, and Pranitha for all the support.

I would like to thank all my seniors, especially Jyothi, Nazma, Shafi, Anu, Renu, Nafisa, Gayatri, Mayuri, Rahul, Jagdish, Debashish, and Raj.

I would like to extend my gratitude to our director Prof. Ravi Subrahmanyan, Administrative officer Mr. C. S. R. Murthy, and Mr. Naresh, for all the academic and administrative help.

I am thankful to Mr. Radhakrishna, Ms. Marisa, Ms. Radha, Ms. Vidya and Mr. G. Manjunatha for all the help with paper works.

Thanks to all the library staff to maintain an excellent collection in the library. I would like to thank Ms. Meera B. M, Mr. Nagaraju, Mr. Manjunath K., Mr. M. Manjunath, Ms. Vani, for all the efforts to keep the library as a peaceful place to study.

Thanks to staffs of computer department and workshop for their help.

I would like to thank Murali and Raja for all their help.

I am thankful to purchase and account departments for their help with travel and buying lab equipment.

I am grateful to all canteen staff who serve food with the daily dose of a smile and all the security staff and drivers for making us feel safe all the way.

I thank Madhavan, Anupama, Aksharan, Ambaran, Usha, Maya, Divya, Swati, and GB for all the fun moments and the care they have shown to me.

Finally, I thank my parents, sisters, brother, and brother in law for all the support. Without them, I am nothing. Special thanks to Parvathy (puppy) to make me feel alive every day.

List of Publications

'Interaction of mononucleotide UMP with a fluid phospholipid bilayer', S. Sasidharan, S. Pochinda, P.N. Elgaard-Jørgensen, S. Rajamani, H. Khandelia and V. A. Raghunathan, *Soft Matter,2019,15, 8129-8136*

'Direct imaging of rippled structures of lipid-cholesterol membranes using Cryo-SEM and AFM', S. Sasidharan and V. A. Raghunathan, *Bull Mater Sci 43, 184 (2020).*

'Hydrotropic behaviour of uridine monophosphate',S. Sasidharan, PP.N. Elgaard-Jørgensen,M. P. Pandey , N. Verma, S. Rajamani, H. Khandelia, V. A. Raghunathan *submitted in Phys. Chem. Chem. Phys, 2020*

'Formation of extended solid supported lipid bilayers using acetic acid induced rupture and fusion of GUVs', S. Sasidharan and V. A. Raghunathan, *To be submitted*

Abstract

This thesis deals with investigations on the influence of some biologically relevant molecules, such as uridine monophosphate (UMP), acetic acid, cholesterol and hydroxycholesterol, on the structure and phase behavior of phosphocholine (PC) bilayers. We have used a variety of experimental techniques including x-ray scattering, optical and electron microscopy, spectroscopy and calorimetry to probe the underlying interactions present in the aforementioned systems. We also present a novel method for the preparation of solid supported lipid bilayers (SSLB) by the addition of acetic acid to a suspension of giant unilamellar vesicles (GUVs).

This thesis consists of 7 chapters. Starting with a brief introduction to amphiphiles and the principles governing their self assembly, chapter 1 gives an overview of the systems of our interest, as well as of the various experimental techniques used to characterize them. Lipids are amphiphilic molecules and are the basic building blocks of cell membranes. Above a certain concentration, called the critical micellar concentration (CMC), lipids self assemble in water to form aggregates due to their amphiphilic nature [1, 2]. The double-tailed lipids studies here preferentially self assemble into bilayers. Such bilayers, made up of either a single lipid or mixtures of lipids, are widely used as model systems for cell membrane related studies. Cell membranes play a vital role in many biological functions such as signaling, endocytosis and ion transport [2, 3, 4, 5]. Understanding the interaction of model membranes with different biomolecules will give insights into the functional aspects of cell membranes. With this motivation we have studied the interaction of some biologically relevant molecules, namely, UMP, acetic acid, cholesterol and two of its derivatives, with PC lipid bilayers using various experimental techniques. In this chapter we have also outlined the basic principles of small angle x-ray scattering (SAXS), wide angle x-ray scattering (WAXS), cryogenic scanning electron microscopy (cryo-SEM), confocal fluorescence microscopy, micro Raman spectroscopy, fluorescence and UV-visible spectroscopy, atomic force microscopy (AFM) and differential scanning calorimetry (DSC).

It has been proposed that the non-enzymatic synthesis of ribonucleic acid (RNA) or RNA-

like molecules from mononucleotides in a lipid environment has played an important role in the origin of life on Earth [6, 7, 8, 9]. In this context, we have studied the influence of uridine monophosphate (UMP) - the signature monomer of RNA - on the structure and phase behavior of 1,2-dimyristoyl-sn-glycero-3-phosphocholine (DMPC) bilayers. These investigations are described in chapter 2, which is divided into two sections. The first section deals with studies on the influence of UMP on DMPC bilayers in the fluid phase, using SAXS and cryo-SEM. We observe that the doubly charged UMP molecules bind to the headgroup region of DMPC bilayers. This leads to a strong electrostatic repulsion between the bilayers, which destabilizes their multilamellar stacks, resulting in the formation of unilamellar vesicles (ULV). SAXS data of these systems show profiles consistent with the bilayer form factor, as expected for a dispersion of ULVs. Detailed analysis of SAXS profiles shows that the adsorption of UMP results in a reduction in the bilayer thickness. Remarkably, this behaviour is not observed when UMP is replaced with its disodium salt (UMPDSS). In this case the samples preserves their multilamellar structure and the interaction of UMPDSS does not perturb DMPC bilayers significantly. The observed tendency of UMP to adsorb on lipid membranes is consistent with the proposed role of these lipid-mononucelotide systems in the synthesis of RNA-like polymers on early Earth.

In the second part of chapter 2 we present studies on the influence of UMP on the phase behavior of DMPC bilayers. It is observed that upon incubation at 60°C, the ULV dispersion initially formed, due to the electrostatic repulsion between the bilayers, is converted into a highly swollen lamellar phase. This fluid lamellar phase transforms into the gel phase on cooling at a higher temperature (42°C) compared to pure DMPC (24°C). This elevation of the chain melting transition temperature (T_m) is consistently observed using different techniques such as DSC, WAXS, SAXS and fluorescence microscopy. Raman spectroscopy studies indicate that the orientation of DMPC head group in the bilayer changes in the presence of UMP. On increasing the incubation time further, the bilayers form an interdigitated phase, where the hydrocarbon chains of lipid molecules in the two leaflets of each bilayer interpenetrate, leading to a drastic reduction in the bilayer thickness and a concomitant increase in the area per head group. The interdigitated phase melts at 50°C on heating, forming an inverted hexagonal phase. In this structure, UMP molecules reside in the aqueous cores of the inverted hexagonal micelles. The resulting one-dimensional confinement may further facilitate the non-enzymatic polymerization of UMP, envisaged in the RNA world hypothesis of the origin of life on Earth.

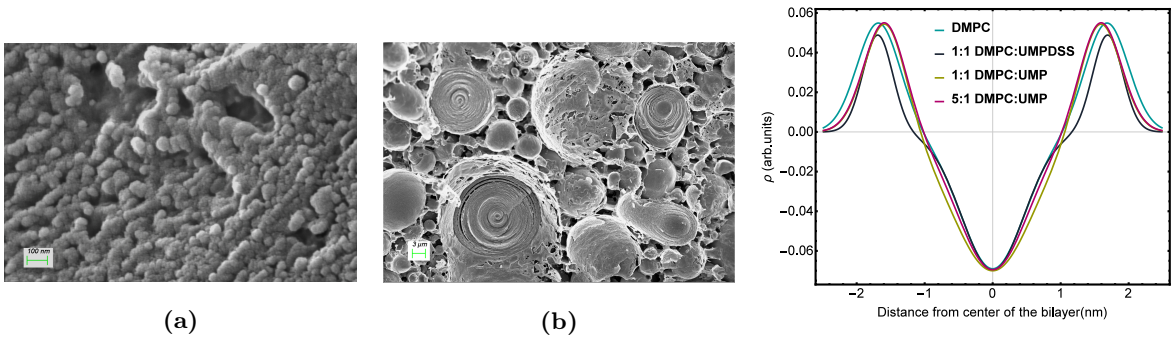

(a) **(b)** **(c)**

Figure 1: Cryo-SEM images of 1:1 molar DMPC:UMP system showing vesicular structure (a) and 1:1 molar DMCP:UMPDSS system showing multilamellar vesicles (b). (c) shows electron density profiles obtained from SAXS data which indicate a reduction in the bilayer thickness in the presence of UMP.

Chapter 3 describes the aggregation behaviour of UMP and its disodium salt (UMPDSS) in water. These studies were undertaken in order to understand the remarkable differences in their effects on the phase behaviour of DMPC bilayers, described in the previous chapter. It has been reported in the literature that certain biomolecules, such as ATP (adenosine triphosphate magnesium salt) and bile acid salts, form small clusters in water either by themselves or in the presence of hydrophobic solutes [10, 11]. The aggregation of these molecules can enhance the solubility of otherwise insoluble nonpolar solutes in water. This phenomenon is known as hydrotropy. The hydrotropic action of biomolecules is believed to be important in many biological functions [10, 12]. Structurally hydrotropes are similar to surfactants, having a polar head group region and a nonpolar tail region. However, unlike surfactants, most of the hydrotropes do not spontaneously self assemble in water. This is due to the relatively small size of the hydrocarbon region of hydrotropes. Although hydrotropes have been studied extensively, the importance of head group polarity in their aggregation behaviour has not been investigated in much detail. In this context we compare the aggregation behavior of UMP and its disodium salt in water in the presence of different hydrophobic solutes such as pyrene, fluorescein diacetate (FDA) and 8-anilino-1-naphthalenesulfonic acid magnesium salt (ANS), which are some of the commonly used indicators of hydrotropic behaviour [13, 14, 15]. UMPDSS is found to exhibit hydrotropic behavior, whereas in the case of UMP no clear evidence for such a behavior is seen. These results reflect the differences in their effects on the structure and phase behaviour of DMPC bilayers discussed in Chapter 2.

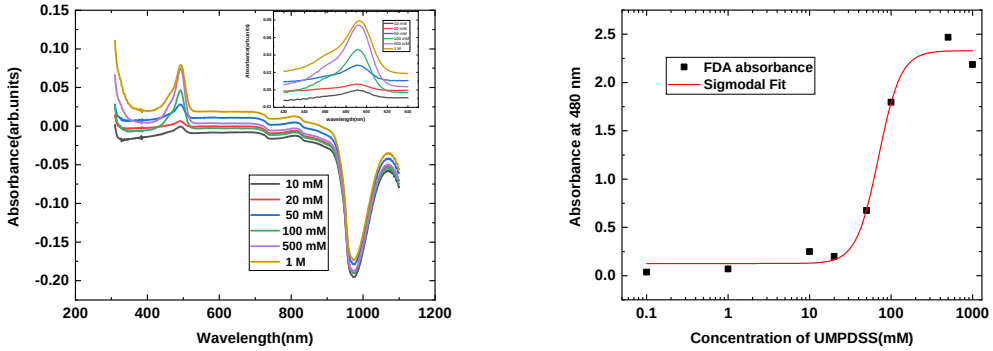

(a) **(b)**

Figure 2: (a) Appearance of absorbance peak at 480 *nm* from FDA monomers as a function of UMPDSS concentration in the solution. (b) Absorbance at 480 *nm* as a function of UMPDSS concentration showing typical sigmoidal behavior as expected for hydrotropes.

Chapter 4 describes a novel method for the preparation of solid supported lipid bilayers (SSLBs) by the rupture of giant unilamellar vesicle (GUVs) using acetic acid. We find that acetic acid is able to create pores in lipid bilayers, which lead to the rupture of GUVs settled on a substrate. We have studied the rupture of GUVs at different concentrations of acetic acid and have characterized the SSLB formed by this method by lipid diffusion measurements using FRAP for different substrates and for different chain lengths of the lipid. Values of the diffusion coefficient obtained are found to be in good agreement with those reported in the literature. We also establish the effect of substrate interaction on the chain melting transition temperature of DPPC (1,2-dipalmitoyl-sn-glycero-3-phosphocholine) by temperature dependent diffusion measurements. As an illustrative application of this technique, the fluid-fluid phase coexistence in a SSLB made from a ternary mixture of DPPC, DOPC(1,2-dioleoyl-sn-glycero-3-phosphocholine) and cholesterol is studied.

Motivated by the results of the previous chapter on SSLB formation, in chapter 5 we investigate the interaction of acetic acid with a lipid bilayer using SAXS, WAXS, DSC and Raman spectroscopy. Although acetic acid is miscible with water, we find that it preferentially binds to lipid membranes. Interestingly, the effect of acetic acid on DMPC bilayers is found to resemble very closely that of UMP. Similar to UMP, acetic acid reduces the bilayer thickness in the fluid phase of DMPC. It also forms an electrostatically swollen lamellar phase with an elevated chain melting transition temperature of 42° C. Further, it induces the interdigitated phase on long incubation, which melts into an inverted hexagonal phase at 50° C. Raman

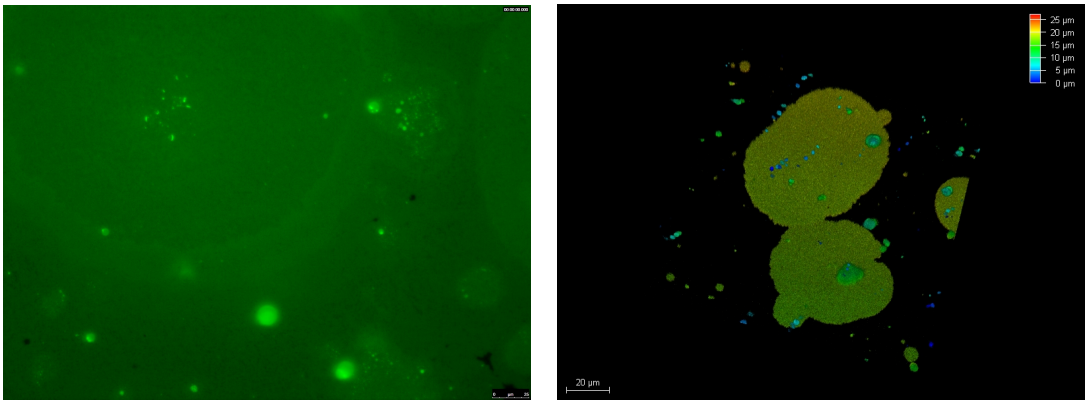

(a) **(b)**

Figure 3: (a) Fluorescence image of SSLB formed by the rupture and fusion of DOPC GUVs in the presence of acetic acid. The entire region in the image is covered by the SSLB formed. (b) Confocal Image showing the fusion of GUVs with SSLB.

spectroscopy studies reveal that the lipid head group conformation changes in the presence of acetic acid as is observed with UMP. The only major difference between the two systems is that the time scale for these transformations is about twice longer in the case of acetic acid compared to UMP.

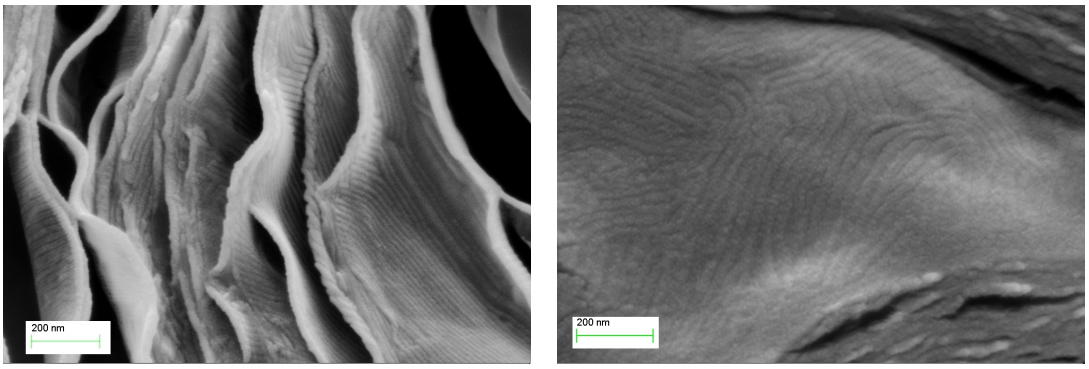

(a) **(b)**

Figure 4: Cryo-SEM images of the ripple phase of pure DPPC bilayers (a) and of DPPC bilayers containing 10 mol% cholesterol (b). Note the much longer ripple wavelength in the presence of cholesterol.

Chapter 6 and chapter 7 deals with cryo-SEM and AFM studies on the phase behavior of PC lipids in the presence of either cholesterol or one of its two derivatives. The chapter 6 describes studies on the ripple phase of DPPC-cholesterol membranes, using cryo-SEM and

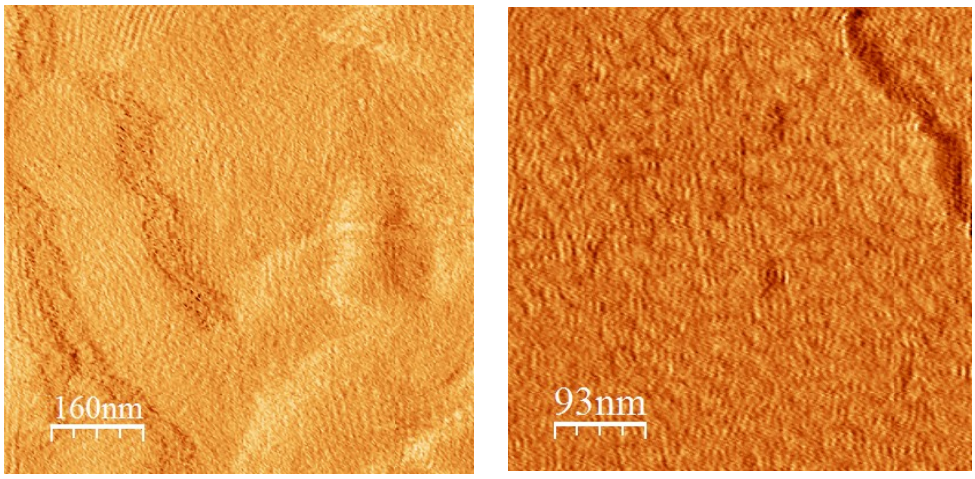

(a) **(b)**

Figure 5: AFM images of (a) the ripple phase in DPPC-Cholesterol (10 mol%) multilayers showing a periodicity of 16 nm and amplitude of 3.5 nm and (b) ripple phase in DPPC-Cholesterol (15 mol%) showing a periodicity of 8 nm and amplitude of 0.6 nm

AFM techniques. DPPC bilayers are known to exhibit an asymmetric ripple ($P_{\beta'}$) phase characterized by a one-dimensional height and thickness modulations of the bilayer. Previous studies, using small angle neutron scattering and freeze fracture electron microscopy, have shown that the wavelength of the ripples (λ) in the ripple phase of DPPC increases with increasing cholesterol concentration [16, 17]. These studies are rather indirect and are plagued by artifacts. Hence additional more direct observations are required to confirm these results. Using cryo-SEM techniques, we have been able to obtain unambiguous evidence for higher wavelength ripples in DPPC multilayers containing cholesterol. Previous x-ray scattering experiments have reported a novel symmetric ripple (P_{β}) phase induced by cholesterol in DPPC membranes [18]. This phase is characterized by a much shorter ripple wavelength compared to the ripple phase in pure DPPC; it also has a much smaller amplitude of height modulation. Surprisingly, there are no reports of the observation of this phase using any other experimental technique. Here we have obtained the first direct evidence of this phase from AFM studies on DPPC-Cholesterol multilayers supported on a solid substrate. Wavelength and amplitude of the ripple measured correlate well with the reported values obtained from x ray scattering experiments.

Fluid-fluid phase coexistence in binary mixtures of PC lipids and 25- hydroxycholesterol or 27- hydroxycholesterol is studied in chapter 7. Liquid domains in lipid membranes have been extensively studied due their relevance to the compositional heterogeneities, called rafts, present in cell membranes. It is now well known that ternary mixtures consisting of choles-

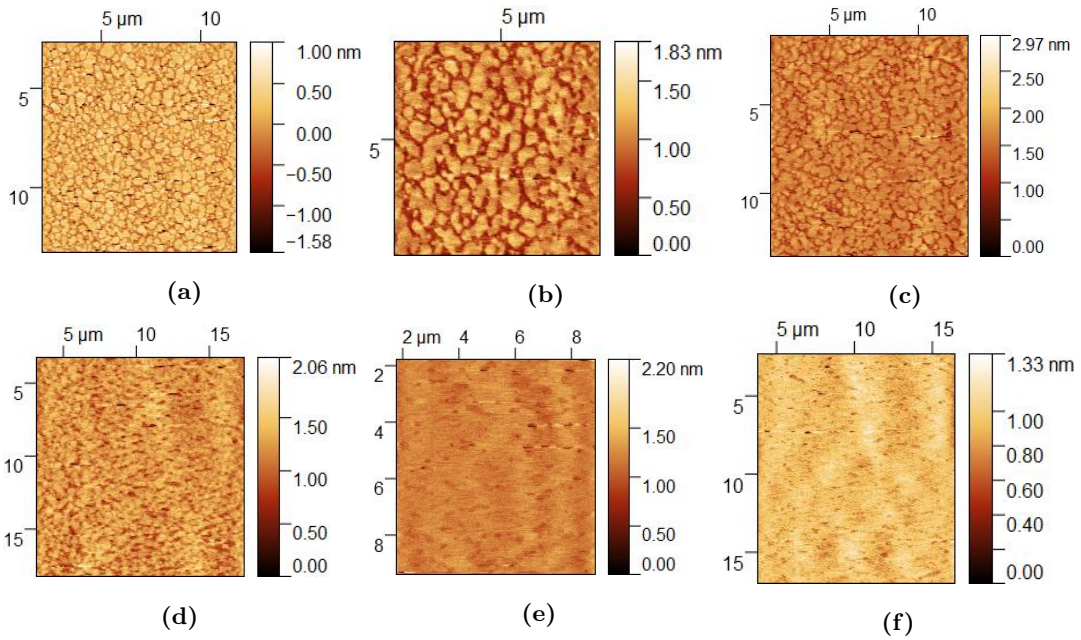

Figure 6: AFM images of fluid-fluid phase coexistence in DMPC-25 hydroxycholesterol (20 mol%) supported bilayer as a function of temperature. (a) 26°C, (b) 33°C, (c) 36°C, (d) 38°C, (e) 39°C and (f) 43°C. Note the appearance of a uniform phase in (f).

terol and two lipids with widely different chain melting transition temperatures (T_m) exhibit the coexistence of two liquid phases over a temperature range below the T_m of the higher melting lipid [19, 20]. Recently it has been observed that binary mixtures of PC lipids with 25-hydroxycholesterol and 27-hydroxycholesterol show fluid-fluid coexistence over a range of temperatures above the T_m of the lipid [21]. Using AFM, we have studied phase separation in supported bilayers made from these mixtures and have characterized the two coexisting fluid phases. The two-phase region is found to occur below an upper critical temperature, which is well above the T_m of the lipid. The sterol rich fluid phase is found to have a slightly higher thickness compared to that of the pure lipid. The difference in thickness of these two fluid phases is around 1 nm, These observations support the results of earlier x-ray scattering experiments and provide additional information on the structure and composition of the two coexisting phases.

Chapter 8 summarizes the important observations and conclusions drawn from the studies presented in this thesis. In addition, we also discuss possible directions for future work on the systems described here.

Bibliography

[1] Jacob N Israelachvilli. *Intermolecular and surface forces.* Elsevier, third edition, 2014.

[2] J M Berg, J K Tymoczko, and L Stryer. *Biochemistry.* Newyork:W.H. Freeman, fifth edition, 2002.

[3] Kai Simons and Elma Ikonen. Functional rafts in cell membrane. *Nature*, 8(387):569–572, 1997.

[4] H Lodish, A Berk, and S L Zipurskyl. *Molecualr Cell Biology.* Newyork:W.H. Freeman, fourth edition, 2000.

[5] S. Mukherjee, R. N. Ghosh, and F. R. Maxfield. Endocytosis. *Physiological Reviews*, 5(3):759–803, 1997.

[6] Sebastian Himbert, Mindy Chapman, David W. Deamer, and Maikel C. Rheinstädter. Organization of nucleotides in different environments and the formation of pre-polymers. *Scientific Reports*, 6:31285–31297, 2016.

[7] C. V. Mungi and S. Rajamani. Characterization of RNA-like oligomers from lipid-assisted nonenzymatic synthesis: implications for origin of informational molecules on early earth. *Orig. Life Evol. Biosph.*, 38:57–74, 2008.

[8] S. Rajamani, A. Vlassov, S. Benner, and A. Coombs. Lipid-assisted synthesis of RNA-like polymers from mononucleotides. *Orig. Life Evol. Biosph.*, 38:57–74, 2008.

[9] Laura Toppozini, Hannah Dies, David W. Deamer, and Maikel C. Rheinstädter. Adenosine monophosphate forms ordered arrays in multilamellar lipid matrices: Insights into assembly of nucleic acid for primitive life. *PLOS ONE*, 8(5):62810–62818, 2013.

[10] Avinash Patel, Liliana Malinovska, Shambaditya Saha, Jie Wang, Simon Alberti, Yamuna Krishanan, and Anthony A. Hyman. ATP as a biological hydrotrope. *Science*, 356(19):753–756, 2017.

[11] John Y. L. Chiang. Bile acid metabolism and signaling. *Compr Physiol*, 3(3):1191–1212, 2013.

[12] R. Zana and D. Guveli. Florescence probing study of the association of bile salts in aqueous solutions. *J. Phys. chem.*, 89:1687–1690, 1985.

[13] K. P. Ananthapadmanabhan, E. D. Goddard, N. J. Turro, and P. L. Kuo. Florescence probes for critical micelle concentration. *Langmuir*, 1:1687–1690, 1985.

[14] J. Shobha and D. Balasubramanian. Microenvironmental difference amongst micelles of various shapes and structures. *Proc. Inadian Acad. Sci(Chem.Sci)*, 98:469–478, 1987.

[15] D. Balasubramanian, V. Srinivas, V.G. Gaikar, and M.M. Sharma. Aggregation behavior of hydrotropic compounds in aqeous solution. *J. Phys.Chem*, 93:3865–3870, 1989.

[16] K. Mortensen, W. Pfeiffer, E. Sackmann, and W. Knoll. Structural properties of a phosphatidylcholine-cholesterol system as studied by small-angle neutron scattering: ripple structure and phase diagram. *Biochim. Biophys Acta*, 945(2):221–45, 1988.

[17] B. R. Copeland and H. M. McConnel. The rippled structure in bilayer membranes of phosphatidylcholine and binary mixtures of phosphatidylcholine and cholesterol. *Biochim. Biophys Acta*, 599(1):95–109, 1980.

[18] Sanat Karmakar and V. A. Raghunathan. Cholesterol-induced modulated phase in phospholipid membranes. *Phys Rev Lett.*, 91(9):098–102, 2003.

[19] Frederick A. Heberle and Gerald W. Feigenson. Phase separation in lipid membranes. *Cold Spring Harb Perspect Biol.*, 3(4):a004630, 2011.

[20] Miranda L., Schmidt, and James H. Davis. Liquid disordered–liquid ordered phase coexistence in lipid/cholesterol mixtures: A deuterium 2d nmr exchange study. *Langmuir*, 33(8):1881–1890, 2011.

[21] Mohammad Arif Kamal. Thesis submitted to JNU 2012.

Contents

List of Figures

List of Tables

Chapter 1

Introduction

Lipids are one of the major constituents of cell membranes. The complex structure of cell membranes consisting of a multitude of proteins and lipids under different environmental conditions is still unresolved. Hence the complete characterization of the structure and phase behavior of model lipid membranes under different biological conditions can contribute a significant amount of information to the much-related cell membrane studies. Studies with model systems have focused on the interaction of different lipids as well as of lipids with proteins when incorporated together in the membrane. This thesis comprises of our investigations on the interaction of certain bio-active molecules such as uridine-5'- monophosphate, acetic acid, cholesterol, and its derivatives with phosphocholine (PC) lipid bilayers. The first part of this chapter explains the theoretical background on self-assembly of amphiphiles and different kinds of interactions present between such self-assembled bilayers. The second section discusses all the experimental techniques used during this thesis work.

1.1 Lipid bilayer and self-assembly

It is now well known that the basic structure of the plasma membrane is formed out of a lipid bilayer. Although the first experimental proof of this was established in 1925 [1], it took almost 50 years to arrive at an approximate structure of the cell membrane. One of the most celebrated models of the cell membrane is the fluid-mosaic model put forwarded by Singer and Nicholson in 1972 [2]. This model considers the cell membrane as a homogeneous mixture of dynamic lipid molecules, in which proteins are diffusing around. Experimental advances in microscopy and other techniques invalidated the fluid-mosaic model soon after the discovery of detergent resistant compositional inhomogeneities in cell membranes [3, 4, 5]. These inhomogeneities are termed as rafts and are believed to be involved in many important

biological functions such as signal transduction, protein trafficking, etc. [6].

The function and existence of rafts in cell membranes is an unresolved topic in the field of biophysics [7, 8]. Studies on the interactions of model membranes with bioactive molecules and their phase behavior under different physiological conditions can form the basic platform for further explorations.

The cell membrane consists of a wide variety of different lipids. Lipids are amphiphilic molecules. They have a head group region that can be charged, neutral or zwitterionic, and a hydrocarbon chain region. The two parts of the molecule interact differently with water, hence the name amphiphile. The polar head group region interacts favourably with water molecules, while tail region formed from hydrocarbon chain/chains, much like oil, is hydrophobic. The three major categories of lipids found in the eukaryotic cells are phospholipids, glycolipids, and cholesterol. The structure of a typical phosphocholine (PC) lipid and the categorization of different lipids are shown in fig.1.1. PC lipids have a head region made up of positively charged choline and negatively charged phosphate moieties, giving it a zwitterionic nature. The head group region is linked to the hydrocarbon tail region via a glycerol backbone. PC lipids are mainly found in the exoplasmic outer leaflet of cell membranes, and in pulmonary surfactant [9, 10].

Once dissolved in water, the competition between hydrophilic and hydrophobic interactions of lipid with water results in the formation of self-assembled bilayer structures above a certain monomer concentration called the critical micellar concentration (CMC). The general principle behind self-assembly from a thermodynamical point of view is given below. A thorough review of self-assembly and various interactions present in the self-assembled system can be found in ref.[11, 12, 13].

1.2 Thermodynamics of self-assembly

Consider a dispersion of amphiphiles in water with a concentration C « 1. C is generally expressed in terms of the total volume fraction or molar fraction of monomers in the solution.

The chemical potential of a monomer in dispersed state [11] is expressed as,

$$\mu = {\mu_1}^0 + \frac{KT}{1}\log(\frac{X_1}{1}) \tag{1.1}$$

where ${\mu_1}^0$ is the interaction potential of the monomer in the dispersed state and $\frac{KT}{1}\log(\frac{X_1}{1})$ is the entropy of mixing with K the Boltzmann's constant and T the temperature.

For a monomer in an aggregate of aggregation number N, the chemical potential is given by,

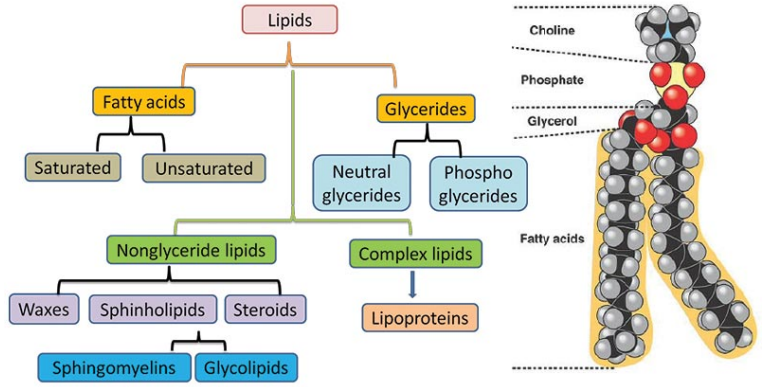

(a)

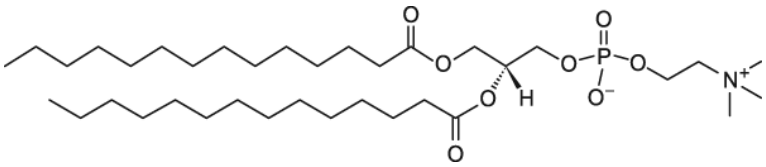

(b)

Figure 1.1: (a) Schematic showing the major categories of lipids and the structure of a typical phosphocholine lipid adapted from [14] (b) Chemical strcuture of DMPC (1,2-dimyristoyl-sn-glycero-3-phosphocholine)

$$\mu = \mu_N = {\mu_N}^0 + \frac{KT}{N}\log(\frac{X_N}{N}) \tag{1.2}$$

where ${\mu_N}^0$ is the interaction potential experienced by a monomer in an aggregate of aggregation number N. $\frac{KT}{N}\log(\frac{X_N}{N})$ is the entropy of mixing with X_N is the fraction of monomers in aggregates of aggregation number N and has the same unit as C.

Assume the system is under thermodynamic equilibrium, where the monomers are coexisting with aggregates. This means the chemical potential of each monomer in the dispersed state, as well as, in aggregates of different aggregation number should be the same. This can be expressed as,

$$\mu = {\mu_1}^0 + \frac{KT}{1}\log(\frac{X_1}{1}) = {\mu_2}^0 + \frac{KT}{2}\log(\frac{X_2}{2}) = {\mu_3}^0 + \frac{KT}{3}\log(\frac{X_3}{3}) = ... \tag{1.3}$$

From the above equations,

$$\mu = {\mu_1}^0 + \frac{KT}{1}\log(\frac{X_1}{1}) = {\mu_N}^0 + \frac{KT}{N}\log(\frac{X_N}{N}), \tag{1.4}$$

one can obtain

$$X_N = N(X_1 \exp\alpha)^N, \tag{1.5}$$

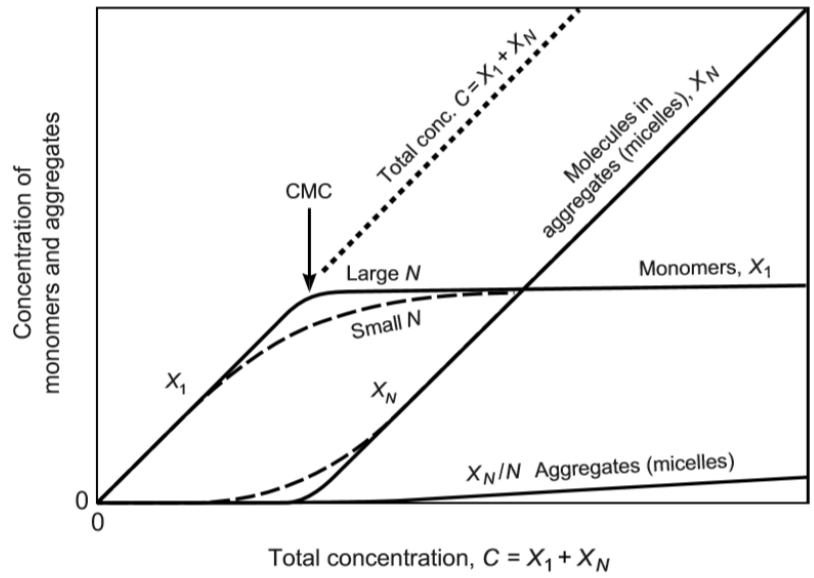

Figure 1.2: Monomer and aggregate concentration as a function of total concentration [11].

where

$$\alpha = \frac{{\mu_1}^0 - {\mu_N}^0}{KT} \tag{1.6}$$

The above equation tells us that when the monomer concentration X_1 is sufficiently low, for any value of α, $X_1 \exp \alpha$ is less than 1 and $X_1 > X_2 > X_3 > .. > X_N$. Thus at low concentrations, most of the molecules are in the dispersed state and, therefore, C $\sim X_1$. As X_1 increases and reaches the value $\exp(-\alpha)$, the condition that C or X_N can not exceed 1 indicates that there will not be any further increase in X_1. This concentration of monomers at which aggregates start forming is called the critical micellar concentration (CMC) or critical aggregation concentration. For amphiphiles with a single chain having 12-16 carbons per chain, the CMC is in the range of 10^{-2} to 10^{-5} M, and for double-chained amphiphiles, it is in the nM range.

The self-assembled structure formed by different amphiphiles depends on the molecular geometry of the amphiphile itself. For example, single chained amphiphiles with large head groups effectively resembling the geometry of a cone can form spherical micelles since the cones can easily pack into a sphere (fig.1.3). This geometrical constraint in the formation of different self-assembled structures is incorporated in a dimensionless number called the shape parameter or critical packing parameter (CPP) which is given by the expression,

$$CPP = \frac{\nu}{a_0 l_c} \tag{1.7}$$

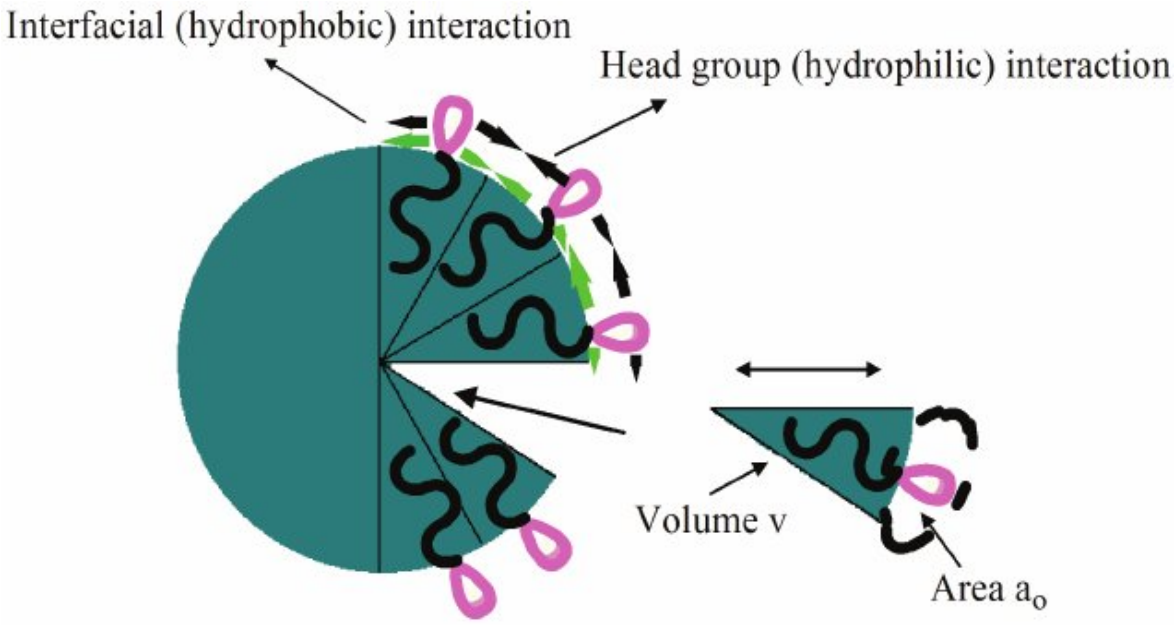

Figure 1.3: Micelle structure formed by monomer of CPP = 1/3. Figure is adapted from [15]

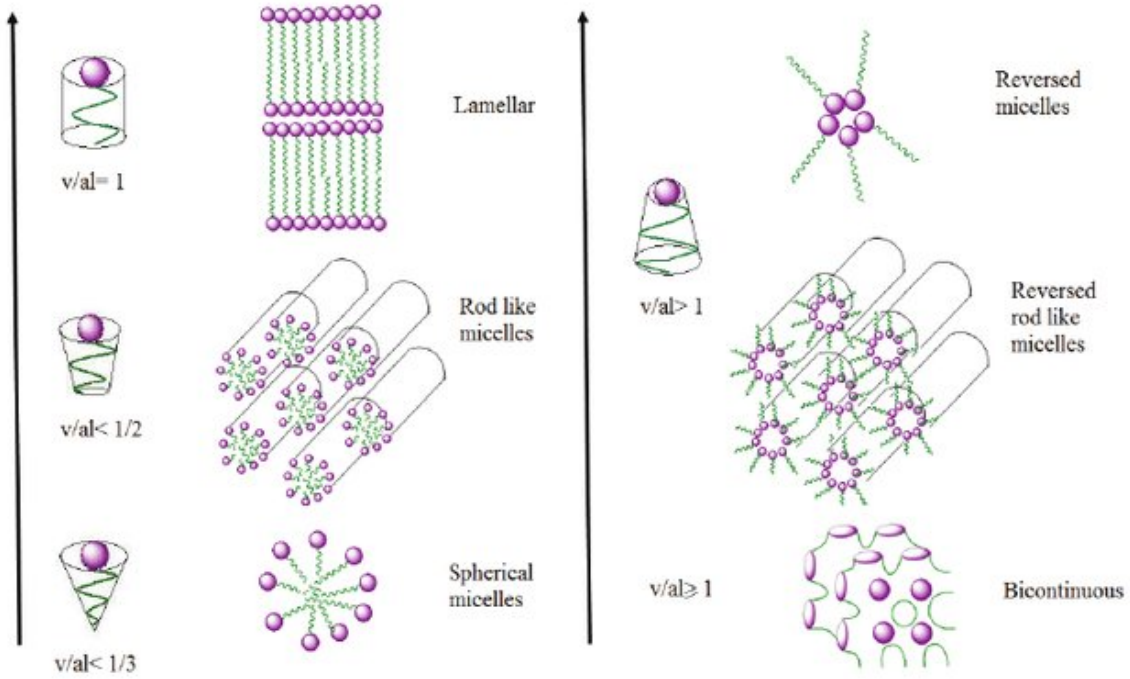

Figure 1.4: Different self assembled structures formed by monomers of different geometries. Figure is adapted from ref.[15]

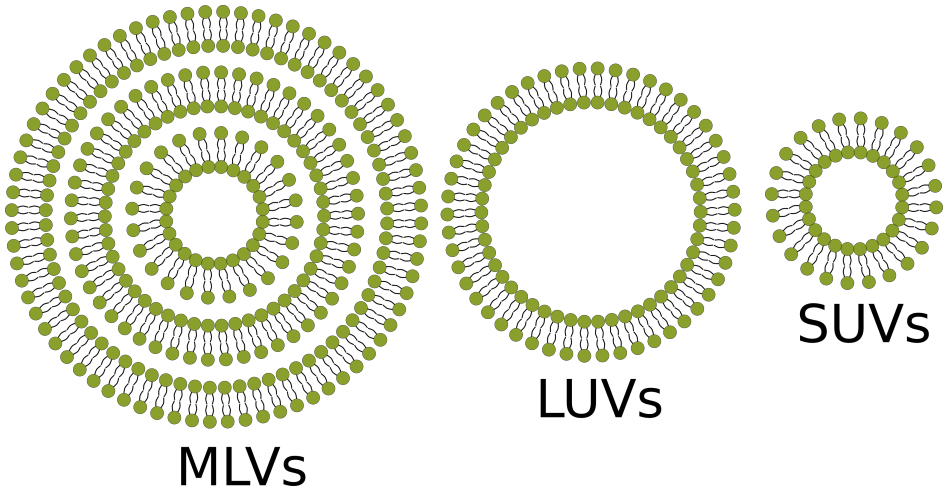

Figure 1.5: Schematic of Multilamellar vesicle (MLVs), Large unilamellar vesicle (ULVs) and Small unilamellar vesicle (SUVs).

where a_0 is the head group area, l_c is the critical chain length (length of extended chain above which it is no longer considered as fluidic) and ν is the volume of hydrocarbon chain. Different self-assembled morphologies formed by molecules having different packing parameters are shown in fig. (1.4)

At high hydration, PC lipids with CPP $\sim$ 1, in general form bilayers. Since the edges of the bilayer patches are exposed to water, there exists a hydrophobic interaction of the chains with water, which is unfavorable. Above a certain threshold size, the bilayer patches can curl up and form vesicles. The formation of vesicles also costs energy because of the bending energy of the bilayer. The interplay between hydrophobic interaction and bending energy decides the minimum size of vesicles formed (fig.1.5). The vesicles formed can also be multilayered. Multilamellar vesicles (MLVs) are usually microns in size. For specific application large unilamellar vesicles (LUVs) of size range 100-500nm [16] or giant Unilamellar vesicles (GUVs) of size range 1-30 μm can be formed by special techniques such as electroformation or gentle hydration [17, 18]. By disrupting MLVs or ULVs using sonication or extrusion, unilamellar vesicles of very small sizes (20 -100 nm) can be obtained, which are known as small unilamellar vesicles (SUVs) [19, 20]. Under specific conditions, lipids can also form non-bilayer structures. A change in CPP can transform one structure to another. The head group area of a lipid is affected by many parameters, including pH of the solution, temperature, and salt concentration. For anionic lipids, the head group area is reduced in the presence of Ca^{2+} ions and by lowering the pH [11]. Chain packing or l_c is affected by the introduction of branching or unsaturation in the alkyl chains. The effective volume of hydrocarbon chains ν, is affected by the penetration of low molecular weight alkanes [11].

The different aspects of self-assembly so far discussed have assumed the hydrophobic chain region to be fluidic. For any hydrocarbon chain, there exists a temperature above which the chains are fluidic and is called the chain melting transition temperature (T_m). Correspondingly, for each lipid, there exists a temperature above which the bilayers are in the fluid phase and below which they are in the gel phase. Saturated phospholipids with the number of carbon atoms in each hydrocarbon chains less than 14 are fluidic at room temperature [21]. The introduction of a double bond in the hydrocarbon chain can reduce the transition temperature considerably. Also, the level of hydration can change the structures formed by the lipids. The following section discusses various interactions present in self-assembled lipid bilayers and the influence of external parameters such as pressure, pH, and interaction of incorporated molecules on the phase behavior of lipids.

1.3 Different types of interactions governing self-assembly of amphiphilic molecules

The basic driving forces for self-assembly are the interplay between the hydrophilic and hydrophobic interactions of the polar head group and hydrocarbon chains, respectively, with water. Once the self-assembled structures are formed, there will be interactions between monomers within each aggregate. The following part discusses the possible interactions which are responsible for self-assembly and intermolecular interactions in the aggregates. Also, at higher concentrations of self-assembled structures, there will be interactions among the structures, which lead to the formation of different thermodynamic phases of the aggregates.

1.3.1 Hydrophilic and hydrophobic interactions

As we have already discussed, the interplay between hydrophilic and hydrophobic interactions of amphiphiles with water leads to the formation of self-assembled structures.

Hydrophobic interactions

Water can form hydrogen bonds with themselves as well as with polar solutes. The hydrophobic interaction between a non-polar solute and polar solvent can be explained, by taking the example of de-mixing of an oil and water dispersion. At first instant, it seems that the dispersion of oil in water has more entropy of mixing in comparison to its phase-separated state. But the lack of hydrogen bonding sites in the oil molecules leads to the phase separation of oil from water. The microscopic explanation of this phenomenon is not quite well understood.

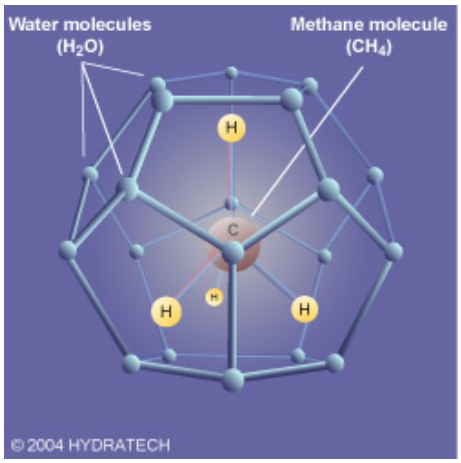

Figure 1.6: Clathrate like arrangement of the water molecule around hydrophobic methane molecule [22]

Out of all the models which explain the hydrophobic effect, the most well-accepted model is that around a hydrophobic solute, water molecules adopt an ordered cage-like clathrate structure [23] having more number of hydrogen bonds per water molecule (4 hydrogen bonds) compared to that in the bulk water (3-3.5 hydrogen bonds) (fig.1.6). The ordered arrangement of water molecules around the solute reduces the entropy of water molecules and thereby the total entropy of the system. When two such non-polar molecules come together, their cage-like regions overlap and release a part of trapped ordered water molecules. This leads to an overall increase in entropy of the system. Hence the clustering and phase separation of oil-like substances from water can reduce the unfavorable interface, increase the entropy of the system and thereby lower the free energy. But hydrophobic interaction alone is not sufficient to drive self-assembly. As we know, it can merely phase separate the hydrophobic molecules from water. Amphiphilicity of a monomer is, therefore, the necessary condition for self-assembly.

Hydrophilic interactions

Although there is no interaction specifically called hydrophilic interaction, the propensity of certain molecules to strongly repel each other in water, in general, is considered as hydrophilic interaction. Hydrophilic molecules are hygroscopic, i.e., they prefer to be in contact with water than in the presence of each other. On the other hand, hydrophobic molecules attract each other in water. All molecules which are able to make a hydrogen bond with water, fall into the category of hydrophilic molecules. This means a hydrophilic molecule should possess a non-zero net dipole moment. Even an uncharged or apolar molecule with the correct geometry can be hydrophilic in addition to hydrated ions and zwitterionic molecules [11]. The solubility of

molecules in water due to their hydrophilicity can be altered by the addition of a hydrophobic part to it, and this effect is vice versa with hydrophobic molecules. Hence hydrophobic and hydrophilic interactions are inter-dependant, nonadditive, but long-ranged [11].

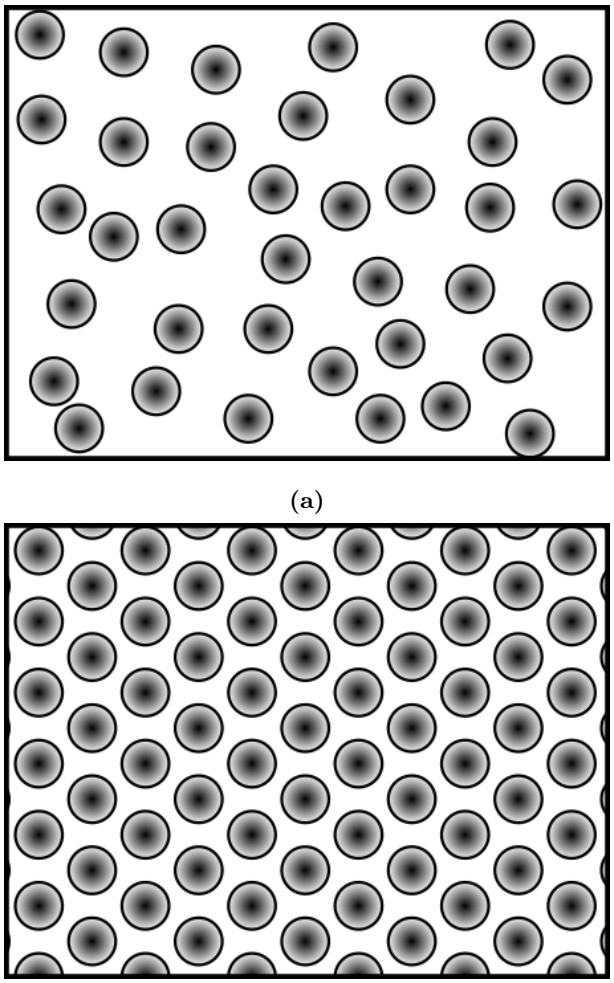

(a)

(b)

Figure 1.7: Schematic representation of positions of chains in (a) Fluid phase and (b) Gel phase of the lipid bilayer

Within the self-assembled structure, the monomers can have different interactions with each other. They can be broadly classified into attractive and repulsive interactions. The attractive interactions mainly arise due to van der Waal's interaction between the chains [24]. Below T_m, the chains are mostly in the trans configuration where the interaction between the chains is strong enough to create an in-plane chain ordering resulting in a lattice. In the case of PC lipids, in the gel phase, the chains get locked into a hexagonal lattice (fig.1.7(b)). But in the fluid phase, positions of the chains are random in the plane of the bilayer (fig.1.7(a)). Long-range correlations between the chains in the gel phase can give peaks in wide-angle x-ray diffraction. But in the fluid phase, the diffraction pattern shows a diffuse peak due to

positional correlations that are short-ranged. The gel to fluid transition does not affect the ordering of the head groups. Under certain conditions such as incubating the sample below gel phase temperature for a prolonged time, the head groups of PC lipids themselves can form a lattice [25]. The interaction between the head groups is usually repulsive, which is mainly coming from steric and hydration repulsions. Around any polar molecule, water forms an ordered arrangement called water of hydration, in which the mobility of water is restricted compared to the bulk water. Hydration forces are assumed to arise from this hydration shell around a strongly hydrated ion. The overlapping of the hydration shell of two polar molecules can give rise to a strong repulsion. This extremely short-ranged interaction comes in to picture only below a range of 1 nm and the strength of which has an exponential decay profile. At a still smaller distance, the interatomic electron clouds can overlap and give rise to a strong short-ranged repulsion called hardcore repulsion or steric repulsion. If the head group is charged, then there exists an electrostatic repulsion between the head groups in addition to repulsion due to hydration and steric interactions. The phase behavior of a lipid bilayer is largely affected by the extent of these different interactions present in the system.

At a sufficiently large concentration of aggregates, inter aggregate interactions can become prevalent, leading to the formation of mesomorphic macro structures. These structures can be ordered arrays of cylinders, stacks of bilayers, or a complex 3D network of interconnected bilayers. Both repulsive and attractive interactions between the aggregates can induce morphological transitions. The repulsive forces arise from electrostatic, steric, and hydration interactions between the aggregates. The competition between these forces can result in the formation of a closely packed structure, which minimizes the free energy of the system. The attractive interactions between the aggregates can also results in a transition of small micelles or vesicles, into large liposomes [11] especially when the electrostatic repulsion between the aggregates is absent or is screened out using salt. The interactions which are significant in stacks of bilayers or multilayers are detailed below.

1.3.2 Van der Waals interaction between two planar surfaces

Van der Waals force between any two molecules originates from three different fundamental electrostatic interactions: dipole-dipole, dipole-induced dipole and dispersion interactions. Dispersion forces are quantum mechanical in nature. It arises due to the presence of an instantaneous dipole in an atom or a molecule which induces, instantaneous dipole moment in the nearby molecule. Although the interaction between the two molecules is very weak in the case of the van der Waals interaction, the interaction energy of a macroscopic object is

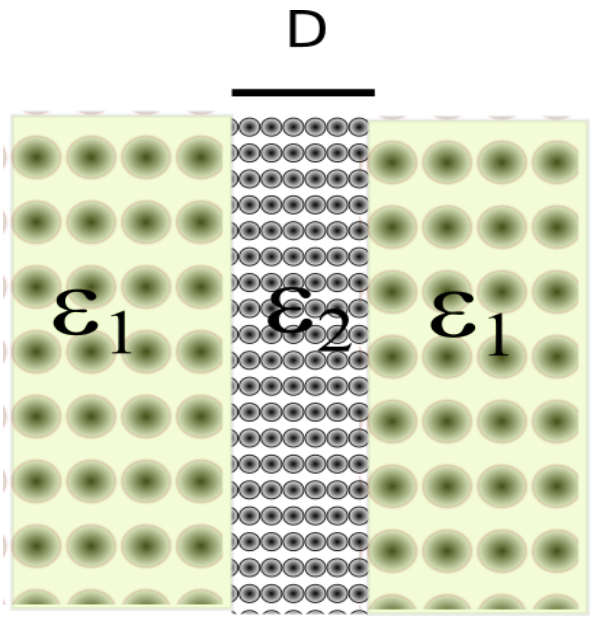

Figure 1.8: Geometry considered for the calculation of van der Waals interaction between two similar surfaces in a medium kept at distance D

stronger because of the additive nature of van der Waals force.

The interaction energy per unit area W(D) of two interacting planar surfaces (fig.1.8) at distance D, given by Lifshitz theory (assuming the interacting particles are forming a continuous medium) is,

$$W(D) = \frac{-A}{12\pi D^2} \tag{1.8}$$

where A is the Hamaker constant, which depends on the dielectric permittivities of interacting particles and that of the medium in between. It can be positive or negative. For two similar surfaces in a dissimilar medium, this interaction is always attractive [11].

1.3.3 Electrostatic interactions

The most realistic version of the model system mimicking the cell membrane is a charged membrane placed in an ionic medium. Therefore, studies on the interaction of charged bilayers in the presence of salt have much biological significance. Contrary to the usual intuition that the repulsion between two charged surfaces is due to electrostatics, the real reason for the repulsion between two charged surfaces in an electrolytic medium is entropic in nature [11].

Consider a charged bilayer which dissociates and releases counterions when placed in water. Much of the released counterions stay near to the surface, forming a layer called the Stern layer, whereas a fraction diffuses to the bulk aqueous phase. The distribution of the counterions as well as of added ions if present, in between two similarly charged bilayers can

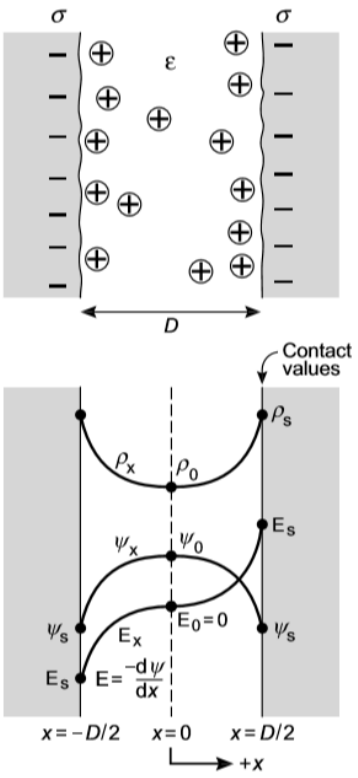

Figure 1.9: Two negatively charged surfaces with surface charge density σ placed in water at a distance D. Ions in the medium are the counterions dissociated from the surface (Top Image). The counterion density profile ρ_x, and the electrostatic potential ψ_x are shown in the bottom figure. E_s, Ψ_s, ρ_s are the corresponding surface or "contact values" of electric field, potential and counterion density [11].

be derived as follows [11],

Case 1: Only counterion

In an aqueous medium, the ionisable groups in the lipid head group release counterions to the bulk and get a surface charge density σ. The chemical potential of released counterions with a valency of Z at any distance x between the two such bilayer surfaces is given by,

$$\mu_x = Ze\psi + KTlog(\rho) \tag{1.9}$$

where ψ is the electrostatic potential (E = -$\frac{d\psi}{dx}$), ρ - number density of ions at any distance x from the midplane. At the mid-plane, $\psi_0 = 0$ where $\rho = \rho_0$ and $|\frac{d\psi}{dx}|_0 = 0$ by symmetry. In thermodynamic equilibrium the chemical potential of the ions should be the same everywhere, i.e.,

$$\mu_x = \mu_0 \tag{1.10}$$

$$Ze\psi + KTlog\rho = Ze\psi_0 + KTlog\rho_0 \tag{1.11}$$

$$Ze\psi = KTlog\frac{\rho_0}{\rho} \tag{1.12}$$

$$\exp(\frac{Ze\psi}{KT}) = \frac{\rho_0}{\rho} \tag{1.13}$$

$$\rho = \rho_0 \exp -(\frac{Ze\psi}{KT}) \tag{1.14}$$

This equation gives the expected Boltzmann distribution of counterions. The net charge density at any point x should satisfy the Poisson equation, which can be represented as,

$$eZ\rho = -\epsilon\epsilon_0 \frac{d^2\psi}{dx^2} \tag{1.15}$$

$$\frac{d^2\psi}{dx^2} = \frac{-Ze\rho}{\epsilon\epsilon_0} \tag{1.16}$$

$$\frac{d^2\psi}{dx^2} = \frac{-Ze\rho_0}{\epsilon\epsilon_0} \exp -(\frac{Ze\psi}{KT}) \tag{1.17}$$

This equation is called the Poisson - Boltzmann equation (PB equation). The solution of this second-order equation with valid boundary conditions gives the electric field at any point x, and is given by,

$$\psi(x) = \frac{KT}{Ze} \ln \cos^2 Mx \tag{1.18}$$

with

$$M^2 = \frac{(Ze)^2\rho_0}{2\epsilon\epsilon_0 KT} \tag{1.19}$$

The above equation gives the screened potential between the charged surfaces at any point x, away from the midplane. If any charge was introduced between the plates in the absence of the counterions, the charge would experience no force since the electric field between the plates mutually cancel each other. The distribution of counterions arises only because of the mutual repulsion between the charges. When the surfaces are moved towards each other, the counterion distribution changes, which induces an osmotic pressure on the surfaces. The

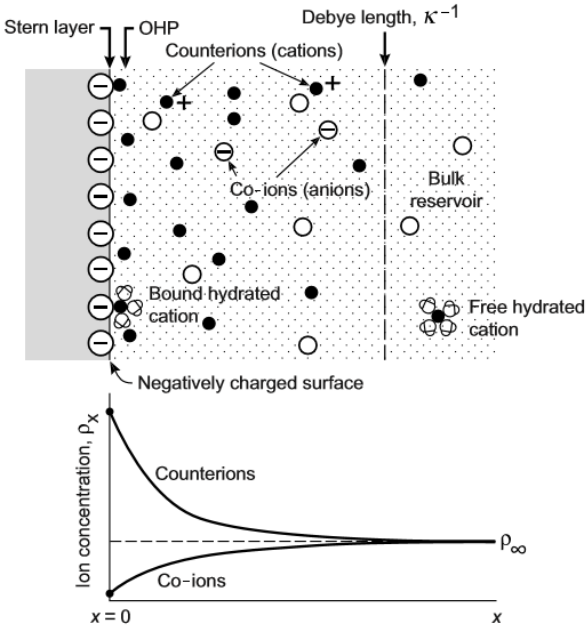

Figure 1.10: Accumulation of counterions and depletion of coions from the charged surface in an 1:1 electrolyte is shown in top figure. OHP (Outer Helmholtz Plane) represents the region beyond which PB equation is satisfied. Bottom image shows profile of counterion and coion concentrations away from the surface [11].

expression for pressure exerted by the counterion distribution on the charged surfaces kept at a distance D is given by [11],

$$P(D) = KT\rho_0(D) \tag{1.20}$$

The equation shows that the pressure on the charged surface depends on the counterion concentration at the mid-plane when the separation between the surfaces is D.

For small σ and D $\longrightarrow$ 0,

$$P(D) \sim \frac{2\sigma KT}{ZeD} \tag{1.21}$$

when D $\longrightarrow \infty$ and large σ

$$P(D) \sim 2\epsilon_r\epsilon_0(\frac{\pi KT}{Ze})^2\frac{1}{D^2} \tag{1.22}$$

Case 2: In the presence of a salt

In the presence of added salt, the electrostatic potential get screened out at any point x between the surfaces.

The PB equation for charged surfaces in an electrolyte solution can be written as,

$$\frac{d^2\psi}{dx^2} = -\sum_i \frac{Z_i e}{\epsilon_r \epsilon_0} {\rho_i}^0 \exp(\frac{Z_i e\psi}{KT}) \tag{1.23}$$

As the counterion concentration $Z_i e$ increases, the potential ψ reduces. Using Debye - Huckel approximation [26],

$$\frac{d^2\psi}{dx^2} = -\sum_i \frac{Z_i e}{\epsilon_r \epsilon_0} {\rho_i}^0 (1 - \frac{Z_i e\psi}{KT}) \tag{1.24}$$

The solution of this equation under valid boundary condition is,

$$\psi = \psi_0 \exp(-kx) \tag{1.25}$$

where

$$k^2 = \sum_i \frac{Z_i \rho_i^0 e^2}{\epsilon_r \epsilon_0 KT} \tag{1.26}$$

where k is known as the Debye length of the diffuse electric double layer. The magnitude of Debye length depends on the solution properties, not on the surface charge density.

The pressure experienced by the surfaces at a separation D is given by [11],

$$P(D) = \frac{1}{2}\epsilon_0 \epsilon_r K^2 {\psi_s}^2 \exp(-kD) \tag{1.27}$$

where ψ_s is the potential at the surface. From the above equation it can be seen that the pressure decreases exponentially with seperation when the solution contains salt.

1.3.4 Entropic interactions

When the bilayers are flexible and thermal energy is enough to compensate for the bending energy of the membrane, the membranes exhibit thermal fluctuations. When two such fluctuating membranes are brought near to each other, undulation modes of each bilayer get suppressed by the presence of the other (fig.1.11). This effectively reduces the entropy of the bilayer, resulting in an effective long-ranged repulsive interaction, which is called undulation repulsion. The expression for pressure exerted by the undulating bilayers at an average seperation D, given by Helfrich [27, 28] is as follows,

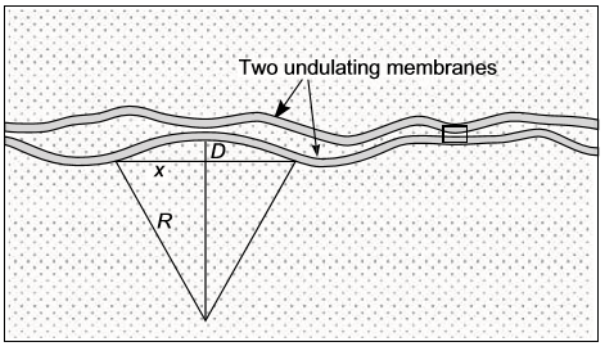

Figure 1.11: Schematic showing two undulating flexible bilayers with an undulation amplitude D [11].

$$P(D) = \frac{3\pi^2(KT)^2}{64\kappa_b D^3} \sim \frac{K^2T^2}{2\kappa_b D^3} \tag{1.28}$$

κ_b is the bending modulus of the bilayer. For a charged lipid membrane, κ_b is much higher than for an uncharged lipid membrane. During the gel to fluid phase transition κ_b decreases.

Similar to undulation repulsion, another kind of entropic repulsion exists between two surfaces decorated with polymer brushes, when the chains from the two surfaces overlap. This repulsion is called steric repulsion and is used for preventing coagulation of colloidal particles by coating the colloidal particles with polymers [11].

1.4 Phase behavior of PC lipids

In a bilayer, lipid molecules that are loosely bound by the hydrophobic and hydrophilic interactions, constantly exhibit in-plane thermal diffusive motion. This lateral mobility of lipid molecules responds non-linearly to the temperature change. As discussed above for each lipid, there exists a well-defined temperature above which the hydrocarbon chains melt and become fluidic. This temperature is called main transition temperature (T_m). Around this transition temperature, there is a discontinuity in lipid mobility and other bilayer parameters, including head group area and thickness. The chain melting transition in the lipid bilayer is a cooperative phenomenon and is affected by a number of intrinsic and extrinsic parameters.

The transition temperature of the lipid bilayer is largely determined by the strength of van der Waals interaction between the chain. For longer chains, interaction strength is higher and they have higher transition temperatures. The presence of a double bond in unsaturated

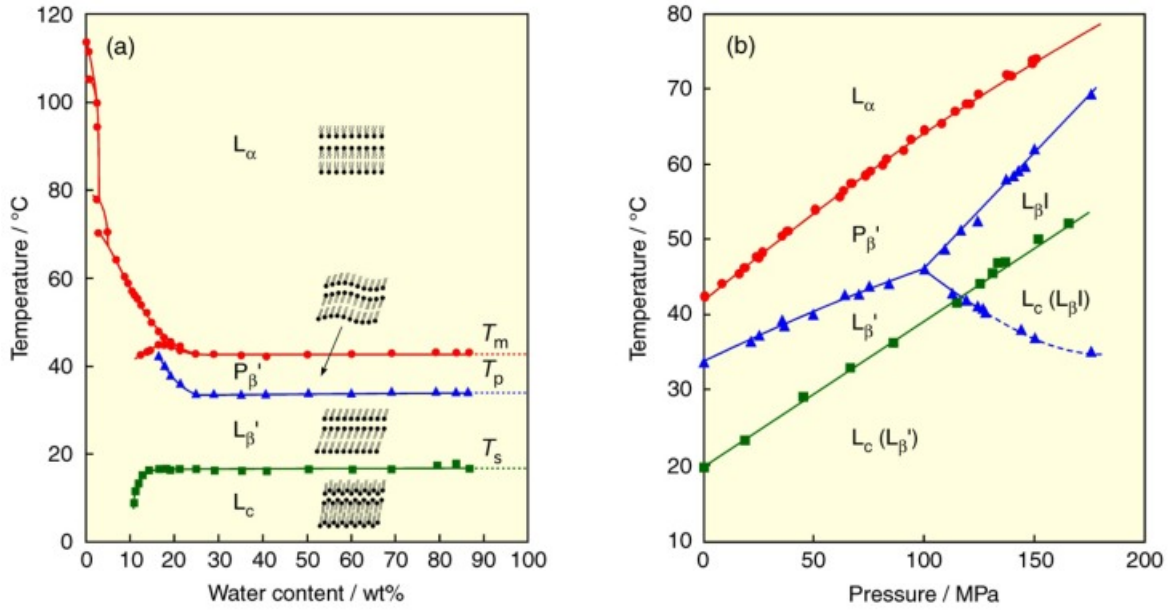

Figure 1.12: Phase diagram of aqueous solutions of DPPC in the temperature - concentration plane at atmospheric pressure (a), and in the temperature - pressure plane at moderate hydration. Here T_m is the main transition temperature corresponding to fluid to ripple phase transition T_p is called pre-transition temperature which corresponds to the transition of ripple phase into a tilted gel phase [29].

lipids can reduce the packing efficiency of chains and hence the transition temperature. The chain melting transition can also be affected by the introduction of other interacting molecules such as cholesterol as well as external parameters such as pressure or tension. Apart from a reduction in lateral mobility and changes in bilayer parameters, the gel phase of the lipid bilayer is also characterised by a well-defined lattice formed by the hydrocarbon chains. In PC lipids, below T_m chains form a hexagonal lattice.

The temperature vs. concentration phase diagram of DPPC lipid is shown in fig.1.12. PC lipids under crystalline conditions show lamellar aggregates. Adding water hydrates the polar headgroups, and forms a hydration layer around it. The interactions between the bilayers limit the water layer thickness, and excess water is phase-separated out from the bilayers and forms bulk water. Lipids with zwitterionic headgroup show only lamellar morphology above 10 wt% water content at atmospheric pressure [29]. PC lipids with saturated chains can exhibit four different types of lamellar phases (fig.1.13). L_c is the sub-gel phase which forms at low temperature characterised by in-plane ordering of the head group region in addition to the formation of the chain lattice. $L_{\beta'}$ phase is the tilted gel phase, that has a lattice formed by chains which are tilted with respect to the layer normal, $P_{\beta'}$ is the ripple phase in which the bilayers are corrugated and L_α is the fluid phase. Each transition is defined by a specific

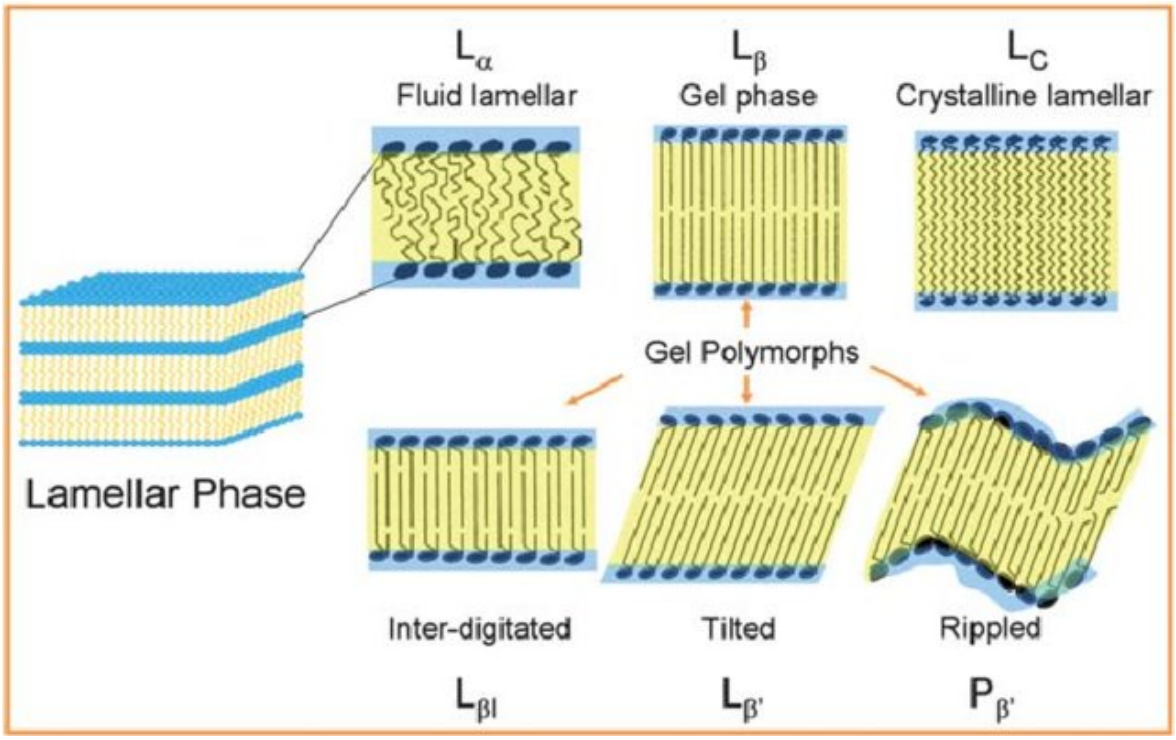

Figure 1.13: Different types of lamellar structures formed by PC lipids adapted from [30]

temperature, which remains as a plateau above 20 wt% of water content (fig.1.12). These transitions are affected by different parameters such as pressure, pH, and the presence of other chemical species, particularly sterols. As an example, (fig.1.12) shows the effect of pressure on the phase behavior of lipid bilayers. At higher pressures, the bilayers form an interdigitated phase. Usually, the interdigitated phase forms in lipid bilayers with large head group area where the two leaflets can interpenetrate each other. Schematics of the interdigitated lipid bilayer and other lamellar phases are shown in fig.1.13.

1.5 Experimental techniques

This section describes the working principles of all the experimental techniques used in this thesis. The theory of x-ray diffraction is detailed in the first part of this section, followed by experimental protocols of small-angle and wide-angle x-ray diffraction. The basic principles of spectroscopic methods such as Fourier Transform Infra Red spectroscopy (FTIR), UV-Vis spectroscopy, fluorescence spectroscopy, and Raman spectroscopy are briefly described. The details of imaging techniques used, such as fluorescence microscopy, Scanning Electron Microscopy (SEM), cryo-SEM, and Atomic Force Microscopy (AFM), are discussed in latter parts of this section. Also, the extraction of diffusion coefficients from the Fluorescence Recovery After Photobleaching (FRAP) technique is explained in the confocal microscopy

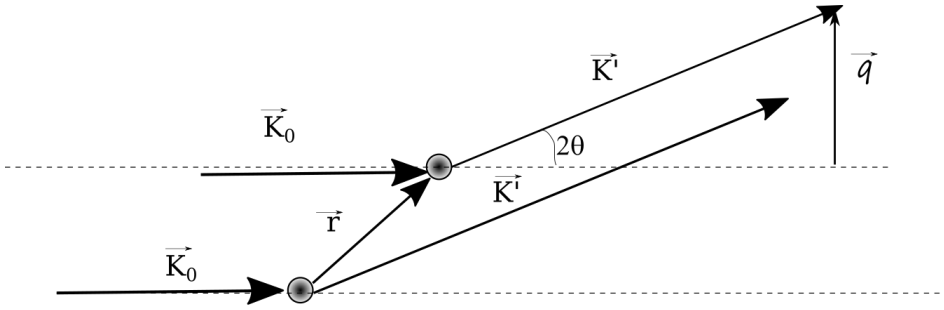

Figure 1.14: Schematic of scattering from 2 point scatterers

section.

1.5.1 Basic principles of x-ray diffraction

Light travels in a constant direction in a homogeneous medium of constant refractive index. Any inhomogeneities in the refractive index of the medium can deviate the traversing direction of light. This effect is called scattering. The scattered light contains information about the nature of scatterers.

X-rays are electromagnetic waves of wavelength ranging between 0.01 nm to 10 nm, which get scattered by electron density variations in a medium. These variations can be periodic, as in crystals as well as non-periodic. Bragg's equation of x-ray diffraction relates the angle at which x-rays get diffracted to the periodicity of the electron density variations. This relation shows that the diffracted x rays will constructively interfere at an angle 2θ, when the incident beam sees a periodicity of $\lambda/(2\text{Sin}\theta)$. This shows that shorter length scale variations in the electron density scatter at larger angles and higher wavelength variations at smaller angles. These limits are correspondingly named as Small Angle X-ray Scattering (SAXS) and Wide Angle X-ray Scattering (WAXS).

The basic principle behind the formation of scattering patterns from any general system can be understood in the following way [31].

Consider two scattering points displaced by a distance $\vec{r}$ from each other (fig.1.14). The incoming plane wave takes the form given below, with ϕ_0 as the amplitude and $\vec{K_0}$ as the wave vector,

$$\phi_{inc} = \phi_0 \exp\left(i\vec{K_0}.\vec{r}\right), \tag{1.29}$$

,

which gets scattered by the point scatterers. The scattered waves with a wave vector $\vec{K'}$ interfere at a distance R » r. The amplitude of diffraction pattern produced from this

arrangement is given by,

$$\phi_{sc} = \frac{\phi_0 S}{R} \exp(i\vec{K'}.\vec{R}) = \frac{\phi_0 S}{R} \exp(i[\vec{K_0}.\vec{R} - \vec{q}.\vec{r}]), \tag{1.30}$$

where S is the scattering strength of the medium and $\vec{q} = 4\pi \sin\theta / \lambda$ is the scattering vector corresponding to the scattering angle 2θ and x-ray wavelength λ.

Consider N number of scatterers instead of two-point scatterers depicted above. The amplitude of the total scattered x-rays at a distance R is given by

$$\phi_{sc} = \frac{\phi_0 S}{R} \exp(i\vec{K_0}.\vec{R}) \sum_{n=1}^{N} \exp(-i\vec{q}.\vec{r}_n) \tag{1.31}$$

which can be written as,

$$\phi_{sc} = \frac{\phi_0 S}{R} \exp(i\vec{K_0}.\vec{R}) \sum_{n=1}^{N} \delta(\vec{r} - \vec{r_n}) \exp(-i\vec{q}.\vec{r}) \tag{1.32}$$

The function $\delta(\vec{r} - \vec{r_n})$ defines the positions of the scatterers. For a system with a continuous electron density distribution, the discrete function $\delta(\vec{r} - \vec{r_n})$ can be replaced with a continuous electron density function $\rho(r)$. Thus the above equation takes the form,

$$\phi_{sc} = \frac{\phi_0 S}{R} \exp(i\vec{K_0}.\vec{R}) \int \rho(r) \exp(-i\vec{q}.\vec{r}) dr \tag{1.33}$$

Hence diffraction pattern obtained is nothing but the Fourier transform of electron density profile of the system. The intensity of diffraction pattern is given by,

$$I(\vec{q}) = |\frac{\phi_0 S}{R} \exp(i\vec{K_0}.\vec{R}) \int \rho(r) \exp(-i\vec{q}.\vec{r}) dr|^2 = A|G(q)|^2 \tag{1.34}$$

where $G(q) = \int \rho(r) \exp(-i\vec{q}.\vec{r}) dr$ and A is a constant independent of q

Electron density profile of any periodic lattice can be constructed by the convolution of a lattice function with a basis function. Lattice function $\rho_l(\vec{r})$ describes the positions of all the repeating units in space. The individual repeating units are called the basis of the system, and the basis function $\rho_b(\vec{r})$ describes the electron density of the repeating unit. The convolution of these two functions, therefore, generates the entire arrangement of the crystal in real space. This can be represented mathematically in the following way,

$$\rho(\vec{r}) = \rho_l(\vec{r}) \circledast \rho_b(\vec{r}) \tag{1.35}$$

As explained in the previous section, the diffraction phenomena can be easily explained in the reciprocal space of $\rho(\vec{r})$. This means the intensity variations of x-ray diffraction patterns

obtained from the medium corresponds to the Fourier transform of electron density variations in real space. The Fourier transform of the above equation gives,

$$f(\vec{q}) = f_l(\vec{q}).f_b(\vec{q}) \tag{1.36}$$

This expression is the direct readout of amplitudes of the diffraction pattern. But x-ray instrument can only measure the intensities of the x-ray beam scattered as a function of scattering vector $\vec{q}$. The diffraction pattern intensities can be written as

$$I(\vec{q}) = |f(\vec{q})|^2 = S(\vec{q})|f_b(\vec{q})|^2 \tag{1.37}$$

here S(q) is called the structure factor of the system, which contains information about the lattice structure or positions of the basis. $f_b(\vec{q})$ the form factor, gives information about the electron density distribution of individual scatterers or basis.

The above equation represents the calculated intensity of x-ray diffraction for a given sample with structure factor S(q) and form factor $f_b(\vec{q})$. To compare with the experimentally observed intensities, this expression has to be corrected for different geometrical and physical corrections, including detector - sample geometry, polarisation, and absorption by the sample [32]. The intensity of scattered x-rays detected by a one-dimensional (1D) detector should be multiplied with q^2 to account for the 3D scattering from the sample. In the case 2D detector, this factor is q. Also, the path traversed by x-rays in directions in of the sample could be different, which means that even in the relative scale, the absorption of x-rays is different at different peaks in the diffraction pattern. The corresponding correction requires a complete knowledge of the thickness of the sample at each point. Scattering of x-rays from an electron is considered to be Thomson scattering in a classical sense, which defines a preferred polarisation for the scattered x-rays, even for unpolarised incident x-rays. This factor is given by,

$$P = \frac{1 + \cos^2(2\theta)}{2} \tag{1.38}$$

For small-angle scattering, P $\sim$ 1. More than one set of planes can satisfy Bragg condition simultaneously and contribute to the intensity observed at a given q value. This correction is called multiplicity factor and can be taken care of by calculating all possible Bragg planes contributing to the diffraction intensity.

The studies described in this thesis use both SAXS and WAXS for unoriented lipid dispersions using a 1D detector. Aligned multilayer stacks of lipids under controlled humidity conditions were characterized using a 2D detector.

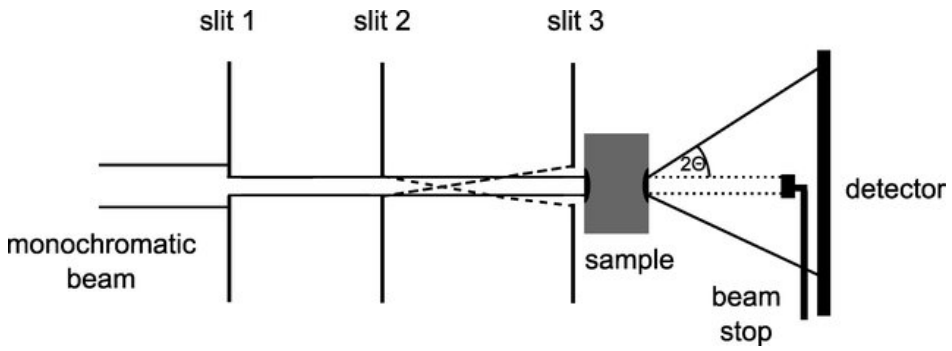

Figure 1.15: Schematic showing 1D SAXS setup

1.5.2 Small Angle X-ray Scattering (SAXS)

Small-angle X-ray scattering studies were performed using a HECUS S3 Micro system equipped with a Cu anode X-ray generator (Genix) and a 1D position-sensitive detector (PSD), the schematic of which is shown in fig.1.15. Samples were taken in 0.7 or 1.0 mm capillaries and were flame sealed. A Peltier-controlled stainless steel holder was used to maintain the sample temperature, which can span a range of 5°C to 85°C. Data were acquired for 1 to 2 h, over a range of the magnitude of the scattering vector (q) from 0.2 nm^{-1} to 6.0 nm^{-1}. Analysis of the SAXS data was carried out using the procedure described in [33] and discussed below.

Lipids, such as DMPC, self-assemble in water to form bilayers. A dilute lipid solution, in general consists of isolated bilayers in the form of unillamellar vesicles (ULV), and correlated stacks of bilayers in the form of multilamellar vesicles (MLV). The scattered intensity from such a dispersion can be written as [33],

$$I(q) \propto \frac{1}{q^2}(S(q)|F(q)|^2 + N_b|F(q)|^2), \tag{1.39}$$

where q is the magnitude of the scattering vector, S(q) the structure factor, describing the lamellar structure within the MLVs, and F(q) the form factor of a bilayer. N_b is the relative fraction of ULVs.

The structure factor of lamellar phase is given by,

$$S(q) = N + 2\sum_{k=1}^{N-1}(N-k)\cos(kqd) \times \exp[-d^2q^2\eta_1\gamma/(2\pi)^2](\pi k)^{-d^2q^2\eta_1/(2\pi)^2}, \tag{1.40}$$

where N is the number of correlated bilayers, d the lamellar periodicity, γ the Euler's constant and η_1, the Caillé parameter, defined as, $\eta_1 = q^2KT/(8\pi\sqrt{\varepsilon B})$, where ε and B are the curvature and compression moduli of the lamellar phase, respectively, and K is the

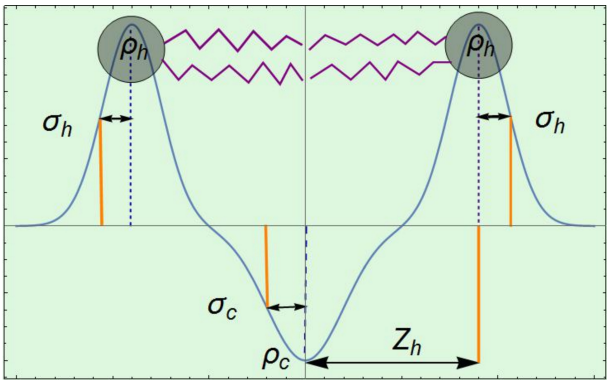

Figure 1.16: Schematic of the 3-Gaussian model for the transbilayer electron density profile. ρ_h and ρ_c are the amplitudes of the two Gaussians representing the headgroup region and the bilayer center, respectively; σ_h and σ_c are their widths. z_h is the separation between the centers of these two Gaussians, so that $2z_h$ is a measure of the bilayer thickness.

Boltzmann constant. ε can be expressed in terms of the bilayer bending rigidity modulus κ_b, as, $\varepsilon = \kappa_b/d$, where d is the lamellar periodicity.

Form factor F(q) is the Fourier transform of the trans-bilayer electron density profile $\rho(z)$, which can be represented in terms of three Gaussians, describing the two headgroup regions and the bilayer mid-plane (fig.1.16) [34].

$$\rho(z) = \rho_m + \bar{\rho}_c \exp[-z^2/2\sigma_c^2] + \bar{\rho}_h \left(\exp[-(z-z_h)^2/2\sigma_h^2] + \exp[-(z+z_h)^2/2\sigma_h^2]\right), \quad (1.41)$$

where $\bar{\rho}_c = \rho_c - \rho_m$ is the relative chain electron density with respect to the methyl group and $\bar{\rho}_h = \rho_h - \rho_m$ is the relative headgroup electron density. σ_h and σ_c are the widths of the headgroup and chain Gaussians, respectively. z_h is the distance from the bilayer center to the centre of the head group region; $2z_h$ is, therefore, a measure of the bilayer thickness.

Fourier transforming $\rho(z)$, the following expression for the bilayer form factor is obtained,

$$F(q) = 2F_h(q) + F_c(q), \quad (1.42)$$

where

$$F_h(q) = \sqrt{2\pi}\bar{\rho}_h\sigma_h \exp[-\sigma_h^2 q^2/2]\cos(qz_h), \quad (1.43)$$

and

$$F_c(q) = \sqrt{2\pi}\bar{\rho}_c\sigma_c \exp[-\sigma_c^2 q^2/2]. \quad (1.44)$$

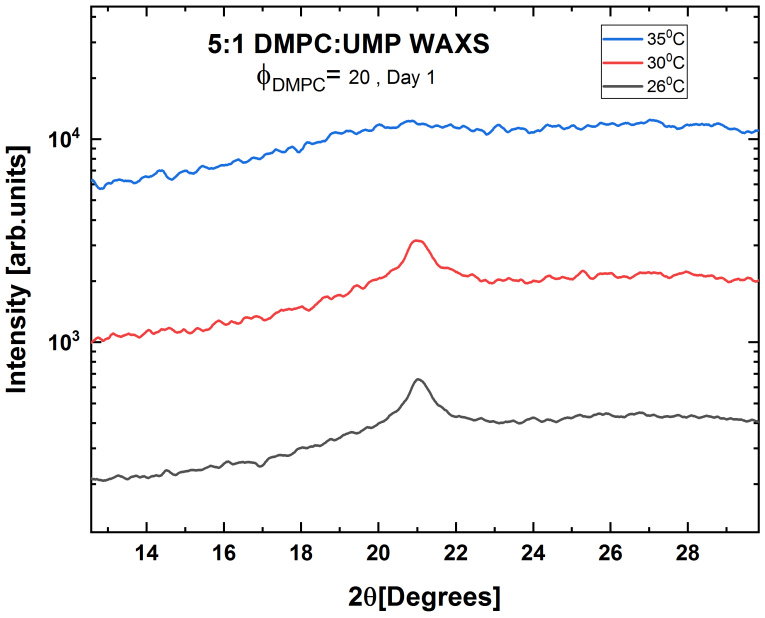

Figure 1.17: WAXS data obtained for the gel to the fluid transition of 5:1 DMPC: UMP sample. The presence of a single sharp peak indicates that the chains form a hexagonal lattice which melts between 30°C and 35°C

SAXS data obtained from MLV dispersions were fitted to eqn.2.1 using a nonlinear fitting algorithm from Mathematica. Average values of bilayer structural parameters obtained from at least 10 data sets were used to construct the electron density profiles. The first term in eqn.2.1 was neglected in the case of samples containing only ULVs.

1.5.3 Wide Angle X-ray Scattering (WAXS)

As discussed before, WAXS gives information about the shorter length scale electron density variations in the system. Below T_m of each lipid, the chains pack into a lattice, and WAXS data contain corresponding peaks. Therefore thermal phase behavior of lipid systems can be monitored using WAXS. The T_m of the lipid is affected by different interacting molecules. Hence the effect of the interaction of different molecules on the phase behavior of pure lipid can be probed using WAXS (fig.1.17). Samples were filled in 0.7 mm or 1 mm capillaries for WAXS measurement. Samples were placed in a temperature-controlled chamber (LINKHAM) to execute WAXS measurements at different temperatures. Diffraction measurements were carried out using PANalytical Empyrean system equipped with a Cu x-ray LFF tube source having a line beam profile, working at 45 kV and 40 mA. The diffracted x-rays were collected in the angle range 1° to 30° using a PIXcel detector. The chain lattice parameters were calculated

by accurate indexing of the peaks obtained in the wide-angle region of the diffractogram.

1.5.4 Aligned 2D X-ray Diffraction

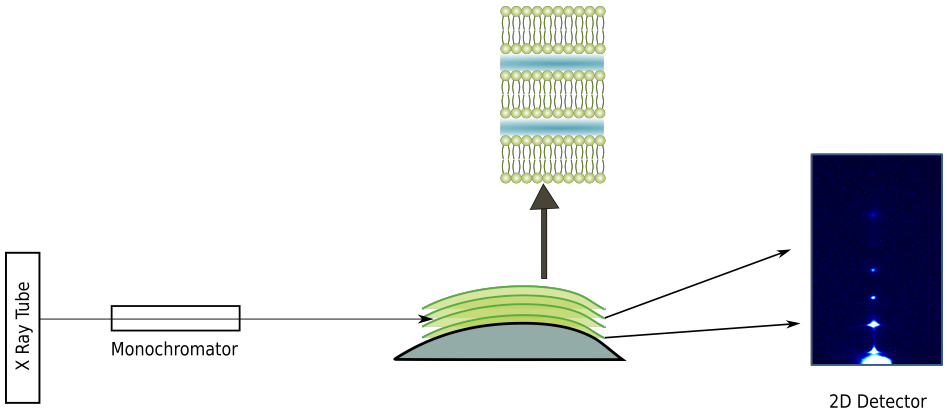

Figure 1.18: Schematic of the experimental setup used to study aligned lipid samples under hydration

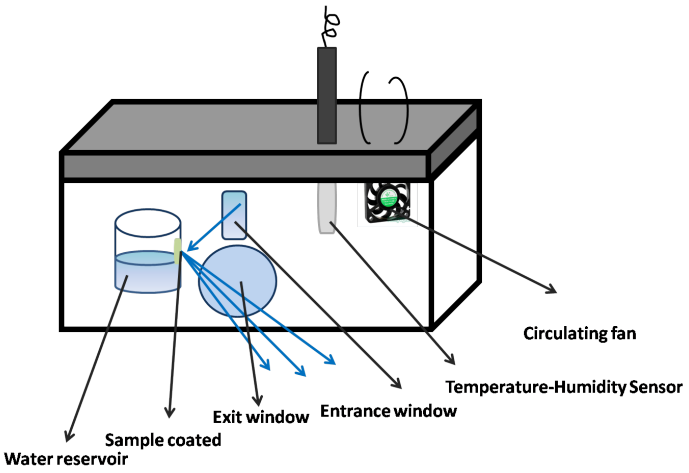

Figure 1.19: Schematic of the temperature- humidity controlled sample chamber for aligned samples

Multilayer stacks of lipid bilayers were prepared by coating the sample solution in chloroform, on a curved glass substrate. The samples were incubated in a hydration chamber and cycled through the transition temperature to get good alignment. The samples were then transferred to a home built chamber with temperature control through water circulation (Julabo). The entrance and exit windows of the chamber are covered with Mylar sheets. The humidity inside the chamber is maintained at 100% by a water reservoir. Further, the humid air is circulated inside the chamber using a circulating fan. The possibility of water condensation on the relative cooler window regions of the chamber is avoided using hot air blowers at the windows. The x-rays are produced from a GeniX 3D (Xenocs) x-ray generator operating at 50 kV and 0.60 mA. The sample is exposed to a Cu K_α x-ray beam (λ = 1.54 Å) using a multilayer mirror and scatter-less slit collimating arrangement. X-ray diffraction pattern is

collected using a 2D image plate MAR345 (Marresearch). Sample to detector distance can be tuned to measure SAXS and WAXS scattering from the sample. Pixel size chosen was either 100 μm or 150 μm. Sample to detector distance is calibrated using a silver behenate sample having a periodicity of 58.38 Å. A temperature-hygrometer (Testo 610) is inserted in the chamber to measure the temperature and relative humidity inside the chamber.

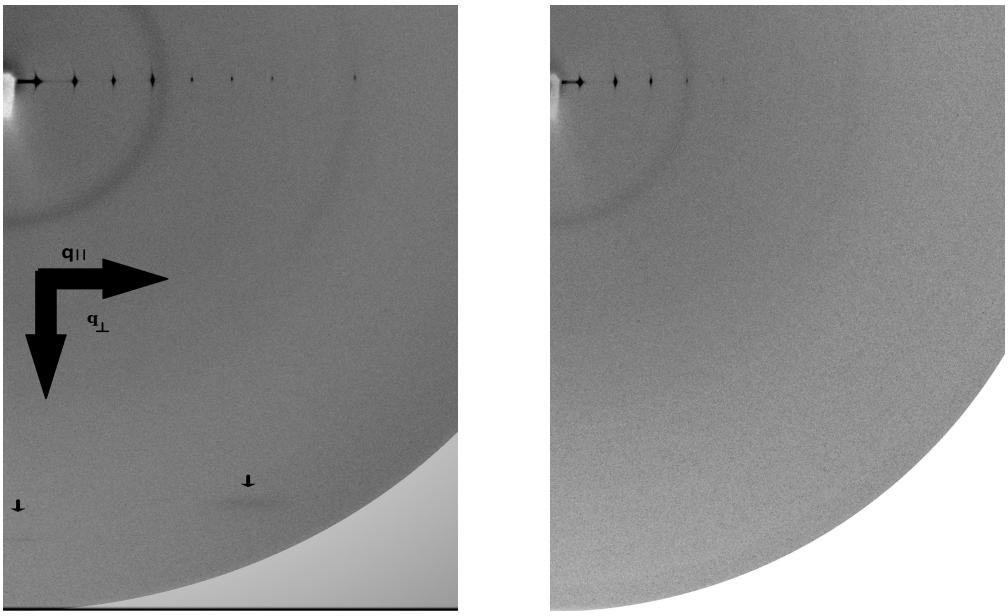

(a) **(b)**

Figure 1.20: X-ray data from aligned DMPC multilayers taken (a) at 10°C, showing, off-axis peaks that correspond to the tilted gel phase (b) Fluid phase at 31°C showing no peak in the wide region.Peaks in the small angle region correspond to the lamellar periodicity of the two phases.

The multilayer stacks of hydrated lipid bilayers get aligned normal to the substrate surface. X-ray diffraction patterns obtained from such aligned samples can give information about the orientation of the chains with respect to the bilayer normal [35]. As an example, the DMPC gel phase is characterised by a hexagonal chain lattice with a chain titled away from the bilayer normal towards the nearest neighbour. The mismatch between the large head group area and the cross-sectional area of the chains leads to the tilt of chains in the gel phase of DMPC. Correspondingly aligned sample show, off-axis peaks in the q perpendicular plane (fig.1.20(a)).

1.5.5 Fourier Transform Infrared Spectroscopy (FTIR)

FTIR is used extensively as a non-invasive method of material analysis. The basic principle behind this technique is the absorption of the input IR band by different molecules [36]. IR band excites the vibrational levels of chemical bonds in the sample. Different compounds will

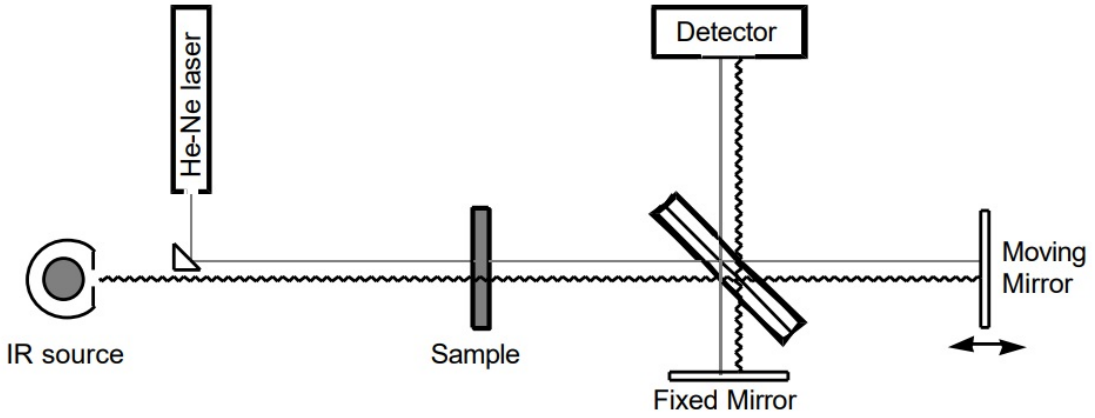

Figure 1.21: Diagram of FTIR setup adapted form [36]

have different chemical groups and bonds and thereby different vibrational energies. Each vibrational energy state has a particular wavelength of absorbance in the IR band and hence becomes the signature of the compound. A spectrometer is used to decode the frequencies and corresponding transmittance values of the output IR beam from the sample [36]. Besides material identification, FTIR can also give quantitative information about the amount of different compounds in a mixture, by analysing the shape and size of individual absorbance peaks.

In a conventional spectrometer, the IR beam is allowed to pass through the sample as well as a reference in a dual-beam geometry. The difference in transmitted intensity is recorded precisely at each wavelength using a grating or prism. This process is slow, due to the various filters and gratings involved, which usually takes a few minutes to complete. FTIR uses a smarter way to analyse the same absorbance information in a lesser time ($\sim$ 2s). This became possible after the invention of the Michelson interferometer, which is the heart of the modern FTIR setup. The interferometer is included in the sample chamber just after the sample cell. IR radiation of different frequencies is allowed to pass through the sample. The output band is fed into the interferometer. The basic structure of the interferometer is shown in fig.1.21. The input beam is split into two perpendicularly propagating beams by a beam splitter, which gets reflected from two mirrors kept in their path. The position of one mirror is fixed, whereas the other mirror can travel a maximum distance of a few millimeters (2-3 mm). The reflected beams interfere at the beam splitter. The interference pattern contains information about the difference in path length traversed by the two beams, which can be correlated to

the constructive interference of different frequencies. Hence by moving the mirror, different frequencies ranging from 400 cm^{-1} to 4000 cm^{-1} can be spanned. Since distance moved by the mirror is in the time domain, the final output data is a Fourier transform of signal (transmitted intensity as a function of time) reaching the detector. As the intensity of the light transmitted by the sample is weak and contains thermal noise, the interference from a He - Ne laser is used as the reference for the frequencies spanned [37]. All the FTIR experiments in this thesis used Shimadzu FTIR 8400/8900 equipped with a neon laser having an output of 0.5 mW.

1.5.6 UV - Vis Spectroscopy

Much similar to FTIR spectroscopy, UV-Vis spectroscopy [38] is an absorbance spectroscopy that works in the UV-Vis region of the electromagnetic spectrum spanning the wavelength range 200 nm - 800 nm. This region of light excites the electronic transitions in the sample. Hence the absorbance peaks correspond to the different allowed transitions from the ground to the excited electronic states. Besides this, the absorbance of light is also affected by macroscopic properties of the sample, such as the concentration of the sample, path length of the light through the sample, etc. Beer - Lambert law gives the qualitative measure of the concentration of the sample using the expression below,

$$A(\nu) = -log(I/Io) = \epsilon(\nu) * C * l \tag{1.45}$$

where A(ν) is the absorbance value at different frequencies ν, I is the intensity of transmitted light, and Io is the initial incident intensity of light. $\epsilon(\nu)$ is the molar extinction coefficient, which is the measure of how strongly the sample absorbs a given wavelength per molar concentration. C is the concentration of the sample, and l is the path length of the light inside the sample.

UV-Vis spectrometer from Perklin-Elmer (lambda 35) is used in all the studies in the thesis. Two radiation sources, a deuterium lamp, and a tungsten halogen lamp cover the working range of the spectrometer. The transmitted light is collected using a photo-diode detector.

1.5.7 Fluorescence Spectroscopy

Fluorescence spectroscopy is complementary to UV-Vis spectroscopy [38, 39]. Fluorescence spectroscopy gives a direct readout of fluorescence emission from the sample. As previously discussed, the absorbance of electromagnetic radiation in the UV-Vis region excites the elec-

tronic transitions in the sample. The excited electronic levels of the molecules are shortlived. The system comes back to the ground state either by radiative emission or by non-radiative energy transfers. The molecules having fluorescence properties will relax to the ground state by the radiative process. This will correspond to defined emission peaks in the fluorescence spectra. Although samples radiate fluorescence emission in all directions, the measurement is done at 90° to avoid direct transmitted light. The typical experimental setup is shown in fig.1.22.

The xenon lamp is the source of UV-Vis excitation radiation. Two monochromators, respectively, in excitation and emission pathways, set the frequency. Since the energy of emitted light is always lower than that of the incident light, the excitation filter is set at lower frequencies compared to emission filters. A photon-counting detector measures the emitted light from the sample. Since the fluorescence spectrometer has two monochromators, excitation spectra also can be recorded for a given emission peak. All the fluorescence spectra measurements were done in the Horiba Fluoromax-4 spectrophotometer.

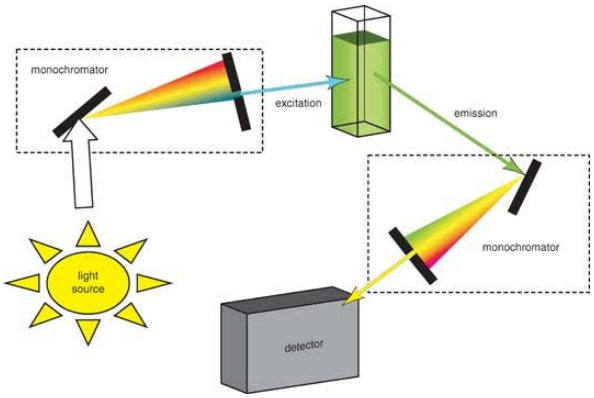

Figure 1.22: Diagram of fluorescence spectroscopy adapted form [39]

1.5.8 Raman Spectroscopy

Raman spectroscopy is a scattering technique [40]. When a monochromatic light interacts with a sample, the sample scatters the light mostly by elastic scattering, where the wavelength of scattered light is the same as that of the incident light (Rayleigh scattering). The scattered light also contains a small fraction of inelastically scattered light, which has information about the vibrational levels of the compound. This inelastically scattered light can have wavelength lower or higher than that of the incident light. When the wavelength of scattered light is higher, the frequency shift is called the Stokes shift. When the wavelength of scattered radiation is lower, it is called an anti-Stokes shift. The Stokes shift is due to the transitions of molecular vibrational state from a lower energy state to a higher energy state. They are more

intense than the anti-Stokes lines and hence measured in conventional Raman spectrometers. The magnitude of the Raman shift does not depend on the wavelength of the incident light. Hence it can be treated as a signature of the sample. A change in the polarizability of the states is essential to show Raman scattering [40].

Raman Spectra are usually recorded from 5 or 400 Δcm^{-1} to 3800 to 4000 Δcm^{-1}, depending on the spectrometer design and optical components involved. A microscope is used to focus the incident light(usually lasers) on the sample. The scattered light is collected at 90° angle using a photomultiplier tube or CCD. All the Raman scattering data in this thesis were collected using HORIBA Jobin Vyon T64000 Raman Microscope.

1.5.9 Differential Scanning Calorimetry (DSC)

DSC measures the heat capacity of the sample as a function of temperature. A known mass of the sample is heated, and the change in heat flow is measured for each rise in temperature. Any process such as phase transition, glass transitions, or aging involves a certain amount of heat inflow or release, which is detected in DSC measurements. Hence heat capacity and enthalpy can be easily measured along with the precise transition temperature.

In a typical DSC measurement, the sample and a reference are heated simultaneously, and the heat flow/energy for each rise in temperature is monitored [41]. The difference in heat flow for the same temperature between the reference and the sample during phase transition, aging, etc. will give information about the enthalpy of phase transition. The gel to fluid transition in lipid bilayers can be easily detected using DSC. Typical transition enthalpy is around 5 kJ/mol for the pre-transition and 25 kJ/mol for the main transition of saturated lipid DMPC. Metler Teledo DSC 3 model was used for all the DSC experiments.

1.5.10 Fluorescence Microscopy and Confocal Fluorescence Microscopy

Fluorescence microscopy uses the property of fluorescence of dye molecules to image materials instead of absorption, reflection, attenuation, and scattering. In this, the specimen is illuminated with a beam of light from a nearly monochromatic source [42]. The fluorophores embedded in the sample absorb the light and re-emit at a wavelength higher than the excitation wavelength. The weak re-emitted fluorescent signal is separated from the background scattering using a dichroic beamsplitter and emission filter arrangement (fig.1.23). Most of the fluorescence microscopes work in epi-fluorescence mode, where the illumination of the sample, as well as the collection of re-emitted light, is done using the same objective. Since this configuration can avoid all the intense transmitted direct light, only reflected light needs

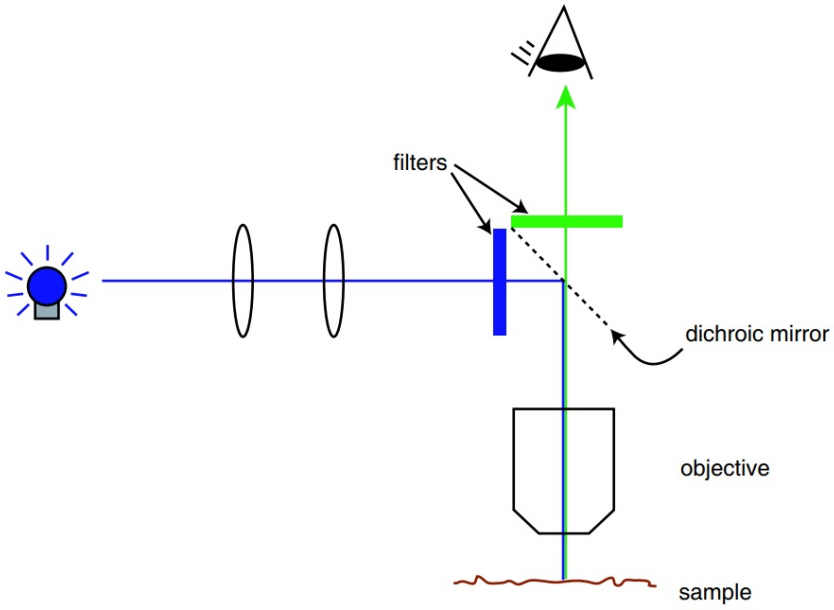

Figure 1.23: Diagram of a fluorescence microscope [42]

to be separated from the fluorescence signal, which improves the signal to noise ratio. The reflected light is separated from the fluorescence signal using a dichroic mirror, which acts as a wavelength-specific filter transmitting the fluorescent light while blocking the excitation light [42]. Fluorescence imaging of the samples was carried out using an Olympus epi-fluorescence microscope (model number IX 70).

In fluorescence microscopy, the entire area of the sample is illuminated. The resolution of the image is mainly limited by the background light from unfocused regions of the specimen. Confocal microscopy beats this drawback of wide-field fluorescence microscopy by using pointwise illumination and a pointwise detection of [42]. This is achieved using two pinhole apertures in the illumination and detection pathways. The working of confocal can be understood from the simple description below. Confocal microscopy setup from Leica with model number TCS Sp8 was used for all the confocal imaging and FRAP measurements.

Two parallel lens system focuses light from the focal point of the objective to that of the eyepiece (fig.1.24). The dark blue point represents the point that is focused, and the light blue path represents light from the unfocused region. Clearly, the image formation of the light blue light path is at a different region of detector compared to dark blue. The unnecessary light which reaches detector form light blue region can be controlled by the use of a pinhole aperture at the image formation plane. Again the illumination region can also be controlled by using specific illumination of dark blue point using another pinhole in the

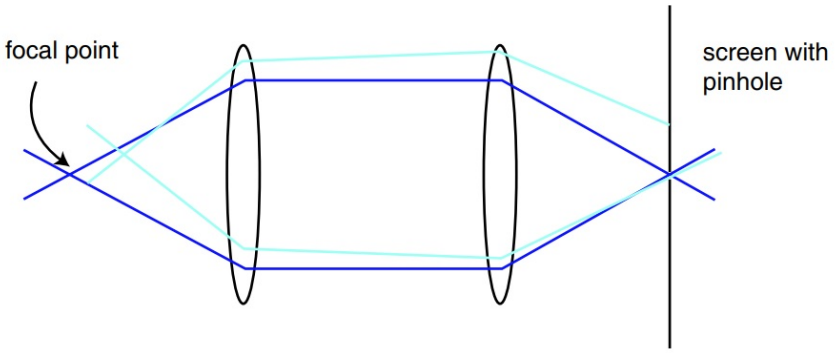

Figure 1.24: Diagram of confocal fluorescence microscopy setup adapted form [42]

illumination pathway. With the two pinhole arrangement confocal microscope considerably reduces the background light from the unfocused regions of the sample. Since the pinhole plane is in conjugation with the lens focal plane, this technique is called confocal fluorescence microscopy. The use of pinhole to reduce the background scattering also reduces the amount of light reaching the detector. In order to increase the signal to noise ratio, in modern confocal microscopes, lasers are used as the light source. The specimen is illuminated point by point, and data is collected correspondingly using motor-driven vertically and horizontally scanning mirrors, which control the path of incoming and outgoing light. The weak fluorescent signal is collected using sensitive detectors such as photomultiplier tube (PMT) or avalanche photodiode (fig.1.25). The image created by confocal microscopy is a thin section of the sample, and therefore the image generation method is called optical sectioning. This ability of confocal microscope to generate a well-focused optical section is used in 3D imaging of samples.

The use of intense light and localised focusing introduces significant photobleaching of fluorophores. This effect is used as the application of confocal microscopy to measure the diffusion of particles. A region of interest is photobleached using an intense laser beam, and recovery of fluorescence is monitored and measured as a function of time. From the recovery curve, the diffusion of molecules in the sample can be measured. This method is called Fluorescence Recovery After Photobleaching or FRAP [43]. Diffusion of lipids in supported lipid bilayers can be easily studied using this method.

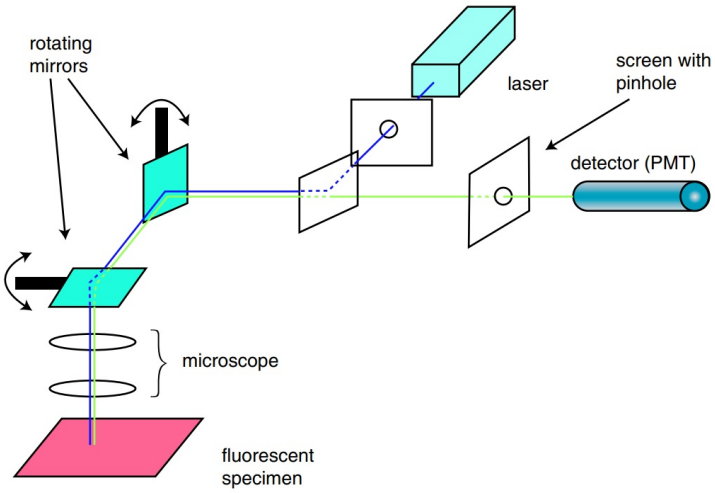

Figure 1.25: Diagram of fluorescence microscopy setup adapted form [42]

1.5.11 Lipid diffusion measurement by Fluorescence Recovery After Photobleaching (FRAP)

Diffusion measurements of proteins and lipids elaborate the understanding of how lipids and proteins interact with their environment, such as binding of transcription factors with DNA and association of proteins and lipid with membrane domains [43, 44]. Biologists use many ways to measure the diffusion coefficients of proteins and lipids, which include single-particle tracking (SPT), fluorescence correlation microscopy (FCS), photoactivation, and FRAP. FRAP is a very straight forward way of measuring diffusion coefficients using confocal laser scanning microscopy [45]. In a typical FRAP experiment, a region of interest (ROI) in the fluorescent sample is bleached using a high-intensity laser beam. As the fluorophore bleaches out, the intensity of the ROI goes down. The recovery of fluorescence intensity due to the diffusion of fluorophores from the other regions of the sample is measured as a function of time. From the recovery curve, the diffusion coefficient can be extracted. In the case of supported lipid bilayers, the recovery of intensity by diffusion of dye molecules represents the diffusion of lipid itself. In all the studies done in this thesis, circular ROIs (10-20μm) were chosen. The laser beam was shot onto the ROI for about 10 - 15 s to bleach the region. The recovery of intensity is obtained as a function of time. Diffusion coefficients were extracted from the recovery curve using the procedure described in [46], which is briefly discussed below and summarised in the chart.

Assume the concentration of fluorescent lipids C satisfies the diffusion equation,

$$\delta C/\delta t = D\Delta C \tag{1.46}$$

where D is the diffusion coefficient and $\Delta = \delta^2/\delta x^2 + \delta^2/\delta y^2$.

The solution of the above equation is computed by a convolution of the initial concentration profile with the fundamental solution of the diffusion equation. This can be understood in the following way.

Consider the bleaching of a circular ROI. Immediately after bleaching the dye concentration profile only depends on the beam profile. Hence C(x,y,0) is independent of molecular diffusion. The concentration profile at any later instant is therefore given by the convolution of the initial profile with the fundamental solution of the diffusion equation.

$$C(x,y,t) = \int\int C(x-x',y-y',0)\phi_{Dt}(x',y')dx'dy' \tag{1.47}$$

The fundamental solution of diffusion equation in two dimensions is given by,

$$\phi_{Dt}(x,y) = \frac{1}{4\pi Dt} exp - (\frac{x^2+y^2}{4Dt}) \tag{1.48}$$

The total fluorescence intensity F(t) of ROI at any time t depends on the concentration of fluorescent molecules and intensity of incident light I_{r_n}. i.e.,

$$F(t) = q\int\int \epsilon I_{r_n}(x,y)C(x,y,t)dxdy \tag{1.49}$$

Where q is the quantum yield of the dye, C(x,y,t) is the concentration of the fluorescent molecule in the confocal volume at t, ϵ is related to the attenuation factor of the beam during the observation.

It was empirically demonstrated that confocal post bleach profile can be expressed as a Gaussian of the form

$$C(x,y,0) = C_i(1 - k.\exp(\frac{-2(x^2+y^2)}{{r_e}^2})) \tag{1.50}$$

where C_i is the prebleach fluorescent dye concentration, r_e is the effective radius of post bleach profile which is different from nominal radius of ROI (r_n). r_e is estimated by fitting the postbleach line intensity profile with a Gaussian function.

For a given initial condition C(x,y,0) and unknown diffusion coefficient D, the diffusion FRAP equation evaluated by Axerold et.al [47, 48] is given by,

$$F(t) = F_i(1 - \frac{k}{1+\gamma^2+\frac{2t}{\tau_d}})M_f + (1-M_f)F_0 \tag{1.51}$$

where $\tau_d = {r_e}^2/4D$ and $\gamma = r_n/r_e$ and M_f is the mobile fraction of molecules.

$$M_f = \frac{F_\infty - F_0}{F_i - F_0} \tag{1.52}$$

where F_i is the prebleach intensity and F_0 is the post bleach intensity, F_∞ is the post bleach steady state fluorescence intensity.

At t = 0 F(0) = F_0, k can be evaluated from equation 1.51 and takes the form

$$k = \frac{F_i - F_0}{F_i}(1 + \gamma^2) \tag{1.53}$$

Let t = $\tau_{\frac{1}{2}}$ at which the fluorescence intensity recovers by half, which is defined as, $F_{\frac{1}{2}}$ = (F_0+F_∞)/2

Now from equation 1.51 the following equation can derived,

$$F(_{\frac{1}{2}}) = F_i(1 - \frac{k}{1 + \gamma^2 + \frac{2\tau_{\frac{1}{2}}}{\tau_d}})M_f + (1 - M_f)F_0 \tag{1.54}$$

Using its definition and eqn.1.52, $F_{\frac{1}{2}}$ is related to M_f by the following equation,

$$F(_{\frac{1}{2}}) = \frac{F_i - F_0}{2}M_f + F_0 \tag{1.55}$$

Using the above two equations and equation 1.53 one could arrive at the following expression,

$$\frac{2\tau_{\frac{1}{2}}}{\tau_d} = 1 + \gamma^2 \tag{1.56}$$

Finally by solving for D in $\tau_d = {r_e}^2/4D$ and applying $\gamma = r_n/r_e$, diffusion of molecules in a circular confocal volume is estimated as,

$$D_{conf} = \frac{{r_e}^2 + {r_n}^2}{8\tau_{\frac{1}{2}}} \tag{1.57}$$

when $r_e = r_n$, D = 0.25 ${r_n}^2/\tau_{\frac{1}{2}}$

The first prebleach image is fitted to equation 1.50 to obtain r_e and time for half the intensity is taken as $\tau_{1/2}$. Diffusion of fluorescent lipid and therefore the diffusion of lipid in the supported bilayer is measured by this method. The supported lipid bilayer was made either from SUV solution [49] or by rupture of GUVs using acetic acid as described in chapter 4. Treated cover glass or mica was used as the substrate for deposition of lipid bilayer. Temperature of sample was controlled by using a home built, Peltier element chamber with Ferrotec FTC 100 controller.

1.5.12 Scanning Electron Microscopy (SEM)

SEM is a versatile tool to examine microstructure morphology and analyse chemical composition [50]. Instead of light in a conventional microscope, SEM uses a focused electron beam to produce high-resolution images. The electron beam is generated from a Schottky field emitter, which serves as the gun. The filament is heated by applying filament current. Electrons emitted from the heated filament are focused on the sample using an electromagnetic lens. This focused beam scans the sample surface to create a surface image as well as to do material characterisation. The interaction of an electron beam with the sample creates two kinds of signals: elastically scattered and inelastically scattered electrons. Electrons which get scattered elastically at angles more than 90° are called backscattered electrons. They yield useful information about the sample topography as an image. The electrons which scatter inelastically mostly transfer a substantial amount of energy to the sample interactive volume, which ionizes the material and creates secondary electrons. The secondary electrons having relatively lower energies ($<$ 50 eV) are used for image formation. In addition, to these, the interaction of the electron beam also produces characteristic x-rays, Auger electrons, and cathodoluminescence, which are used in material characterization. Different scattered signals from the samples are collected by different detectors, which include scintillation detectors for backscattered electrons, secondary electron detector, and semiconductor x-ray detector [50].

1.5.13 cryogenic-Scanning Electron Microscope (cryo-SEM)

Cryo-SEM is an advanced form of SEM for biological and soft samples containing water or other solvents. In this technique, the hydrated samples can be imaged as such by freezing the sample to prevent water loss. This allows the observation of samples in naturally hydrated state, which is particularly useful for biological samples. For cryo-SEM imaging, around 20-30 μl of the sample was filled in a brass rivet and immediately quenched in liquid nitrogen. It was then transferred to a PP3000T cryogenic unit (Quorum Technologies) maintained at a temperature of -180°C, and fractured using a cold knife. The sample was sublimated at -90°C for 15 minutes and then sputtered with platinum for 90 seconds to form a nanometer-thick coating on the fractured surface. Imaging of samples was carried out using a Zeiss Ultra Plus Cryo-SEM.

1.5.14 Atomic Force Microscopy (AFM)

AFM is a three-dimensional topographical imaging technique that belongs to the category of scanning probe microscopy (SPM). Unlike conventional light and electron microscopy, where

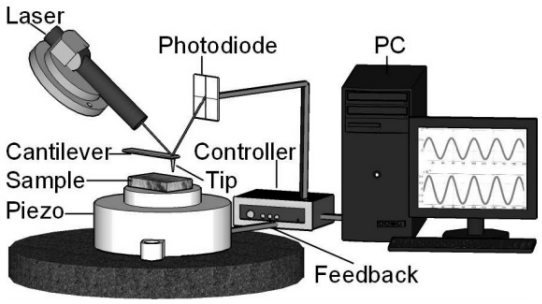

(a)

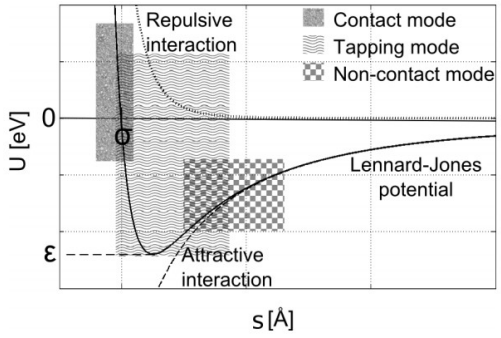

(b)

Figure 1.26: (a) Schematic of AFM setup (b) Tip -surface interaction potential.(adapted from [42])

light-matter interactions are used for imaging the sample features, SPM uses the probe - surface interaction for high-resolution sub-nanometer-scale 3D imaging. Apart from AFM, Scanning Tunneling Microscopy (STM) and Near field Scanning Optical Microscopy (NSOM) also belong to this category [51].

1.5.15 Basic principles of AFM

AFM exploits the interaction between a sharp Si or SiN tip and the sample surface to image the topological features down to a resolution of a few angstroms in the Z direction and a few nm in the X-Y direction [51]. The typical L shaped AFM probes are called cantilevers, which have a very sharp tip having a radius of 20-60 nm at one end. Cantilevers have a typical length of 100-200 μm. The sharp tip interacts with the sample while doing raster scanning over it. This interaction can be attractive or repulsive depending on the sample properties and the distance between the tip and the sample surface. Cantilevers can also measure different types of forces present in the system in addition to revealing the surface morphology. The force between tip and sample can be monitored by pulling the tip away from the surface after

landing on the sample surface. The deflection of the cantilever is measured in nanometer-scale accuracy using different methods such as tunneling current measurement, optical deflection technique, fiber interferometry, and piezoresistive methods [51]. In the AFM system used in this work, the motion of cantilever was detected using the optical deflection technique. Laser light is focused on the reflecting surface of the cantilever. The reflected beam was collected by a photodiode.

The typical cumulative force profile experienced by the cantilever near the sample surface is shown in fig.1.27b(b). At a distance of 10-100 nm, the tip experiences attractive interaction mainly due to the van der Waal's force exerted by the sample. The repulsive force experienced by the tip when it is very near to the sample surface can be explained by hard-sphere repulsion, Pauli exclusion interaction, and e^- - e^- coloumbic interaction. These forces decay exponentially away from the surface.

AFM works in different modes called contact mode, non-contact mode, and intermittent force mode or tapping mode depending on the distance from the sample surface. In contact mode, tip scans the surface close to the contact with the surface. At this distance tip experiences a repulsive force of the order 10^{-9}N. While the tip scans the sample, the tip is in physical contact with the sample, and the sample topography induces a vertical deflection. The feedback brings this deflection back to the set value. This response is used to generate the image. In non-contact mode, the tip oscillates with very low amplitude (2-3 nm) away from the surface. The attractive van der Waals interaction between the tip and surface changes the oscillation parameters. The shifts in frequency, amplitude, and phase of the oscillations are used for imaging the surface. Tapping mode AFM works in the region between contact and non-contact mode. In this case, the tip is oscillated with a large amplitude (20 nm) away from the sample and brought near to the surface while imaging. Near to the surface due to the interaction and surface topography, the amplitude of oscillation changes and feedback response creates the image.

Phase separation in binary lipid mixtures and ripples in DPPC multilayers were imaged using Molecular Imaging Pico scan AFM3000 in the tapping mode with a cantilever of spring constant 0.02 N/M, with the resonance frequency set to 70 KHz. To study phase-separation in the binary hydroxysterol-lipid system, solid-supported lipid bilayers were prepared by suv fusion method [49] or GUV rupture method described in chapter 4 with mica as the substrate in a fluid cell under controlled temperature. The bilayers were made at high-temperature for a uniform phase and then cooled down slowly to room temperature. Care was taken to maintain a sufficient water level while imaging. The schematic of the experimental setup is

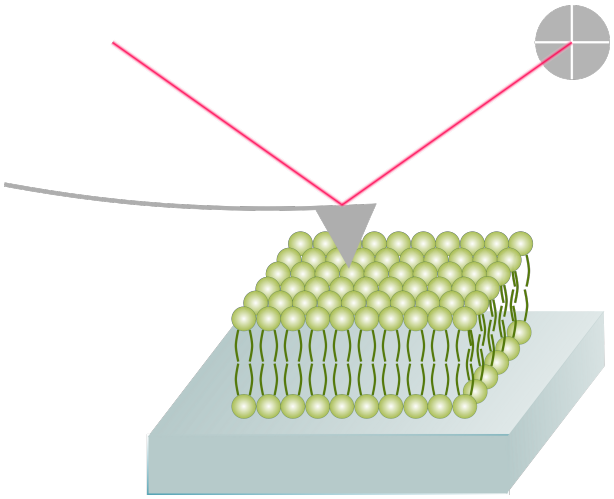

(a)

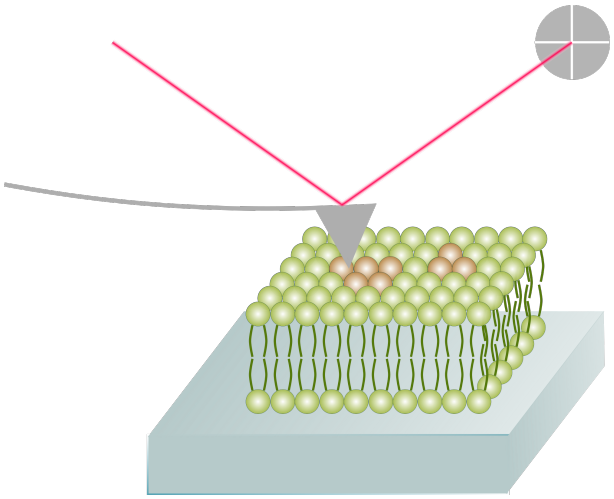

(b)

Figure 1.27: (a) Schematic of AFM measruements on bilayer (b) schematic of AFM measurements on bilayer with two phase coexistence

shown in the fig.1.27b.

1.6 Dynamic Light Scattering (DLS)

Dynamic Light Scattering measures the particle size typically in the sub-micron level by measuring the correlation between the scattered light from the sample [52]. A coherent monochromatic laser beam is used to illuminate the sample. The scattering pattern from the sample, which is usually a dispersion of particles in an appropriate solvent, is collected using a 2D detector as a function of time.

Since particles execute Brownian motion, the scattering pattern (Speckle pattern) collected from the sample changes as a function of time. The correlation between two consecutive pat-

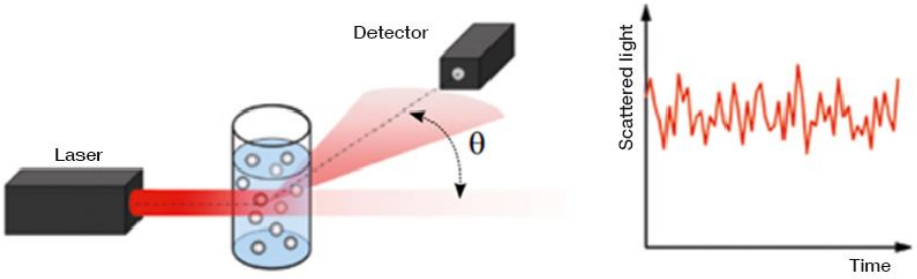

Figure 1.28: Diagram of Dynamic Light Scattering setup adapted from [52]

terns with a delay time τ depends on parameters such as particle size, temperature, viscosity, and pH of the solvent. For a known value of solvent parameters and temperature, smaller particles show rapid fluctuations of the speckle pattern compared to larger particles and hence a lower correlation between two events. This autocorrelation function of scattered intensity at a given point G(τ) can be expressed as,

$$G(\tau) =< I(t)I(t+\tau) > \tag{1.58}$$

For a mono dispersed sample the correlation function decay exponentially as a function of time as given in the equation,

$$G(\tau) = A[1 + Bexp - (\Gamma)t] \tag{1.59}$$

where A - Baseline of the autocorrelation function B - intercept of correlation function and Γ is given by the equation,

$$\Gamma = Dq^2 \tag{1.60}$$

where D is the translational diffusion coefficient and q depends on experimental setup through the following relationship,

$$q = (4\pi * n * /\lambda_0)/\sin\theta/2 \tag{1.61}$$

where n is the refractive index of the sample, λ_0 is the wavelength of the illuminating light and θ is the scattering angle.

D is related to hydrodynamic radius of the diffusing particle d(H) by Stokes-Einstein

relation,

$$d(H) = KT/(3\pi\eta D) \tag{1.62}$$

where K is the Boltzmann constant, η is the viscosity of the solvent, and T is the temperature of the dispersion.

Therefore by fitting the autocorrelation function to a single exponential function, one can calculate the translational diffusion coefficient, and equation 1.62 relates it to the corresponding size of the diffusing particle.

In this thesis, all the Dynamic light scattering (DLS) experiments were carried out using a BI-200SM spectrometer (Brookhaven Instruments) in conjunction with a 532 nm solid-state laser (Spectra Physics).

1.7 Electrophoretic mobility measurements

When a charged particle is kept under a uniform electric field in a uniform medium without counterions or coions, it moves with an acceleration proportional to the particle's total charge. But in the case of charged particles dispersed in a solvent containing co ions and counterions, the particles move with a constant velocity for a given applied voltage. This velocity can be determined by parameters such as zeta potential, dynamic viscosity, and dielectric permittivity of the medium. The direction of migration of ions/ particles towards anode or cathode depends on its surface charge nature. According to double-layer theory, when charged particles are suspended in a solvent, around the particles, a layer of diffuse ions exists, which has an absolute charge equal to the surface. When an electric field is applied, the diffuse ions experience a force opposite to the force which is experienced by the particles. Hence it creates a drag on the particle's migration. This drag force is called electrophoretic retardation force (F_{el}). Along with the retardation force, the particles also experience a frictional force (F_f) due to viscous drag from the solvent. Under steady-state conditions, the particle moves with a constant velocity, and the total force (F_{total})on the particle is zero.

$$F_{total} = F_{el} + F_f + F_{ret} = 0 \tag{1.63}$$

In the case of low Reynold's number solvent and moderate electric field strength (E), the mobility of the charged particle μ_e can be related to the measured velocity of particle v as,

$$\mu_e = v/E \tag{1.64}$$

The mobility is related to the zeta potential of the charged particle at the slipping plane by the expression given by Marian Smoluchowski as,

$$\mu_e = (\epsilon\zeta)/\eta \tag{1.65}$$

where ϵ is the dielectric permittivity of the medium, ζ is the zeta potential, and η is the dynamic viscosity of the medium.

In this thesis, a home-built electrophoretic chamber was used to apply an electric field to the charged GUVs in the presence of the UMP solution. The motion of GUVs tagged fluorescent dyes is monitored using fluorescence microscopy as a function of time. The steady-state velocities were calculated from the analysis of the sequential images of the motion of the particles. Zeta potential at the GUV surface is obtained from the above equation.

Bibliography

[1] E. Gorter and F. Grendel. On bimolecular layers of lipoids on the chromocytes of the blood. *J. Exp. Med.*, 41:439–444, 1925.

[2] S. J. Singer and G. L. Nicolson. The fluid mosaic model of the structure of cell membranes. *Science*, 175:720–731, 1972.

[3] M. J. Karnovsky, A. M. Kleinfeld, R. L. Hoover, and R. D. Klausner. The concept of lipid domains in membranes. *J. Cell Biol.*, 94:1–6, 1982.

[4] A.Stier and E.Sackmann. Spin labels as enzyme substrates heterogeneous lipid distribution in liver microsomal membranes. *Biochim. Biophys. Acta*, 311:400–408, 1973.

[5] J. N. Israelachvili, S. Marčelja, and R. G. Horn. Physical principles of membrane organization. *Q. Rev. Biophys.*, 13:121–200, 1982.

[6] K. Simons and E. Ikonen. Functional rafts in cell membrane. *Nature*, 387:569–572, 1997.

[7] E. Sevcsik and G. J. Schütz. With and without raft? alternative views on cell membrane. *Bioessays*, 38:129–139, 2016.

[8] I. Levental and S. Veatch. The continuing mystery of lipid rafts. *J. Mol. Biol.*, 428:4749–4764, 2016.

[9] R. Veldhuizen, K. Nag, S. Orgeig, and F. Possmayer. The role of lipids in pulmonary surfactant. *Biochim. Biophys. Acta*, 1408:90–108, 1998.

[10] H. I. Ingoòlfsson, M. N. Melo, F. J. van Eerden, C. Arnarez, C. A. Lopez, T. A. Wassenaar, X. Periole, A. H. de Vries, D. P. Tieleman, and S. J. Marrink. Lipid organization of the plasma membrane. *J. Am. Chem. Soc.*, 136:14554–14559, 2014.

[11] J. N. Israelachvilli. *Intermolecular and surface forces.* Elsevier, third edition, 2014.

[12] R. A. L. Jones. *Soft Condensed Matter.* Oxford Master Series in Physics, OUP Oxford, 2002.

[13] R. Lipowsky and E. Sackmann. *Structure and Dynamics of membranes : Generic and specific interactions*, volume 1B. North Holland,Elsevier, first edition, 1995.

[14] S. Aryal. Microbe notes, 2010 (accessed 22 October 2019).

[15] S. K. Mehta and Gurpreet Kaur. Microemulsions: Thermodynamics and dynamic properties. In *Thermodynamics.* Intechopen, 2011.

[16] E. Rideau, R.Dimova, P. Schwille, F. R. Wurm, and K. Landfester. Liposomes and polymersomes: a comparative review towards cell mimicking (review). *Chem. Soc. Rev*, 47:8572–8610, 2018.

[17] S. Karmakar. *Structure and phase behaviour of lipid-cholesterol membranes.* PhD thesis, J. N. U, Delhi, India, 2006.

[18] N. F. Morales-Penningston, J. Wu, and E. R. Farkas et al. Guv preparation and imaging: Minimizing artifacts. *Biochim. Biophys. Acta*, 1798:1324–1332, 2010.

[19] N.-J. Cho, L. Y. Hwang, J. J.R. Solandt, and C. W. Frank. Comparison of extruded and sonicated vesicles for planar bilayer self-assembly. *Materials*, 6:3294–3308, 2013.

[20] G. Maulucci, M.De Spirito, G. Arcovito, F. Boffi, A. C. Castellano, and G. Briganti. Particle size distribution in dmpc vesicles solutions undergoing different sonication times. *Colloids Surf B Biointerfaces.*, 181:837–844, 2019.

[21] Marsh D. *CRC Handbook of Lipid Bilayers.* CRC Press; Boca Raton, FL, USA, first edition, 1990.

[22] Hydratech. Techniques for the quantification of methane hydrate in european continental margins, 2004.

[23] J. Grdadolnika, F. Merzela, and F. Avbelja. Origin of hydrophobicity and enhanced water hydrogen bond strength near purely hydrophobic solutes. *Proc. Natl. Acad. Sci. U. S. A.*, 114:322–327, 2017.

[24] B. Kheyfets, T. Galimzyanov, and S. Mukhin. Microscopic description of the thermodynamics of a lipid membrane at a liquid–gel phase transition. *JETP Lett.*, 107:718–724, 2018.

[25] V. A. Raghuanthan and J. Katsaras. Structure of the l_c' phase in a hydrated lipid multilamellar system. *Phys. Rev. Lett.*, 74(22):4456–4460, 1995.

[26] J. R. Black. *Debye-Hückel Equation. In: White W.M. (eds) Encyclopedia of Geochemistry. Encyclopedia of Earth Sciences Series.* Springer, first edition, 2018.

[27] W. Helfrich. Passages in lecithin-water systems. *Z. Naturforsch.*, A33(9):1013– 1017, 1978.

[28] W. Helfrich and R. M. Servuss. Undulations, steric interaction and cohesion of fluid membranes. *Nuovo Cimento Soc. Ital. Fis. D*, 3(1):137–151, 1984.

[29] H. Matsuki, M. Goto, K. Tada, and N. Tamai. Thermotropic and barotropic phase behavior of phosphatidylcholine bilayers. *Int. J. Mol. Sci.*, 14:2282–2302, 2013.

[30] C. V. Kulkarni. Lipid crystallization : From self assembly to hierarchical and biological ordering. *Nanoscale*, 4:5779–5791, 2012.

[31] P. M. Chaikin and T. C. Lubensky. *Principles of condensed matter physics.* Cambridge University Press, Cambridge, 2000.

[32] M. J. Buerger. The correction of x-ray diffraction intensities for lorentz and polarization factors. *Proc. Natl. Acad. Sci.*, 11:637–642, 1940.

[33] G. Pabst, M. Rappolt, H. Amenitsch, and P. Laggner. Structural information from multilamellar liposomes at full hydration: Full q-range fitting with high quality x-ray data. *Phys. Rev. E*, 62(3):4000–4009, 2000.

[34] M. C. Wiener, R. M. Suter, and J. F. Nagle. Structure of the fully hydrated gel phase of dipalmitoylphosphatidylcholine. *Biophys. J*, 55(315):315–325, 1989.

[35] G. Pabst, F. A. Heberle, and J. Katsaras. *Encyclopedia of Biophysics, 2013:s.* [Ch.X-Ray Scattering of Lipid Membrane].

[36] *Instrumentation (Appendix: Lab tutorial MIT)*, 2003 (accessed 26 September 2019). https://ocw.mit.edu/courses/chemistry/5-32-intermediate-chemical-experimentation-spring-2003/labs/Appendix_1_Qual_Instrumentation_03.pdf.

[37] B. C. Smith. *Fundamentals of Fourier Transform Infrared Spectroscopy*. CRC press, first edition, 1996.

[38] B. Munjanja and E. Sanganyado. *Handbook of Food Analysis*. [Ch.31: UV-Visible Absorption, Fluorescence ,and Chemiluminescence Spectroscopy].

[39] Z. Smith and C. Roman. *Fluorescence*, 2019 (accessed 26 September 2019). https://chem.libretexts.org/Bookshelves/Physical_and_Theoretical_Chemistry_Textbook_Maps/Supplemental_Modules_(Physical_and_Theoretical_Chemistry)/Spectroscopy/Electronic_Spectroscopy/Radiative_Decay/Fluorescence.

[40] G. S. Bumbrah and R. M. Sharma. Raman spectroscopy - basic principle, instrumentation and selected applications for the characterization of drug of abuse. *Egypt J. Forensic Sci.*, 6:209–215, 2016.

[41] P. Gill, T. T. Moghadam, and B. Ranjbar. Differential scanning calorimetry: Applications in biology and nanoscience. *J. Biomol. Tech.*, 21:167–193, 2010.

[42] D. Semwogerere and E. R. Weeks. *Encyclopedia of biomaterials and biomedical engineering*. [Ch. Confocal Microscopy].

[43] F. Muller, D. Mazza, T. J. Stasevich, and J. G. McNally. Frap and kinetic modeling in the analysis of nuclear protein dynamics: what do we really know? *Curr. Opin. Cell Biol.*, 22:403–411, 2010.

[44] C. A. Day and A. K. Kenworthy. Tracking microdomain dynamics in cell membranes. *Biochim. Biophys. Acta*, 1788:245–253, 2009.

[45] A. Miyawaki. Proteins on the move: insights gained from fluorescent protein technologies. *Nat. Rev. Mol. Cell Biol.*, 12:656–668, 2011.

[46] M. Kang, C. A. Day, A. K. Kenworthy, and E. DiBenedetto. Simplified equation to extract diffusion coefficients from confocal frap data. *Traffic*, 13:1589–1600, 2012.

[47] D. Axelrod, D. E. Koppel, J. Schlessinger, and W. W. Webb. Mobility measurement by analysis of fluorescence photobleaching recovery kinetics. *Biophys. J.*, 16:1055–1069, 1976.

[48] D. M. Soumpasis. Theoretical analysis of fluorescence photobleaching recovery experiments. *Biophys. J.*, 41:95–97, 1983.

[49] S. J. Attwood, Y. Choi, and Z. Leonenko. Preparation of dopc and dppc supported planar lipid bilayers for atomic force microscopy and atomic force spectroscopy. *Int. J. Mol. Sci.*, 14:3514–3539, 2013.

[50] W. Zhou, R. Apkarian, Z. L. Wang, and D. Joy. Fundamentals of scanning electron microscopy (SEM). In *Scanning Microscopy for Nanotechnology*. Springer, New York, NY, 2006.

[51] Y. Seo and W. Je. Atomic force microscopy and spectroscopy. *Rep. Prog. Phys.*, 71:016101(23pp), 2008.

[52] Anton Paar. *The principles of dynamic light scattering)*, 2003 (accessed 9 April 2021). https://wiki.anton-paar.com/en/the-principles-of-dynamic-light-scattering/.

Chapter 2

Part 1: Interaction of the mononucleotide UMP with a fluid phospholipid bilayer

2.1 Introduction

Lipid molecules are the building blocks of cell membranes and consist of a polar head group and nonpolar hydrocarbon chains. Their amphiphilic nature leads to the formation of self assembled bilayer structures in aqueous solutions, above a critical lipid concentration, which is typically of the order of a few nM [1]. The interaction of lipid membranes with biologically active molecules such as sterols and drug molecules has been the subject of innumerable studies [2, 3]. On the other hand, the interaction of mononucleotides with lipid membranes has not been investigated in much detail, in spite of their proposed role in the origin of life on Earth. According to the RNA World hypothesis, RNA-like polymers can be synthesized nonenzymatically from mononucleotides in a lipid environment under conditions that mimic prebiotic hydrothermal sites undergoing periodic changes in temperature and hydration [4]. Confining the nucleotide molecules in a lipid matrix increases their local concentration and makes it possible to bring the functional groups involved in the condensation reaction in proximity [5, 6, 7].

Molecular organization of mononucleotides within a multilamellar lipid membrane matrix under low-humidity conditions has been the subject of some recent x-ray diffraction studies [8, 9]. Adenosine 5'-monophosphate (AMP) molecules sandwiched between 1,2-dimyristoyl-*sn*-glycero-3-phosphatidylcholine (DMPC) lipid multilayers form nano crystallites, which have the potential to promote nonenzymatic polymerization of the nucleotide. Apart from lipid

bilayers, certain inorganic minerals such as NaCl, KCl, NH_4Cl and montmorillonite clay also favour the formation of similar ordered nucleotide structures [6, 8, 9]. The influence of temperature and humidity on the mobility of AMP molecules within the lipid matrix has been studied using elastic incoherent neutron scattering [10].

Most of the studies on lipid-mononucleotide systems till now have focused on the formation of ordered arrays of nucleotides due to the confining effect of the lipid matrix, but the effect of the nucleotide on the organization of the lipid membrane remains poorly understood. In the first part of this chapter, the effect of UMP on the structural parameters of fluid 1,2-dimyristoyl-*sn*-glycero-3-phosphatidylcholine (DMPC) bilayers at 60^{o}C under excess water conditions is studied using Small Angle X-ray Scattering (SAXS), cryogenic scanning electron microscopy (Cryo-SEM), Dynamic Light Scattering (DLS) and electrophoretic mobility measurements. We also probe the influence of the counterion on the nucleotide-membrane interaction. SAXS and cryo-SEM studies show that adsorption of UMP on DMPC bilayers leads to their charging and results in the formation of unilamellar vesicles in dilute solutions. Concommitantly, a slight reduction in the bilayer thickness of DMPC is observed. These effects are seen only in the case of the acid form of UMP and not in the case of its disodium salt. To gain a deeper understanding of the experimental observations, Dr. Himanshu Khandelia's group from University of Southern Denmark, Denmark has carried out molecular simulations of the binding of UMP on fluid DMPC membranes using CHARMM36 all atom force field. Results of the simulations are in very good agreement with the experimental observations [11]. UMP adsorbs at the head group region of the bilayer and leads to a non-zero surface charge density. Unlike its acid form, disodium salt of UMP does not bind directly to the membrane, but forms small clusters in water, which subsequently bind to the membrane-water interface, without significant perturbation of the bilayer. Radial distribution functions obtained from the simulations show the interaction between the ribose sugar region of UMP and the phosphate group of DMPC to be the strongest.

2.2 Results

2.2.1 Cryo-SEM and DLS

DMPC: UMP samples form clear solutions upon hydration, whereas pure DMPC and DMPC−UMPDSS samples are highly turbid. These observations suggests the formation of unilamellar vesicles (ULV) in the case of DMPC:UMP mixtures, and multilamellar vesicles in DMPC: UMPDSS and pure DMPC systems [12]. Cryo-SEM images of 1:1 and 5:1 DMPC: UMP samples show

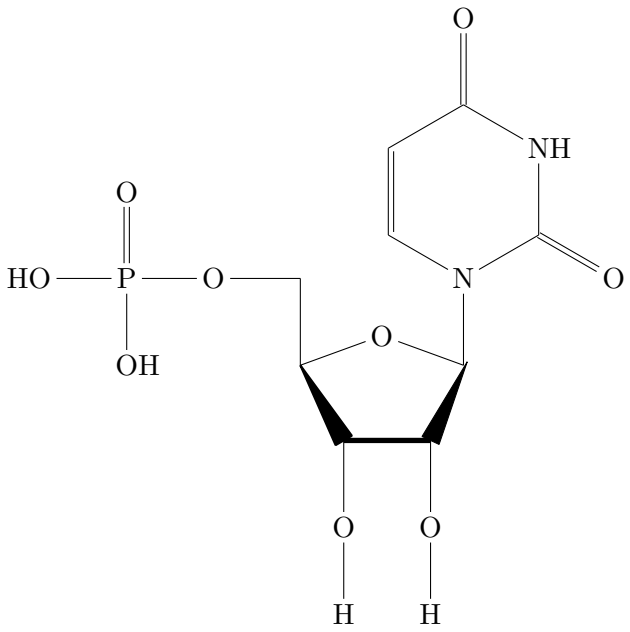

Figure 2.1: Chemical structure of uridine monophosphate (UMP)

the presence of vesicles, whose diameter ranges from about 20 to 80 nm with an average of about 50 nm (fig. 2.2(a)). This size range is very similar to that reported for small unilamellar vesicles (SUVs) produced by sonication in the literature [13]. The average vesicle size is known to shift to lower values with longer sonication time, due to the creation of smaller bilayer patches that curl up to form vesicles in order to reduce the edge energy at the expense of curvature energy. On the other hand, cryo-SEM images of DMPC:UMPDSS and pure DMPC samples clearly show the formation of multilamellar vesicles (MLV) (fig. 2.2(b)).

DMPC: UMP samples were characterised by DLS and the size distribution of small unilamellar vesicles (SUV) formed was measured. The samples were equilibrated at 60°C before the measurement. The particle size distributions presented in figs.2.3 (a) and (b) show that the average radius of the SUVs formed for 1:1 and 5:1 samples were 30 nm and 28 nm, respectively. DLS measurements on pure DMPC and DMPC:UMPDSS samples were not carried out since the samples are very turbid due to the presence of multilamellar vesicles in both cases.

2.2.2 Electrophoretic measurements

The charge on the DMPC membrane due to the adsorption of UMP was estimated by electrophoretic measurements. DMPC GUVs were transferred into an electrophoretic chamber containing UMP solution at pH 4. This value of pH was chosen so as to be very far from the

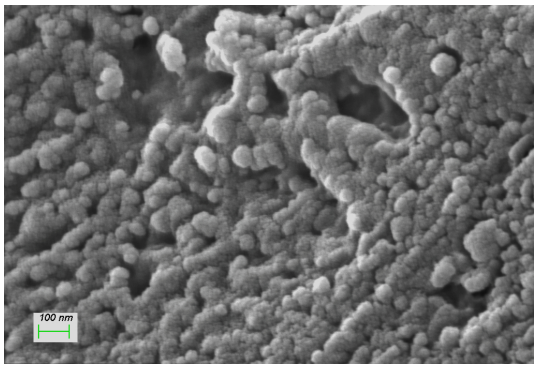

(a)

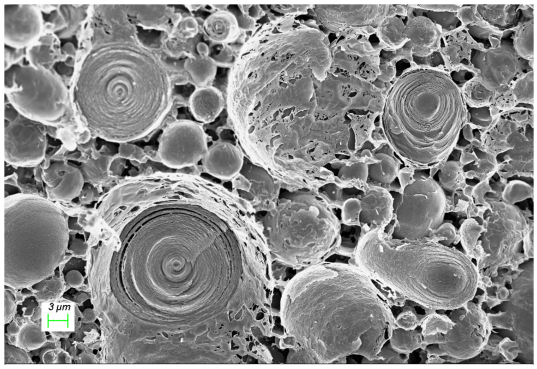

(b)

Figure 2.2: Cryo-SEM images of (a) 1:1 DMPC: UMP sample showing vesicular structures and (b) of 1:1 DMPC: UMPDSS sample showing multilamellar vesicles.

pKa (= 1.0) of the phosphate moiety in the choline headgroup of DMPC, thus ensuring the neutrality of the lipid. The velocity of the vesicles were calculated as a function of the applied voltage from real time imaging using fluorescence microscopy. From this, mobility and hence surface potential was calculated. The zeta potential is found to be -20 mV, confirming the charging of the bilayers due to the adsorption of UMP ions from the solution.

2.2.3 SAXS

SAXS patterns of pure DMPC samples at 60 °C show sharp peaks corresponding to a lamellar structure having a periodicity of 6.12 nm (fig.2.5(a)). In the case of DMPC: UMPDSS samples, a diffraction pattern similar to that of pure DMPC is obtained (fig.2.5(b)), but with a higher lamellar periodicity of 7.72 nm at 60 °C. On the other hand, both 1:1 and 5:1 DMPC: UMP samples show a broad SAXS profile without any sharp peaks at 60°C (figs. 2.6(a), 2.6(b)). This indicates the absence of long-range translational order in these systems, as would be expected from a dispersion of ULVs.

SAXS profiles of all samples were analyzed using the procedure detailed in ref. [14] and outlined in chapter 1. Lipids, such as DMPC, self-assemble in water to form bilayers. A dilute

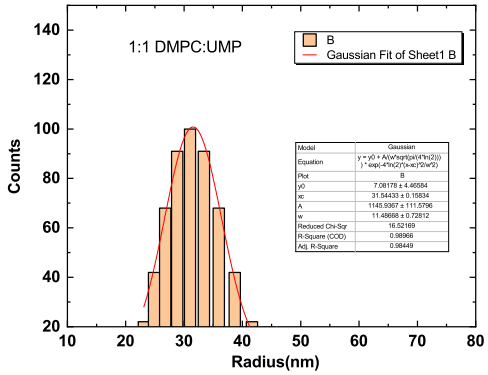

(a)

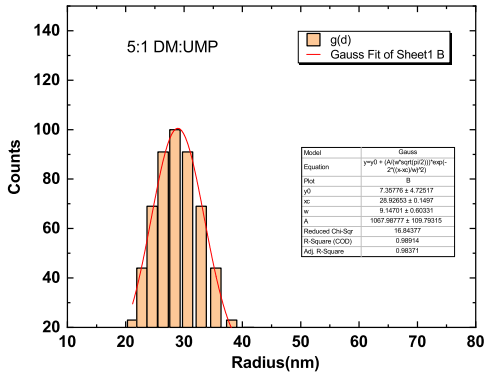

(b)

Figure 2.3: Particle size distribution of (a)1:1 and (b) 5:1 DMPC: UMP samples measured by DLS.

lipid solution, in general, consists of isolated bilayers, in the form of unillamellar vesicles (ULV), and correlated stacks of bilayers, in the form of multilamellar vesicles (MLV).The intensity of the SAXS pattern obtained from such a sample can be expressed as,

$$I(q) \propto \frac{1}{q^2}(S(q)|F(q)|^2 + N_b|F(q)|^2), \tag{2.1}$$

where q is the magnitude of the scattering vector, S(q) the structure factor, describing the lamellar structure within the MLVs, and F(q) the form factor of a bilayer. N_b is the relative fraction of ULVs.

SAXS data obtained from MLV dispersions were fitted to eqn.2.1 using a nonlinear fitting algorithm from Mathematica. Average values of bilayer structural parameters obtained from at least 10 data sets were used to construct the electron density profiles. The first term in eqn.2.1 was neglected in the case of samples containing only ULVs. Data from DMPC: UMP samples could be fitted using only the bilayer form factor, showing that these samples contain ULVs. On the other hand, data from pure DMPC and DMPC: UMPDSS samples are

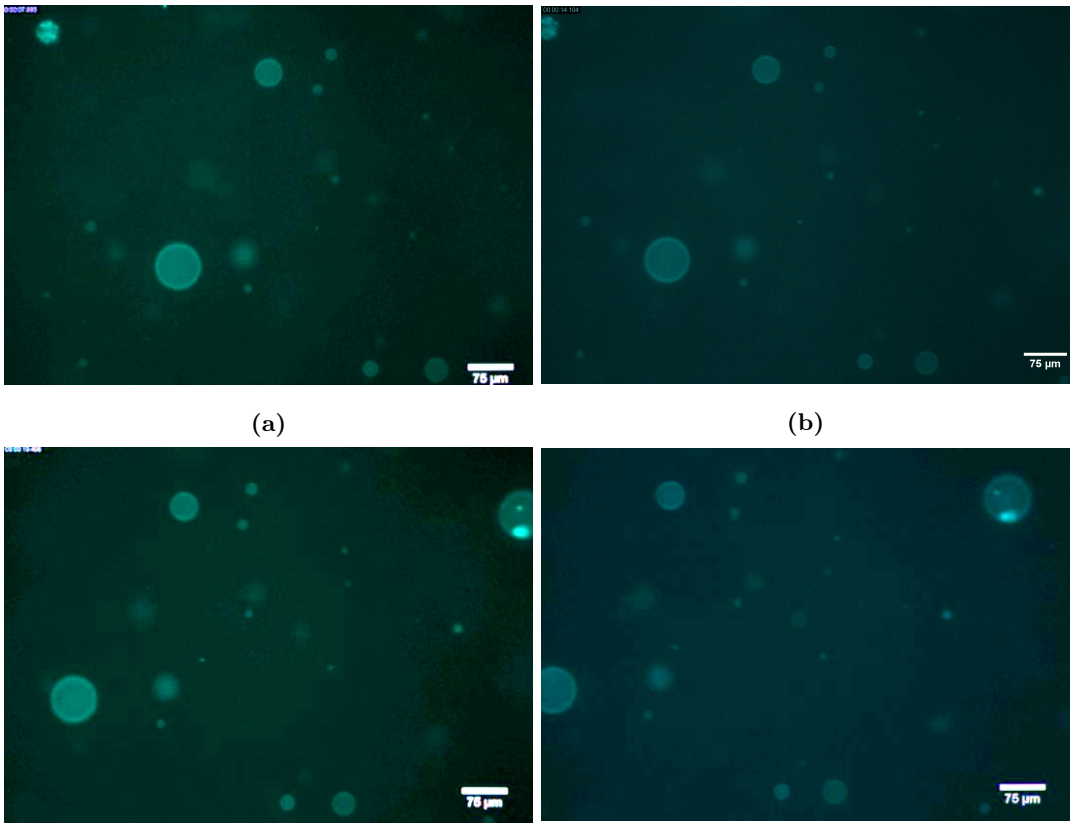

(a) **(b)**

(c) **(d)**

Figure 2.4: Time elapsed images of electrophoretic mobility of DMPC vesicles in UMP solution (a) 0 s (b) 5 s (c) 11 s (d) 17 s. Applied voltage 9V/cm to the right side. Vesicles are moving towards the left side indicating a negative surface charge.

consistent with a dispersion of MLVs with a relatively small concentration of ULVs. table.2.1 gives values of the model parameters obtained from the analysis, and the bilayer electron density profiles of different systems calculated using these are shown in fig.2.7. z_h for DMPC is 1.68 nm, which is close to the value of 1.71 nm reported in ref.[15]. It decreases by about 0.2 nm in the two mixed bilayers containing UMP, although no significant difference is found between the 1:1 and 5:1 compositions. Concomitant with the lowering of z_h, σ_c increases in the DMPC: UMP bilayers, consistent with increased chain disorder in thinner bilayers. In the case of DMPC: UMPDSS bilayers the value of z_h is almost identical to that for pure DMPC bilayers, although the lamellar periodicity of these mixed membranes is slightly higher. Interestingly, for the DMPC: UMPDSS system, the Caillé parameter $\eta_1 = 0.22 \pm 0.02$, which is much higher than the value of 0.06 ± 0.02 found for DMPC. Caillé parameter is defined as, $\eta_1 = q^2KT/(8\pi\sqrt{\varepsilon B})$, where ε and B are the curvature and compression moduli of the lamellar phase, respectively, and K is the Boltzmann constant. ε can be expressed in terms of the bilayer bending rigidity modulus κ_b, as, $\varepsilon = \kappa_b/d$, where d is the lamellar periodicity.

Therefore the observed increase in Caillé parameter suggests a significant lowering of the bending rigidity modulus κ_b in the presence of UMPDSS.

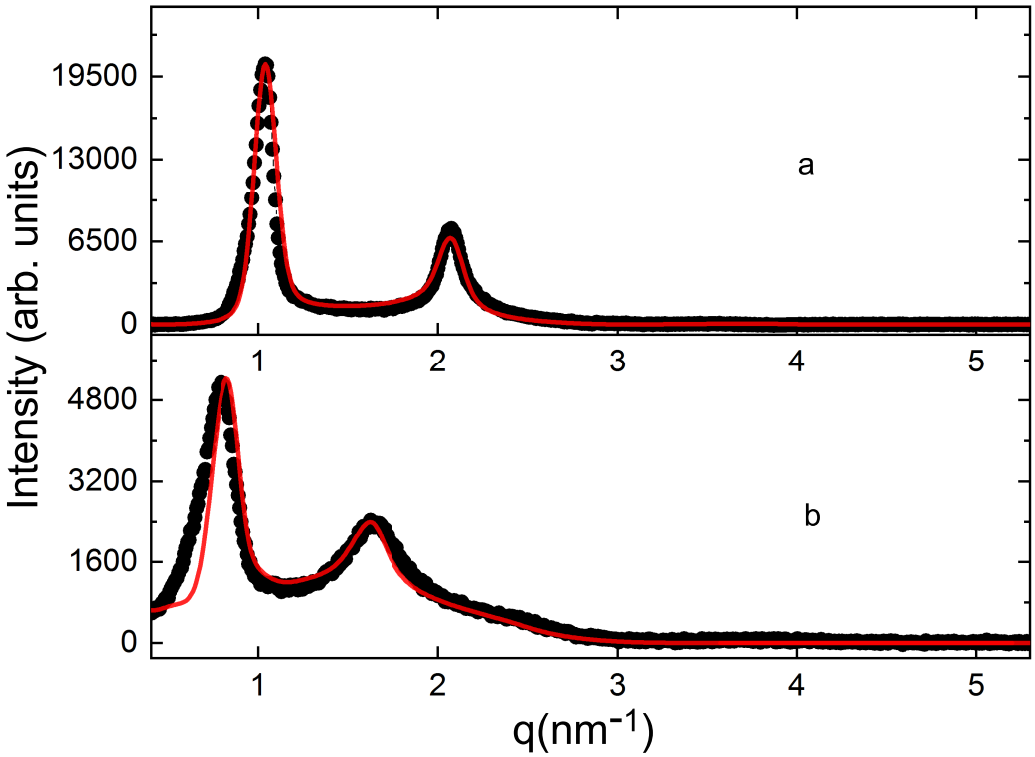

Figure 2.5: SAXS patterns of (a) pure DMPC and (b) 1:1 DMPC:UMPDSS samples at 60 °C. The solid lines are fits to the model described in the text.

Sample	$\sigma_h(nm)$	$\sigma_c(nm)$	ρ_h/ρ_c	z_h (nm)
DMPC	0.31±0.01	0.45±0.04	0.8±0.1	1.68±0.02
DMPC:UMP 1:1	0.30±0.02	0.56±0.02	0.8±0.1	1.58±0.02
DMPC:UMP 5:1	0.29±0.02	0.49±0.02	0.8±0.1	1.59±0.02
DMPC:UMPDSS 1:1	0.23±0.02	0.47±0.05	0.7±0.1	1.69±0.02

Table 2.1: Values of the electron density model parameters obtained from the analysis of SAXS data. ρ_h and ρ_c are the amplitudes of the Gaussians describing the headgroup region and the centre of the bilayer, respectively, and σ_h and σ_c are their widths. z_h is the separation between the centers of these two Gaussians.

2.3 Discussion

Previous x-ray diffraction studies on mononucleotides confined in a carrier matrix have reported two different organizations corresponding to nearest neighbor distances of 0.46 nm and 0.36 nm, which were ascribed to a glassy disordered packing and an ordered stacking

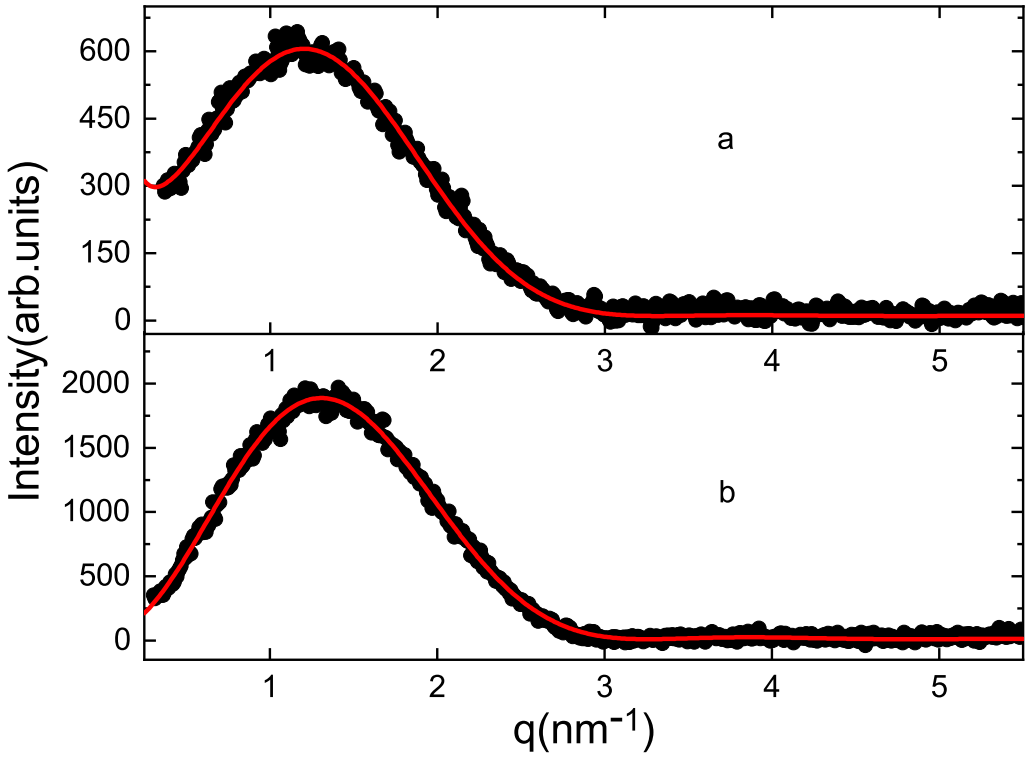

Figure 2.6: SAXS patterns of (a) 1:1 and (b) 5:1 DMPC: UMP samples at 60 °C. The solid lines are fits to the model described in the text.

of the nucleotides, respectively [8, 9]. The extent of ordered phase formed was different in different environments. In the case of adenosine 5-monophosphate (AMP) in DMPC membranes, formation of nano crystallites was observed at low humidity, whereas in the case of UMP a disordered structure was observed under similar conditions. In all these studies the lipid membrane is in the gel phase, characterized by in-plane crystalline order, due to the low humidity. In contrast, studies described here have been carried out at 60 °C and in excess water, conditions under which DMPC bilayers form the fluid lamellar phase with a lamellar periodicity of 6.12 nm. In the presence of UMP the lamellar phase of DMPC is destabilized, resulting in the formation of ULVs. Since UMP is doubly charged at neutral pH, the enhanced interbilayer repulsion responsible for this behaviour arises from their adsorption on the membranes, which endows the membrane-water interface with an electric charge density. The resulting electrostatic repulsion between the membranes is able to overcome the van der Waals attraction and stabilize a dispersion of ULVs. Formation of ULVs even in the 5:1 DMPC: UMP sample indicates the high affinity of UMP for the membrane surface, in spite of its rather high solubility in water (50 mg/ml).

In agreement with these observations, our computer simulations show that UMP molecules

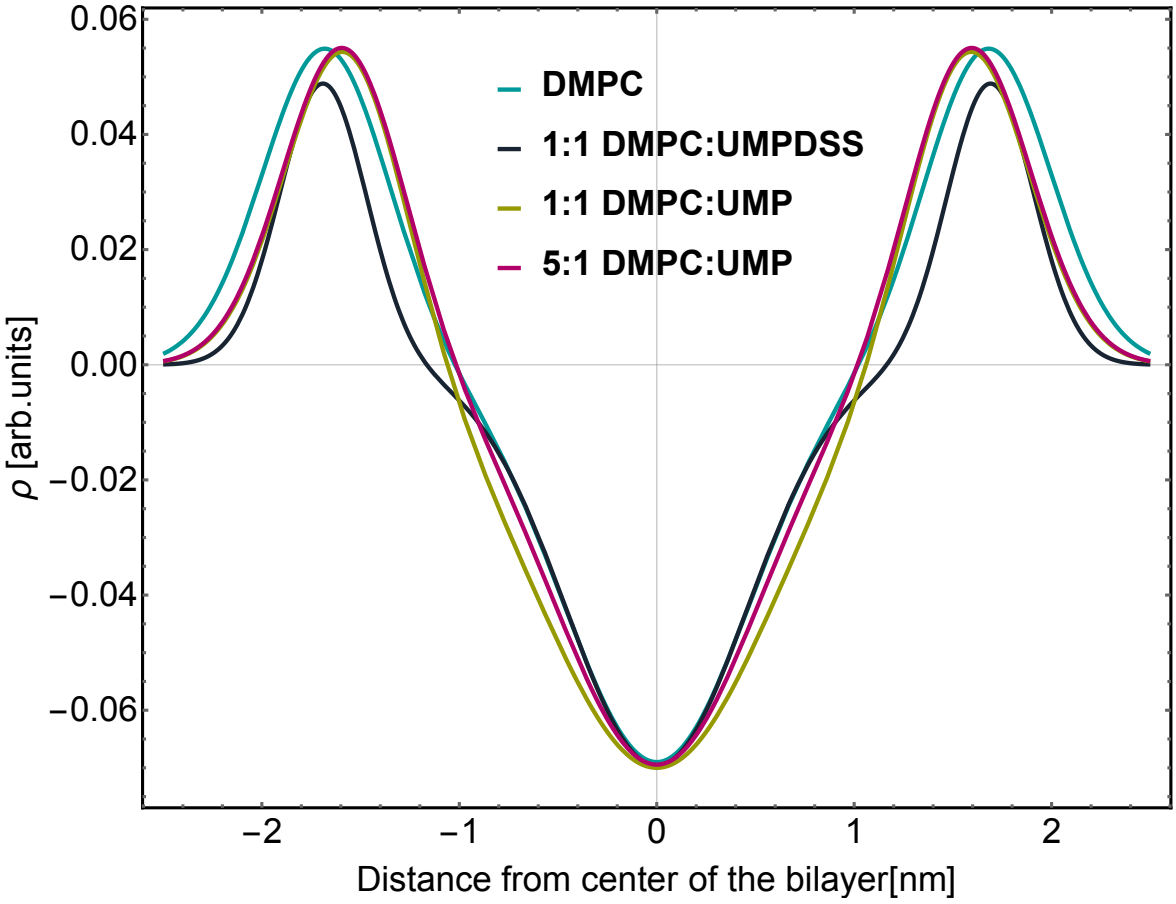

Figure 2.7: Transbilayer electron density profiles of the different systems, determined using the values of the model parameters given in Table 2.1.

bind to the DMPC membrane in the absence of Na^+ counterions [11]. This will lead to a strong electrostatic repulsions between the membranes, as observed in the experiments.

There is a vast literature on the interaction of biologically relevant small molecules with lipid bilayers. Cholesterol and related sterols increase chain ordering and hence the bilayer thickness, by inserting into the bilayer with their long axes almost parallel to the bilayer normal [16, 17]. On the other hand, another class of molecules, which includes small alcohols and other polar molecules, is known to bind to the headgroup region of the bilayer, thereby increasing the effective area per headgroup, resulting in a reduction in the bilayer thickness and in chain order [18, 19, 20, 21, 22]. A similar effect is also found in the case of certain antimicrobial peptides, that adsorb on the bilayer surface [23]. Acetyl salicylic acid, the main ingredient of aspirin, also interacts with the lipid head group and increases the fluidity of the bilayer [24]. It is, therefore, understandable that UMP, which binds to the interfacial region of the bilayer, leads to the thinning of the bilayer.

In the case of DMPC: UMPDSS we observe a lamellar structure with a periodicity of 7.72

nm, whereas lamellar periodicity of DMPC under similar conditions is 6.12 nm. Thus the interaction of UMPDSS with DMPC bilayers is very different from that of UMP. Concentration of UMPDSS in the 1:1 DMPC: UMPDSS sample is 170 mM, whereas that of UMP in the 5:1 and 1:1 DMPC: UMP samples is 16 mM and 80 mM, respectively. Hence the striking difference in their behaviors cannot be attributed to differences in the concentrations and should arise from differences in the interaction of these two species with the DMPC bilayer. Indeed, simulation studies show that UMP has limited effect on the bilayer in the presence of Na^+ counterions. UMP molecules interact with Na^+ and form small aggregates which do not penetrate the membrane headgroup region, but still have the ability to bind to the membrane. This aggregation formation is somewhat reminiscent of the micellization of bile salts [25, 26]. Further work carried out to understand this behaviour is described in chapter 3.

Analysis of the SAXS profiles indicates a slight thinning of DMPC bilayers in the presence of UMPDSS. Therefore, the increased lamellar periodicity of the DMPC: UMPDSS system results from a thicker water layer separating the bilayers. Such a swelling can result if the bilayers acquire a small charge density in the presence of UMPDSS. However, the SAXS patterns are not consistent with electrostatic stabilization, since the peaks are slightly broader in the case of DMPC: UMPDSS compared to pure DMPC, whereas the higher bending rigidity of charged bilayers should have resulted in a reduction in the peak width [27]. Analysis of the SAXS profiles show that the Caillé parameter η_1 has a much higher value of 0.22 for the DMPC:UMPDSS system, compared to 0.06 for pure DMPC, suggesting a lowering of the bilayer bending rigidity κ in the presence of UMPDSS. As mentioned earlier, UMP molecules in the DMPC: UMPDSS system form small nanoparticle- like aggregates near the membrane. In this context,it is interesting to note that the adsorption of anionic nanoparticles on neutral bilayers has been reported to lead to a slight lowering of κ [28]. The microscopic mechanism responsible for this effect remains poorly understood at present.

2.4 Conclusion

We have carried out SAXS and cryo-SEM experiments on the interaction of the mononucleotide UMP and its disodium salt, UMPDSS, with fluid DMPC membranes. The lipid membranes are found to acquire a surface electric charge density due to the binding of UMP molecules, which are charged in aqueous solutions. The resulting long-range inter-bilayer electrostatic repulsion leads to a pronounced swelling of the lamellar phase of DMPC membranes and the formation of a dispersion of ULVs in dilute solutions. Binding of UMP also lowers the bilayer thickness of DMPC. A vastly different behavior is observed in the presence of Na^+

counterions. UMPDSS leads to negligible swelling of the lamellar phase of DMPC with only a slight increase in the lamellar periodicity. Computer simulations [11] provide further insights into the striking differences in the effects of UMP and UMPDSS on fluid DMPC membranes. UMP molecules bind directly to the membrane, whereas UMPDSS molecules form small aggregates in water, which then bind to the membrane surface. Further, radial distribution functions calculated from these simulations reveal the microscopic interactions between the mononucleotide molecules and the headgroups of lipids.

Bibliography

[1] J. N. Israelachvilli. *Intermolecular and surface forces.* Elsevier, third edition, 2014.

[2] E. Sezgin, I. Levental, S. Mayor, and C. Eggeling. The mystery of membrane organization: composition, regulation and roles of lipid rafts. *Nat Rev Mol Cell Biol*, 6:361–374, 2017.

[3] A. M. Seddon, D. Casey, R. V. Law, A. Gee, R. H. Templera, and O. Cesab. Drug interactions with lipid membranes. *Chem. Soc. Rev.*, 38:2509–2519, 2009.

[4] P.G. Higgs and N. Lehman. The RNA world: Molecular cooperation at the origins of life.

[5] S. Rajamani, A. Vlassov, S. Benner, and A. Coombs. Lipid-assisted synthesis of RNA-like polymers from mononucleotides. *Orig. Life Evol. Biosph.*, 38:57–74, 2008.

[6] L. Da Silva, M.-C. Maurel, and D. Deamer. Salt-promoted synthesis of RNA-like molecules in simulated hydrothermal conditions. *J Mol Evol.*, 80(2):86–97, 2015.

[7] C. V. Mungi and S. Rajamani. Characterization of RNA-like oligomers from lipid-assisted nonenzymatic synthesis: implications for origin of informational molecules on early earth. *Orig. Life Evol. Biosph.*, 38:57–74, 2008.

[8] L. Toppozini, H. Dies, D. W. Deamer, and M. C. Rheinstädter. Adenosine monophosphate forms ordered arrays in multilamellar lipid matrices: Insights into assembly of nucleic acid for primitive life. *PLOS ONE*, 8(5):62810–62818, 2013.

[9] S. Himbert, M. Chapman, D. W. Deamer, and M. C. Rheinstädter. Organization of nucleotides in different environments and the formation of pre-polymers. *Scientific Reports*, 6:31285–31297, 2016.

[10] L. Misuraca, F. Natali, L. da Silva, J. Peters, B. Demé, J. Ollivier, T. Seydeland, V. Laux-Lesourd, M. Haertlein, G. Zaccai, D. Deamer, and M. C. Maurel. Mobility of a mononucleotide within a lipid matrix: A neutron scattering study. *Life*, 7(2), 2017.

[11] S. Sasidharan, S. Pochinda, P. N. Elgaard-Jørgensen, S. Rajamani, H. Khandelia, and V. A. Raghunathan. Interaction of the mononucleotide ump with a fluid phospholipid bilayer. *Softmatter*, 40:8129–8136, 2019.

[12] D. D. Lasic. The mechanism of vesicle formation. *Biochem. J*, 256:1–11, 1988.

[13] R. Silva, H. Ferreira, C. Little, and A. Cavaco-Paulo. Effect of ultrasound parameters for unilamellar liposome preparation. *Ultrasonics Sonochemistry*, page 628–632, 2010.

[14] G. Pabst, M. Rappolt, H. Amenitsch, and P. Laggner. Structural information from multilamellar liposomes at full hydration: Full q-range fitting with high quality x-ray data. *Phys. Rev. E*, 62(3):4000–4009, 2000.

[15] N. Kučerka, M.-P. Nieh, and J. Katsaras. Fluid phase lipid areas and bilayer thicknesses of commonly used phosphatidylcholines as a function of temperature. *Biochim. Biophys. Acta*, 1808:2761–2771, 2011.

[16] J. Czub and M. Baginski. Comparative molecular dynamics study of lipid membranes containing cholesterol and ergosterol. *Biophys. J*, 90:2368–2382, 2006.

[17] N. Kučerka, J. D. Perlmutter, J. Pan, S. Tristram-Nagle, J. Katsaras, and J. N. Sachsz. The effect of cholesterol on short- and long-chain monounsaturated lipid bilayers as determined by molecular dynamics simulations and x-ray scattering. *Biophys. J*, 95:2792–2805, 2008.

[18] H. V. Ly, D. E. Block, and M. L. Longo. Interfacial tension effect of ethanol on lipid bilayer rigidity, stability, and area/molecule: A micropipet aspiration approach. *Langmuir*, 18:8988–8995, 2002.

[19] W. Kopec, J. Telenius, and H. Khandelia. Molecular dynamics simulations of the interactions of medicinal plant extracts and drugs with lipid bilayermembranes. *The FEBS Journal*, 280:2785–2805, 2013.

[20] M. Patra, J. Holopainena, E. Salonen, E. Terama, M. Karttunen, I. Vattulainen, R. Faller, and B. W. Lee. Under the influence of alcohol: The effect of ethanol and methanol on lipid bilayers. *Biophys. J*, 90:1121–1135, 2006.

[21] R. Notman, M. Noro, B. O'Malley, and J. Anwar. Molecular basis for dimethylsulfoxide (dmso) action on lipid membranes. *J. Am. Chem. Soc.*, 128(43):13982–13983, 2006.

[22] W.-C. Hung, F.-Y. Chen, C.-C. Lee, Y. Sun, M.-T. Lee, and H. W. Huang. Membrane-thinning effect of curcumin. *Biophys. J*, 94:4331–4338, 2008.

[23] C. Neale, J. C. Y. Hsu, C. M. Yip, and R. Pomes. Indolicidin binding induces thinning of a lipid bilayer. *Biophys. J*, 106:L29–L31, 2014.

[24] M. A. Barrett, S. Zheng, G. Roshankar, R. J. Alsop, R. K. R. Belanger, C. Huynh, N. Kučerka, and M. C. Rheinstädter. Interaction of aspirin (acetylsalicylic acid) with lipid membranes. *Plus One*, 7(8), 2012.

[25] P. Garidel, A. Hildebrand, R. Neubert, and A. Blume. Thermodynamic characterization of bile salt aggregation as a function of temperature and ionic strength using isothermal titration calorimetry. *Langmuir*, 16:5267–5275, 2000.

[26] L. B. Pártay, P. Jedlovszky, and M. Sega. Molecular aggregates in aqueous solutions of bile salts. molecular dynamics simulation study. *J. Phys. Chem. B*, 111:9886–9896, 2007.

[27] D. Roux and C.R. Safinya. A synchrotron x-ray study of competing undulation and electrostatic interlayer interactions in fluid multimembrane lyotropic phases. *Journal de Physique*, 49(2):307–318, 1988.

[28] I. Hoffmann, M.-S. Appavou, R. Michel, F. Polzer, M. Sharp, B. Farago, O. Holderer, and M. Gradzielski. Softening of phospholipid membranes by the adhesion of silica nanoparticles – as seen by neutron spin-echo (nse). *Nanoscale*, 6:6945–6952, 2014.

Part2 : Influence of UMP on the phase behavior of DMPC bilayers

2.5 Introduction

Phase behavior of DMPC: UMP is found to change with time. Adsorption of charged UMP molecules onto the lipid head group region leads to repulsion between the bilayers, resulting in the formation of unilamellar vesicles, as described in the last section. With time, the unilamellar vesicles are transformed into an electrostatically stabilised swollen lamellar phase. Adsorption of UMP also affects the thermal phase behavior of lipid bilayers. The swollen lamellar phase formed has a higher main transition temperature compared to pure DMPC. Adsorption of UMP could replace the water of hydration around the head group region leading to the observed increase in the main transition temperature. The transition temperature of the lamellar phase slowly increased and saturated at 42°C upon incubation. On longer incubation for periods of the order of days, the lipid bilayers formed an interdigitated phase, which melts above 50°C into an inverted hexagonal phase in the case of samples with 5:1 DMPC: UMP molar ratio. Diffraction patterns from 1:1 samples, on the other hand, showed a broad peak corresponding to an isotropic dispersion at temperatures above 50°C. We probed the time-dependent phase behavior of DMPC: UMP samples (1:1 and 5:1) using SAXS, WAXS, DSC, Raman scattering, and fluorescence microscopy. These studies are described below.

2.6 Results

Phase behavior of DMPC: UMP samples at different UMP concentrations and hydrations

DMPC: UMP samples of different water contents were prepared at two different molar ratios, 1:1 and 5:1, and incubated at room temperature ($\sim$ 27°C) for a day. The lipid content in the samples was varied from 5 wt% to 20 wt%. SAXS, WAXS, and DSC measurements were

carried out to characterise the phase behavior of these systems. The electron density profiles (EDP) obtained by analysing the x-ray diffraction data showed a change in bilayer thickness as a function of temperature. Further, 20 wt% samples analysed using DSC and WAXS showed an increase in the gel to the fluid phase transition temperature of DMPC in the presence of UMP.

2.6.1 SAXS

SAXS patterns obtained for 1 day of incubation of the 5 wt% samples(1:1 & 5:1 molar ratio), as a function of temperature on cooling and heating are shown in fig.(2.8). In both cases, the diffraction patterns broadened upon heating. This behavior is reproducible for both samples on cooling as well as heating.

SAXS profiles of DMPC: UMP (5:1) sample at different hydration levels are shown in fig.2.9. All the samples show SAXS profiles consisting of a single broad pattern. Detailed analysis of these patterns, using the procedure discussed in chapter 1, section SAXS, indicates that these patterns correspond to the form factors of the bilayer without any inter-bilayer correlations. From the SAXS data, transbilayer electron density profiles (EDP) were obtained for different temperatures and concentrations. The temperature dependence of EDP showed a drastic increase in the bilayer thickness at 30°C compared to 40°C and above (fig.2.10). The change in EDP at 30°C indicates that the bilayer is in the gel phase at 30°C. Pure DMPC has the main transition temperature of 23.8°C. Hence the interaction of UMP leads to an increase in gel phase transition temperature. This behavior is reproduced on cooling as well, which rules out the possibility of the formation of a metastable phase. The nature of this gel phase is characterised by WAXS, 2D aligned x-ray diffraction and DSC, the details of which are described in the latter part of this chapter. In the case of 1:1 samples, the broad diffraction pattern corresponding to the form factor of the bilayer is observed till 10 wt% of lipid, above which samples showed sharp peaks corresponding to the swollen lamellar phase along with a broad form factor background (fig.2.11). Similar to the case of 5:1 sample, the electron density profiles obtained for the 1:1 sample (5 wt% and 10 wt%) showed an abrupt increase in bilayer thickness at 30°C on cooling (fig.2.12). For samples having still higher lipid concentrations of 15wt% and 20 wt%, peaks corresponding to a swollen lamellar phase were found to coexist with a broad form factor background. Hence electron density profiles were not evaluated in these cases. The EDPs obtained at different hydration levels of 5:1, and 1:1 samples showed not much dependence on the hydration level at any given temperature (fig.2.13). We chose to work with the highest lipid concentration (20 wt%) to further explore

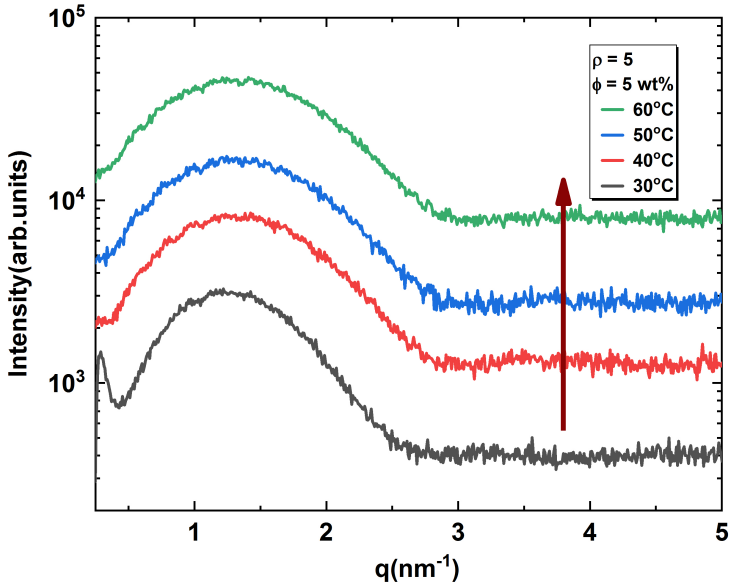
ρ = 5
ϕ = 5 wt%
60°C
50°C
40°C
30°C
Intensity(arb.units)
q(nm-1)

(a)

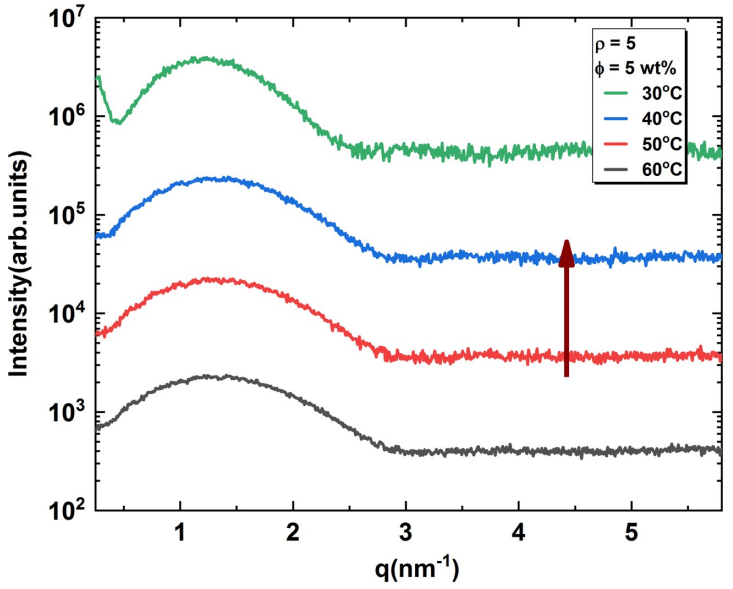
ρ = 5
ϕ = 5 wt%
30°C
40°C
50°C
60°C
Intensity(arb.units)
q(nm-1)

(b)

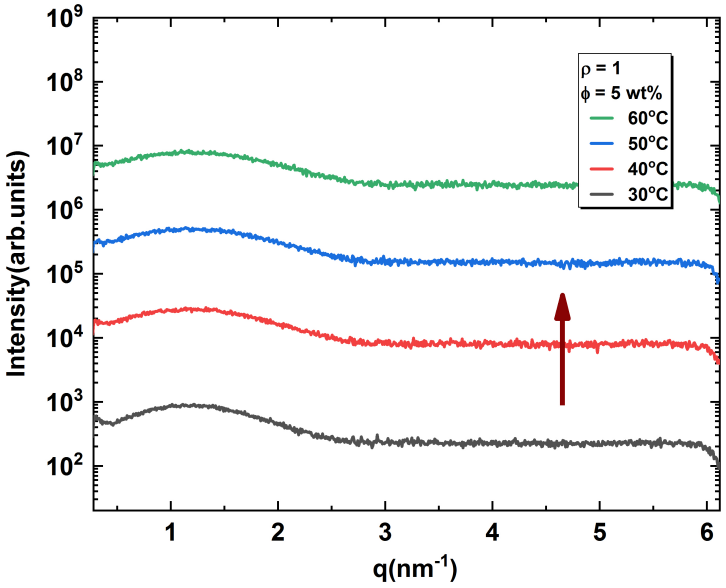

(c)

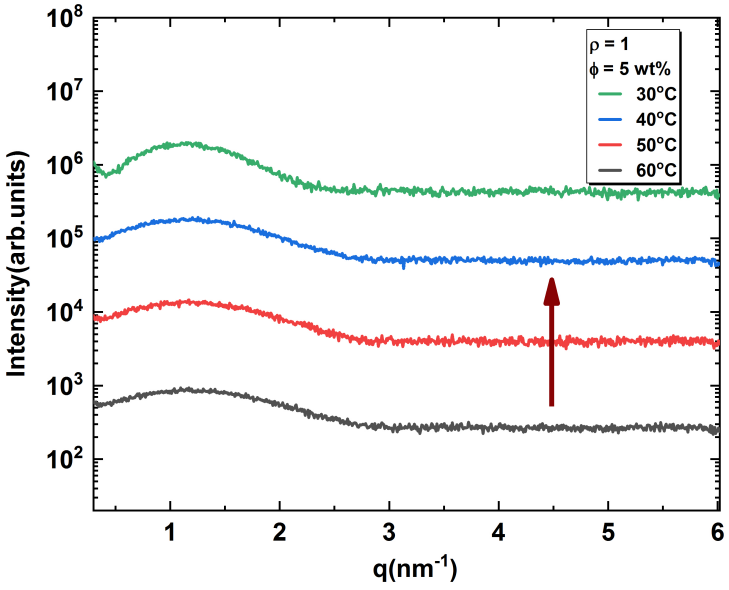

(d)

Figure 2.8: DMPC:UMP (5:1) (a) & (b) and (1:1) (c) & (d) 5 wt% sample on heating and cooling.

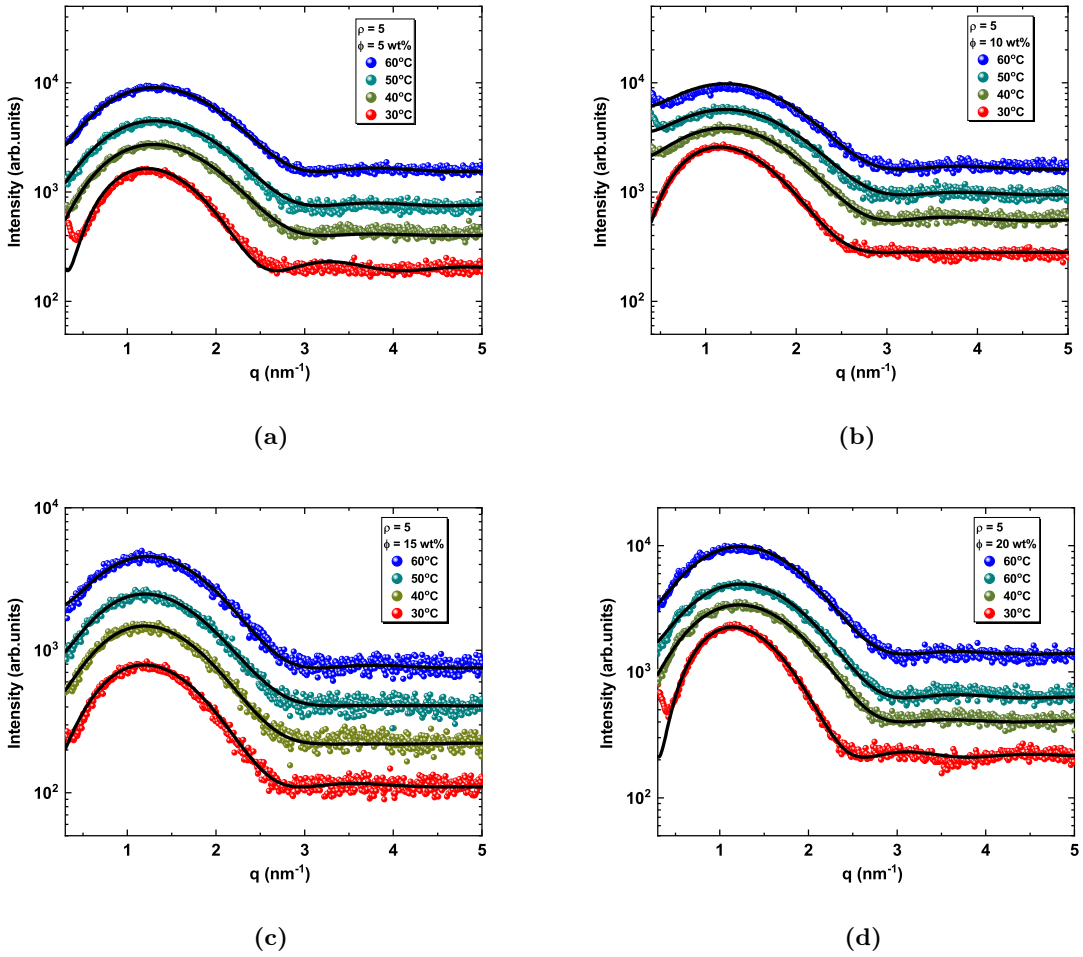

Figure 2.9: SAXS patterns of DMPC:UMP (5:1) (a) 5 wt% (b) 10 wt% (c) 15 wt% (d) 20 wt% samples on heating. The solid lines are fits to the model.

the incubation time dependence of this phase behavior.

2.6.2 WAXS and DSC

The abrupt change in the bilayer thickness at 30°C suggested that there could be an elevation of the main gel phase transition temperature of DMPC upon the adsorption of UMP. Below T_m (23.8°C), DMPC forms the ripple phase, which on further cooling is transformed into the crystalline gel phase at 14°C. The gel phase of lipids is characterised by a quasi-hexagonal lattice of chains in the plane of the bilayer. This in-plane chain lattice can be probed using WAXS. Fig.2.14 shows the wide-angle scattering from DMPC: UMP samples incubated at room temperature for a day. A wide-angle peak was observed with a spacing of 0.42 nm for both samples for temperatures (35°C and 40°C respectively for 5:1 and 1:1 samples) much above T_m of DMPC. The presence of chain reflection in the WAXS pattern above T_m of lipid indicates the elevation of the gel phase transition temperature of DMPC in the presence of

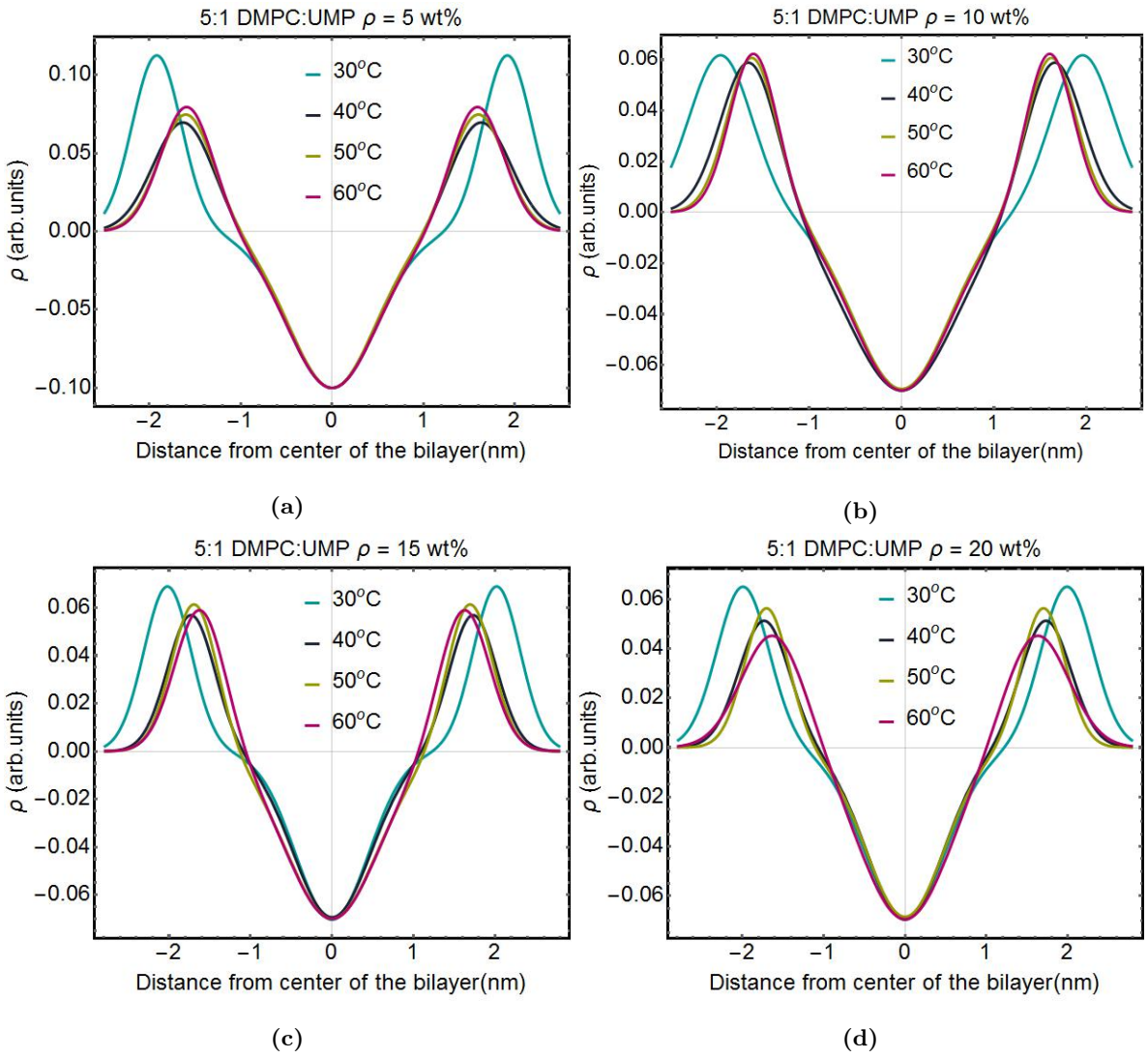

Figure 2.10: Electron density profiles obtained from SAXS patterns of DMPC:UMP (5:1) (a) 5 wt% (b) 10 wt% (c) 15 wt% (d) 20 wt% samples

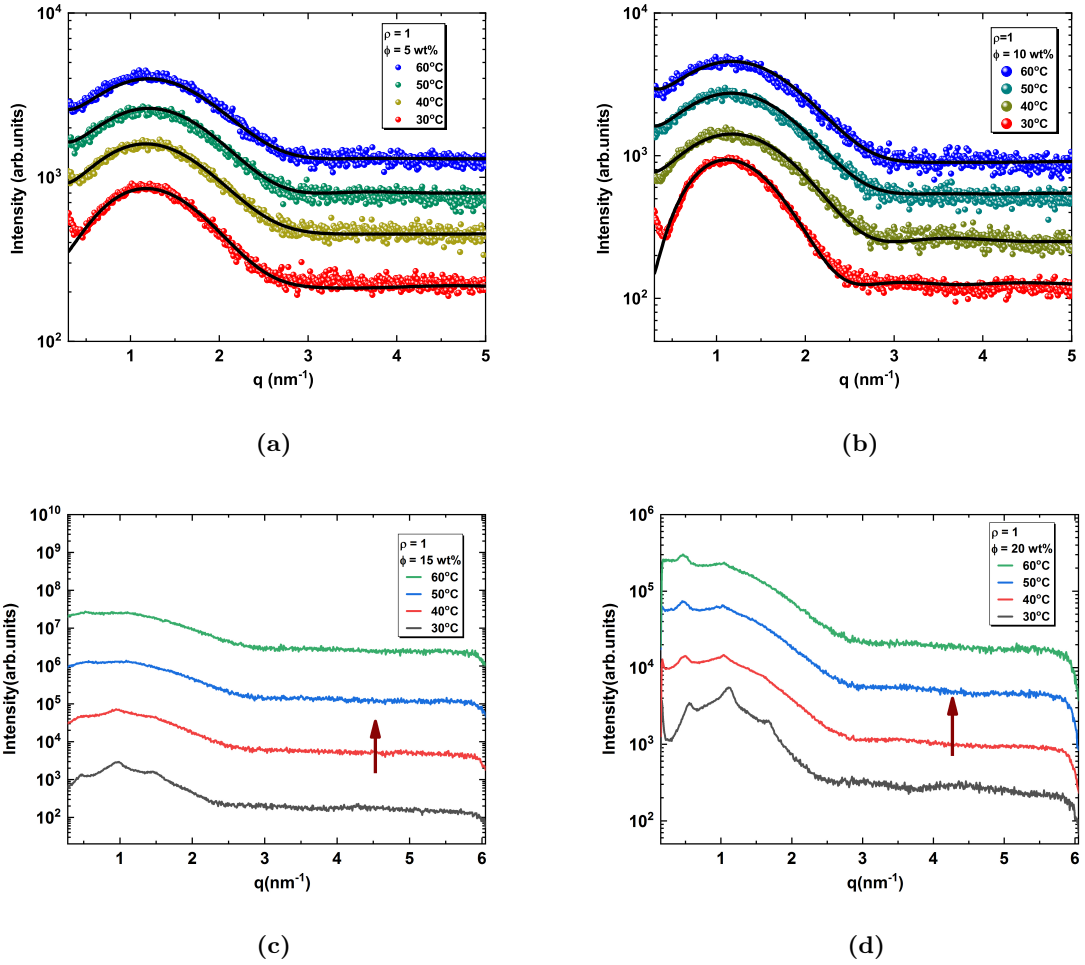

Figure 2.11: SAXS patterns of DMPC:UMP (1:1) (a) 5 wt% (b) 10 wt% (c) 15 wt% (d) 20 wt% samples on heating

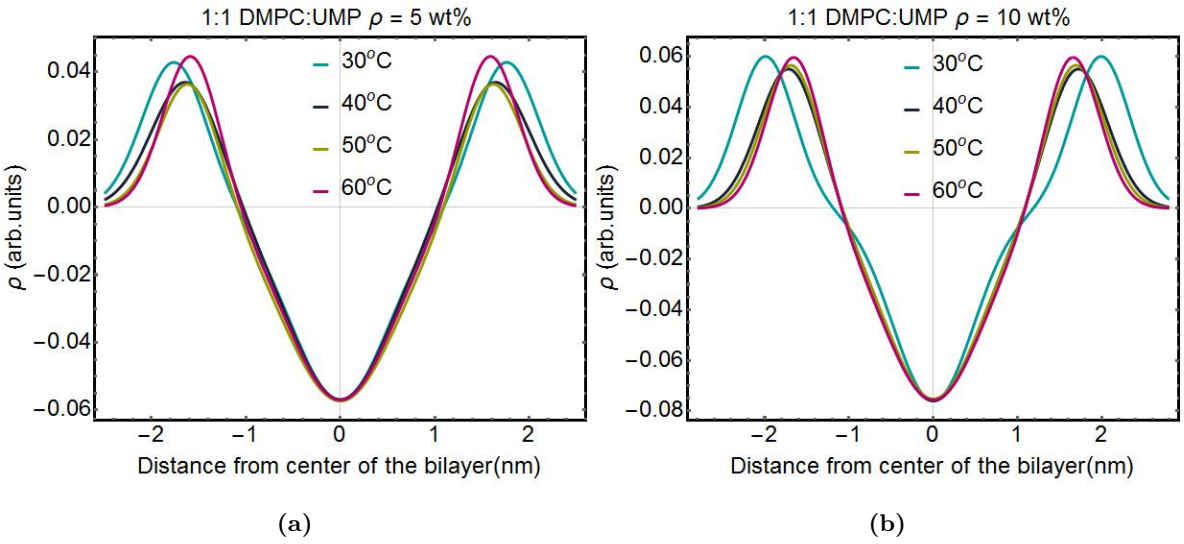

Figure 2.12: Electron density profiles obtained from saxs patterns of DMPC:UMP (1:1) (a) 5 wt% (b) 10 wt% samples

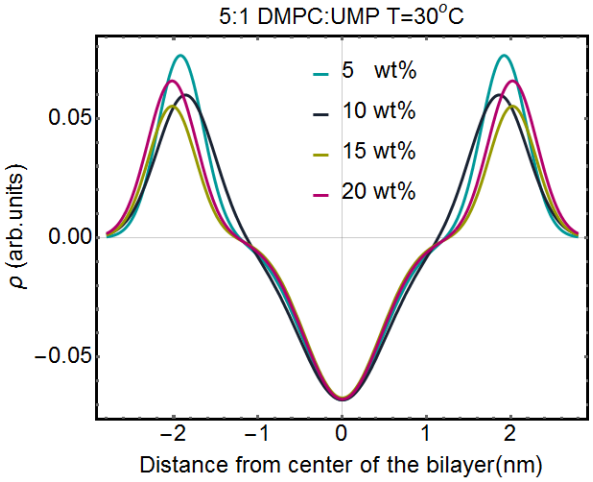

(a)

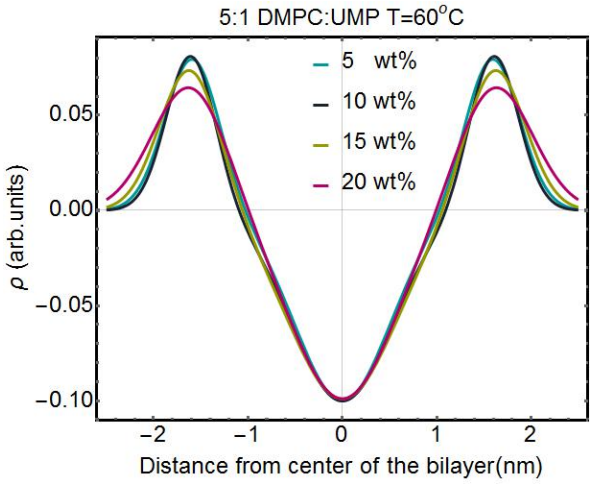

(b)

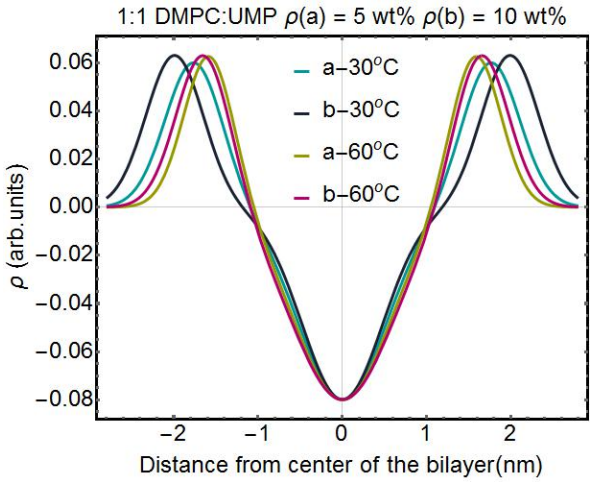

(c)

Figure 2.13: Comparison of electron density profiles obtained for of DMPC:UMP 5:1 at different hydration at a given temperature (5 wt%, 10 wt%, 15 wt% and 20 wt%) (a) 30°C (b) 60°C (c) that of 1:1 (5 wt% and 10 wt%) at 30°C & 60°C

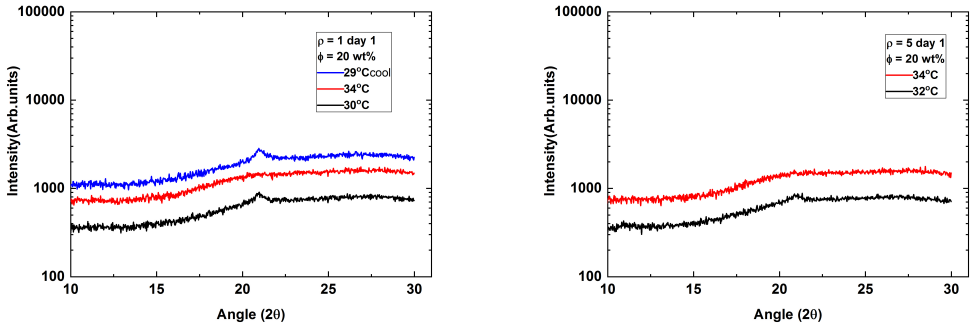

(a) **(b)**

Figure 2.14: WAXS pattern obtained as a function of temperature for 1:1 and 5:1 DMPC:UMP samples incubated for a day at room temperature

UMP.

Differential scanning calorimetry measures the enthalpy of a phase transition [1]. The change in transition temperature can also be detected by monitoring the phase transition of DMPC as a function of UMP content. From the thermogram obtained, it can be seen that the main transition temperature of DMPC has shifted to around 30°C and 33°C, respectively, for 5:1 and 1:1 samples (fig.2.15).

2.6.3 2D XRD and fluorescence microscopy

Aligned multilayer stacks of DMPC: UMP samples under high humidity conditions were analysed by 2 D x-ray diffraction (figs. 2.16,2.17,2.18). Depending on the molar ratio, above a certain temperature, which is much higher than T_m of DMPC, patterns corresponding to the single fluid phase is obtained for 4:1 and 5:1 samples. On cooling, the sample showed the formation of gel-fluid phase coexistence. On further cooling, depending on DMPC: UMP molar ratio, the sample showed a single gel phase above T_m of pure DMPC. On increasing the molar concentration of UMP, in the 1:1 sample, the gel-fluid coexistence was not seen. In this case, below 42°C, the sample showed the gel phase. The wide-angle pattern from the gel phase showed an on-axis peak, which indicates that the chains are not tilted with respect to the layer normal [2]. This single peak can be indexed to a hexagonal in-plane lattice formed by the chains. An off-axis peak is observed in the wide-angle diffraction pattern of the gel phase of pure DMPC since the chains are tilted due to the larger area of the head group compared to the cross-sectional area of the chains. Hence the on-axis wide-angle peak observed from the gel phase of DMPC: UMP sample is surprising since the effective head group area is expected to increase on adsorption of small molecules. Raman spectroscopy studied later in this chapter

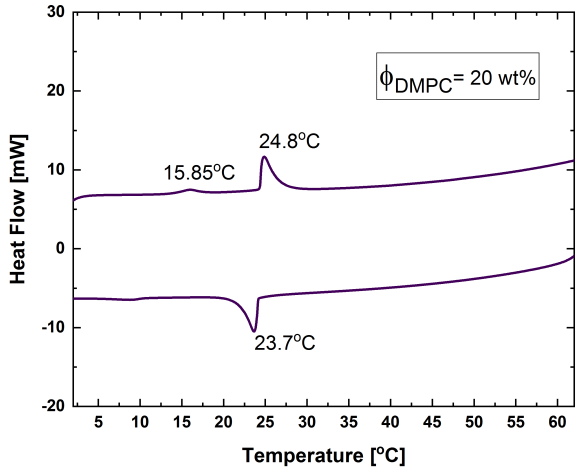

(a)

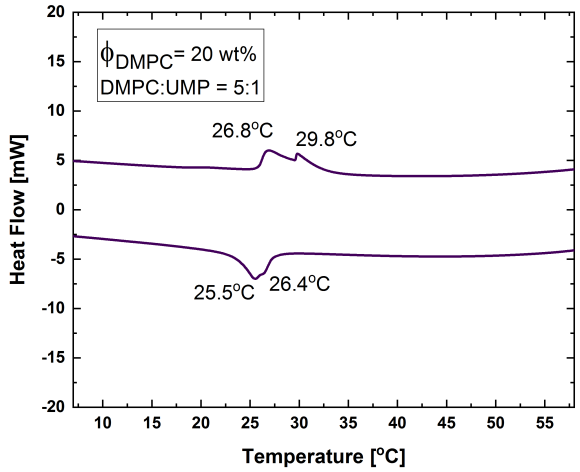

(b)

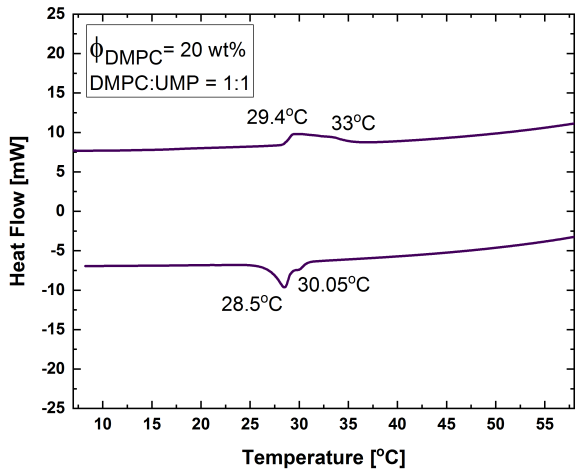

(c)

Figure 2.15: DSC data obtained for (a) DMPC (b) 5:1 DMPC:UMP and (c) 1:1 DMPC:UMP at lipid weight percentage $\phi = 20$ wt% at room temperature.

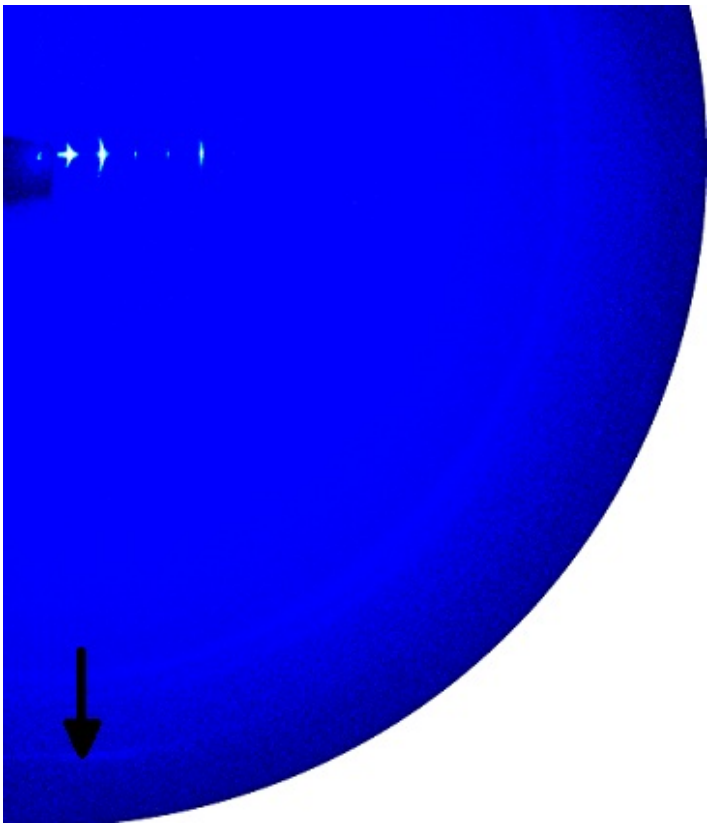

Figure 2.16: 2D x-ray diffraction data from 4:1 (DMPC:UMP) sample showing gel phase at 26 °C on cooling.The black arrow indicates the on axis peak corresponds to the untilted gel phase.

indicate that the adsorption of UMP on the bilayer leads to a change in the conformation of the head group. A lower effective area of this conformation can account for the absence of chain tilt in the gel phase of DMPC-UMP bilayers.

Fluorescence microscopy images of multilayer stacks of DMPC: UMP binary system of varying compositions, labeled with 0.1 mol% of Rhodamine-DHPE lipid, are shown in figures 2.19 and 2.20. The samples were imaged at high hydration (RH>99%). Rhodamine-DHPE has a preference for the fluid phase over the gel phase, and it is extensively used for visualizing phase coexistence in lipid systems [3]. Above a certain temperature, depending on the molar ratio, the samples showed a uniform fluid phase, which on cooling showed nucleation and growth of dark regions corresponding to the gel phase. These observations can be correlated to the x-ray diffraction patterns of the aligned lipid samples under high hydration. Gel-like domains are also observed in GUVs suspended in UMP solution as well as in supported lipid bilayers formed out of ruptured GUVs (figs. 2.21 and 2.22).

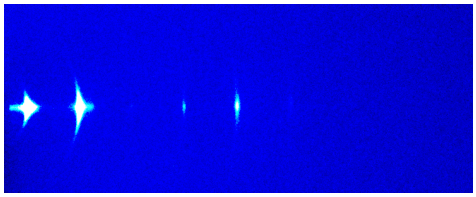

(a) T 27.5°C-SAXS (d1-7.2)

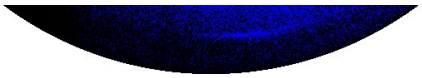

(b) T 27.5°C-WAXS (d1- 0.42 nm)

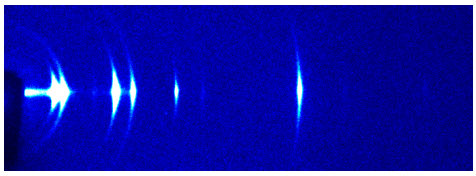

(c) T 29°C-SAXS (d1- 7.2 nm, d2-6.7 nm)

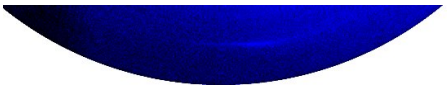

(d) T 29°C-WAXS (d1- 0.42 nm)

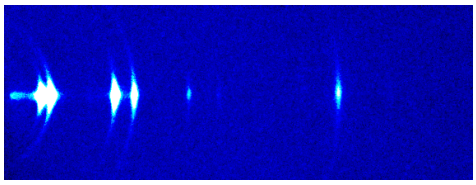

(e) T 32°C-SAXS (d1-7.2 nm,d2- 6.7 nm)

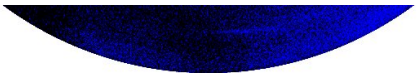

(f) T 32°C-WAXS (d1- 0.42 nm)

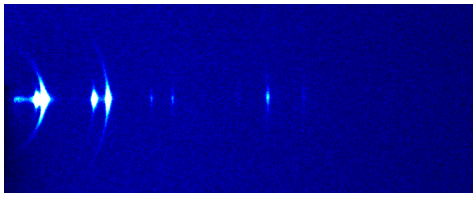

(g) T 36°C-SAXS (d1-6.9 nm, d2-6.2 nm)

(h) T 36°C-WAXS (no peak)

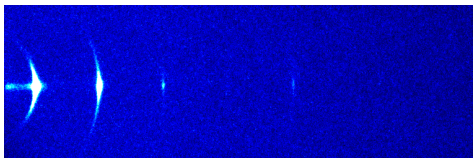

(i) T 38.5°C-SAXS (d1- 5.8 nm)

(j) T 38.5°C-WAXS (no peak)

Figure 2.17: 2D x-ray diffraction data from 4:1 (DMPC:UMP) sample showing gel-fluid coexistence in the small angle region (Left) and on axis peak in the wide angle region from untilted chain lattice (Right). The temperature at which the patterns were collected and the spacings corresponding to the peaks observed are indicated.

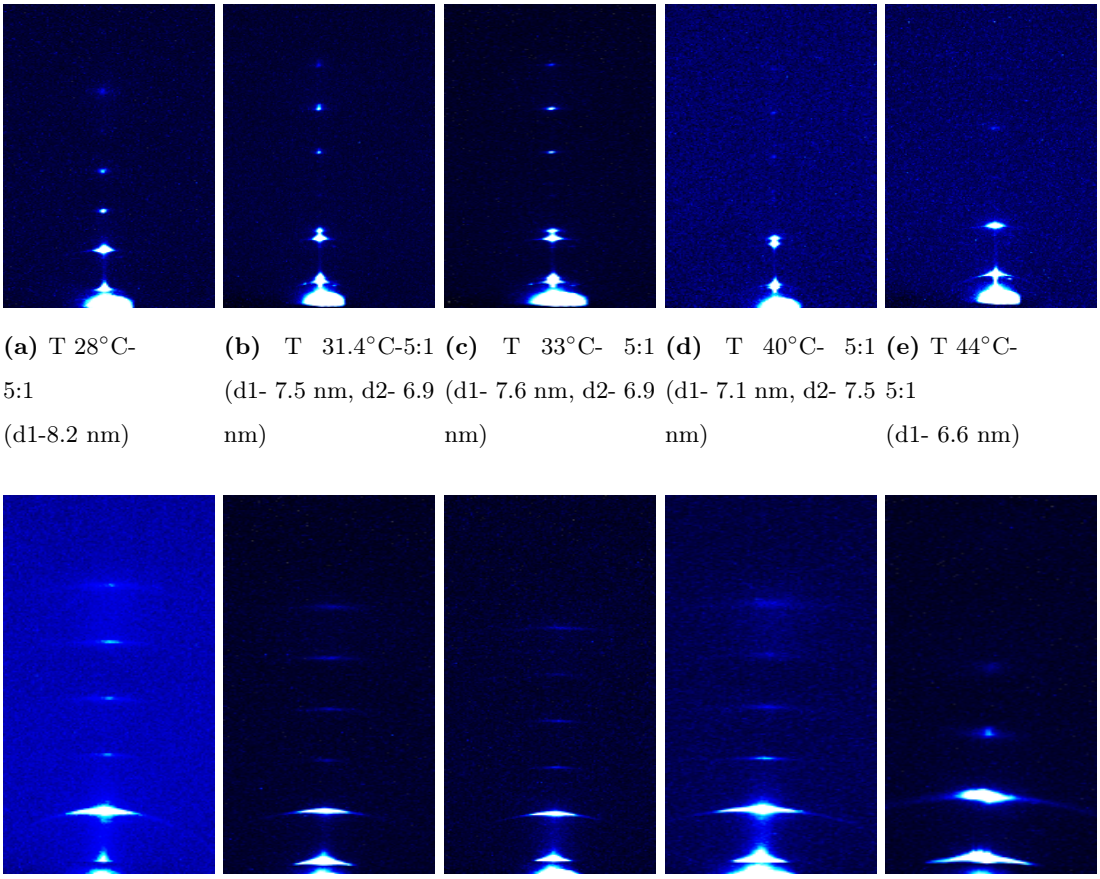

(a) T 28°C-5:1 (d1-8.2 nm) **(b)** T 31.4°C-5:1 (d1- 7.5 nm, d2- 6.9 nm) **(c)** T 33°C- 5:1 (d1- 7.6 nm, d2- 6.9 nm) **(d)** T 40°C- 5:1 (d1- 7.1 nm, d2- 7.5 nm) **(e)** T 44°C-5:1 (d1- 6.6 nm)

(f) T 21°C-1:1 (d1-7.3 nm) **(g)** T 30°C-1:1 (d1-7.5 nm) **(h)** T 35°C-1:1 (d1-7.8 nm) **(i)** T 39°C-1:1 (d1-7.9 nm) **(j)** T 44°C-1:1 (d1-7.0 nm)

Figure 2.18: 2D x-ray diffraction data from 5:1 (DMPC:UMP) sample showing gel-fluid coexistence in small angle region and 1:1 sample showing single gel phase below 44°C. Both the samples show wide peak at 0.42 nm below 44°C. The temperature at which the patterns were collected and the spacings corresponding to the peaks observed are indicated.

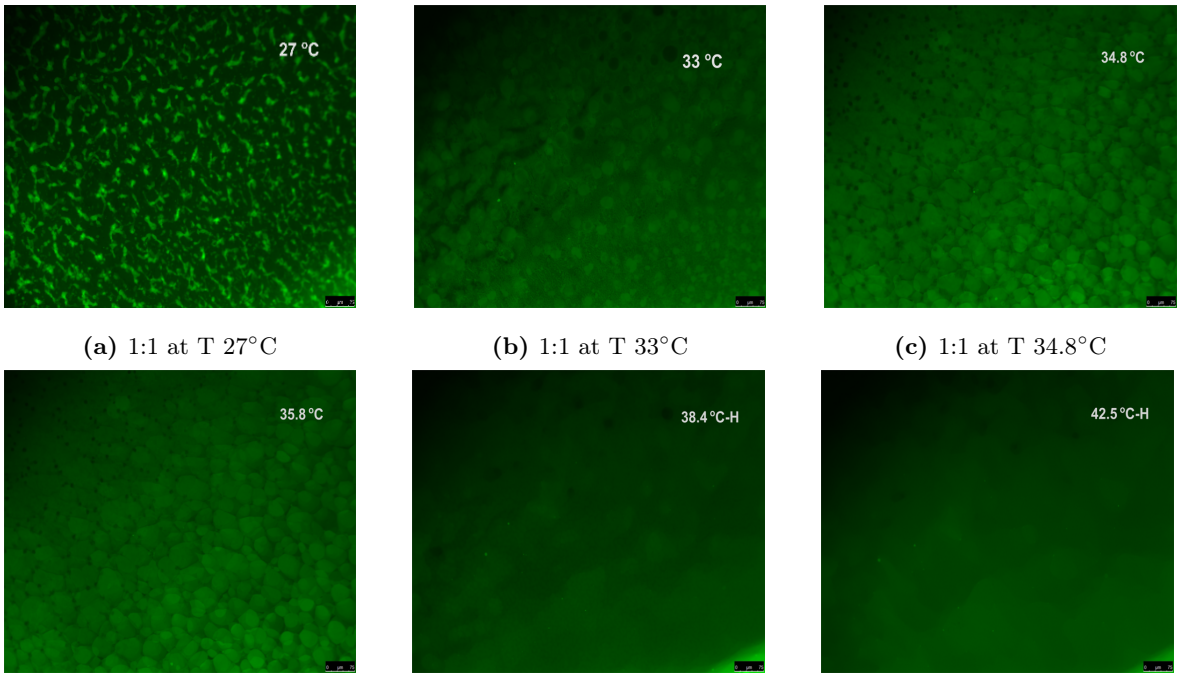

(a) 1:1 at T 27°C **(b)** 1:1 at T 33°C **(c)** 1:1 at T 34.8°C

(d) 1:1 at T 35.8°C) **(e)** 1:1 at T 38.4°C **(f)** 1:1 at T 42.5°C)

Figure 2.19: Fluorescence images obtained from the multilayer stacks of 1:1 DMPC:UMP at varying temperature. Scale bar shown is 75μm

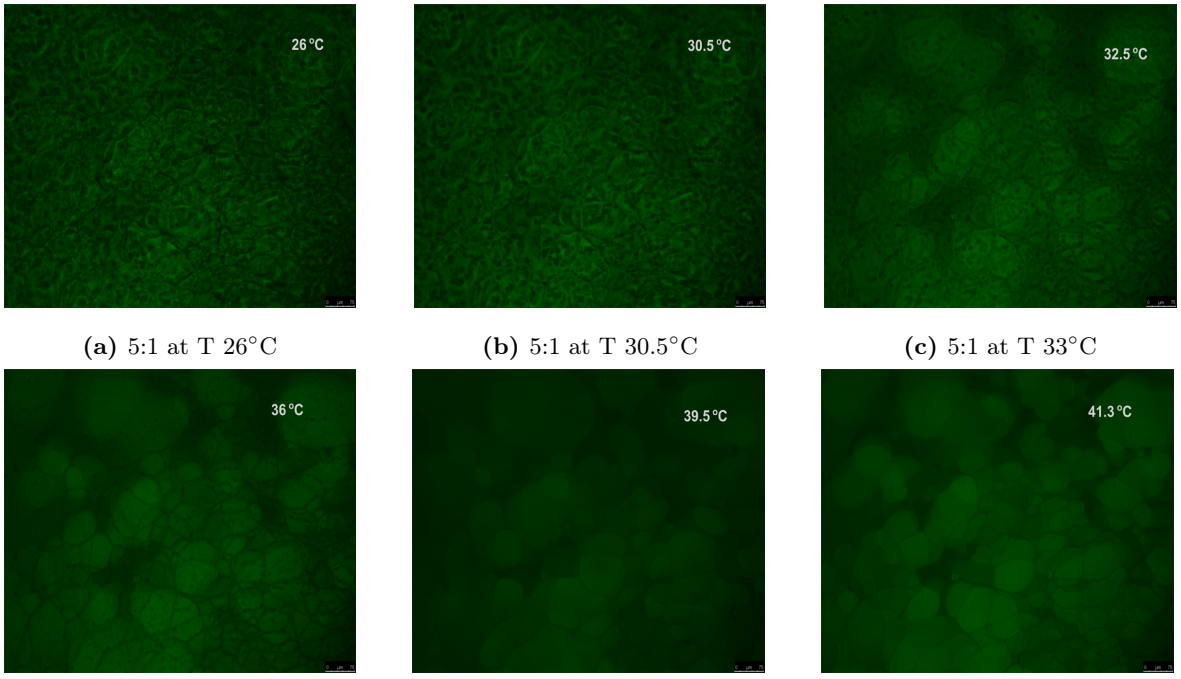

(a) 5:1 at T 26°C **(b)** 5:1 at T 30.5°C **(c)** 5:1 at T 33°C

(d) 5:1 at T 36°C **(e)** 5:1 at T 39.5°C **(f)** 5:1 at T 41.35°C

Figure 2.20: Fluorescence images obtained from the multilayer stacks of 5:1 DMPC:UMP at varying temperatures. Scale bar shown is 75μm

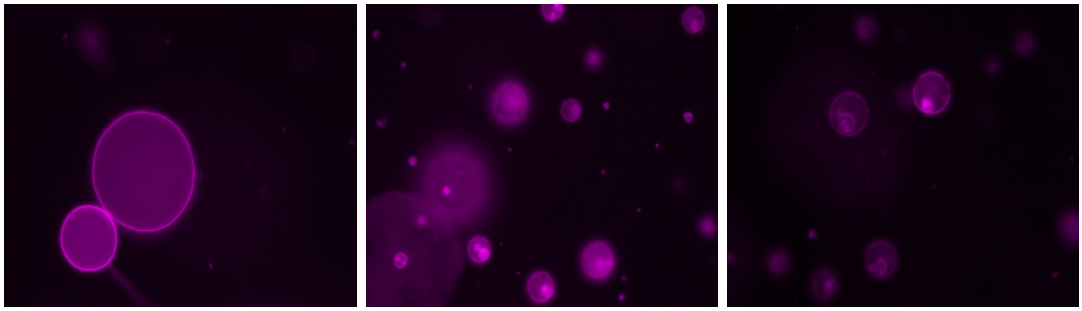

(a) **(b)** **(c)**

Figure 2.21: Fluorescence images of Giant unilamellar vesicles suspended in 110 mM dextrose solution (a) without UMP looking uniform whereas (b) and (c) with addition of 5 mg/ml UMP solution at 30°C showing phase seperation.

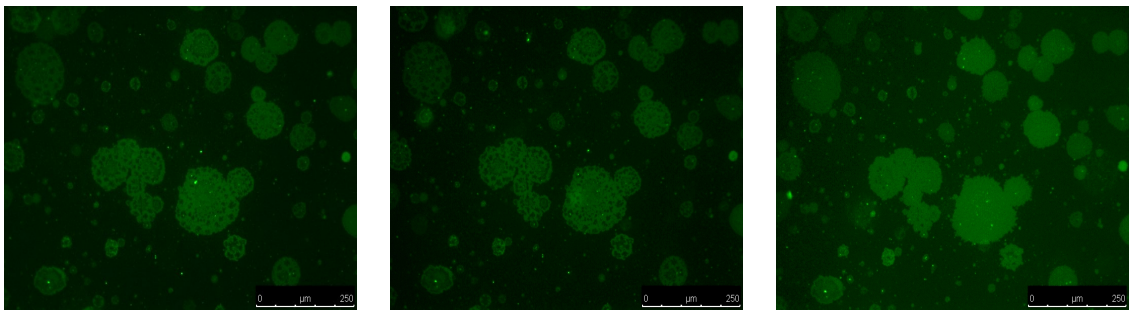

(a) **(b)** **(c)**

Figure 2.22: Supported bilayer formed by rupture of GUV showing black gel like domain at (a) 38°C (b) 40°C and (c) uniform phase at 48 °C

2.6.4 FTIR

The symmetric CH_2 ($\nu_{CH_2}S$) stretching vibration of the lipid chain is IR active and has been used for spectroscopic detection of gel-fluid transition in lipids. In the gel phase of the lipid, the chains are ordered and are in the trans configuration. Symmetric stretching vibrations of CH_2 give a peak at 2850 cm^{-1}. In the fluid phase, chains are more disordered, and the peak shifts towards higher wave number around 2852 cm^{-1} [4, 5]. FTIR measurements were carried out for both 1:1 and 5:1 samples with lipid concentration $\phi = 10$wt% as a function of temperature starting from room temperature (fig.2.23). Pure DMPC sample showed the peak at 2852 cm^{-1} corresponding to the fluid phase for all the temperatures measured, whereas 1:1 and 5:1 samples showed a change in the peak position, from 2850 cm^{-1} to 2852 cm^{-1} only above 30°C. This indicates the gel phase of DMPC is stabilized much above T_m of the pure lipid in the presence of UMP. In the case of 1:1 as well as 5:1 a shift in peak position was observable starting at 34°C. 1:1 sample showed the complete transition of the gel phase to the fluid phase around 40 °C, whereas the 5:1 sample showed the complete transition at 36 °C.

Variation of the phase behavior of DMPC: UMP samples with incubation time

Changes in the phase behavior of samples with incubation time were also studied. With incubation of a few days at room temperature ($\sim$ 27°C), DMPC: UMP samples were found to form a swollen lamellar phase (L^s) from the unilamellar dispersion obtained soon after sample preparation. The L^s phase transforms into an untilted gel phase below 42°C. With longer incubation time, the sample showed the formation of the interdigitated gel phase, which melts at 52°C on heating. The kinetics of this phase behavior is also affected by the incubation temperature and is rather slow when incubated at room temperature.

2.6.5 SAXS

SAXS patterns for 5:1 and 1:1 samples (20 Wt%) as a function of time are shown in figures.2.24 and 2.26. Both the samples showed a highly swollen lamellar phase with large d-spacing initially. 1:1 sample showed a swollen lamellar phase with a d-spacing of 12.2 nm, and, 5:1 sample showed a d-spacing of 13.9 nm. The difference in d-spacing between the 1:1 and 5:1 samples can be accounted for the fact that the sample weight percentages were calculated only considering the concentration of lipid. Hence, in the case of the 1:1 sample, the higher concentration of UMP in the solution results in a lower concentration of water, which limits

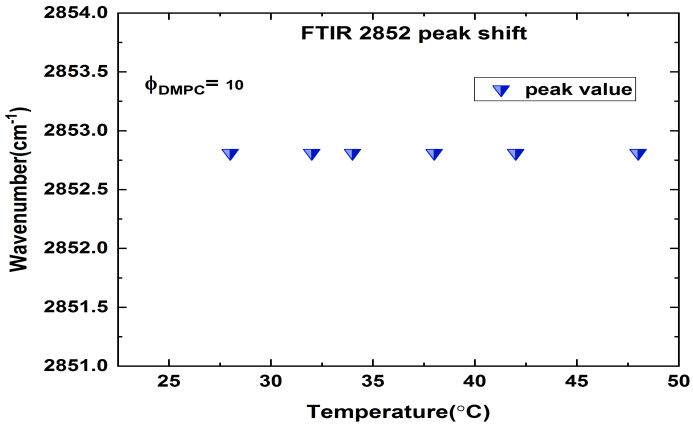

(a)

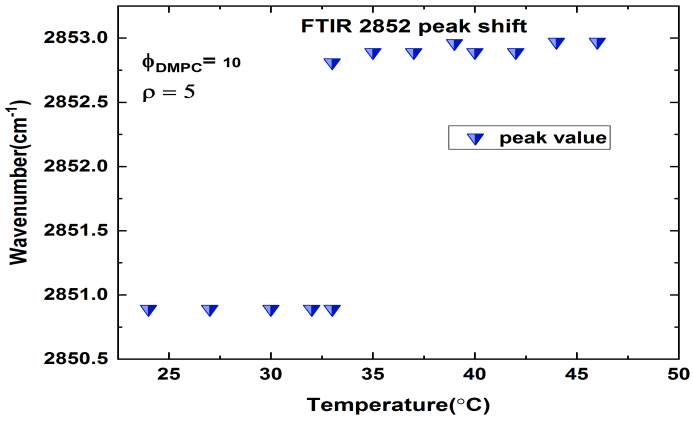

(b)

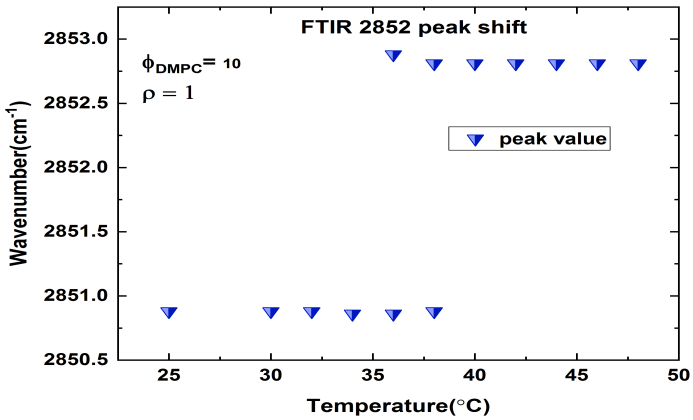

(c)

Figure 2.23: ν_{CH_2}S value obtained from FTIR spectra of (a) DMPC (b) 5:1 DMPC:UMP (c) 1:1 DMPC:UMP samples as a function of temperature

.

the maximum swelling possible. SAXS pattern of both samples changed at 42°C, showing the melting of the gel phase to the fluid phase. With further incubation for another 5-9 days, the samples formed a white precipitate. SAXS pattern of these samples showed the coexistence of a swollen lamellar phase with an interdigitated phase (IG phase). Cryo-SEM images of swollen lamellar and interdigitated lamellar phase formed by 1:1 DMPC: UMP samples are shown in fig.2.27. Tables(2.2,2.3) give the d-spacings of the samples as a function of incubation time. The interdigitated phase has a lamellar periodicity of 3.1 nm. The low periodicity of this phase indicate that the leaflets of the bilayer interpenetrate each other and are in a completely interdigitated state. Along with the reduction in bilayer thickness, the d-spacing of the lamellar phase also reduces drastically, suggesting that there is no electrostatic repulsion between the bilayers. The charge on the bilayer should be neutralized while going from the electrostatically stabilised swollen gel phase to the interdigitated phase. On heating, the interdigitated phase is converted into an inverted hexagonal phase in the 5:1 sample, whereas the 1:1 sample showed an isotropic phase above 50°C. The EDPs of the interdigitated phase and inverted hexagonal phase are shown in fig.2.25. The transition temperatures were not affected by the lipid molar ratio as well as the wt% of lipid between the 5:1 and 1:1 samples. But it was seen that the timescales involved in the formation of the swollen lamellar phase and interdigitated phase is affected by DMPC: UMP molar ratio as well as lipid concentration in the solution. In both cases, 5:1 and 1:1, 20 wt% samples showed a faster change in phase behavior compared to lower concentrations. For a given lipid wt% in the sample, 1:1 showed faster phase behavioral change compared to 5:1.

2.6.6 WAXS and DSC

The evolution of gel phase behavior is again analysed using WAXS and DSC measurements. WAXS patterns show the peak corresponding to the gel phase till 42°C on heating in samples incubated at room temperature for a week. The single peak obtained from the gel phase can be indexed to a hexagonal lattice with a lattice spacing of 0.42 nm. On incubating further, the system shows an interdigitated phase with two main peaks at 0.41 nm and 0.38 nm (fig.2.28(b)&(d)). These peaks correspond to the chain reflections from the lattice formed by the interdigitated phase. There is a slight mismatch between the temperature range of IG phase observation using SAXS and WAXS. WAXS pattern showed the formation of the IG phase much before corresponding data from SAXS. This can be explained by the fact that the chain arrangement of lipid responsible for the WAXS pattern is limited to the in-plane behavior of a single bilayer, unlike SAXS pattern, which needs bilayer-bilayer correlations.

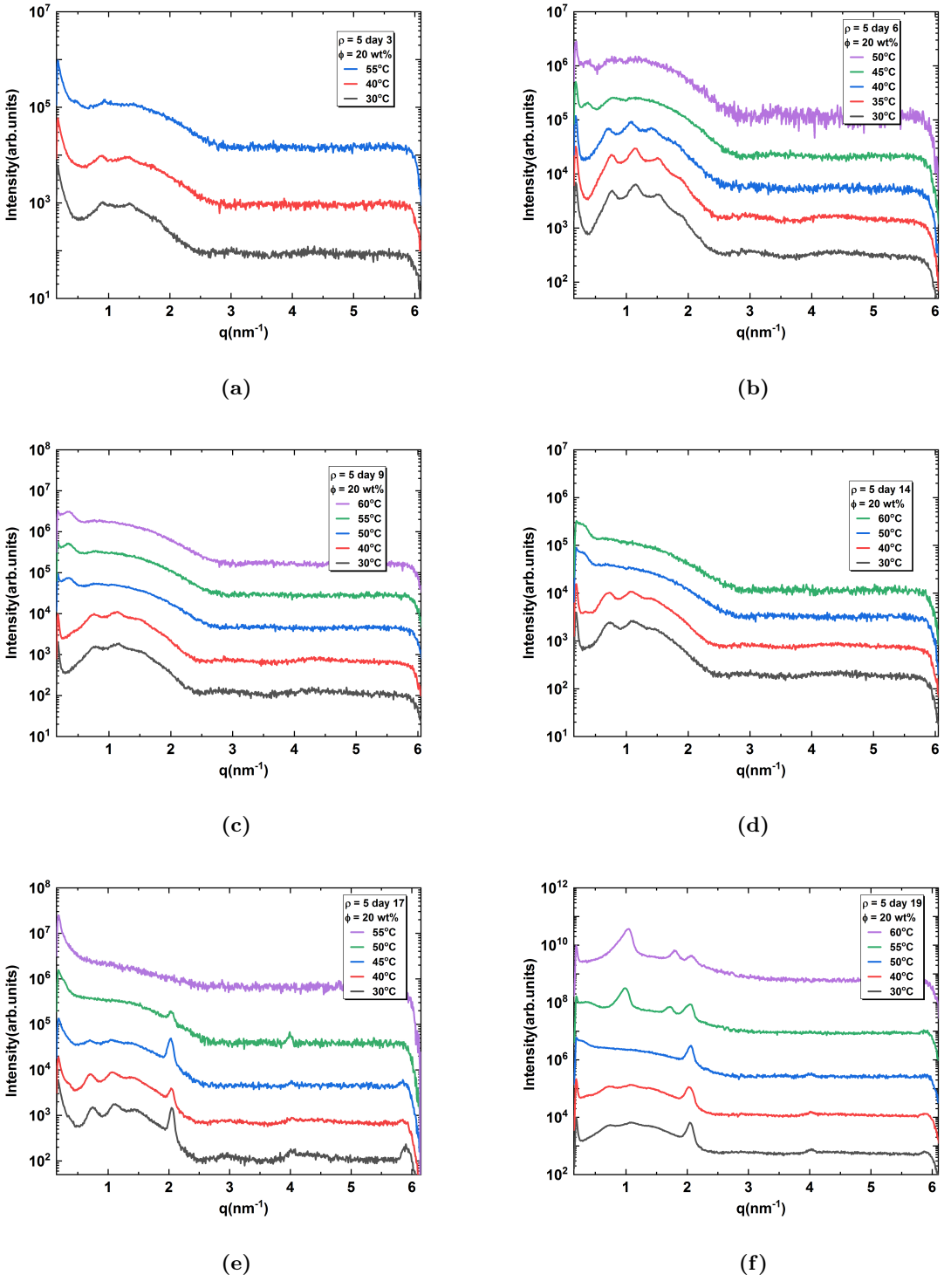

Figure 2.24: SAXS patterns obtained for DMPC:UMP (5:1) 20 Wt% sample incubated at room temperature for different time scales (a) day 3 (b) day6 (c) day 9 (d) day 14 (e) day 17 and (f) day 19. Date were taken on heating

Day #	Temperature	Phase	d-spacing
Day 3	30°C	$L_\beta{}^s$	13.9 nm
	40°C	$L_\alpha{}^s$	14.2 nm
	55°C	$L_\alpha{}^s$	13.4 nm
Day 6	30°C	$L_\beta{}^s$	16.5 nm
	35°C	$L_\beta{}^s$	16.5 nm
	40°C	$L_\alpha{}^s$	18.0 nm
	45°C	$L_\alpha{}^s$	17.0 nm
	50°C	$L_\alpha{}^s$	16.5 nm
Day 9	30°C	$L_\beta{}^s$	16.5 nm
	40°C	$L_\beta{}^s$	16.7 nm
	50°C	$L_\alpha{}^s$	18.3 nm
	55°C	$L_\alpha{}^s$	18.3 nm
	60°C	$L_\alpha{}^s$	18.3 nm
Day 14	30°C	$L_\beta{}^s$	17.6 nm
	40°C	$L_\beta{}^s$	17.8 nm
	50°C	$L_\alpha{}^s$	19.9 nm
	60°C	$L_\alpha{}^s$	21.6 nm
Day 19	30°C	$L_\beta{}^s$	17.4 nm
		L_{IG}	3.07 nm
	40°C	$L_\beta{}^s$	17.3 nm
		L_{IG}	3.07 nm
	50°C	L_{IG}	3.07nm
	55°C	H	6.34 nm
	60°C	H	6.04 nm

Table 2.2: Table showing d-spacings of different phases obtained on incubating 5:1 sample over 19 days. $L_\beta{}^s$- swollen lamellar gel phase, $L_\alpha{}^s$-swollen lamellar fluid phase,L_{IG}-interdigitated phase,H-hexagonal phase

Day #	Temperature	Phase	d-spacing
Day 2	30°C	$L_\beta{}^s$	12.2 nm
	35°C	$L_\alpha{}^s$	12.2 nm
	40°C	$L_\alpha{}^s$	13.4 nm
	50°C	$L_\alpha{}^s$	14.0 nm
	55°C	$L_\alpha{}^s$	14.2 nm
Day 5	30°C	$L_\beta{}^s$	11.4 nm
	40°C	$L_\beta{}^s$	11.0 nm
	44°C	$L_\alpha{}^s$	11.3 nm
	48°C	$L_\alpha{}^s$	15.3 nm
		L_{IG}	3.09 nm
Day 11	30°C	$L_\beta{}^s$	11.0 nm
		L_{IG}	3.12 nm
	40°C	$L_\beta{}^s$	11.0 nm
		L_{IG}	3.12 nm
	45°C	$L_\alpha{}^s$	9.92 nm
		L_{IG}	3.12 nm
	50°C	$L_\alpha{}^s$	10.6 nm
		L_{IG}	3.12 nm
	55°C	I	7.47 nm
		L_{IG}	3.12 nm
	60°C	I	6.24 nm
Day 18	30°C	$L_\beta{}^s$	8.67 nm
		L_{IG}	3.07 nm
	40°C	$L_\beta{}^s$	8.56 nm
		L_{IG}	3.10 nm
	50°C	I	9.96 nm
		L_{IG}	3.07 nm
	55°C	I	6.15 nm
		L_{IG}	3.07 nm
	60°C	I	5.42 nm

Table 2.3: Table showing d-spacings of different phases obtained on incubating 1:1 sample over 18 days. $L_\beta{}^s$- swollen lamellar gel phase, $L_\alpha{}^s$-swollen lamellar fluid phase,L_{IG}-interdigitated phase,I-isotropic phase

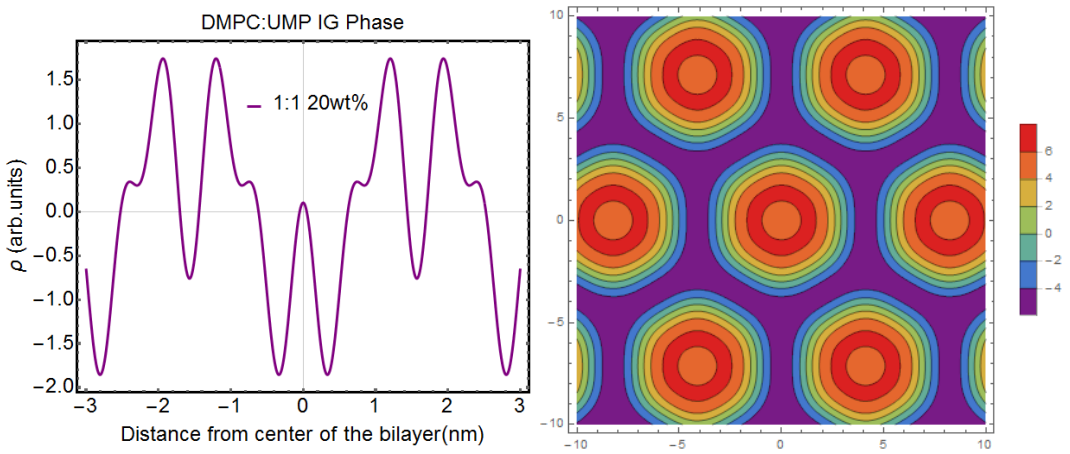

Figure 2.25: EDPs of (a) IG phase of 1:1 DMPC: UMP sample at 40°C on day 11 and (b) Inverse hexagonal phase of 5:1 DMPC: UMP sample at 55°C on day 19

Above 50°C, the interdigitated phase melted into a hexagonal phase and an isotropic phase for 5:1 and 1:1 samples, respectively, and showed no wide-angle peak. This phase behavior of both the samples observed in WAXS are tabulated in tab.2.5 and tab.2.4

DSC measurements were carried out to quantify the phase transition shown by the DMPC: UMP samples. With time it is found that the main transition temperature is shifted to 42°C. On further incubation, an additional peak is observed in the thermogram, which corresponds to the melting of the interdigitated phase.

2.6.7 2D XRD studies of the interdigitated phase

It is not straightforward to obtain information about chain tilt from the WAXS data collected from unoriented samples. Therefore, 2D diffraction studies of aligned samples of 1:1 and 5:1 in the interdigitated phase regime were carried out at different temperatures. The samples showed peaks corresponding to the interdigitated lamellar phase in the SAXS region (fig.2.30 and fig.2.31). The wide-angle region showed two off-axis peaks and one on-axis peak. The on-axis peak disappeared above 45°C indicating, the coexistence of the untitled swollen gel phase with the interdigitated phase until this temperature. The d-spacing of the interdigitated phase is 3.1 nm for both the samples and is consistent with 1D SAXS measurements. The two off-axis peaks obtained from the interdigitated phase disappears above 50°C, and the small-angle region contains two peaks that can be indexed to a hexagonal phase for the 5:1 sample. The d-spacings obtained from the 2D diffraction pattern, considering the tilt of the chains, are 0.473 nm and 0.434 nm, which could not be indexed into any lattice.

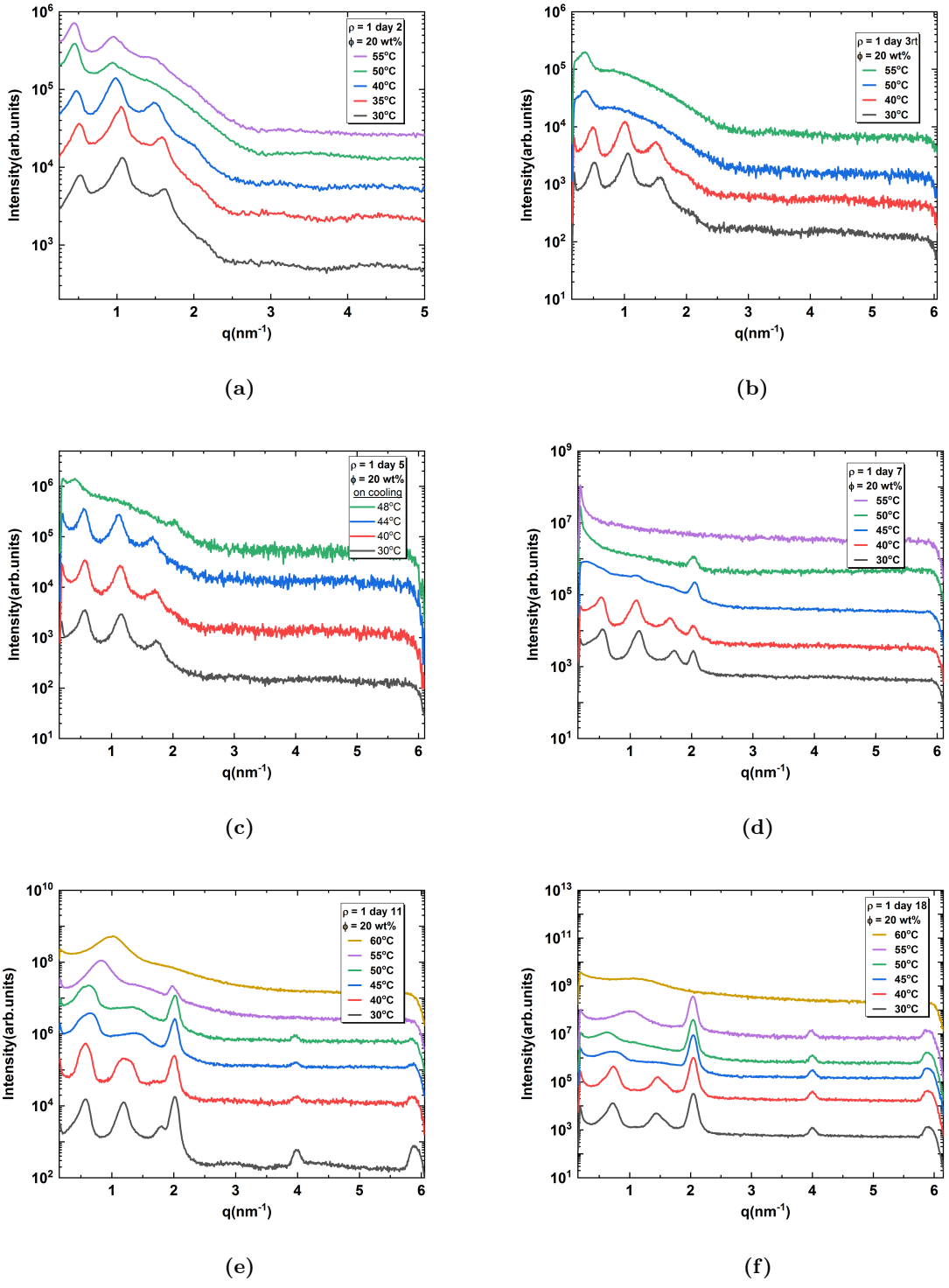

Figure 2.26: DMPC:UMP (1:1) phase behavior on incubation at room temperature for time scales of (a) day 2 (b) day 3 (c) day 5 (d) day 7 (e) day 11 and (f) day 18. Data were taken on heating

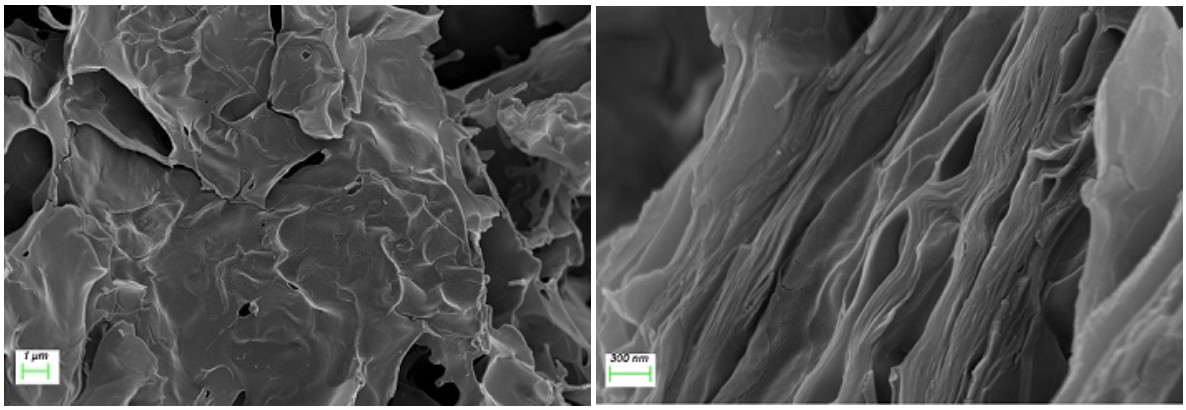

(a) **(b)**

Figure 2.27: Cryo-SEM images of lamellar phase obtained for DMPC:UMP 1:1 in (a) swollen lamellar phase regime and (b) Interdigitated phase regime

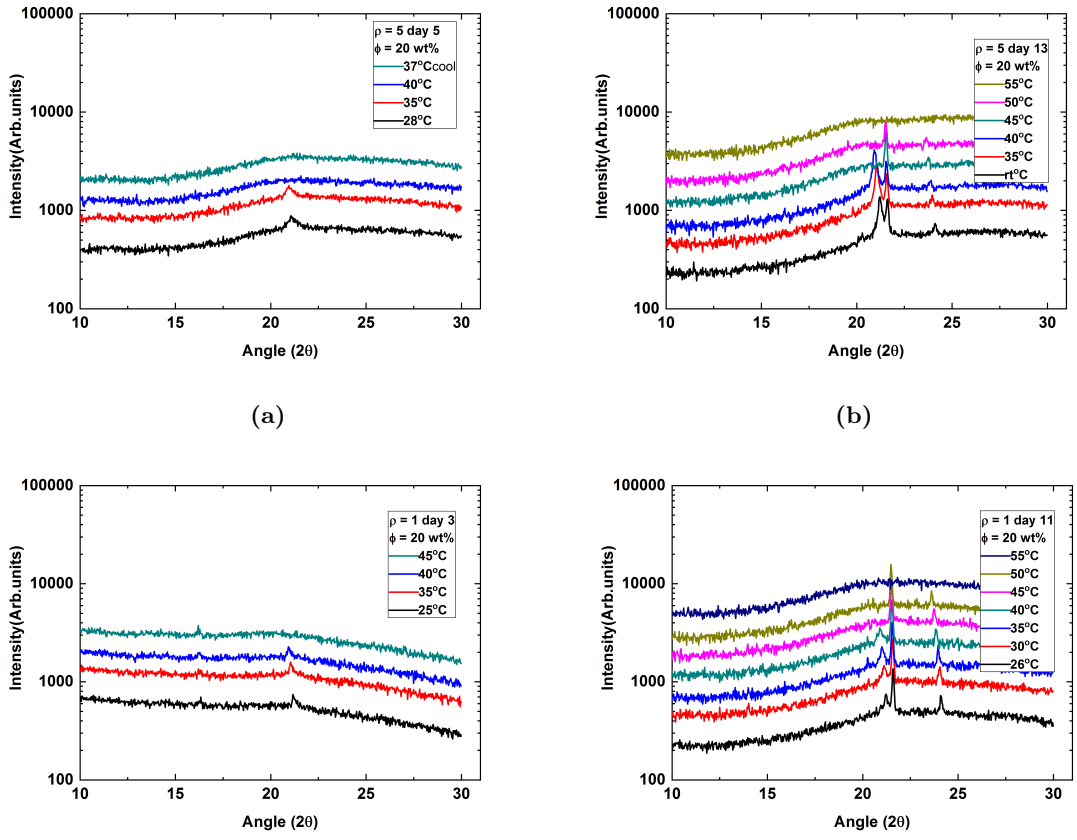

(a) **(b)**

(c) **(d)**

Figure 2.28: WAXS pattern of DMPC: UMP (5:1) on incubation at room temperature for (a) Day 5 showing wide angle reflection from gel phase (b) Day 13 showing IG phase reflection and DMPC:UMP (1:1) on incubation of (c) Day 3 (gel phase) (d) Day 11 (IG phase)

Day #	Temperature	d-spacing
Day 5	28°C	0.42 nm
	35°C	0.42 nm
	40°C	–
	37°C	–
Day 13	26°C	0.44nm
		0.42 nm
		0.41 nm
		0.37 nm
	30°C	0.44nm
		0.42 nm
		0.41 nm
		0.37 nm
	35°C	0.44nm
		0.42 nm
		0.41 nm
		0.37 nm
	40°C	0.44nm
		0.42 nm
		0.41 nm
		0.37 nm
	45°C	0.44nm
		0.42 nm
		0.41 nm
		0.37 nm
	50°C	0.44nm
		0.42 nm
		0.41 nm
		0.37 nm
	55°C	–

Table 2.4: Table showing wide angle peaks observed for 5:1 DMPC: UMP samples incubated for 5 days and 13 days.

Day #	Temperature	d-spacing
Day 3	28°C	0.42 nm
	35°C	0.42 nm
	40°C	0.42 nm
	45°C	–
Day 11	26°C	0.42 nm
		0.41 nm
		0.37 nm
	30°C	0.42 nm
		0.41 nm
		0.37 nm
	35°C	0.42 nm
		0.41 nm
		0.37 nm
	40°C	0.42 nm
		0.41 nm
		0.37 nm
	45°C	0.41 nm
		0.38 nm
	50°C	0.41 nm
		0.38 nm
	55°C	–

Table 2.5: Table showing wide angle peaks observed for 1:1 DMPC: UMP samples incubated for 3 days and 11 days.

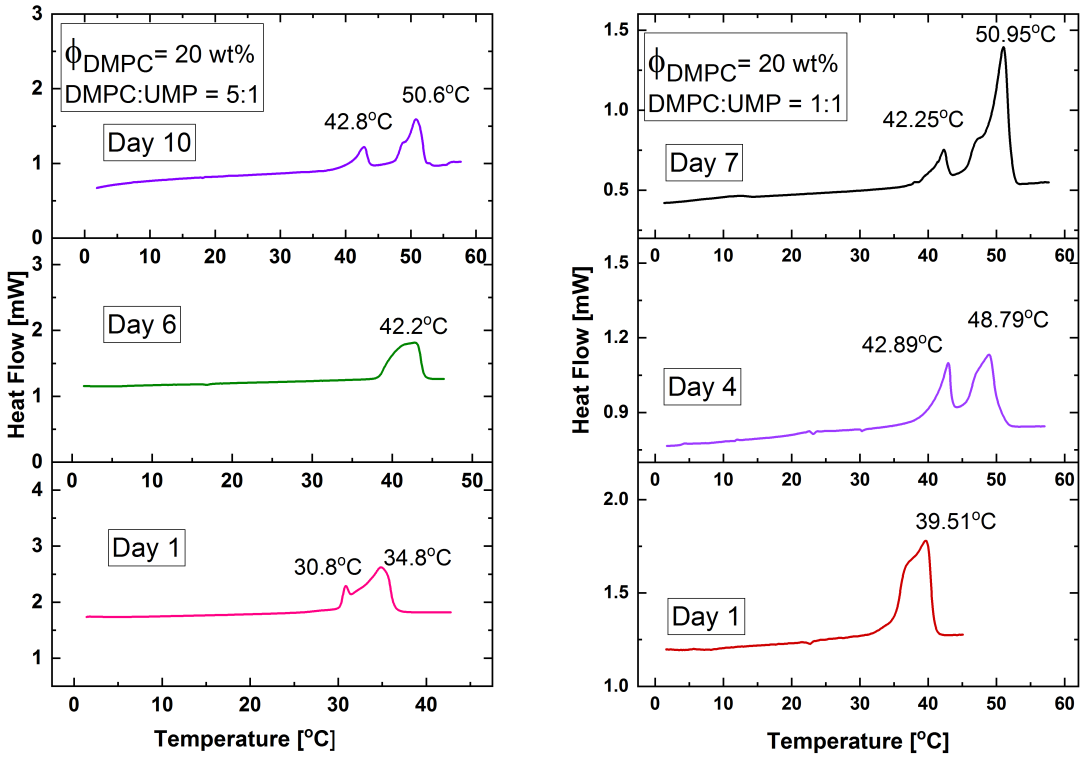

(a) **(b)**

Figure 2.29: DSC data from 5:1 DMPC:UMP and 1:1 DMPC: UMP samples after different incubation times.

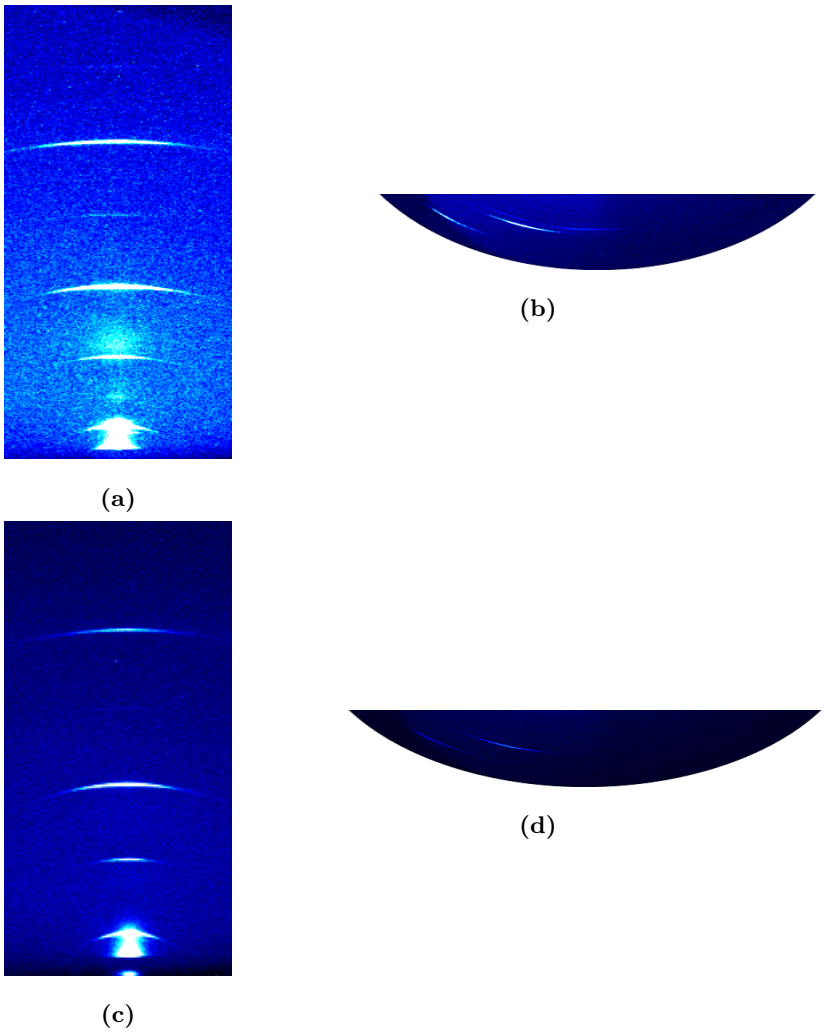

Figure 2.30: Aligned x-ray data of 1:1 DMPC: UMP showing interdigitated with d-spacing 3.14 nm in SAXS region at (a) 40°C and (c) 44°C. Wide region of the sample at 40°C is characterised by 2 off-axis peaks from the interdigitated phase and one on-axis peak from the swollen lamellar phase(b). The on-axis wide angle peak from swollen lamellar phase disappears at 44°C (d)

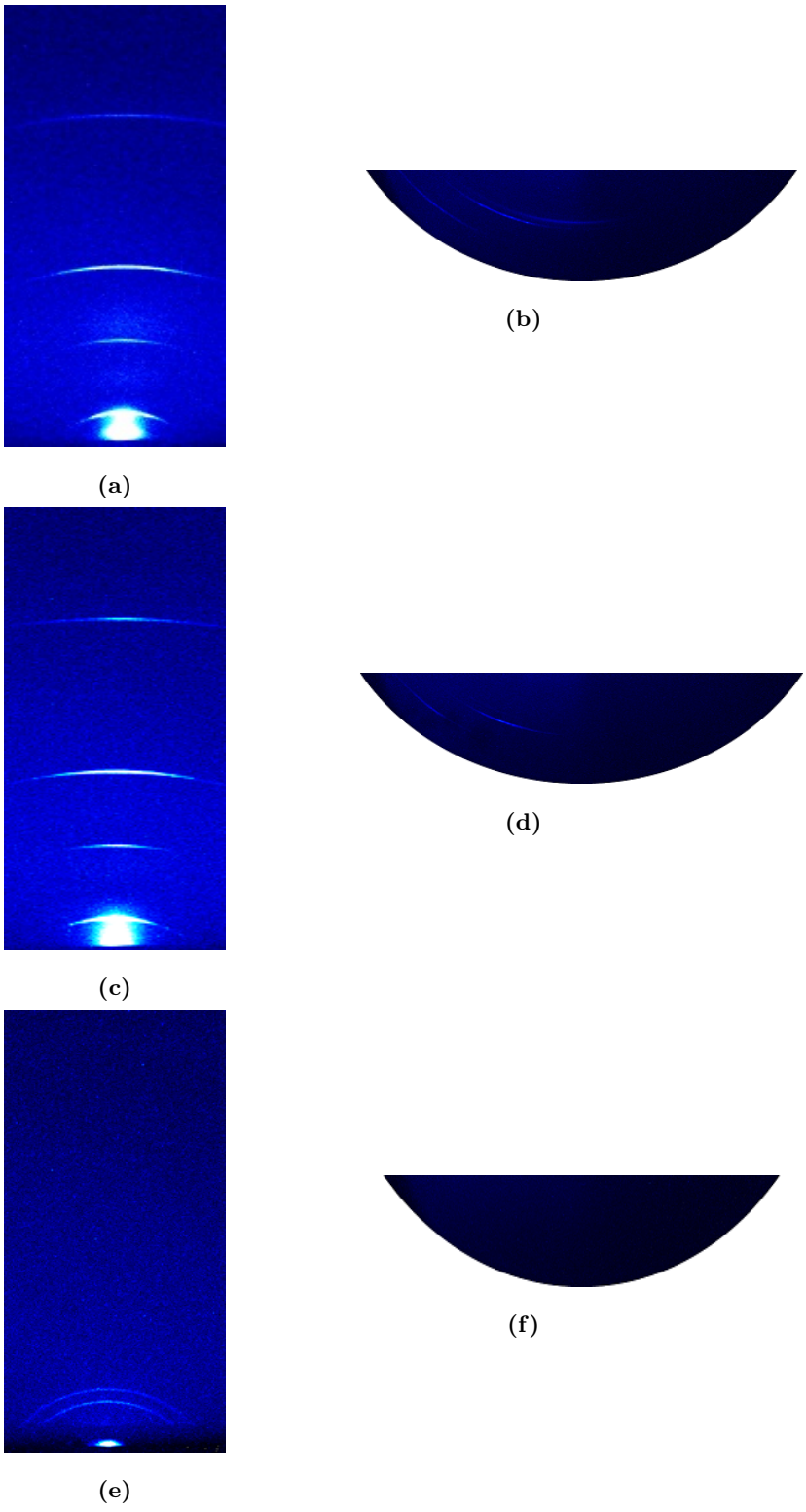

Figure 2.31: Aligned x-ray patterns of 5:1 DMPC:UMP sample showing interdigitated phase with a d-spacing of 3.14 nm at temperatures (a) 40°C (c) 47°C. (e) SAXS pattern a hexagonal lattice formed by melting of interdigitated phase at 52°C. Wide angle region of the (a) is characterised by 2 off-axis peaks from the interdigitated phase and one-on axis peak from the swollen lamellar phase shown in (b). The two wide angle off-axis peaks from interdigitated phase is shown in (d). Hexagonal phase (e) formed at 52°C has no wide angle peaks as indicated in (f).

2.6.8 Raman spectroscopy

Raman spectra show the possible vibrational transitions in a molecule and hence can be considered as a signature of the molecule. In the case of lipids, the Raman spectra are characterised by a number of peaks from the vibrational bands of the head group and hydrocarbon chain regions [6, 7, 8, 9]. Typical Raman spectra obtained from the fluid phase of DMPC are shown in fig.2.32 and corresponding assignments can be found in table.(2.6). It can be briefly categorised into three major groups.

(1) Hydrocarbon chain stretching region (2800 - 3100 cm^{-1})

This region gives information about inter-chain interactions and their conformations. The chain order parameter can be obtained from the relative ratio of symmetric and asymmetric vibrational frequencies of methylene stretching modes, which are respectively at 2850 cm^{-1} and 2880 cm^{-1}. The band at 2835 cm^{-1} is assigned to the bond stretching vibrations of the terminal methyl group. The band at 2845 cm^{-1} is sensitive to chain packing. The bands at 2856 and 2892 cm^{-1} respectively are assigned to symmetric and asymmetric stretching vibrations of CH_2 groups. The peak at 2740 cm^{-1} arises from the scissoring and wagging of methylene groups. The asymmetric stretching vibration of methyl groups in the headgroup gives rise to a peak at 2969 cm^{-1}.

(2) C-C stretching mode region (1000 - 1200 cm^{-1}).

This region detects the inter-molecular trans/gauche conformations of the acyl chain. The bands at 1063 cm^{-1} and 1128 cm^{-1} are assigned to the trans conformation of C-C bonds, whereas the band at 1090 cm^{-1} is attributed to the gauche conformation of the chains. The ratio of these two conformations is widely used to detect the main phase transition in lipids.

(3) Head group vibrational modes (700 - 1000 cm^{-1}).

The peaks at 724 and 878 cm^{-1} are assigned to the symmetric and asymmetric stretching bands of O-C-C-N^+ moiety in the choline group in gauche conformation whereas trans conformation of the same give rise to the bands at 770 and 895 cm^{-1}. O-P-O diester symmetric and asymmetric vibrations are associated with the bands at 760 cm^{-1} and 860 cm^{-1}, respectively.

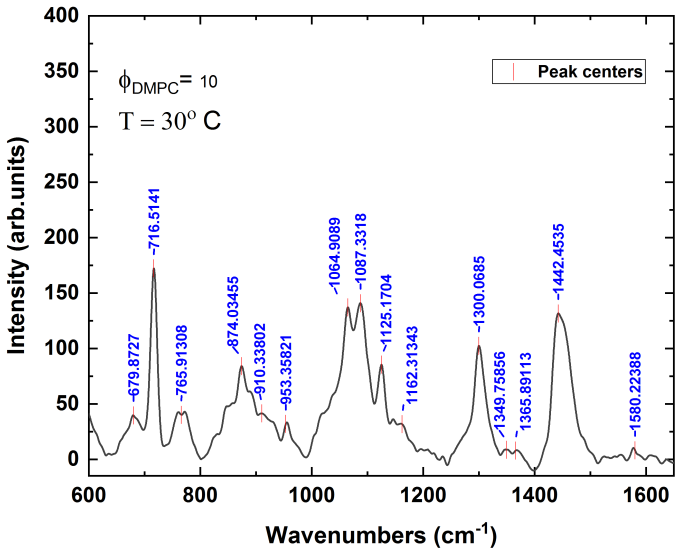

(a)

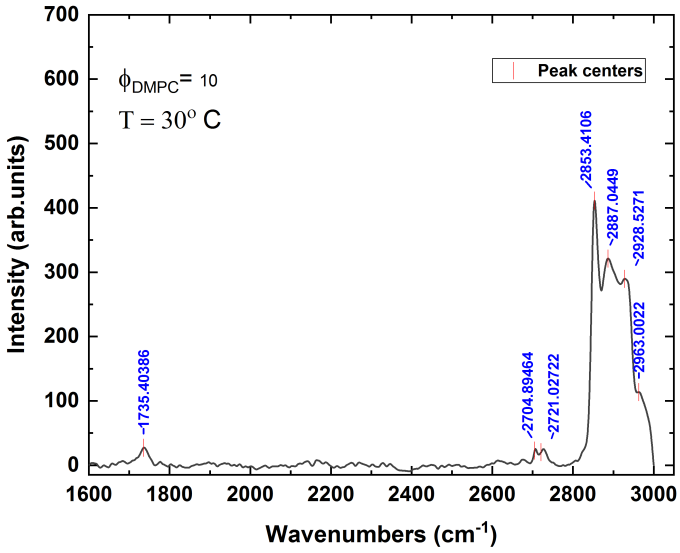

(b)

Figure 2.32: Raman spectra of pure DMPC (10 Wt%) taken at 30°C (a) 600 - 1600 cm^{-1} and (b) 1700 - 3000 cm^{-1} region.

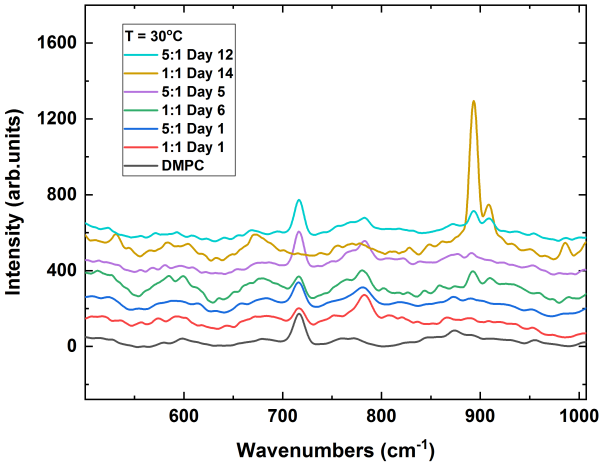

(a)

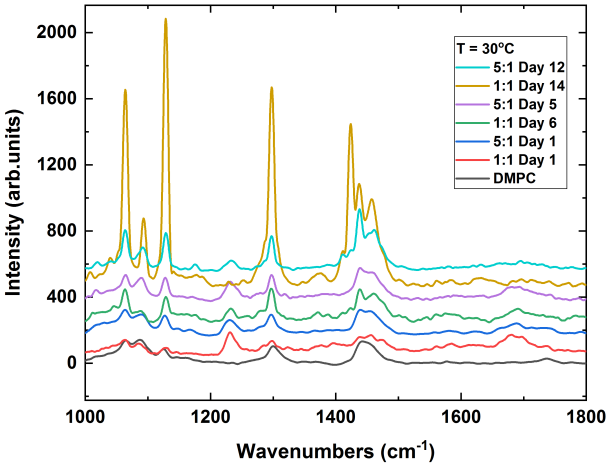

(b)

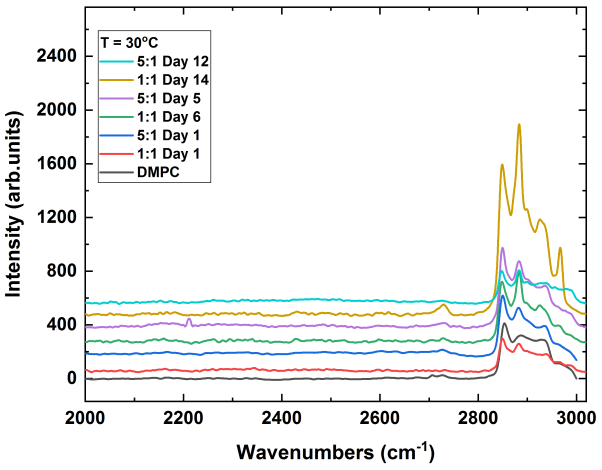

(c)

Figure 2.33: Comparison of Raman spectra of DMPC:UMP samples (1:1 and 5:1) incubated for different duration with pure lipid spectra. All data were taken at 30°C. Wavelength range spanned from 600cm^{-1} to 3000cm^{-1} has split into three different regions (a), (b) and (c) for ease of analysis

Raman bands	Assigned to	origin
716 (S)	ν_s(CN)	Symmetric O-C-C-N^+ (Gauche form) stretching mode
765.9 (M)	ν_s(OPO)	Symmetric O-P-O diester stretching mode
874 (M)	ν_{as}(CN)	Asymmetric O-C-C-N^+ (Gauche form) stretching mode
953 (M)	γ_{CH_2}	CH_2 rocking mode
1064 (M)	$\nu_{C-C_{trans}}$	C-C bond trans form stretching vibration of acyl chain
1087 (M)	$\nu_{C-C_{gauche}} + \nu_{O-P-O_{trans}}$	C-C bond gauche form stretching + phosphodiester trans form stretching vibrations
1125 (M)	$\nu_s(PO_2^{-1})+\nu_{C-Ctrans}$	Symmetric stretching vibrations of (PO_2^{-1}) group + trans C-C bond vibrations
1300(S)	$\tau(CH_2)$	Methylene twisting modes
1365 (Wk)	$\omega(CH_2)$	Wagging mode of CH_2 groups
1442 (S,B)	$\delta_(CH_2)$	Scissoring mode of CH_2 groups
1735 (M)	$\nu_(C=O)$	Carbonyl stretching mode of ester linkage
2853 (S)	ν_s(CH)	Symmetric stretching vibration of C-H bonds in the chain
2887 (M,B)	$\nu_{as}(CH)$	Symmetric stretching vibration of C-H bonds in the chain
2928 (M)	$\nu(\alpha - CH_2)$	CH stretching mode of α methylene group adjacent to ester carbonyl group
2963 (Wk)	$\nu_{as(CH_3)}$	methyl end group asymmetric stretching vibrations

Table 2.6: Table showing Raman vibrational modes of Pure DMPC and corresponding assignment taken from [6, 7, 8, 9]. Here the letters indicates the strength or shape of the peaks. M- Medium, S- Strong, B- Broad, Wk- Weak.

Raman spectra obtained from DMPC: UMP samples (1:1 and 5:1 molar ratio) showed features as listed below.

1) Comparison of spectral features in the region 600 - 1000 cm^{-1}.

At 30°C, pure DMPC showed Raman bands around 716 cm^{-1} and 873 cm^{-1} respectively from the symmetric and asymmetric stretching of the gauche conformation of O-C-C-N^+ moiety. This conformation is mostly seen in the fluid phase regime of the pure lipid. Bands at 769 cm^{-1} and 895 cm^{-1} are relatively weak, and are assigned to the symmetric and asymmetric vibrations of O-C-C-N^+ in trans conformation. This conformation usually dominates in the gel phase of the lipid. When UMP is incorporated in the bilayer, a peak corresponding to uracil ring breathing is observed at 780 cm^{-1}. Interestingly the relative intensity of the trans and gauche forms of O-C-C-N^+ is found to be more in samples with UMP as indicated by the band at 895 cm^{-1} compared to pure DMPC. On incubation for a few days, both 1:1 and 5:1 samples showed a peak at 770 cm^{-1} corresponding to the trans conformation of the O-C-C-N^+ group. The intensity of asymmetric vibration of trans O-C-C-N^+ at 895 cm^{-1} is found to be more dominant than that of the gauche form during this state. On further incubation, this behavior continued to evolve for the 5:1 sample, whereas the 1:1 sample showed a significant difference in the spectral features. 1:1 sample (which is in the interdigitated state) showed a sharp peak centered around 895 cm^{-1} with no peak at 716 cm^{-1} suggesting that all lipids have trans conformation of O-C-C-N^+ in this state. A peak at 910 cm^{-1} accompanied all the bands described above, considered to be an unassigned peak of UMP [10]. Also, for longer incubated 1:1 sample, the peak corresponding to ring breathing of UMP became broader, although the sharp PO_3^{2-} group vibrations of UMP is present at 980 cm^{-1}.

2) Comparison of spectral features in the region 1000 - 1700 cm^{-1}.

The relative intensities of trans to gauche conformations of C-C bonds in the acyl chain region of DMPC: UMP samples were found to increase with time. Initially, for incubation of a day, 1:1 sample showed a slight increase in gauche conformation compared to trans conformation, whereas 5:1 sample showed more trans form than gauche form. On further incubation, both the samples showed an increase in trans conformation, which suggests the elevation of the main transition temperature in the case of DMPC: UMP samples. The intensity and sharpness of peaks in 1000 - 1200 cm^{-1} range of 1:1 sample incubated for 14 days, indicate the condensed nature of interdigitated bilayers formed. The peak at 1233 cm^{-1} is associated with the breathing mode of the uracil ring, which is present in all data except those from 1:1 (day 14) and pure DMPC. A broad-band centered around 1400 cm^{-1} representing interchain packing and methylene vibrational modes, is found to show sharp

features on incubation. The peaks at 1445 and 1465 cm^{-1} represent the twisting and scissoring modes of chain methylene groups. The sharp band at 1295 cm^{-1}, represents the extent of chain ordering of the lipid, which on incubation became sharper for 1:1 and 5:1 samples.

2) Comparison of spectral features in the region 1700 - 3000 cm^{-1}.

The relative ratio of peaks at 2850/2880 is found to decrease with the incorporation of UMP. This indicates increased chain ordering in samples with UMP. As incubation time increases, this behavior becomes more pronounced. In the case of a 1:1 sample incubated for 14 days in the interdigitated state, a sharp peak corresponding to the asymmetric stretching of head group terminal CH_3 at 2969 cm^{-1} is observed (fig.2.33(c)).

The melting transition of the gel phase of DMPC: UMP samples can be probed by analysing the spectral changes arising from chain conformations in the 2000-3000 cm^{-1} range and trans-gauche chain conformation region in the range 1000-1200 cm^{-1} as shown in fig.2.34.

2.7 Phase behavior of DMPC: UMP samples incubated at higher temperatures

Time scales involved for changes in the phase behavior of DMPC: UMP samples indicate that the kinetics of the system is slow. This can be either due to the low adsorption rate of UMP to the bilayer from the solution or due to the elevation of gel phase transition temperature by UMP adsorption, which slows down the further evolution of the phase behavior. In either case, the incubation of samples at higher temperatures will facilitate a faster evolution of the phase behavior. The samples were incubated at 55°C to check the effect of incubation temperature on the kinetics of the phase behavior. As expected, both 1:1, as well as 5:1, samples showed the formation of the interdigitated phase in less time (within 2 days of incubation) (fig.2.35 and tabs.(2.7 and 2.8)). The lamellar periodicity of the swollen lamellar phase of the samples incubated at 55°C is slightly lower compared to those incubated at room temperature. Also, the shape of the peaks is broader and asymmetric in this case. The broadness of peaks may be due to the much lower time given for equilibration.

2.8 Discussions

The phase behavior of DMPC: UMP samples studied using different experimental techniques indicate that the adsorption of UMP significantly alters the phase behavior of DMPC bilayer. Due to the electrostatic charging by adsorption of charged UMP molecules, DMPC bilayer forms small unilamellar vesicles initially. Upon incubation, the samples formed an electro-

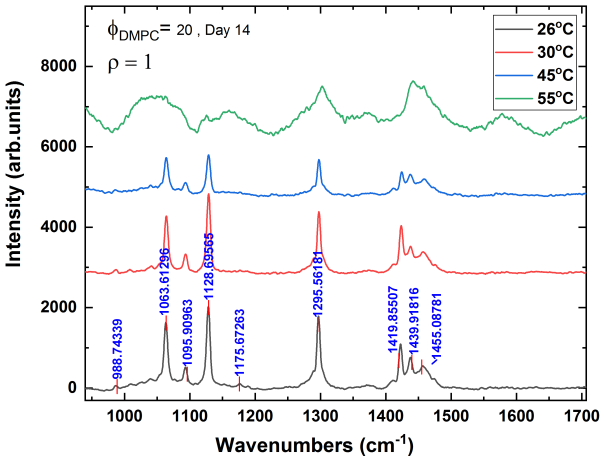

(a)

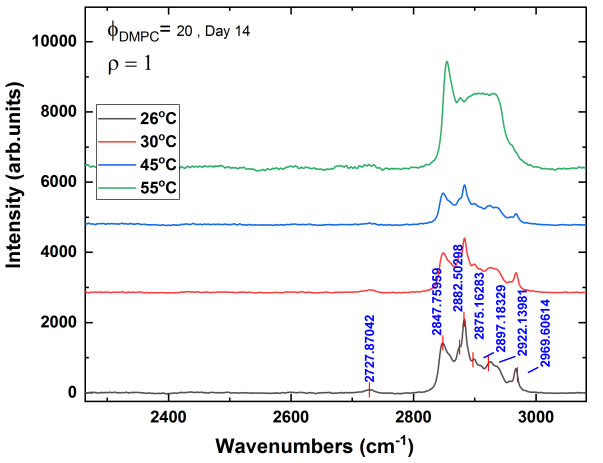

(b)

Figure 2.34: Raman Spectra of 1:1 DMPC: UMP sample incubated for 14 days showing chain melting transition as a function of temperature in wavelength range (a) 1000-1700cm^{-1} (b) 1700-3100cm^{-1}

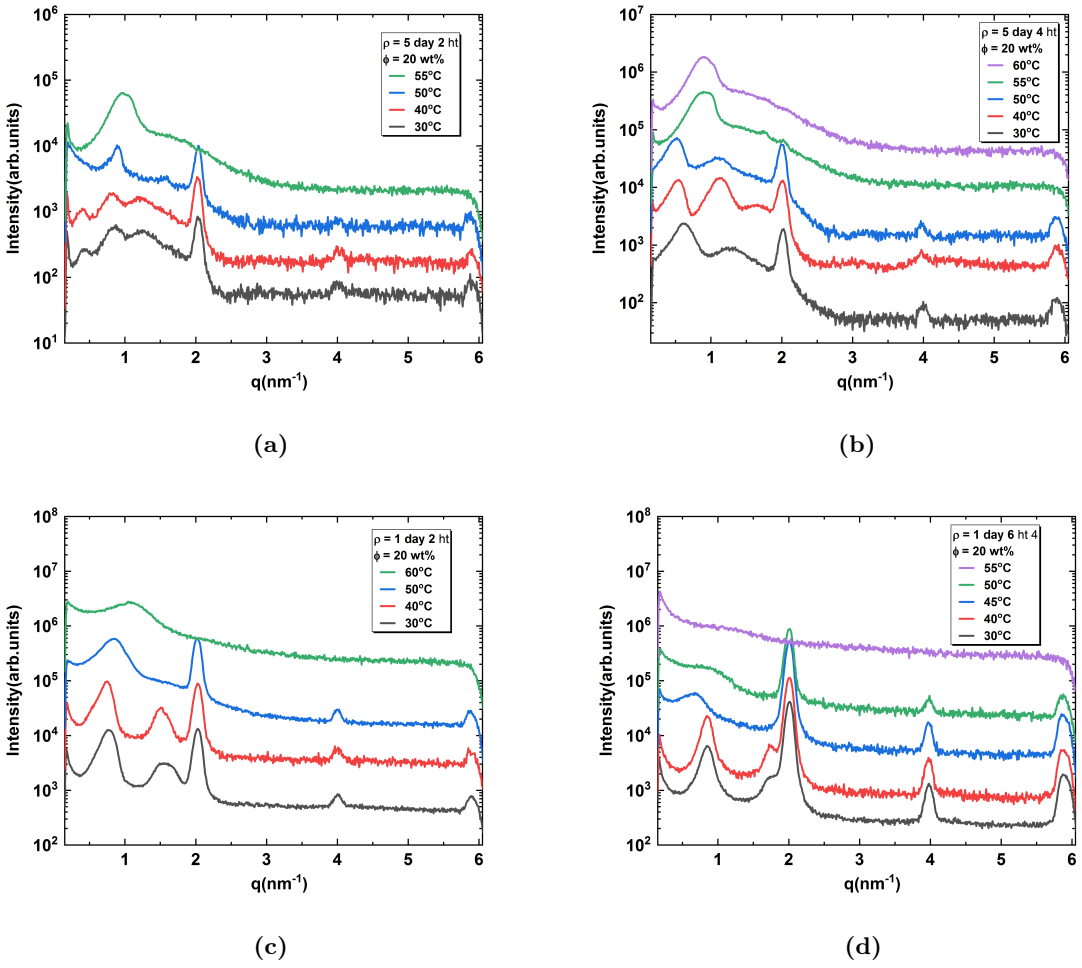

Figure 2.35: SAXS patterns of DMPC: UMP 1:1 sample obtained after incubation at 55°C for a duration of (a) day 2 (b) day 4 & (1:1) sample for (c) day 2 (d) day 4

Day #	Temperature	Phase	d-spacing
Day 2	30°C	$L_\beta{}^s$	15.3 nm
		L_{IG}	3.08 nm
	40°C	$L_\beta{}^s$	15.3 nm
		L_{IG}	3.08 nm
	50°C	$L_\alpha{}^s$	6.97 nm
		L_{IG}	3.08 nm
	55°C	I	6.41 nm
Day 4	30°C	$L_\beta{}^s$	10.2 nm
		L_{IG}	3.11 nm
	40°C	$L_\beta{}^s$	11.2 nm
		L_{IG}	3.11 nm
	50°C	$L_\alpha{}^s$	12.2 nm
		L_{IG}	3.11 nm
	55°C	I	7.13 nm
		H	6.22 nm
	60°C	I	7.06 nm

Table 2.7: Table showing d-spacing of different phases obtained on incubating 5:1 sample over 4 days at 55°C. $L_\beta{}^s$- swollen lamellar gel phase, $L_\alpha{}^s$-swollen lamellar fluid phase,L_{IG}-interdigitated phase,I-isotropic phase,H-hexagonal phase

Day #	Temperature	Phase	d-spacing
Day 2	30°C	$L_\beta{}^s$	8.07 nm
		L_{IG}	3.10 nm
	40°C	$L_\beta{}^s$	8.36 nm
		L_{IG}	3.10 nm
	50°C	$L_\alpha{}^s$	7.38 nm
		L_{IG}	3.10 nm
	55°C	I	5.64 nm
Day 6	30°C	$L_\beta{}^s$	7.38 nm
		L_{IG}	3.12 nm
	40°C	$L_\beta{}^s$	7.38 nm
		L_{IG}	3.12 nm
	50°C	$L_\alpha{}^s$	9.14 nm
		L_{IG}	3.12 nm
	55°C	I	6.80 nm
		L_{IG}	3.12 nm
	60°C	Broad peak	

Table 2.8: Table showing d-spacing of different phases obtained on incubating 1:1 sample over 6 days at 55°C. $L_\beta{}^s$- swollen lamellar gel phase, $L_\alpha{}^s$-swollen lamellar fluid phase,L_{IG}-interdigitated phase,I-isotropic phase,H-hexagonal phase

statically swollen lamellar phase with high d-spacing. The swollen lamellar phase formed has the main transition temperature higher than that of pure DMPC. 2D XRD data of aligned multilayer stacks of DMPC:UMP samples showed that the gel phase formed has untilted chains. In the case of the gel phase of pure DMPC, chains are titled since the head group area is larger compared to the chain area. In general, the interaction of small molecules at the bilayer interface increases the headgroup area. Instead, here we found that the interaction of UMP, results in untilted chains in the gel phase, mostly due to a reduction of head group area. Raman spectroscopic studies on DMPC: UMP samples have shown that the O-C-C-N^+ groups showed more trans conformation than usual gauche conformation. The resultant head group conformation has less head group area. With further incubation, the sample showed the formation of the interdigitated phase, which melts at 52°C. The interdigitated phase formed has a very low d- spacing of around 3.14 nm. This small d-spacing means that the bilayers in the interdigitated phase are electrostatically neutral, unlike the case of the swollen lamellar phase. The 2D aligned XRD pattern showed that the interdigitated phase has a tilted chain lattice, as indicated by the two off-axis peaks. Raman spectroscopy studies showed that O-C-C-N^+ moiety shows the trans conformation , which has a lower effective headgroup area. Hence the observed chain tilt can not be substantiated by the change in head group conformation. Further work is needed to understand the charge neutrality and the structure of the interdigitated phase. On heating, the interdigitated phase melts into a hexagonal phase above 55°C. This transition is also observed in aligned multilayer stacks of DMPC: UMP (5:1) sample. Since the hexagonal phase transition appears over a wide range of hydration, this phase is almost certainly the inverted hexagonal phase rather than a direct hexagonal phase. The above observation is surprising since the formation of the interdigitated phase requires a large lipid head group area, whereas inverted hexagonal phase forms only in the case of lipids with small head group area [11]. Hence the mechanism and structure of the interdigitated phase and the formation of the inverted hexagonal phase are not clear with current results. Further experiments are required to establish the exact mechanism.

2.9 Conclusions

Phase behavior of DMPC: UMP system was studied using different experimental techniques. DMPC lipid was found to form a swollen lamellar phase with a higher transition temperature in the presence of UMP. With incubation, both 1:1 and 5:1 (DMPC: UMP) samples showed the formation of the interdigitated phase, which melts at a temperature above 50°C.

Bibliography

[1] C. Demetzos. Differential scanning calorimetry (dsc): a tool to study the thermal phase behavior of lipid bilayer and liposomal stability. *J. Liposome Res.*, 18(3):159–173, 2008.

[2] G. Pabst, F. A. Heberle, and J. Katsaras. *Encyclopedia of Biophysics, 2013:s.* [Ch.X-Ray Scattering of Lipid Membrane].

[3] L. A. Bagatolli and E. Gratton. A correlation between lipid domain shape and binary phospholipid mixture composition in free standing bilayers: A two-photon fluorescence microscopy study. *Biophys J.*, 79:434–447, 2000.

[4] J. M. Arias, M. E. tuttolomondo, S. B. Díaz, and A. B. Altabef. Ftir and raman analysis of l-cysteine ethyl ester hcl interaction with dipalmitoylphosphatidylcholine in anhydrous and hydrated states. *J. Raman Spectrosc.*, 46(4):369–376, 2015.

[5] A.V. Popova and D. K. Hincha. Thermotropic phase behavior and headgroup interactions of the nonbilayer lipids phosphatidylethanolamine and monogalactosyldiacylglycerol in the dry state. *BMC Biophys.*, pages 4–11, 2011.

[6] K. Czamara, K. Majzner, M. Z. Pacia, K. Kochan, A. Kaczor, and M. Baranska. Raman spectroscopy of lipids: a review. *J. Raman Spectrosc.*, 83(6):4–20, 2014.

[7] B. Maherani, E. Arab-Tehrany, E. Rogalska, B. Korchowiec, A. Kheirolomoom, and Michel Linder. Vibrational, calorimetric, and molecular conformational study on calcein interaction with model lipid membrane. *J Nanopart. Res.*, 15(1792):1–17, 2013.

[8] A. Fasanellaa, K. Cosentinob, A. Beneducib, G. Chidichimob, E. Cazzanellia, R.C. Barberia, and M. Castriota. Thermal structural evolutions of dmpc-water biomimetic systems investigated by raman spectroscopy. *Biochim. Biophys. Acta*, 1860:1253–1258, 2018.

[9] H. Akutsu. Direct determination by raman scattering of the conformation of the choline group in phospholipid bilayers. *Biochemistry*, 20:7359–7366, 1981.

[10] C. M. Muntean, I. Bratu, C. Tripon, K. Nal pantidis, M. A. P. Purcaru, and V. Deckert. Molecular relaxation processes in nucleic acids components as probed with raman spectroscopy. *REV.CHIM.(Bucharest)*, 68(10):2471–2476, 2017.

[11] N. Tamai, M Goto, H Matsuki, and S Kaneshina. A mechanism of pressure-induced interdigitation of lipid bilayers. *J. Phys. Conf. Ser.*, 215:012161, 2010.

Chapter 3

Hydrotropic behaviour of disodium salt of uridine monophosphate

3.1 Introduction

Uridine 5'-monophosphate (UMP) is one of the building blocks of RNA [1]. In addition, it plays a vital role in many biological functions. For example, it is involved in the synthesis of synaptic phosphatide and proteins [2, 3]. In humans, uridine is the only pyrimidine nucleoside in circulation, which is also the precursor of cytidine triphosphate (CTP) and other cytidine containing compounds in the liver [4]. It is also considered to be a potential candidate for the treatment of Alzheimer's disease [5, 6, 7, 8]. Consumption of UMP along with docosahexaenoic acid (DHA) and choline increases hippocampal dendritic density in gerbils [9, 10]. The disodium salt of UMP is commercially available as an oral nutritional supplement. UMP consists of a central ribose sugar to which a phosphate moiety and a uridine base are attached. At neutral pH, UMP carries two negative charges and is, therefore, amphiphilic in nature. Since UMP consists of a small polar region and a planar aromatic hydrocarbon region, it can be considered as an amphiphile.

Self-assembly of amphiphilic molecules is a well-established active area of research, which has much relevance to biology. The key structural feature of self-assembling molecules is that they have a polar 'head group' region that interacts favourably with water and a hydrophobic hydrocarbon 'tail', which forms the core of the self-assembled structure. Depending on the relative sizes of the head group and tail, the shape of the self-assembled structure varies. Aromatic compounds are less hydrophobic compared to aliphatic compounds. When the flexible hydrocarbon chains are replaced by rigid aromatic rings, the ability to self-assemble fails, and these molecules usually form small irregular aggregates in water. The reason for the inability

of these molecules to self-assemble is still a topic of much debate in the literature. Costasa et al. suggest that there exists a favourable interaction of pi electrons of aromatics with water that effectively introduces a weak hydrogen bond and thereby increases the solvation of aromatics [11]. Another study finds the hydration Gibbs energies of benzene and of an aliphatic hydrocarbon having the same accessible surface area are different, which is attributed to the stronger van der Waals interaction of benzene with water, due to the larger polarizability of an aromatic ring compared to that of an aliphatic hydrocarbon of equal size [12]. Although there is no clear theoretical understanding of the increased solubility of aromatic compounds in water compared to aliphatics, it is a well-established experimental fact. The weak solubility and largely planar structure of the aromatic part of these molecules deprive them of the rich polymorphism of self-assembled structures that are found in the case of their aliphatic counterparts.

The term hydrotrope was coined more than a century ago for salts of organic acids, which increase the solubility of hydrophobic molecules in water [13, 14]. Hydrotropes are small organic amphiphilic molecules somewhat similar to surfactants. However, unlike surfactants, they do not self-assemble into well-defined micelles above a critical micellar concentration (CMC). Instead, they typically form smaller irregular aggregates above a minimum hydrotrope concentration (MHC), which is not as well-defined as the CMC. Further, due to their relatively smaller hydrophobic moieties, MHCs of hydrotropes are much higher than CMCs of surfactants. It is also observed in many cases that this aggregate can solubilize another hydrophobic solute in water. The definition of a hydrotrope with regard to the structuring of water in the ternary water-hydrotrope-hydrophobe system, adopted from the review by Kunz et al. [14] is as follows.

1) A hydrotrope is a substance whose structuring in water is enforced by the presence of a third immiscible hydrophobic molecule. (Property A)

2) A hydrotrope is a substance whose structuring in an organic solvent is enforced by the presence of water around it. (Property B)

Since these two conditions are also satisfied by surfactants, hydrotrope is defined as a substance having property A and/or B but doesn't form a lyotropic liquid crystal.

Hydrotropes are of both biological and industrial importance. Certain biologically relevant molecules such as adenosine triphosphate, bile acid, bile salts and urea, form aggregates in

water under physiological conditions [15, 16]. Bile acids are involved in the solubilization of fats and lipids in the small intestine and also in the regulation of cholesterol homeostasis [17]. All of these functions are closely related to the hydrotropic action of bile acids. Both bile acids, as well as bile salts, are able to form hydrotropic aggregates in water. MHCs of bile acids are found to be higher compared to those of bile salts [15, 18, 19], indicating that the counterions play a significant role in the aggregation process. The hydrotropic behavior of ATP has been shown to affect protein aggregation in aqueous solutions [16]. These observations have led to the suggestion that the relatively high concentration of ATP (millimolar range) found in cells may be due to its hydrotropic action.

In this chapter, we probe the aggregation behaviour of UMP and its disodium salt, UMPDSS, in aqueous solutions, using a variety of experimental techniques. UMPDSS is found to form aggregates above a threshold concentration of about 20 mM. On the other hand, no clear evidence for aggregate formation is found in the case of UMP. However, changes in the emission spectra of some of the probe molecules suggest the formation of very small and probably very compact aggregates of UMP. Our observations demonstrate the importance of the counterion in the aggregation process.

3.2 Results

3.2.1 Spectroscopy studies on aggregate formation

FDA solubility:

Fluorescein diacetate (FDA) is a widely used dye to probe the aggregate formation of hydrotropes and surfactants [20]. In the monomeric form, FDA has a strong absorption peak at 480 nm in the UV range. The hydrophobic FDA molecules are insoluble in water and remain as aggregate/clusters, which mainly scatter the incident light with negligible absorption. In the presence of a hydrotrope, FDA solubility increases. This is due either to the encapsulation of FDA molecules by pre-existing aggregates of the hydrotrope or to the formation of hydrotrope aggregates around the FDA molecules. The solubilized FDA molecules behave as monomers and show absorbance at 480 nm. Hence FDA absorbance at 480 nm is taken as an indicator of the aggregate formation of hydrotropes.

Absorbance of FDA at 480 nm in UMP and UMPDSS solutions was measured as a function of concentration (fig.3.1). In the case of UMPDSS, the peak at 480 nm starts to appear at a concentration of around 20 mM, and the absorbance shows a sigmoidal dependence on the concentration (fig.3.2). Such behaviour is typical of hydrotropes [20]. In contrast, UMP

solutions do not show an absorption peak at 480 nm up to a concentration of 150 mM, which is close to the limit of its solubility in water.

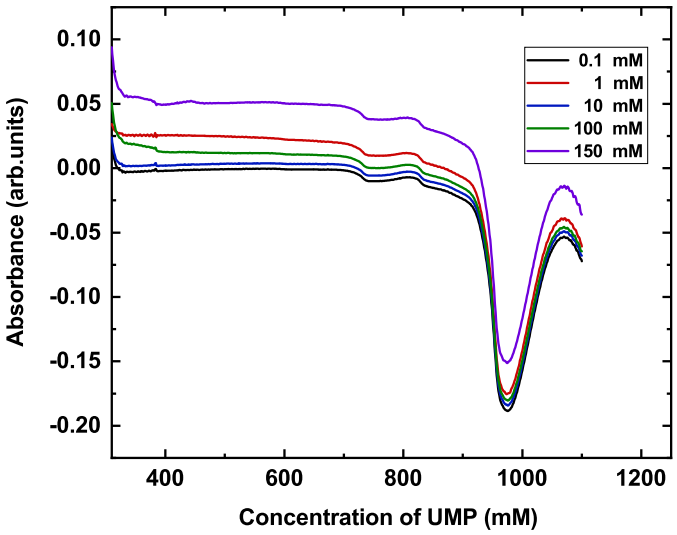

(a)

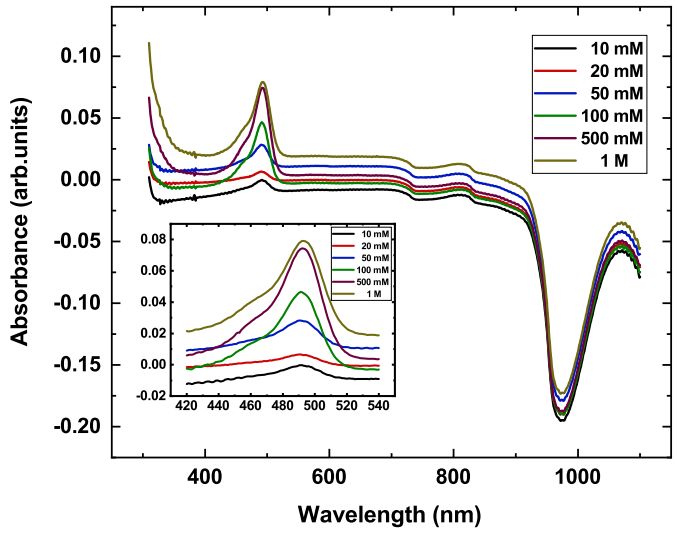

(b)

Figure 3.1: FDA absorbance as a function of (a) UMP concentration and (b) UMPDSS concentration. The concentration of FDA in the solution is 1.25 mg/ml.

ANS fluorescence:

8-anilino-1-naphthalenesulfonic acid (ANS) is a widely used dye to study protein conformational changes and aggregation of hydrotropes and surfactants [21, 22]. The emission spectrum

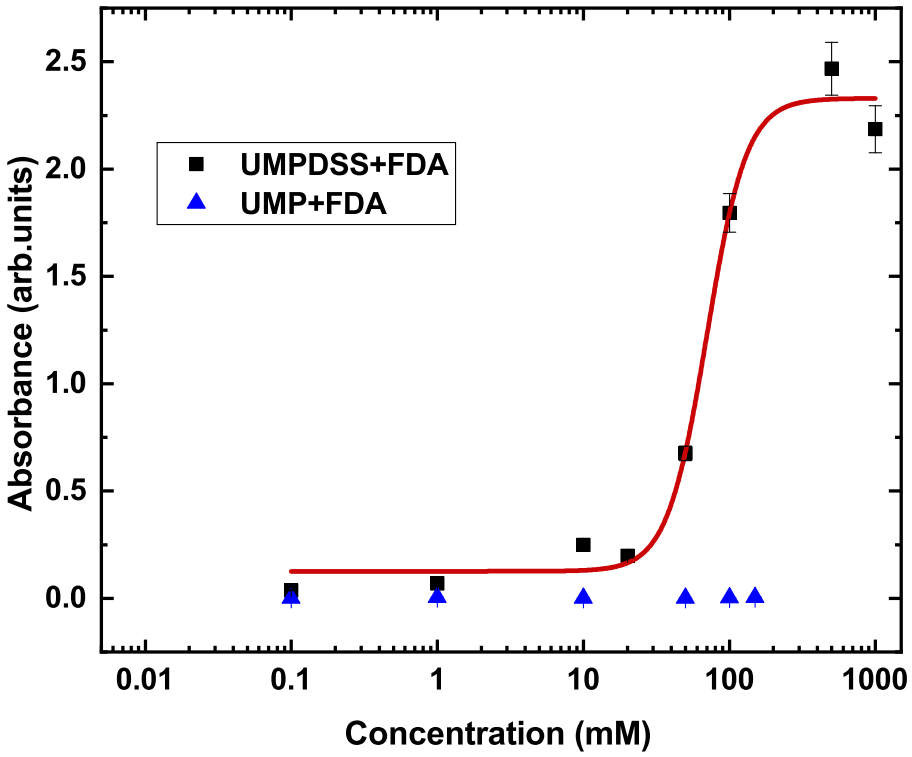

Figure 3.2: Measured absorbance of FDA at 480 nm as a function of concentration of UMP and UMPDSS in the solution. Concentration of FDA in the solution is 1.25 mg/ml.

of ANS has a broad peak at around 500 nm, which is sensitive to the polarity of the environment. The position of this peak gets blue-shifted when the environment becomes less polar with a concomitant increase in the emission intensity [23, 24].

Emission spectra of ANS in aqueous UMPDSS solutions of varying concentrations are shown in fig.3.3. At low concentrations of UMPDSS, the position of the broad peak near 500 nm remains unaltered. However, above 10 mM of UMPDSS, it gets blue-shifted, and its intensity starts to increase substantially. Variation of the peak position with UMPDSS concentration is given in fig. 3.4, and the dependence of the peak intensity on UMPDSS concentration is shown in fig. 3.5. These data show that the environment of the ANS molecules becomes less polar abruptly at [UMPDSS] $\sim$ 20 mM.

In the case of UMP solutions, no significant blue shift of this peak is observed (fig.3.3). However, the shape of the emission spectrum changes drastically at around 10 mM, along with a substantial increase in the fluorescent intensity.

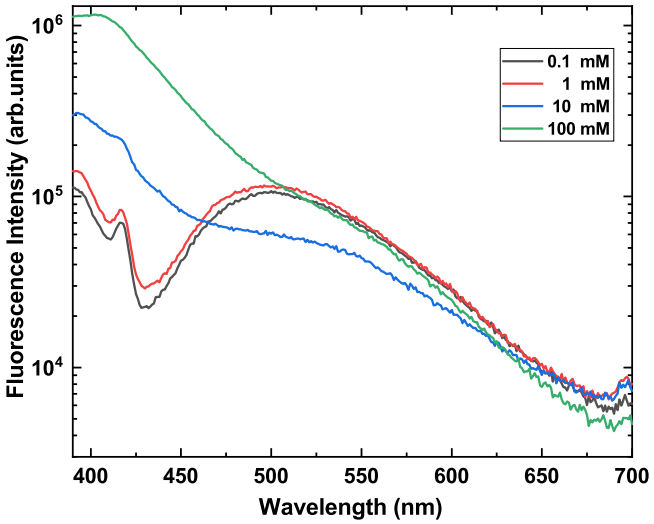

(a)

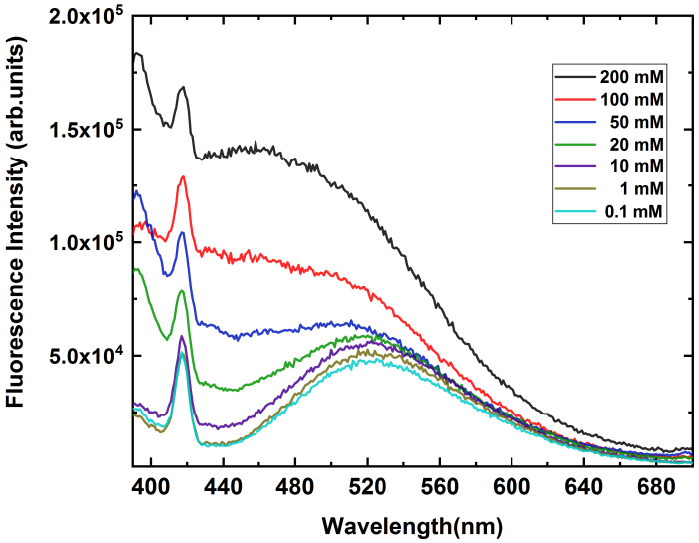

(b)

Figure 3.3: ANS fluorescence spectra as a function of UMP concentration (a) and UMPDSS concentration (b). Concentration of ANS in the solution is 0.3 mM.

Pyrene fluorescence:

Pyrene is a perifused polycyclic aromatic compound extensively used for studying the phase behavior of many micro heterogeneous systems, including peptides, proteins, biological membranes, micelles and surfactants [25]. The excitation of π electrons in the aromatic rings of pyrene leads to the finely structured fluorescence emission bands in the UV region. In the

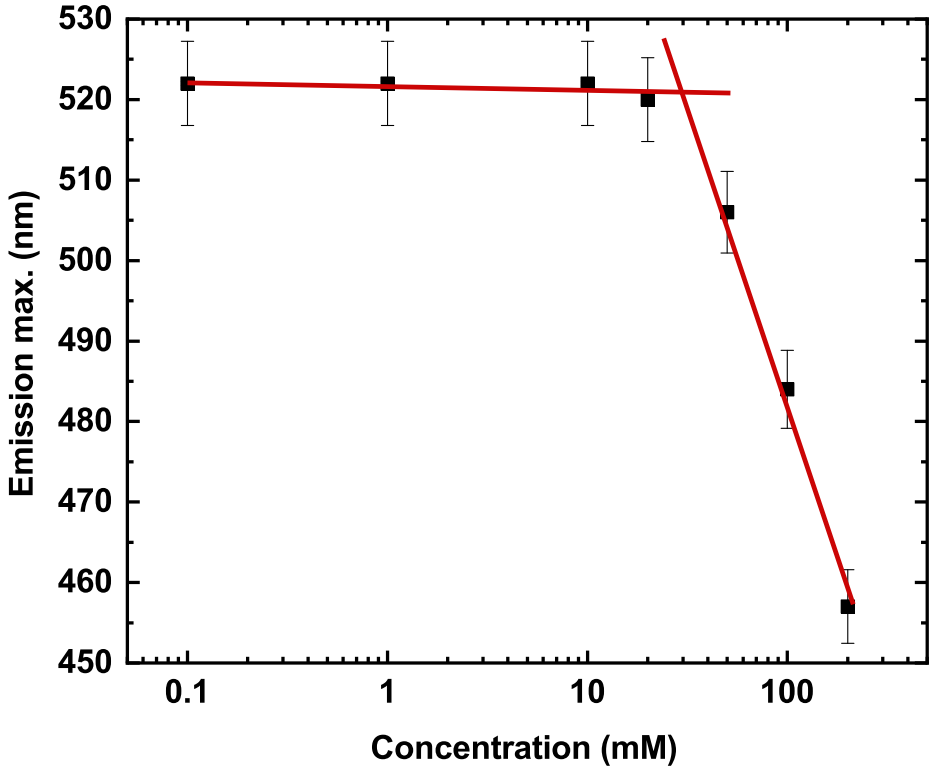

Figure 3.4: Wavelength corresponding to the ANS emission peak as a function of UMPDSS concentration. Concentration of ANS in the solution is 0.26 mM.

monomeric form, the emission spectrum of pyrene consists of five bands at 375 nm, 379 nm, 385 nm, 395 nm, and 410 nm. The ratio of intensities of the first and third bands (I1/I3) is a measure of the polarity of the solvent [26, 27, 28, 29, 30]. Due to the sensitivity of its emission spectrum on the polarity of the microenvironment, pyrene fluorescence is widely used to study the aggregation behaviour of proteins, lipids and surfactants [31, 32, 33]. Apart from monomeric emission, pyrene also exhibits excimer emission centered around 460 nm. Excimers are formed when a pyrene molecule in the ground state interacts with another in an excited state within a 1 nm range [34, 35]. The excimer emission has also been extensively used as a probe to identify conformational changes in proteins, lipids, and aggregate formation in surfactants and hydrotropes [25, 36, 37, 38, 39].

Emission spectra of pyrene in aqueous solutions of UMPDSS of varying concentrations are given in fig.3.6. Dependence of the I_1/I_3 ratio on UMPDSS concentration, deduced from these data, is shown in fig.3.7. This ratio remains unchanged until about 20 mM and then decreases sharply at higher concentrations. In addition, an excimer peak is observed at around 475 nm for concentrations above 10 mM. Multiple peaks are seen in this wavelength range at higher

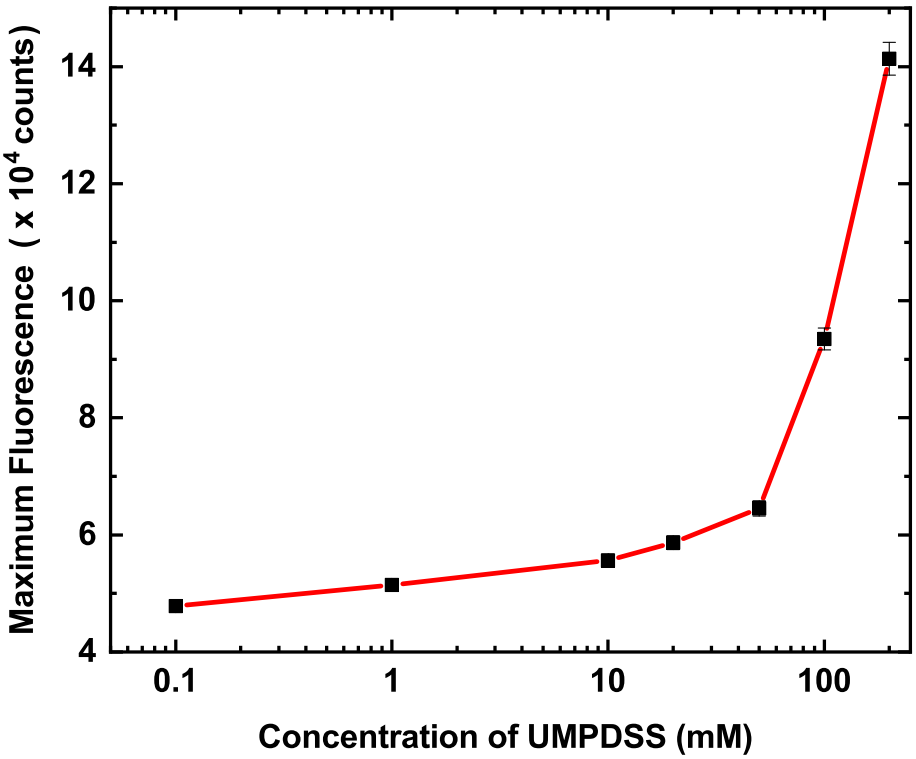

Figure 3.5: Intensity of the ANS emission peak as a function of UMPDSS concentration. Concentration of ANS in the solution is 0.26 mM.

concentrations. At the highest concentration studied, the monomer emission changes to a broad unstructured spectrum.

Fluorescence spectra of pyrene in aqueous solutions of UMP are given in fig.3.6. In this case, the ratio I_1/I_3 is not significantly altered until about 10 mM. Beyond this concentration, the sharp features in the emission spectrum of pyrene disappear, and a very broad profile is obtained. Further, no excimer peak is observed in this case, even for UMP concentrations close to its solubility limit.

3.2.2 DLS and SEM

DLS experiments were carried out on UMPDSS and UMP solutions at 25°C in order to probe the presence of aggregates. The concentration of both solutions was 30 mM. In the case of the UMPDSS solution, the intensity autocorrelation function shows a stretched exponential decay giving an average radius of 120 nm (fig.3.8). On the other hand, the autocorrelation function obtained from the UMP solution could not be fitted to any model since its magnitude was very low, indicating the presence of very much smaller particles if any.

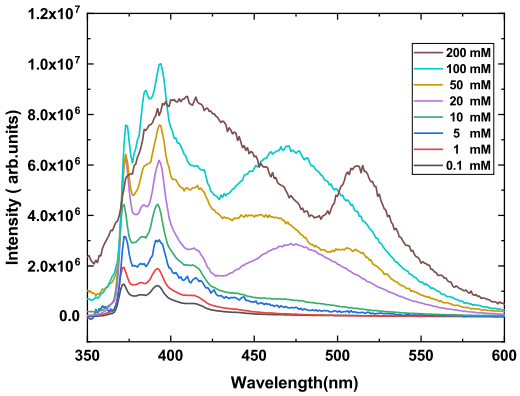

(a)

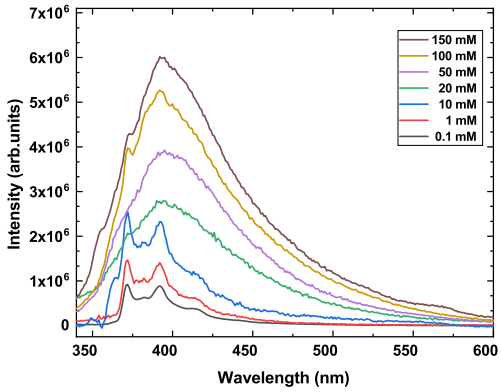

(b)

Figure 3.6: Pyrene fluorescence spectra as a function of UMP concentration (a) and UMPDSS concentration (b). Concentration of pyrene in the solution is 4μM.

The presence of aggregates in these solutions was also probed using SEM. For these experiments, around 100 μl of 30 mM UMP and UMPDSS solutions were drop casted onto a clean silica surface kept at 75°C. This temperature was chosen to fasten the evaporation process and thereby reduce the crystallization of solutes. After the evaporation of the solvent, samples were coated with a 5-10 nm thick layer of platinum to enhance the contrast during SEM imaging.

SEM images of UMPDSS solutions show rod-like aggregates with a well-defined diameter of about 10 nm and length in the range of 20 to 80 nm (fig.3.9). EDX spectroscopy on these aggregates confirmed the presence of all the elements constituting UMPDSS. In the case of UMP solutions, no such aggregates are observed; instead, we find the presence of much larger μm-sized crystallites (fig.3.9).

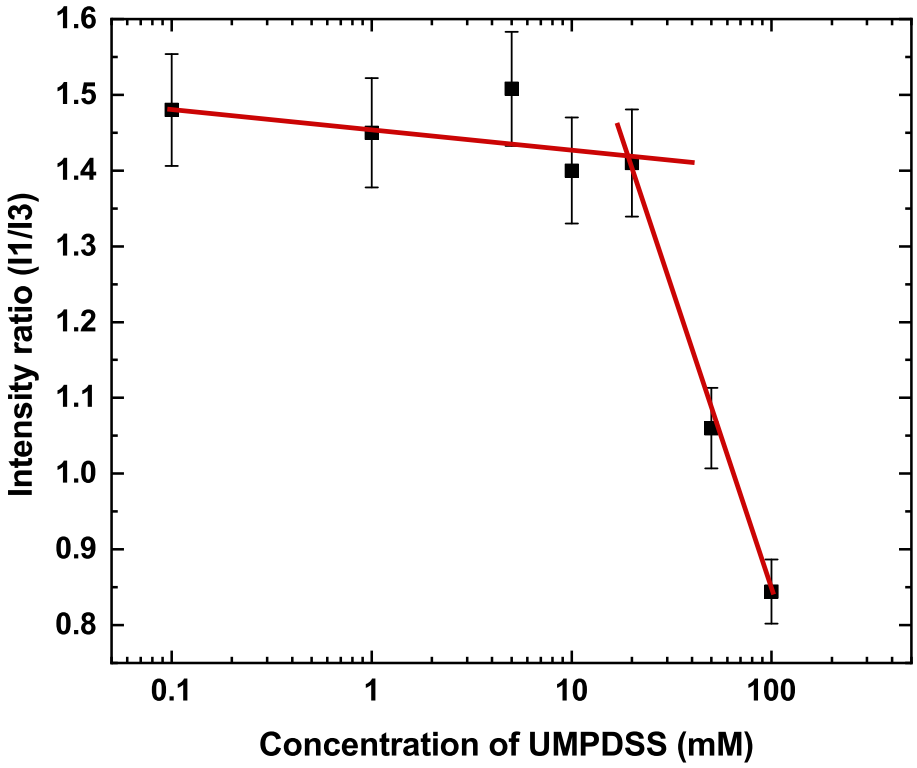

Figure 3.7: Variation of the I1/I3 ratio of pyrene fluorescence spectrum with the concentration of UMP.

3.3 Discussions

Results of spectroscopy studies presented above clearly show that UMPDSS is a hydrotrope with an MHC of about 20 mM. The aggregates formed are able to solubilize hydrophobic molecules such as FDA, ANS, and Pyrene. Observation of pyrene excimer emission indicates that more than one pyrene molecule is incorporated in these aggregates. Multiple excimer peaks are observed at higher UMPDSS concentrations, which may be attributed to different relative orientations of the two pyrene molecules making up the dimer [37]. Above 100 mM UMPDSS concentration the monomer emission changes to a broad unstructured spectrum.

DLS studies confirm the presence of UMPDSS aggregates above its MHC. The average radius of about 120 nm obtained from these studies is consistent with the aggregate size obtained from SEM images.

Although UMP shows some effects on the spectral features of pyrene and ANS, there is no unambiguous evidence for the formation of aggregates of UMP in the solution. The fact

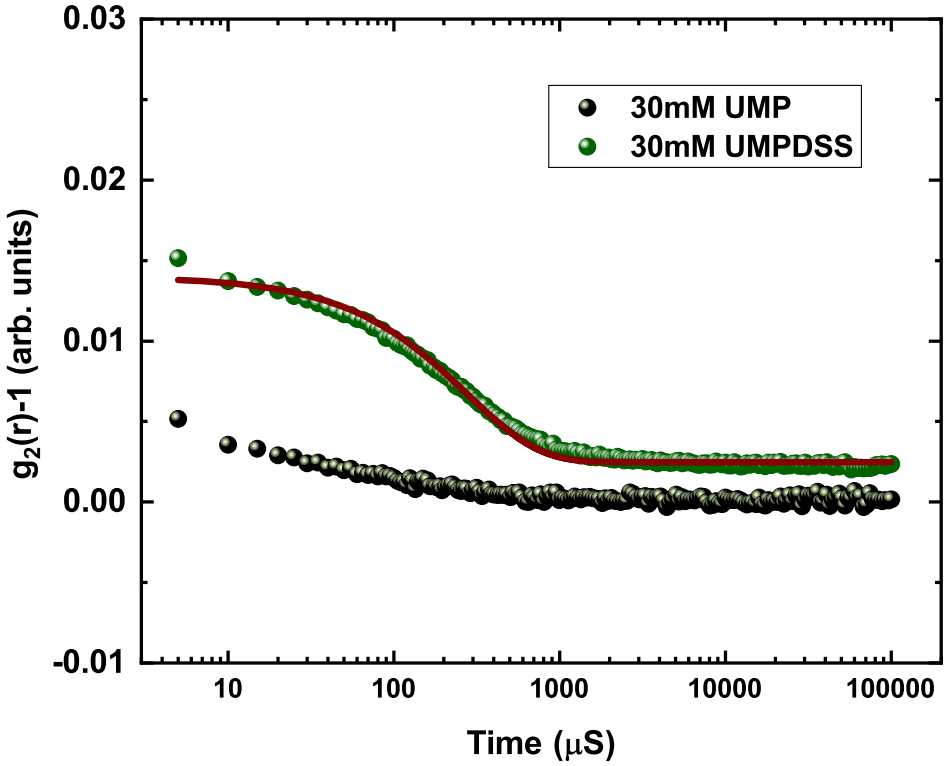

Figure 3.8: DLS data of UMP and UMPDSS (30 mM each) showing decay of autocorrelation function. Decay is faster in the case of UMP compared to UMPDSS. Red line shows the fitting of DLS data of UMPDSS (30 mM) to a stretched exponential decay function. Size of the particle obtained is 120 nm

that both the ANS and pyrene emission spectra are affected above a UMP concentration of 10 to 20 mM, however, suggests changes in the interaction of these molecules with UMP above this concentration range. The broad emission spectrum of pyrene observed above 20 mM is very similar to that reported in the case of DNA [40]. Therefore, it is very likely that UMP forms very small aggregates above 20 mM, which are too small and probably too compact for incorporating the probe molecules. The observed changes in the spectra might result from the binding of ANS and pyrene to these aggregates.

Apart from the counter ions, the pH of the solution may also play a role in the observed differences in the behaviors of UMP and UMPDSS. The uracil base in the UMP molecule can exist in different tautomeric forms depending on the pH [41]. At pH 7, the keto form is the major one, whereas as the pH is decreased, the enol form, which is more hydrophilic, becomes dominant. UMP has pKa values of 9.1, 6.4 and 1.0. Therefore it is doubly charged at neutral pH and becomes singly charged below pH 6.4. As the UMP concentration in the solution is

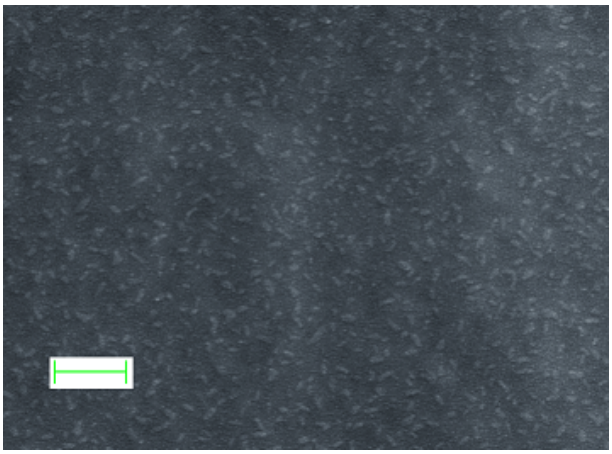

(a)

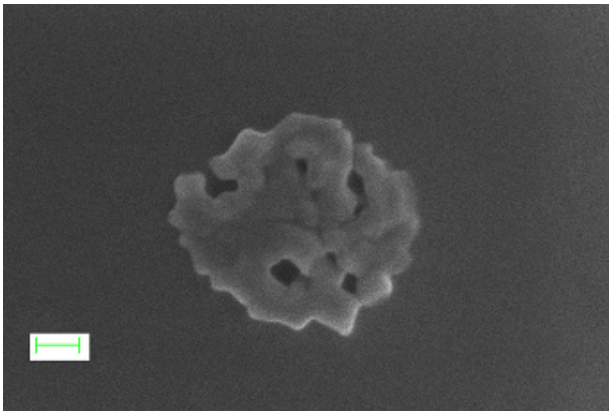

(b)

Figure 3.9: SEM images of (a) UMPDSS (30 mM) showing nm-sized rod-like aggregates (scale bar 200nm) and (c) UMP (20mM) showing μm-sized crystallites (scale bar 100 nm).

increased, its pH decreases, stabilizing the enol form of the uracil base. To check the influence of pH on the aggregate formation, FDA fluorescence measurements were also carried out at neutral pH using a buffered solution. No evidence for aggregates was observed, ruling out the possibility that the more hydrophilic enol form of the base was preventing the formation of UMP aggregates.

3.4 Conclusions

We have studied the aggregation behaviour of UMP and UMPDSS in aqueous solutions using a variety of experimental techniques. UMPDSS is found to behave like a hydrotrope with an MHC of around 20 mM. UMP, on the other hand, does not exhibit unambiguous signatures of hydrotropic behaviour. However, our observations suggest that UMP forms small compact aggregates in water, which are unable to incorporate hydrophobic molecules. This study demonstrates the importance of the counterion in the aggregation process of hydrotropes.

3.5 References

Bibliography

[1] A. L. Lehninger, M. M. Cox, and D. L. Nelson. NewYork: W. H. Freeman, 5th edition, 2008.

[2] M. Cansev, C. J. Watkins, E. M. Van der Beek, and R. J. Wurtman. Oral uridine 5'-monophosphate (ump) increases brain cdp-choline levels in gerbrils. *Brain Res.*, 1058:101–108, 2005.

[3] S. Holguin, J. Martinez, C. Chow, and R. J. Wurtman. Dietary uridine enhances the improvement in learning and memory produced by administering dha to gerbils. *FASEB J.*, 22:3939–3946, 2008.

[4] R. J. Wurtzman, M. Regan, I. Ulus, and L. Yu. Effect of oral cdp-choline on plasma choline and uridine levels in humans. *Biochem. Pharmacol.*, 60:989–992, 2000.

[5] R. D. Terry, E. Masliah, D. P. Salmon, N. Butters, R. DeTeresa, R. Hill, L. A. Hansen, and R. Katzman. Physical basis of cognitive alterations in alzheimer's disease: Synapse loss is the major correlate of cognitive impairment. *Ann. Neurol.*, 30:572–580, 1991.

[6] P. Scheltens, J. W. Twisk, R. Blesa, E. Scarpini, C. A. von Armin, A. Bongers, J. Harrison, S. H. Swinkels, C. J. Stam, and H. de Waal et al. Efficacy of souvenaid® in mild alzheimer's disease—results from a randomized, controlled trial. *J. Alzheimer's Dis.*, 31:225–236, 2012.

[7] P. Scheltens, J. W. Twisk, R. Blesa, E. Scarpini, C. A. von Armin, A. Bongers, J. Harrison, S. H. Swinkels, C. J. Stam, and H. de Waal et al. Efficacy of souvenaid® in mild alzheimer's disease—results from a randomized, controlled trial. *J. Alzheimer's Dis.*, 31:225–236, 2012.

[8] H. De Waal, C. Stam, M. Lansberger, R. Wieggers, P. Kamphuis, P. Scheltens, F. Maestu, and E. van Straaten. The effect of souvenaid® on functional brain network organization in patients with mild alzheimer's disease: A randomized controlled study. *PLoS One*, 2014.

[9] R. J. Wurtman, I. H. Ulus, M. Cansev, C. J. Watkins, L. Wang, and G. Marzloff. Synaptic proteins and phospholipids are increased in gerbil brain by administering uridine plus docosahexaenoic acid orally. *Brain Res.*, 1088:83–92, 2006.

[10] T. Sakamoto, M. Cansev, and R. J. Wurtman. Oral supplementation with docosahexaenoic acid and uridine-5 -monophosphate increases dendritic spine density in adult gerbil hippocampus. *Brain Res.*, 1182:50–59, 2007.

[11] M. Costas and B. Kronberg. Thermodynamics of aliphatic and aromatic hydrocarbon in water. *Biophys. Chem.*, 74:83–87, 1998.

[12] G. Graziano. Aliphatics vs. aromatics hydration thermodynamics. *Biophys. Chem.*, 110:249–258, 2004.

[13] C. Neuberg. Hydrotropic phenomena. *Biochem. Z*, 76:107–176, 1916.

[14] W. Kunz, K. Holmberg, and T. Zemb. Hydrotropes. *Curr. Opin. Colloid Interface Sci.*, 22:99–107, 2016.

[15] A. F. Hofman and A. Roda. Physicochemical properties of bile acids and their relationship to biological properties: An overview of the problem. *J. Lipid Res.*, 25:1477–1489, 1984.

[16] A. Patel, L. Malinovska, S. Saha, J. Wang, S. Alberti, Y. Krishnan, and A. A. Hymen. ATP as a biological hydrotrope. *Science*, 356:753–756, 2017.

[17] M. J. Monte, J. J. Martin, A. Antelo, and J. Vazquez-Tato. Bile acids: Chemistry, physiology and pathophysiology. *World J. Gastroenterol.*, 15:804–816, 2009.

[18] D. Madenci and S. U. Egelhaaf. Self assembly in aqueous bile salt solutions. *Curr. Opin. Colloid Interface Sci.*, 15:109–115, 2010.

[19] R. Parker, N. M. Rigby, M. J. Ridout, A. P. Gunning, and P. J. Wilde. The adsorption-desorption behaviour and structure function relationships of bile salts. *Soft Matter*, 10:6457–6466, 2014.

[20] D. Balasubramanian and V. Srinivas. Aggregation behavior of hydrotropic compounds in aqueous solution. *J. Phys. Chem*, 93:3865–3870, 1989.

[21] N. Alizadeh-Pardar and E. C. Y. Li-Chan. Comparison of protein surface hydrophobicity measured at various pH values using three different fluorescent probes. *J. Agric. Food Chem.*, 48:328–334, 2000.

[22] M. Collini, L. D'Alfonso, and G. Baldini. New insight on beta-lactoglobulin binding sites by 1-anilinonaphthalene-8-sulfonate fluorescence decay. *Protein Sci.*, 9:1968–1974, 2000.

[23] E. De Vendittis, G. Palumbo, G. Parlato, and V. Bocchini. A flourimetric method for the estimation of the critical micelle concentrations of surfactants. *Anal. Biochem.*, 115:278–286, 1981.

[24] E. De Vendittis, G. Palumbo, G. Parlato, and V. Bocchini. A fluorimetric method for the estimation of the critical micelle concentration of surfactants. *Anal. Chem.*, 115:278–286, 1981.

[25] L. Piñeiro, M. Novo, and W. Al-Soufi. Fluorescence emission of pyrene in surfactant solutions. *Adv. Colloid Interface Sci.*, 215:1–12, 2015.

[26] K. Kalyanasundaram and J. K. Thomas. Environmental effects on vibronic band intensities in pyrene monomer fluorescence and their application in studies of micellar systems. *J. Am. Chem. Soc.*, 99:2039–2042, 1977.

[27] A. Nakajima. Solvent effect on the vibrational structures of the fluorescence and absorption spectra of pyrene. *Bull. Chem. Soc. Jpn*, 61:467–469, 1976.

[28] A. Nakajima. Fluorescence spectra of pyrene in chlorinated aromatic solvents. *J. Lumin.*, 11:429–432, 1976.

[29] A. Nakajima. Effect of isometric solvents on vibrational band intensities in fluorescence spectrum of pyrene. *J. Mol. Spectrosc.*, 61:467–469, 1976.

[30] G. K. Bains, S. H. Kim, E. J. Sorin, and V. Narayanaswamy. The extent of pyrene excimer fluorescence emission is a reflector of distance and flexibility: Analysis of the segment linking the LDL receptors binding and tetramerization domains of apolipoprotein E3. *Biochem.*, 51:6207–6219, 2012.

[31] J. Shobha and D. Balasubramanian. Microenvironmental differences amongst micelles of various shapes and structures. *Proc. Indian Acad. Sci*, 98:469–478, 1987.

[32] R. Zana and D. Guvelli. Florescence probing study of the association of bile salts in aqueous solutions. *J. Phys. Chem*, 89:1687–1690, 1985.

[33] D. Balasubramanian, V. Srinivas, V. G. Gaikar, and M. M. Sharma. Aggregation behavior of hydrotropic compounds in aqueous solution. *J. Phys. Chem*, 93:3865–3870, 1989.

[34] S. S. Lehrer. Pyrene excimer fluorescence as a probe of protein conformational change subcell. *Biochem.*, 24:115–132, 1995.

[35] P. Somerharju. Pyrene - labelled lipids as tools in membrane biophysics and cell biology. *Chem. Phys. Lipids*, 116:57–74, 2002.

[36] M. Masuko, H. Ohtani, K. Ebata, and A. Schimadzu. Optimization of excimer forming two probe nucleic acid hybridization method with pyrene as a fluorophore. *Nucleic Acids Res.*, 26:5409–5416, 1998.

[37] I. O. Aparin, G. V. Proskurin, A. V. Golovin, A. V. Ustinov, A. A. Formanovsky, T. S. Zetspin, and V. A. Korshun. Fine tuning of pyrene excimer fluorescence in molecular beacons by alteration of the monomer structure. *J. Org. Chem*, 82:10015–10024, 2017.

[38] G. Bains, A. B. Patel, and V. Narayanaswami. Pyrene : A probe to study protein conformation and conformational changes. *Molecules*, 16:7909–7935, 2011.

[39] N. J. Turro and P-L. Kuo. Pyrene excimer formation in micelles of nonionic detergents and of water - soluble polymers. *Langmuir*, 2:438–442, 1986.

[40] L. Li, J. Lu, C. Xu, H. Li, and X. Yang. Studies on the interaction mechanism of pyrene derivatives with human tumor-related DNA. *Molecules*, 17:14159–14173, 2012.

[41] A. L. Lehninger, D. L. Nelson, and M. M. Cox. *Principles of Biochemistry.* Newyork: Worth publisher, 4þ edition, 2005.

Chapter 4

Formation of solid-supported lipid bilayers by induced rupture of GUVs using acetic acid

4.1 Introduction

Cell membranes play vital roles in many biological processes, the understanding of which demands characterisation of membrane organisation at the molecular level under different physiological conditions. Studies on the dynamics of real cell membranes in response to different biological stimuli is difficult because of the complex interactions of multiple molecules involved in these processes. The decoupling of these processes to study the effect and contribution of different sets of molecules proved to be difficult with real membranes. Hence, there is an absolute need to develop model systems, which mimic real cell membranes. Since the basic building blocks of any cell membrane are lipids, the model systems made up of single, or a few lipids can act as the simplest platform to study various biological processes under controlled environments. Simple model systems made up of lipids span from monolayers at the air-water interface to planar supported lipid bilayers and vesicles of varying sizes [1]. For different experimental studies the choice of the model system used mainly depends on the experimental techniques. Each of these model systems has advantages and disadvantages. Details of different types of model systems extensively used for different experimental studies are discussed below.

This chapter focuses on developing a novel method of formation of supported lipid bilayers from single and multi-component giant unilamellar vesicles (GUV) using acetic acid. We find

that the addition of acetic acid to the GUV solution results in the formation of pores on GUVs and opening up of vesicles. On a substrate, the rupture of adsorbed vesicles results in the formation of supported lipid bilayers. We also find that acetic acid can induce the fusion of GUVs with the bilayer patches on a substrate. Hence this method can form extended supported bilayers on different substrates.

4.1.1 Vesicles

Vesicles are closed spherical structures, which can be formed out of the lipid bilayer. Depending on the number of bilayers forming a single vesicle, they are categorised into multilamellar vesicles (MLVs), and unilamellar vesicles (ULVs). MLVs are the most thermodynamically stable structures formed by uncharged/zwitterionic lipids on hydration. Hence it is the easiest form of the model system to fabricate [2]. Since the cell membrane is made up of a single bilayer, MLVs are usually considered for studies related to interactions and phase behaviour of lipids under different physiological conditions. Unilamellar vesicles, therefore, represent the simplest platform to correlate with real cell membranes. Depending on the size of the unilamellar vesicles, which can be controlled by different experimental techniques of formation, ULVs are categorised into small unilamellar vesicles (SUVs : size range 10-100 nm), large unilamellar vesicles (LUVs : size range 100 nm-0.1μm) and giant unilamellar vesicles (GUVs: size range $>$ 0.1 μm) [3]. Out of these, GUVs are well studied and characterised due to their size being suitable for microscopic studies. SUVs are used mainly for the formation of supported lipid bilayers (SLBs) [4, 5]. LUVs are used in studies related to cargo transport and fusion of vesicles [6, 7, 8]. Extrusion and sonication of MLVs are used for making SUVs and LUVs of different sizes [9]. The preparation of GUVs from single lipids, as well as from a mixture of zwitterionic lipids, is explained in ref.[10]. In the case of charged lipids, gentle hydration technique can be used to form GUVs [11]. GUVs represent the unsupported form of the cell membrane and hence mostly mimic the real cell behaviour. GUVs can be used for investigating different aspects of biomembranes such as lateral lipid heterogeneities, membrane budding and fission induced by reconstituted membrane proteins, permeation of small molecules, cell adhesion etc. [12, 13]. But studies using force microscopy techniques need a flat platform such as supported lipid bilayers or black lipid membranes [1].

4.1.2 Planar membranes

A planar membrane model system can be supported by a substrate or can be free-standing. In the case of a substrate-supported lipid bilayer, the bilayer can be formed directly on the

substrate, or it can be transferred after formation by Langmuir-Blodgett/Langmuir-Schaefer (LB/LS) technique, to different types of substrates [4, 14]. The supported bilayer can be formed on a hydrophilic substrate by rupture of unilamellar vesicles. In this case, mostly SUVs are used, which effectively produce a defect-free bilayer. The sub-microscopic size of SUVs make it difficult to analyse the bilayer formation process. A possible explanation of the formation of SLB is that given a favorable interaction with the substrate above certain coverage, the random rupture of SUVs invokes a cascade of rupturing events [5]. Here the edge of a ruptured SUV can felicitate the rupture of nearby SUVs. Another proposed mechanism is that the SUVs rearrange on the surface, fuse, and above a certain critical radius, they rupture [15]. Even in this case, edges of bilayer patches can trigger the rupture of nearby SUVs [15]. In the case of zwitterionic lipids, the incorporation of certain ions such as Ca^{2+} can favor the fusion of small vesicles whereas, negatively charged lipids can favor the adsorption of vesicles to the substrate. Hence these molecules can help in the formation of SLBs [5, 16]. One disadvantage with the formation of SLB using SUVs is that this technique is highly sensitive to the experimental parameters such as the nature of the substrate, concentration and composition of SUV solution used, deposition temperature, etc. Certain studies, which looked into details of the rupture of GUVs on hydrophilic glass substrates, showed that the rupture is initiated by a pore, which is induced by increased membrane tension due to adsorption to the substrate or illumination with intense light [17]. Studies by Hamai et al. [18] showed that the rupture of GUVs is a spontaneous event taking place mainly along two pathways. The first mechanism corresponds to the formation and expansion of a pore at the apex (anywhere below the midplane near to adsorbed region GUV on the substrate) of the GUV. This results in the formation of an asymmetric bilayer patch on the substrate. In the second case, GUVs get ruptured to form a symmetric bilayer patch in which the formation and expansion of pore starts at the pole of the GUV. But these studies could not establish a systematic procedure for the formation of planar bilayers from GUVs. This is because the creation of tension on GUVs using illumination requires a relatively high amount of dye (0.5-3mol%) to label the bilayer. Also, the size of the bilayer patches formed is limited to the size of the rupturing GUVs.

LB/LS technique uses the sequential transfer of lipid monolayers formed at the air-water interface to form the bilayer [14]. When lipids are deposited on the water surface, they orient in such a way that the head groups face the water, whereas the tail regions are exposed to the air. When this lipid film is laterally compressed, it can form a continuous monolayer [14]. This monolayer can be tailored in a very controlled way and can even incorporate proteins

and other complex molecules. Also, since the bilayer is formed externally and transferred, the bilayers can be formed on any surface. But the constraint of deposition of one monolayer at a time makes the process a little elaborate [1]. In all these cases, there still exists the problem of direct substrate interaction with the lipid bilayer, which can affect its phase behaviour. In order to reduce the substrate interaction, methods such as substrate modifications, including polymer cushioned substrates and the use of tethered lipids for the formation of SLB, etc. have been used [19, 20].

Another class of planar model membranes, which appears less regularly in the literature, is the black lipid membrane or painted lipid bilayer [21]. These are bilayers formed across small orifices supported only at the edges of the membrane. Although the formation of this kind of bilayer is quite straight forward, their lifetime is substantially low compared to bilayers formed by the rest of the methods.

The different types of model systems used with experimental techniques may create difficulty in correlating their results. Most of the studies on GUVs could not be correlated directly with AFM measurements mainly due to the fact that AFM measurements need planar bilayers formed on a substrate which mainly rely on SUV fusion technique rather than GUV rupture method. The formation of bilayer patches using the rupture of GUVs, therefore, can help in correlating fluorescence measurements on GUVs directly with AFM measurements on the planar membrane formed out of GUVs. The difficulty with the rupture of GUVs is that it is not a well-controlled procedure. This chapter explores a novel way of formation of substrate-supported lipid bilayers using GUVs in a controlled way using acetic acid as the rupturing agent.

4.1.3 Previous studies on the rupture of GUVs on different substrates

One of the previous studies which looked at the details of the effect of tension on the stability of GUVs has shown that under tension caused by weak adsorption to a surface or by strong illumination, GUVs show opening up of pores with definite lifetimes [18]. Once a pore opens, it releases a certain amount of internal liquid of the GUV. While doing so, the membrane tension is relaxed, and the pore closes back. This study also showed that when the substrate interaction is stronger, the bilayer tends to adsorb more to the substrate, which increases the tension on the GUV [18]. The increased substrate interaction results in the growth of the pore and rupture of GUVs, which form supported lipid bilayers on the substrate. Later a series of experiments on different substrates showed that charged GUVs could effectively be ruptured on oppositely charged substrates merely due to the electrostatic interactions between vesicles

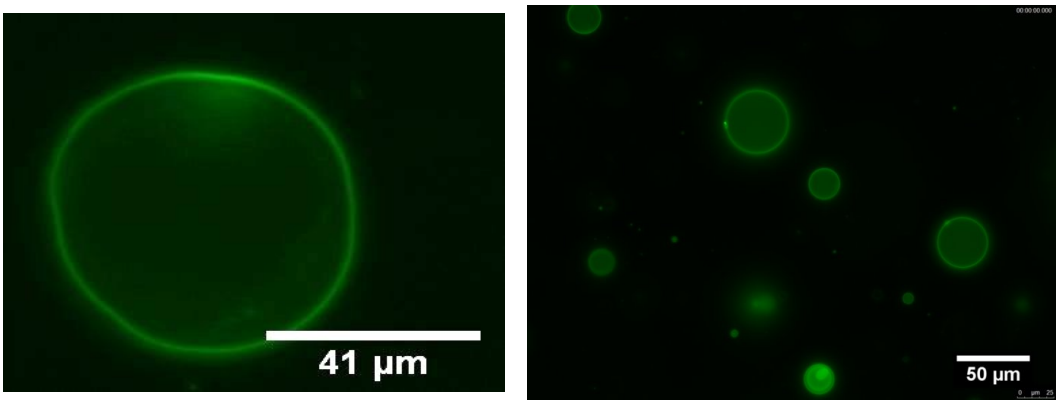

(a) (b)

Figure 4.1: DMPC GUV at 30°C (a) non-spherical due to thermal fluctuations (b) spherical due to tension.

and substrate [17]. The vesicle - substrate interaction is also found to play a huge role in the rupture and fusion of SUVs during the formation of a continuous bilayer on the substrate [17, 22]. Recent studies on the rupture of GUVs and SUVs on homogeneous hydrophobic surfaces show that they form monolayers on the surface [23]. In all the cases of rupture processes, the creation of a pore on the GUVs or SUVs is the initiation step for the formation of SLBs on any substrate.

4.2 Experimental Results

Supported lipid bilayers are formed on weak/strong hydrophilic, and strong hydrophobic surfaces using acetic acid (AA) induced rupture and characterised using fluorescence and confocal fluorescence microscopy. The fluidity of the membrane is analysed using the FRAP technique.

4.2.1 Effect of substrate interaction on GUVs

GUVs were prepared in a 100 mM sucrose solution and transferred to an observation chamber containing 110 mM dextrose solution. The difference in the density of solutions inside and outside the vesicle results in the settling of the GUV at the bottom of the observation chamber. The concentration difference between sucrose and dextrose solutions relaxes the osmotic stress on the GUV, and it exhibits shape fluctuations (fig.4.1(a)). Under tension, the bilayer undulations will be suppressed, and the vesicle appears completely spherical (fig.4.1(b)). GUVs made up of neutral lipids when adsorbed to an untreated glass slide are usually found to be stable for hours without getting ruptured. On the other hand, in the presence of strongly

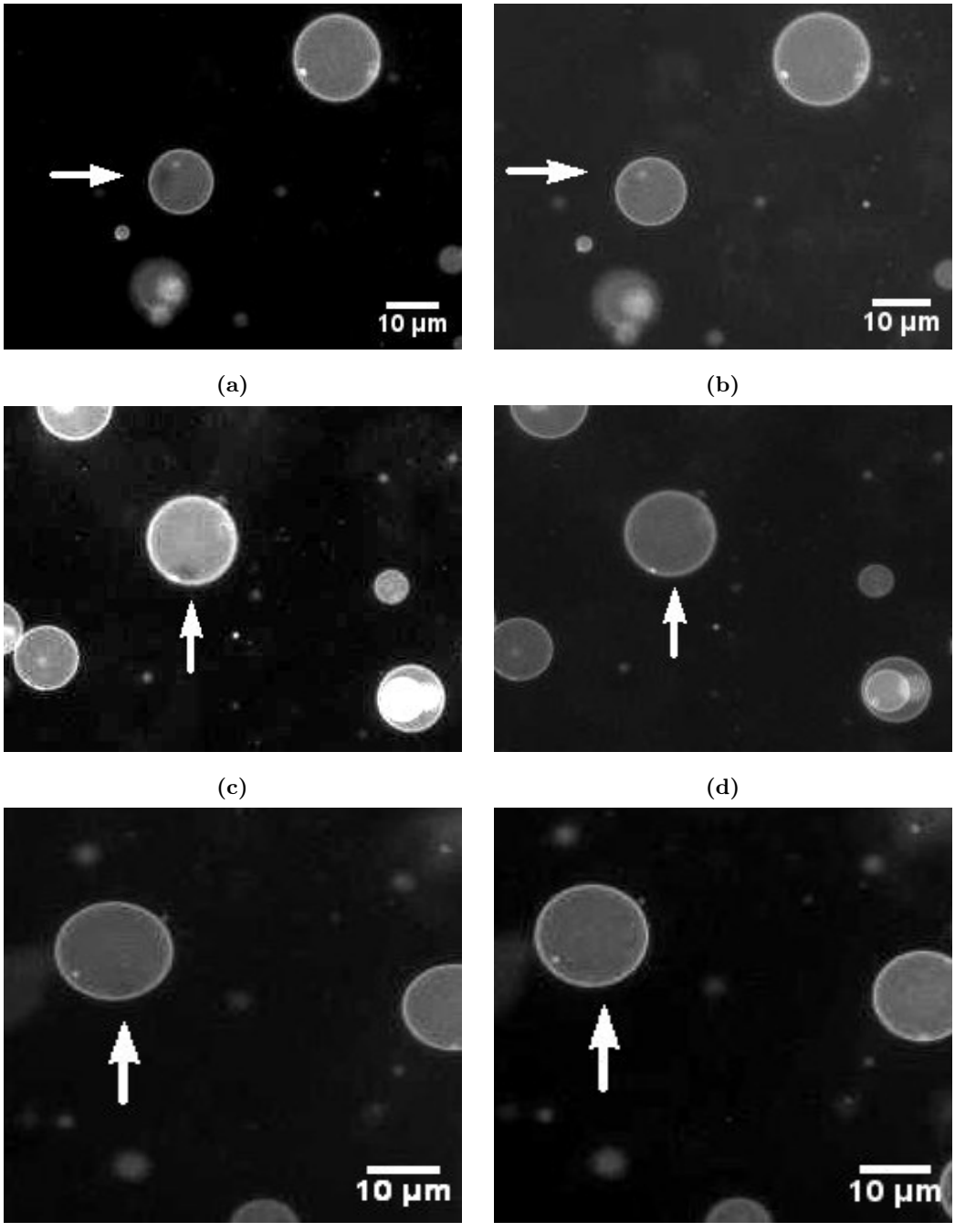

Figure 4.2: DOPC GUVs showing opening (left) and closing (right) of pores

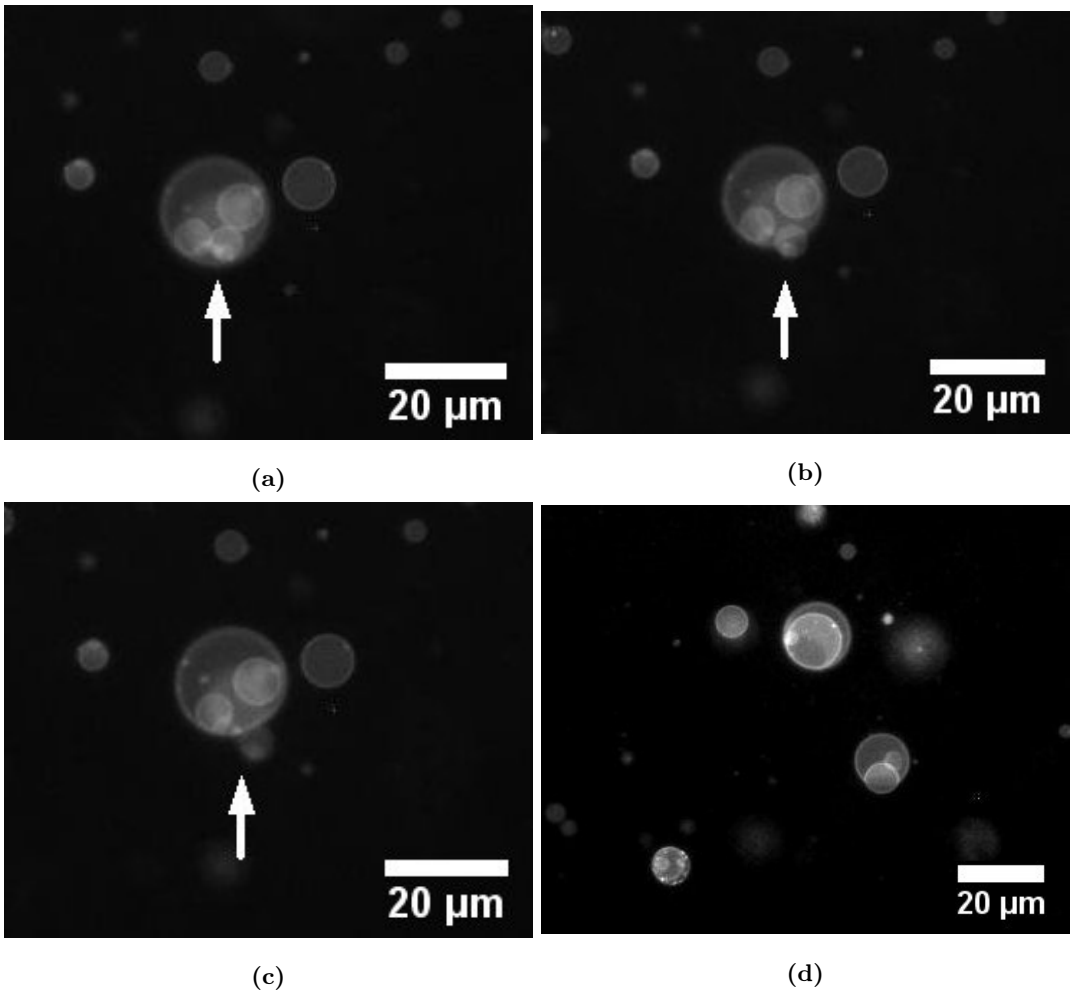

(a) (b) (c) (d)

Figure 4.3: A pore opens and a small vesicle comes out from big tensed vesicle (a),(b) and (c). (d) Image of GUVs with open pores.

hydrophilic substrates the strong substrate-bilayer interaction leads to the rupture of GUVs on the substrate. On untreated coverglass, in the presence of small amounts of acetic acid, the vesicles are found to be tensed. Much of the vesicles also showed release of internal fluid by the opening of pores, which close back within a few milliseconds (fig.4.2). The formation of pores was also confirmed by the release of encapsulated vesicles from a nested vesicle (one or more small vesicles trapped inside the bigger vesicle) as well as the decrease of GUV size with time (fig.4.3). This indicates that although the adsorption is weak in the case of an untreated coverglass, GUVs form pores easily in the presence of acetic acid. This is maybe due to the fact that either acetic acid decreases the energy cost for creating the pore or increases the bilayer-substrate interaction, which in turn creates a tension on the vesicle. Unlike previous experiments where 0.5 to 3 mol% of dye was used to tense vesicles through illumination, these experiments used only 0.05 to 0.1 mol% of total dye concentration. Hence, the effect of illumination on the increase of tension can be eliminated.

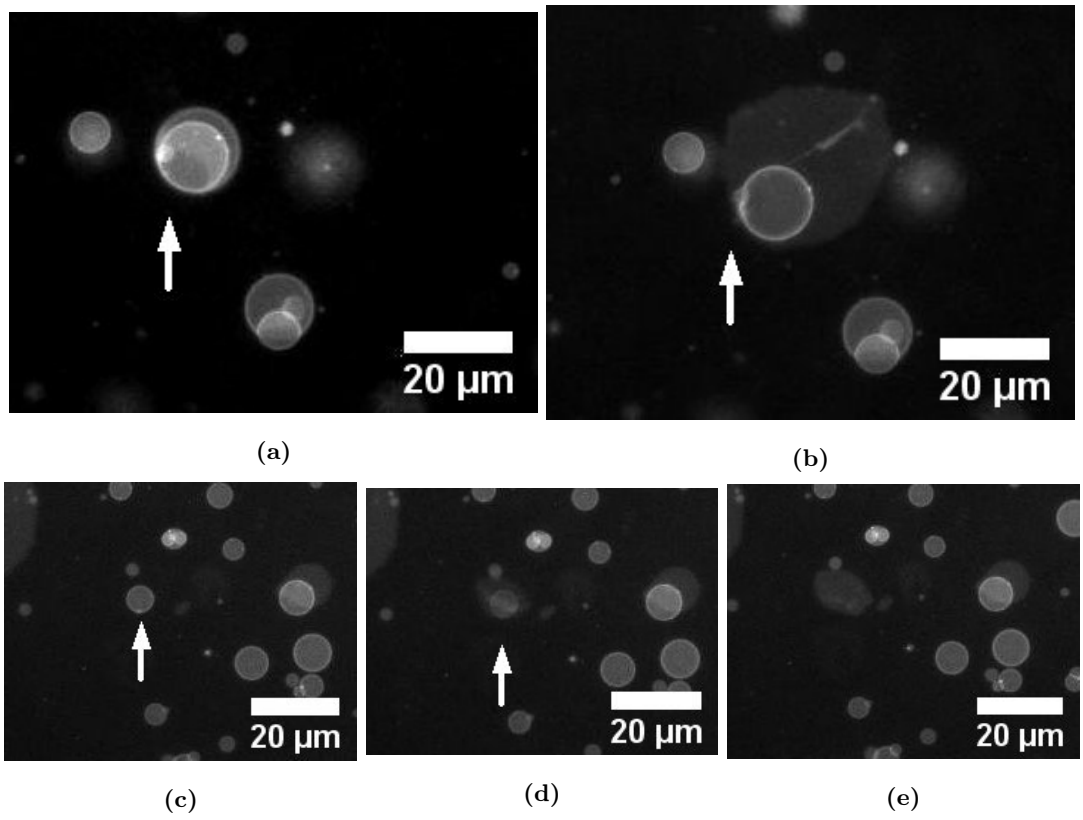

Figure 4.4: Rupturing of a vesicle in the asymmetric pathway. (a) Initial stage (b) Rupture of GUV to form the bilayer, exposing the vesicle inside. (c),(d) and (e) rupture process corresponding to a smaller vesicle. The frames were taken in intervals of 20 ms and rupture taken place in 40 ms to 100 ms. It can be seen here that rupture process is independent of size

With more amount of AA added, the GUV ruptures and forms bilayer on the glass surface. The rupture of vesicles on a normal coverglass with a nominal amount of AA follows different pathways, which result in the formation of bilayer patches with asymmetric and symmetric shapes. Speculated pathways of the formation of bilayers are as follows,

1) Pore opens near the adsorption plane resulting in an asymmetrically shaped bilayer patch (fig.4.4).

2) Pore opens at the centre/pole of GUVs resulting in a symmetric bilayer patch (fig.4.5).

3) Halfway rupture: Rupture may be initiated from the side, a part of the vesicle spreads, whereas the rest of the vesicle fuses to the bilayer formed (fig.4.6).

In all the cases described above, symmetric pathway (2) is found to be the least frequent, whereas pathway (1) is most frequent for low concentrations of AA used. For higher AA concentration used (5 M AA), pathway (3) is found to be most likely.

Normal coverglass cleaned using ethanol alone, represents a weakly hydrophilic surface. Coverglasses, which are plasma cleaned after cleaning with 1% dextran solution, Milli Q

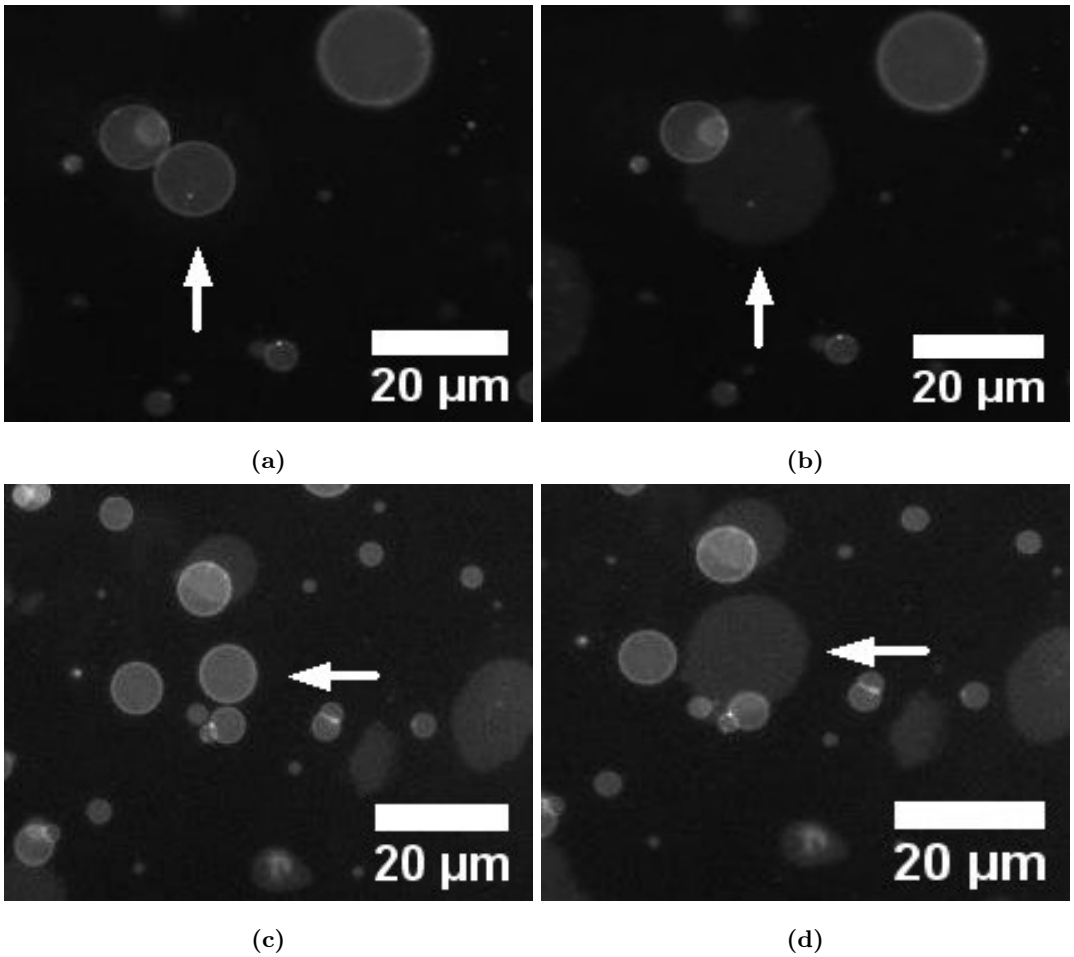

(a) **(b)**

(c) **(d)**

Figure 4.5: Rupturing of a vesicle in symmetric pathway. (a) Initial stage (b) Rupture of GUV forming uniform circular patch. (c),(d) rupture process corresponding to a second vesicle.

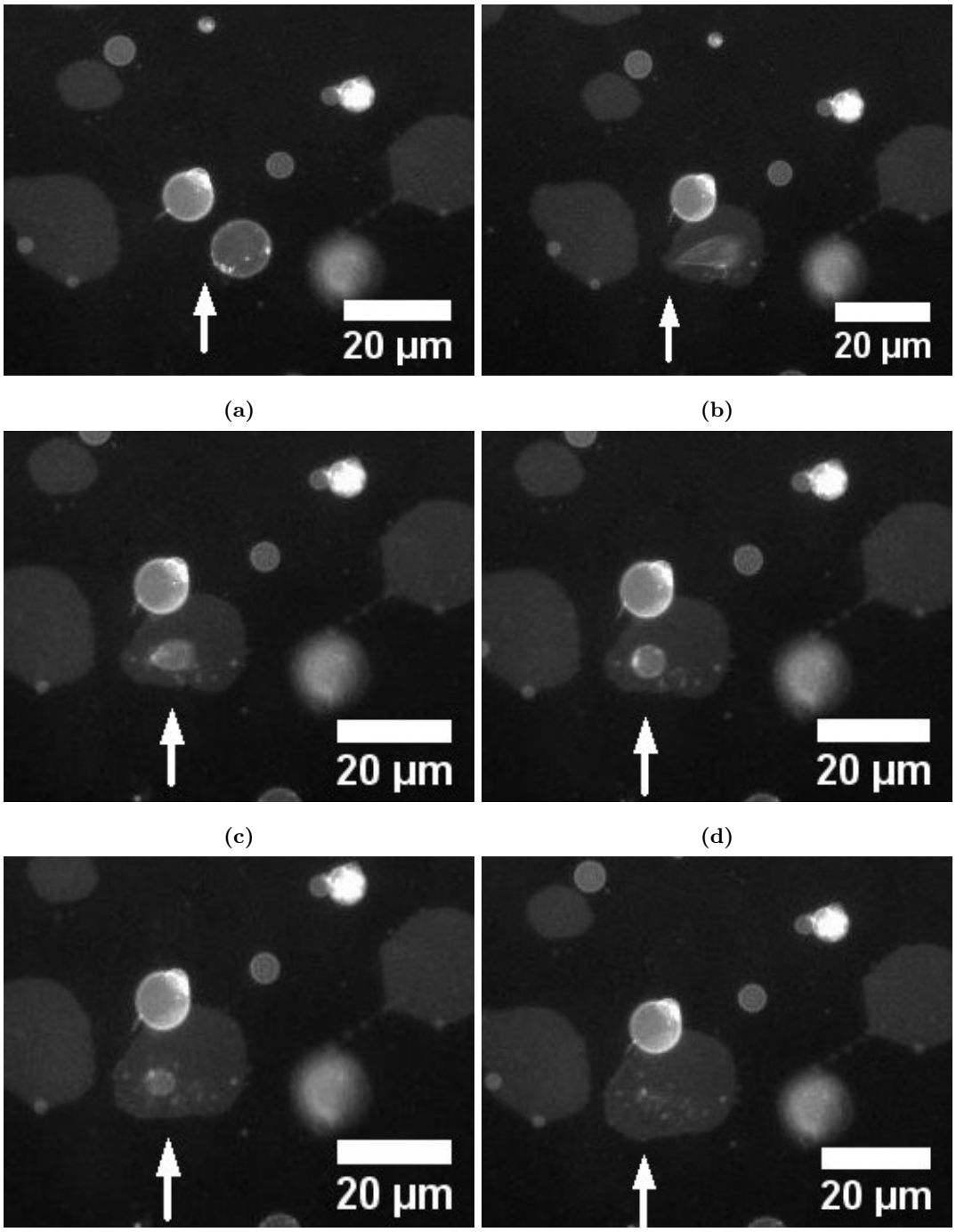

Figure 4.6: Rupturing of a vesicle in the half rupture pathway. The fluorescence intensity distribution shows that the vesicle is single layered (a) Vesicle (b) Rupture of GUV to form bilayer. (c),(d),(e)& (f) fusion of the remaining vesicle part.

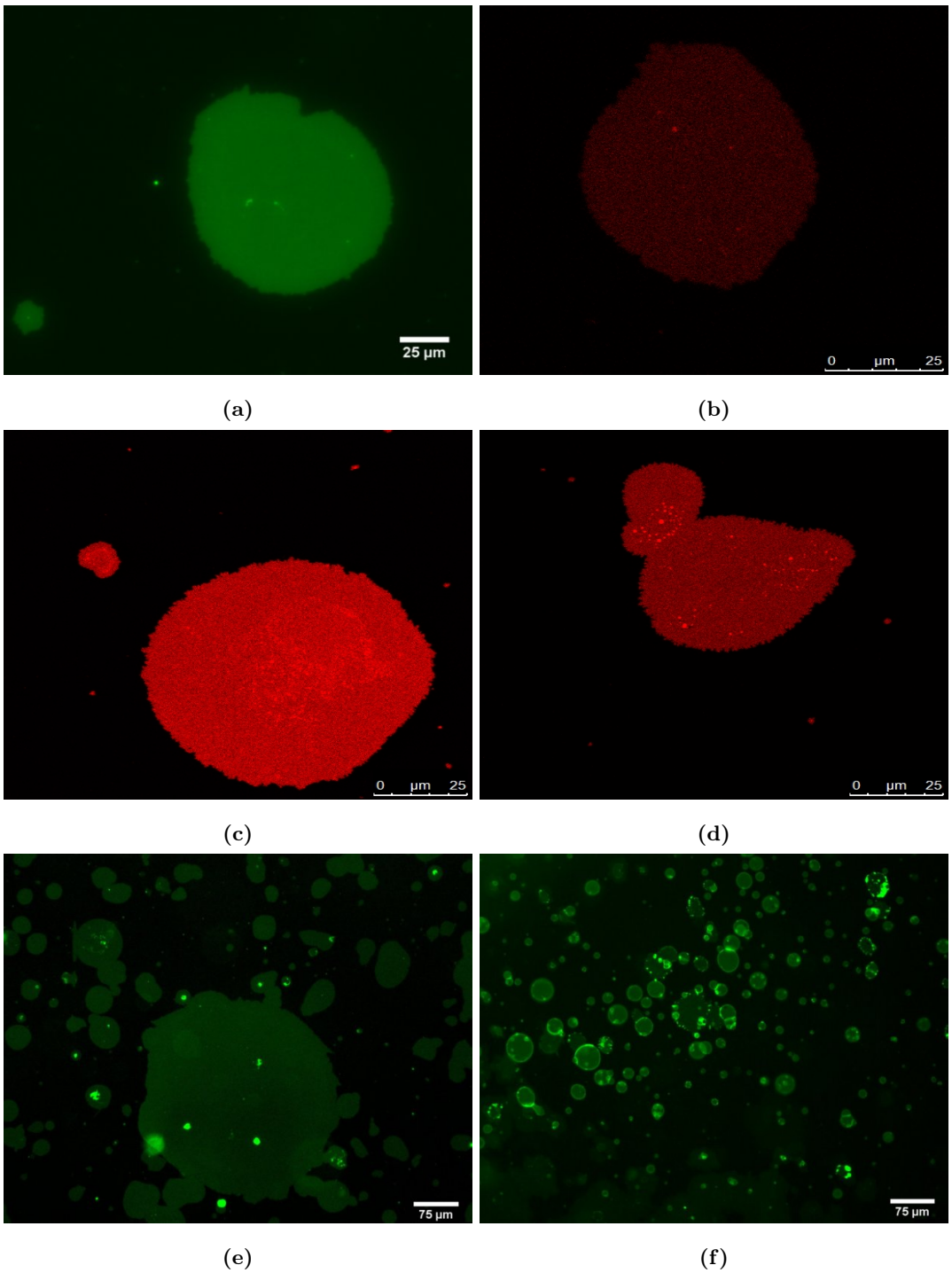

Figure 4.7: DOPC bilayer formed on different substrate by GUV rupture using different concentrations of acetic acid.(a) Mica (b) Normal coverglass (c) Hydrophilic NaOH treated coverglass (Sonication method) (d) Hydrophilic NaOH treated coverglass (24 hr etching) (e) Plasma Cleaned Coverglass (f) Hydrophobic Substrate. The concentration of acid acid used is 1 M

water, and ethanol, represents a highly hydrophilic substrate. The coverglasses were dipped in 2M NaOH solution for 24 hrs or sonicated in 2M NaOH solution for 20 minutes to make them strongly hydrophilic substrates. Another strongly hydrophilic substrate used is a freshly cleaved mica surface. The surface roughness of each substrate was evaluated using AFM. Mica showed the least surface roughness (0.4-0.6 nm) followed by plasma cleaned glass (<0.8 nm), and 24 hr NaOH etched coverglass (< 1 nm). Surface roughness was the highest in the case of coverglass sonicated in NaOH solution (< 5 nm). The hydrophobic surface was prepared by silanizing the coverglass with a silane solution. For all substrates except the hydrophobic surface, a low concentration of AA (100 mM) was enough to rupture the vesicles to form bilayers. The rupture process is found to be faster in the hydrophilic substrate in comparison to weakly hydrophilic coverglass substrate. In the case of the hydrophobic substrate, even at a high concentration of acetic acid (1 M AA or above), most of the vesicles were stable, and only a very few ruptured, mostly forming a monolayer on the substrate rather than a bilayer (fig.4.8).

FRAP measurements were carried out to check the fluidity of the bilayer (fig.4.8). Values of the diffusion coefficient obtained are tabulated in tab.(4.1). It shows that lipid diffusion is faster in bilayers formed on plasma cleaned surface. Hence plasma cleaned coverglass proved to be a better substrate for diffusion studies. The difference between the initial intensity and final recovered intensity in FRAP curves qualitatively represents the fraction of lipid molecules that are unavailable for diffusion. This quantity is called the immobile fraction. The immobile fraction is found to be the least for plasma cleaned surface, i.e. intensity recovered is highest in the case of plasma cleaned substrate. The immobile fraction is found to be the highest in the case of normal coverglass. This difference is probably due to the smooth surface offered by the treated glass and mica compared to normal glass, which facilitates the diffusion of lipids. Also, in the case of highly hydrophilic glass or mica, a layer of water is assumed to be present between the ruptured bilayer and the substrate [22]. The diffusion coefficient is the least in the case of coverglass sonicated in NaOH solution for 20 minutes. This is due to the fact that sonication of coverglass in NaOH solution created nanometer-sized grooves, which may prevent the smooth diffusion of the lipid. The presence of grooves was confirmed by AFM measurements.

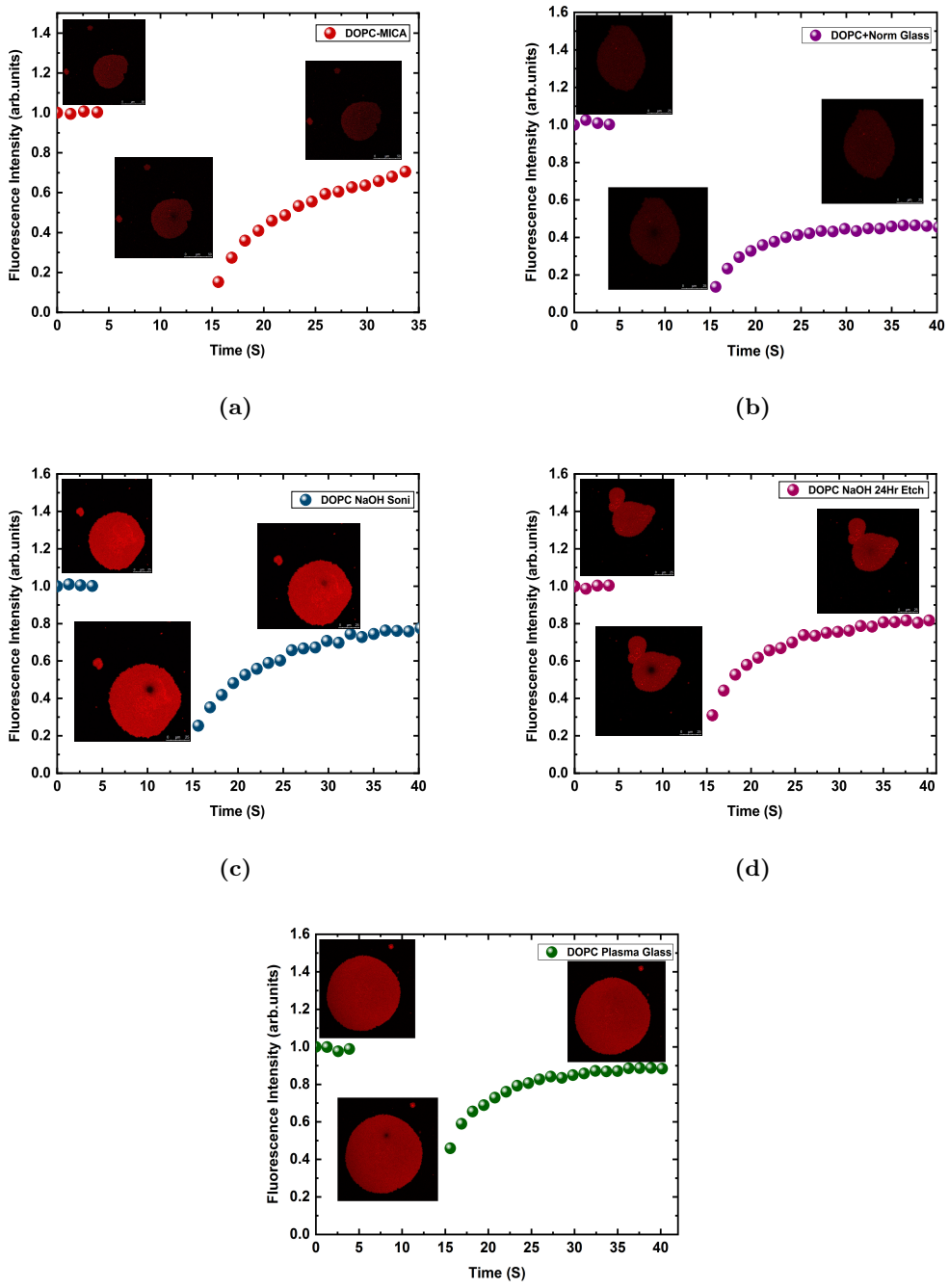

Figure 4.8: FRAP curves of DOPC bilayer formed on different substrate by GUV rupture using different concentration of acetic acid.(a) Mica (b) Normal coverglass (c) Hydrophilic NaOH treated coverglass (Sonication method) (d) Hydrophilic NaOH treated coverglass (24 hr etching) (e) Plasma Cleaned Coverglass

Substrate	Diffusion Coefficient (μm^2/s))
Mica	2.1±0.3
Normal Glass	2.0±0.3
NaOH Glass (sonication)	1.5±0.2
NaOH Glass (24 hr etching)	2.1±0.2
Plasma Cleaned Glass	2.6±0.2

Table 4.1: Diffusion coefficients measured for DOPC bilayer formed on different substrates by acetic acid induced rupturing

4.2.2 Effect of acetic acid concentration on the formation of SLB on plasma cleaned coverglasses

The role of local acetic acid concentration on the rupture of GUV and the formation of bilayers on plasma cleaned substrates was studied. AA solutions of different concentrations were added at the local point of interest, and bilayer formation kinetics were qualitatively analysed.

Previous studies on the formation of SLB have shown that incubation of GUVs made out of PC lipids with a small fraction of a charged lipid on the hydrophilic surface for 30 mins can rupture the vesicle and favor the formation of the bilayer [18]. Similar to this case, on plasma cleaned hydrophilic glass substrates, GUVs were found to rupture on incubation for an hour (fig.4.9). All vesicles which are settled are found to rupture on the substrate. But in the case of untreated glass rupture is a rare event. The bilayer patches on the substrate formed merely due to the adsorption are found to have irregular shapes and edges. Also, certain regions showed double bilayers, which are mostly formed by rupture of encapsulated vesicles on the ruptured vesicle. On the other hand, bilayer formed using the AA rupture method looked more regular.

For 800μl of GUV solution, 200μl of 50 mM AA was used to burst the GUV to form the bilayer. The AA solution was transferred to the GUV solution through a micropipette directly over the point of observation. Similar to the self rupture of GUVs on a hydrophilic substrate, the SLB formed by low concentrations of AA has irregular edges. As the concentration of AA increases, the amount of solution needed to rupture the GUV is reduced, and in the case of 5M AA, the amount of AA solution needed is just 5-20μl. The amount of different AA solutions used only represents a relative comparison since many factors can contribute to the local concentration of AA near GUVs, including temperature, the diffusion rate of AA at different

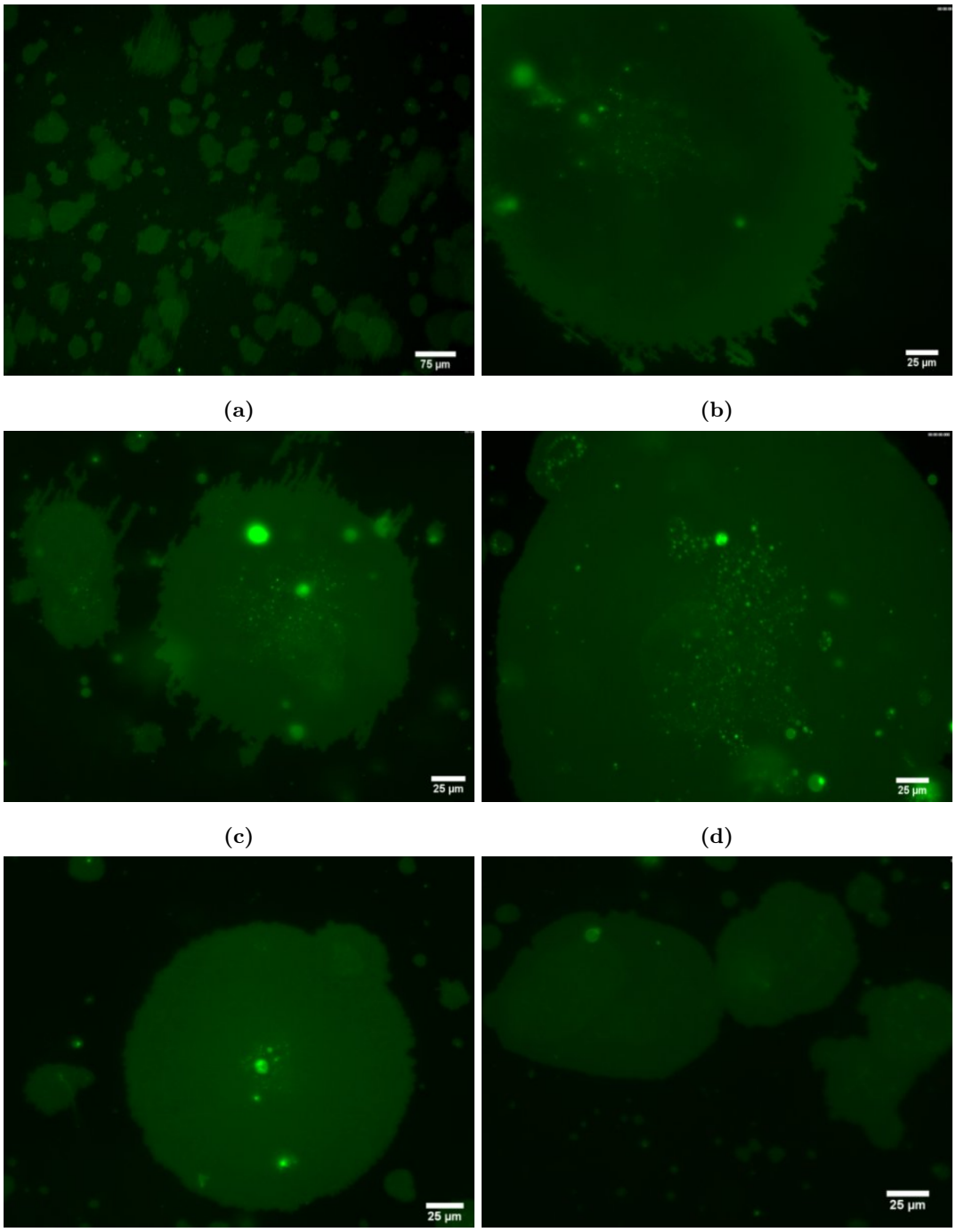

Figure 4.9: DOPC bilayer formed on plama cleaned substrate by GUV rupture using different concentration of acetic acid.(a) 0 mM AA (b) 50 mM AA (c) 200mM AA (d) 500 mM AA (e) 1 M AA (f) 5 M AA

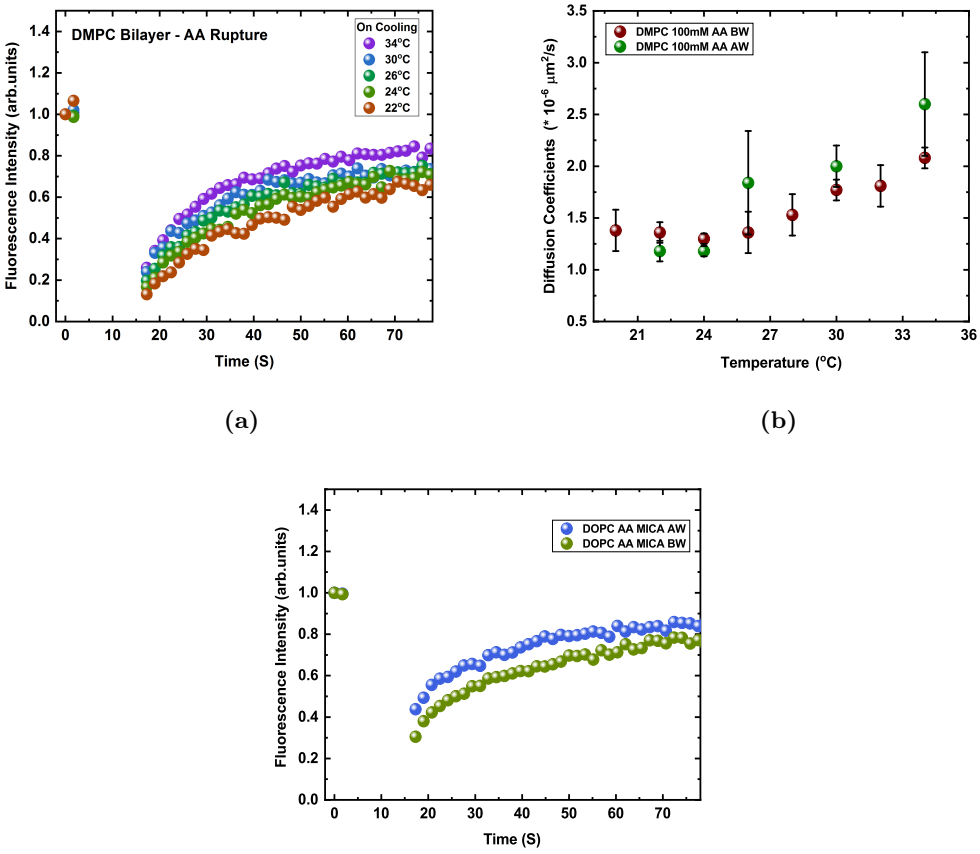

Figure 4.10: Normalized FRAP curve obtained for DMPC bilayer ruptured with (a)rupture using 100 mM acetic acid (b)comparison of diffusion coefficients obtained before and after cleaning (c) Comparison FRAP curve observed at room temperature for DOPC bilayer formed on mica using AA before and after washing.

concentrations etc. Another interesting point is that the bilayer formed by AA solutions of higher concentration look very uniform and clean with smooth edges, compared to the case where a lower AA concentration was used (fig.4.9). Interestingly, at higher concentrations of acetic acid (500 mM and above), the fusion of vesicles with bilayer was observed. This effect is very prominent at 5M AA concentration, the details, and mechanism of which will be discussed in the latter sections of this chapter.

4.2.3 Temperature dependent diffusion measurements of DPPC and DMPC bilayers

The previous section has shown that GUVS readily form bilayer patches on plasma-treated glass with low amounts of acetic acid. After cleaning multiple times with milli-Q water and sucrose solution, the diffusion coefficients obtained for plasma-treated glass is found to be

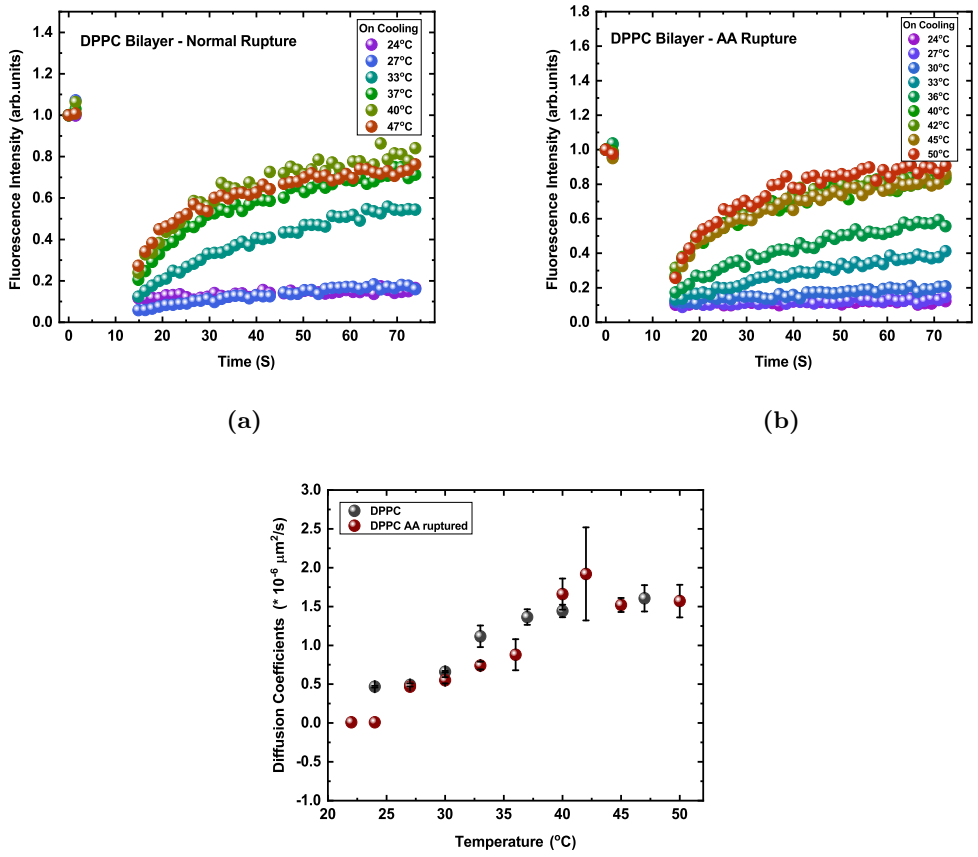

Figure 4.11: Normalized FRAP curve obtained for DPPC bilayer ruptured (a) without acetic acid (b) with acetic acid. (c) Comparison of diffusion coefficients obtained with and without AA.

the highest compared to the values obtained for other substrates. DPPC and DMPC bilayer patches were prepared on plasma cleaned surfaces at 45°C and 30°C respectively above the main transition temperature of the lipids. Diffusion coefficients (D) obtained at different temperatures by FRAP measurements for DPPC and DMPC bilayers are shown in fig.4.10 & fig.4.11. In the case of DPPC, diffusion measurements were also carried out on bilayers formed by self rupture on the substrate. Bilayers formed by rupture induced by acetic acid showed a similar D values to the self-ruptured case above 40°C. Below 40°C, SLBs formed by AA induced rupture showed an abrupt change in diffusion coefficient value in comparison to self ruptured bilayer patches(fig.4.11(c)). The transition region estimated from the change of D is found to be broader in the case of the self ruptured bilayer. This is consistent with many previous reports which claim that the strong interaction of the lower leaflet of the bilayer with the substrate is responsible for the change in transition temperature [24, 25]. This indicate the effect of substrate interaction on the broadening of the transition temperature of lipid is lesser in the case where AA was used. The role of AA incorporated in the bilayer leading to the observed change in diffusion coefficient can be ruled out by considering the fact that the diffusion coefficient of DOPC bilayer on mica after cleaning multiple times with water is same as its value when the bilayer was immersed in a solution having traces of acetic acid (fig.4.10(c)). Also since the diffusion coefficients are the same in the fluid phase of lipids in both, AA ruptured bilayer as well as self ruptured bilyer cases, we can conclude that AA may not be affecting the normal diffusion of lipid. This indicates that AA is not affecting the diffusion coefficient of the lipid.

4.2.4 Extended bilayer formation by induced fusion of GUVs with bilayer patches

One disadvantage with SLB formation using GUV is that the spatial extent of the bilayer is limited by the size of the rupturing GUV. The size of GUVs obtained by the electroformation method ranges from 10-50μm. Hence symmetric bilayer patch with lateral size more than about 100μm can not be produced by rupture of individual GUVs on a substrate. But in the case of the AA-induced rupture method, very large patches can be obtained when the concentration of AA used is 200 mM and above (figures(4.12 and 4.13)). This is possible due to the fact that in the presence of AA GUVs are able to fuse with the already formed bilayer patches on the substrate resulting in the growth of the bilayer patch. Hence this method can be effectively used to make extended bilayers on different substrates. With this method, bilayer patches spanning 1000μm $\times$ 1000μm region with 95% coverage can be obtained. Hence

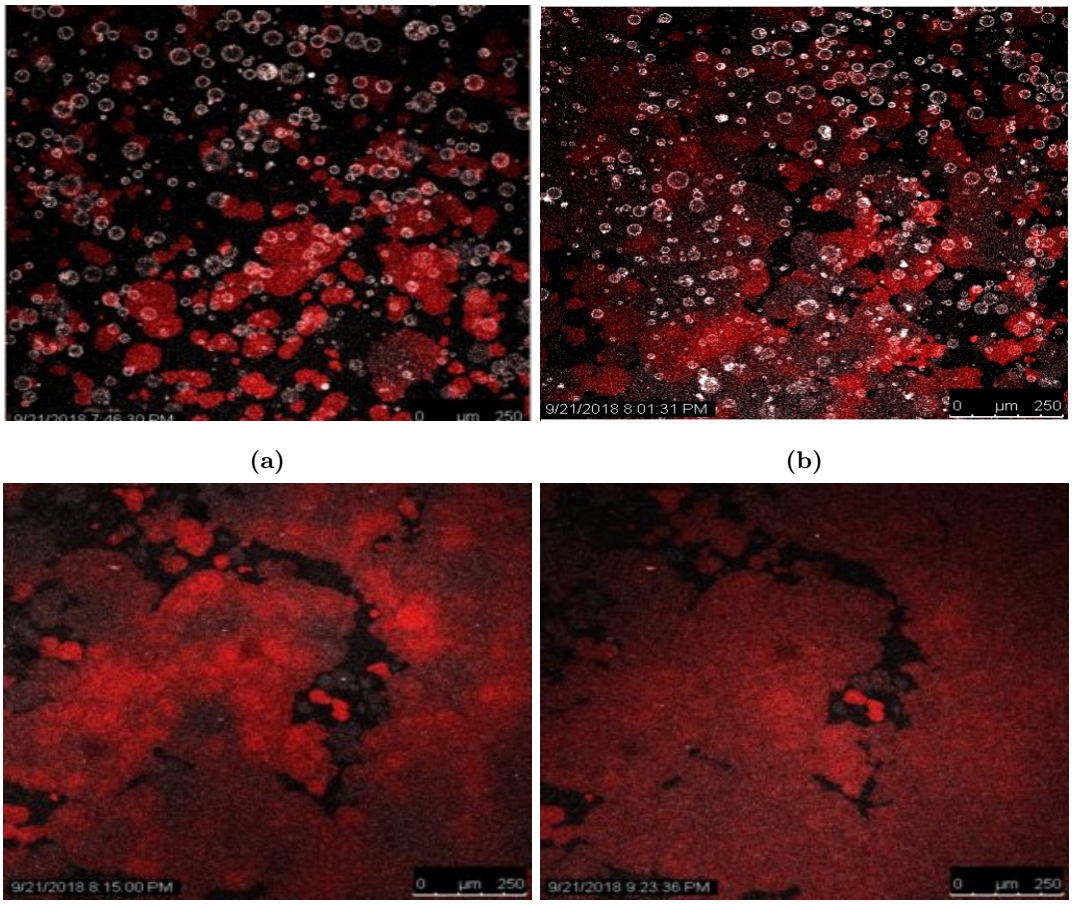

(a) **(b)**

(c) **(d)**

Figure 4.12: Time elapsed images of fusion of guv on already formed bilayer patches (a) initial stage (b) fusion events (c) final stage (d) after incubation for an hour showing diffusion of lipid and homogenization of dye

this method can be effectively implemented for biosensor applications that require extensive bilayer coverage.

Experiments were carried out using two differently labeled vesicles, one forming the bilayer patch and the other forming GUVs fusing to it, to better understand the fusion process. There can be two possible ways of fusion of GUVs to the bilayer, as depicted in fig.4.14. In the first case, the outer leaflet of the GUV fuses with the outer leaflet of the bilayer and inner leaflet of the GUV fuses with the inner leaflet of the bilayer. This forms a continuous fusion cone/stalk. The GUV bilayer parts are dragged into the fusion cone and forced to spread on to the substrate. There is an outflow of the internal liquid of GUV through the water layer between the bilayer patch and the substrate. In this case, the fusion area will be replaced with the second dye and the area of bilayer patch added by fusion will be almost four times the 2D projected area of the GUV. In the other scenario, the pore opens at the top, and only the outer leaflets of both the bilayers are connected. This case will result in the area of new

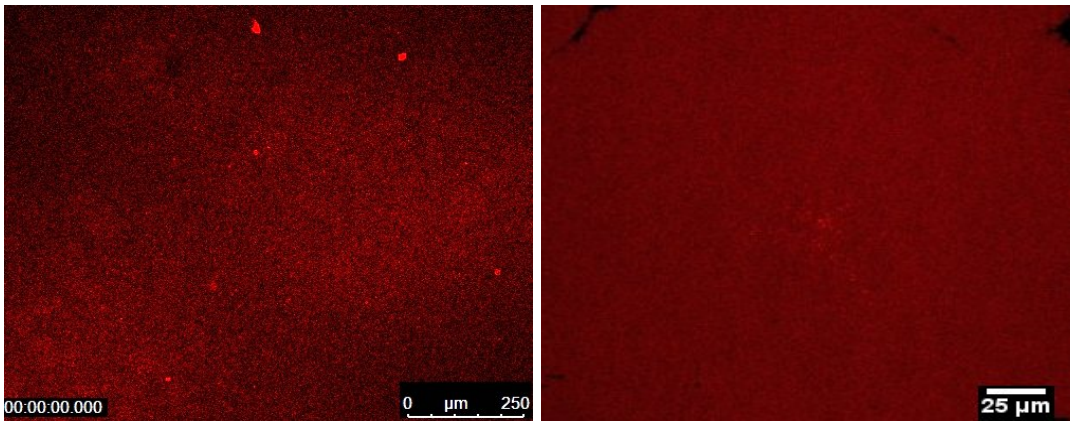

(a) **(b)**

Figure 4.13: Images of SLBs covering entire observation area (a) scale bar 250μm (b) scale bar 25 μm

dye region, which will be almost eight times the 2D projected area of the fusing GUV. The analysis of images has shown that fusion is happening through the first mechanism. This results in an inhomogeneous distribution of the two dyes in the bilayer patches. The fusion area was found to have only the dye of GUVs added. After an hour of incubation, the dye distribution becomes more uniform, indicating the diffusion of lipid across the bilayer.

3D image of bilayer vesicle fusion event captured using a confocal microscope in the case of DOPC on plasma cleaned substrate is shown in fig.4.15.

4.2.5 Liqid-liquid phase separation observed in SLB formed from GUV

On rupture, GUVs are found to preserve the fluid-fluid phase coexistence observed in the ternary mixture of DOPC/DPPC/Chol(2:2:1) as well as in a binary mixture of DLPC:25Hydroxysterol (85:15) (fig.4.16). This allows simultaneous fluorescence microscopy as well as AFM measurements on the same sample. The phase diagram and details of phase separation in DLPC: 25 Hydroxysterol binary mixtures are described in chapter 5.

4.3 Discussions

4.3.1 Mechanism of rupture of GUV in the presence of acetic acid

The mechanism of GUV rupture in the presence of AA can be explained in two possible ways. Firstly, acetic acid can increase the adsorption of the membrane to the substrate. The second possibility is that in the presence of AA, the bilayers form pores more readily, or the already formed pores due to adsorption induced tension, are stabilised in the presence of acetic acid.

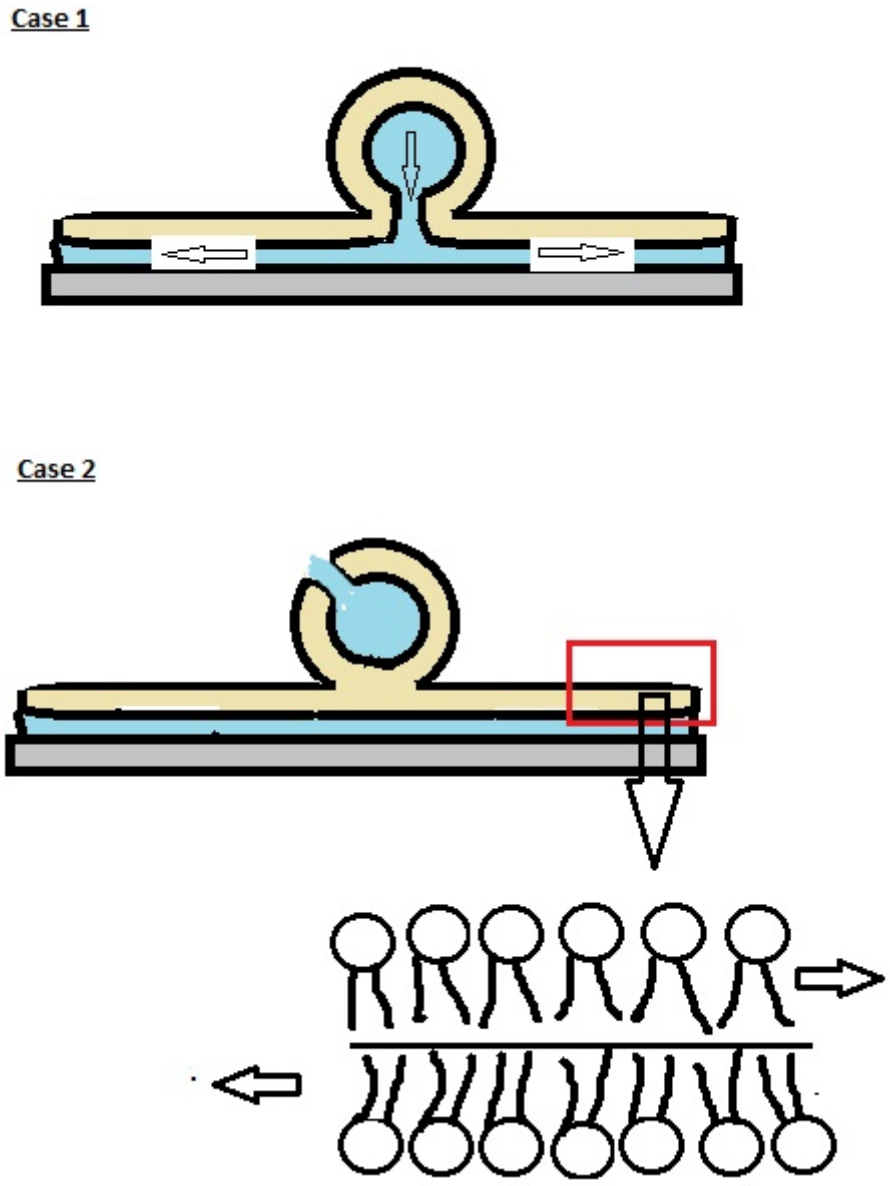

Figure 4.14: Schematic of fusion process. Case 1: Two leaflets of GUV and bilayer are interconnectedby a fusion pore forming at the base of the GUV. Case 2: Pore opens at the top, outer leaflets of GUV and bilayer are interconnected

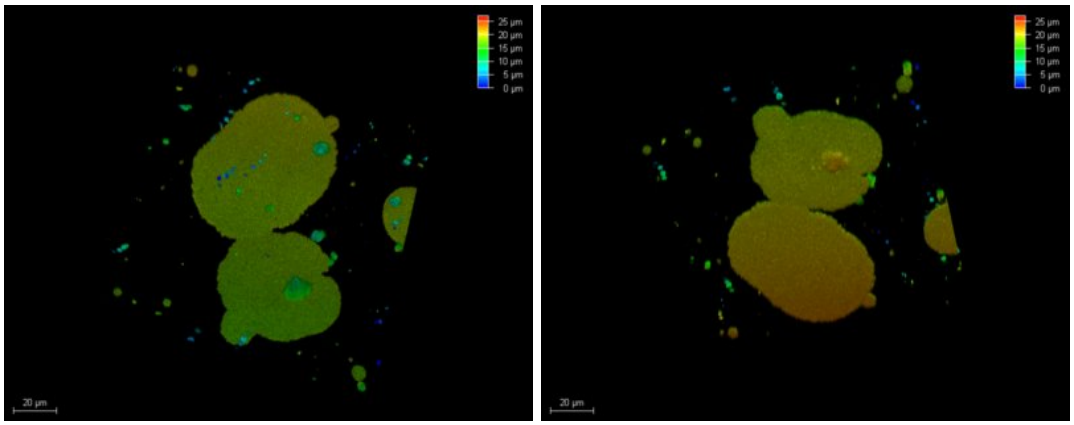

(a) **(b)**

Figure 4.15: Confocal fluorescence image of vesicle fusing on bilayer (a) top view (b) bottom view

In the case of self rupture of GUVs on hydrophilic surfaces, the GUV solution has to remain undisturbed for a certain amount of time. Here the favourable substrate - bilayer interaction has resulted in the rupture of GUVs. But in the case of AA-induced rupturing, the vesicle rupture soon after it touches the substrate. There is no statistical evidence for increased adsorption of a GUV to the substrate. Hence the formation and stabilization of pores by acetic acid are assumed to be the reason for AA-induced rupturing of GUVs on different substrates. In the case of 5M AA, the rupture of GUVs, which touches the hydrophilic surface, is found to be through mechanism 3 (half-way rupture process). In other cases, the bilayer formation is predominantly through the asymmetric pathway.

4.3.2 Mechanism of induced fusion of GUV with SLB

At sufficiently higher concentrations, AA was able to induce fusion of vesicles on the already formed bilayer patches on a substrate. In most of the cases with nested vesicles, the rupture event was followed by the release of the encapsulated vesicle. Hence in most cases, internal vesicles were not tethered to the parent vesicle. The possibility of the pre-existing interconnection of encapsulated vesicles with the parent vesicle leading to their fusion was eliminated by the experiment on GUVs labeled by two different dyes. This study indicates that the fusion process does not require any pre-existing interconnections. The fusion events observed in the presence of high acetic acid concentration can be explained in the following way. The fusion of GUVs to the SLB requires the formation of a fusion stalk between them. The formation of a fusion stalk is the energy barrier between the non-fused and fused states of GUV and the bilayer. In the presence of AA, probably fusion stalks form more easily. Hence AA enhances fusion chances between a GUV and the bilayer.

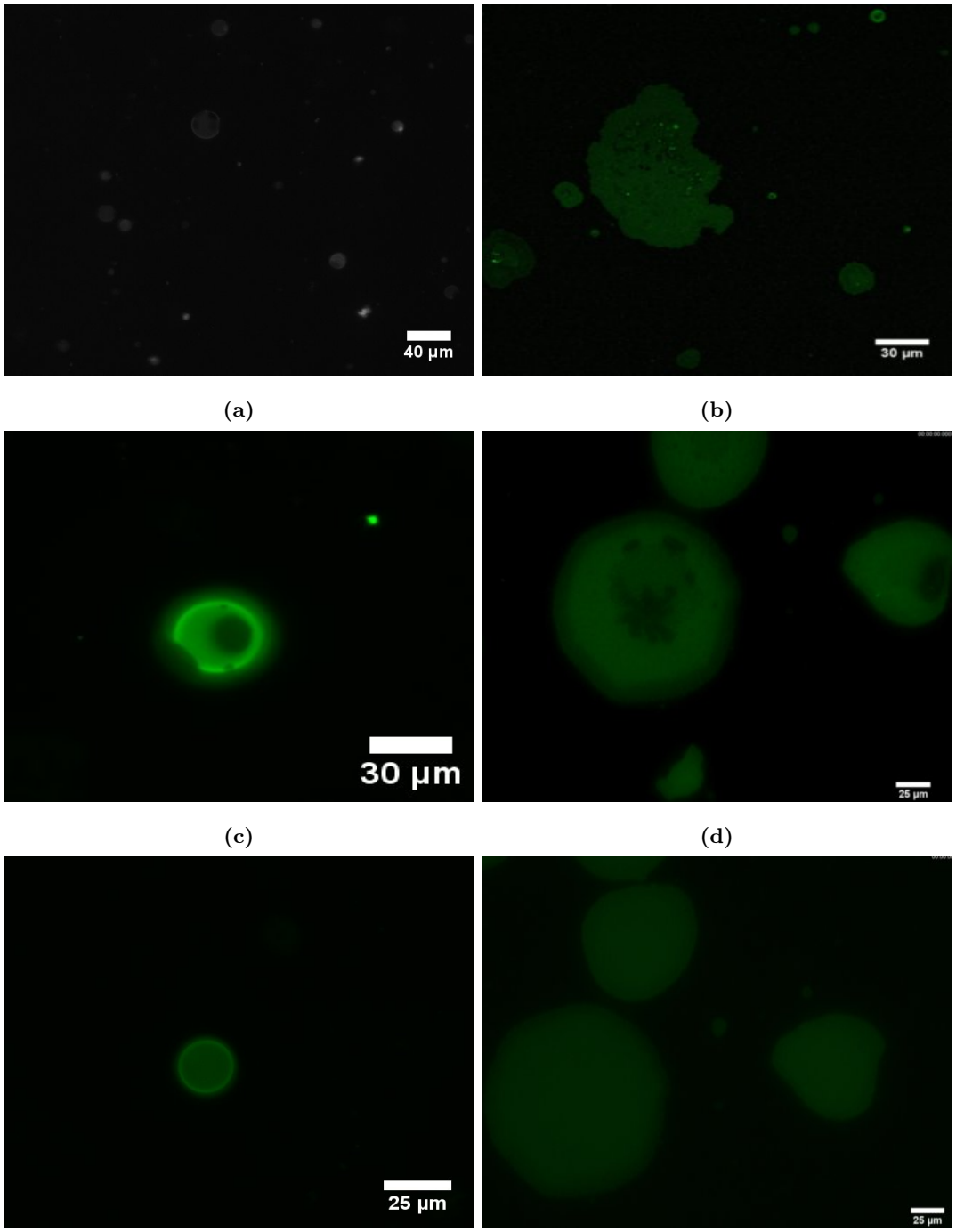

Figure 4.16: Phase separation on GUV and ruptured bilayer observed for (a) DO:DM:CHOL (2:2:1) GUV (b) DO:DM:CHOL (2:2:1) Bilayer at room temperature, for DLPC:25 Hydroxysterol (85:15) (c) vesicle at 15°C (d) bilayer at 15 °C (e) vesicle at 34 °C (f) Bilayer at 33°C

4.4 Conclusion

The formation of extended bilayers on different substrates is achieved using the rupture of GUVs induced by acetic acid solution. In the presence of AA, GUVs were able to fuse with SLB patches.

Bibliography

[1] T.K. Lind and M. Càrdenas. Understanding the formation of supported lipid bilayers via vesicle fusion - a case that exemplifies the need for the complimentary approach (review). *Biointerphases*, 11:020801–020812, 2016.

[2] D. D. Lasic. The mechanism of vesicle formation. *Biochem. J.*, 256:1–11, 1988.

[3] E. Rideau, R.Dimova, P. Schwille, F. R. Wurm, and K. Landfester. Liposomes and polymersomes: a comparative review towards cell mimicking (review). *Chem. Soc. Rev*, 47:8572–8610, 2018.

[4] S. J. Attwood, Y. Choi, and Z. Leonenko. Preparation of dopc and dppc supported planar lipid bilayers for atomic force microscopy and atomic force spectroscopy. *Int. J. Mol. Sci.*, 14:3514–3539, 2013.

[5] R. P. Richter, R. B{'erat, and A. R. Brisson. Formation of solid supported lipid bilayers: An integrated view. *Langmuir*, 22:3497–3505, 2006.

[6] R. Nayar and A. J. Schroit. Generation of ph-sensitive liposomes: use of large unilamellar vesicles containing n-succinyldioleoylphosphatidylethanolamine. *Biochemistry*, 24:5967–5971, 1985.

[7] E. Sezgin and P. Schwille. Model membrane platforms to study protein-membrane interactions. *Mol. Membr. Biol.*, 29:144–54, 2012.

[8] R. B. Lira and R. Dimova. *Chapter Six - Fusion assays for model membranes: a critical review In: R. Lipowsky (eds). Multiresponsive Behavior of Biomembranes and Giant Vesicles*, volume 30. Advances in Biomembranes and Lipid Self-Assembly, 2019.

[9] A. Akbarzadeh, R. R-Sadabady, and S. Devaran et al. Liposomes : classifications, preparations and applications. *Nanoscale Res. Lett.*, 8:102, 2013.

[10] S. Karmakar. Structure and phase behaviour of lipid-cholesterol membranes.

[11] N. F. Morales-Penningston, J. Wu, and E. R. Farkas et al. Guv preparation and imaging: Minimizing artifacts. *Biochim. Biophys. Acta*, 1798:1324–1332, 2010.

[12] S. F. Fenz and K. Sengupta. Giant vesicles as cell models. *Integr. Biol (camb)*, 4:985–995, 2012.

[13] P. Walde, K. Cosentino, H. Engel, and P. Stano. Giant vesicles: preparations and applications. *ChemBioChem*, 11:848–865, 2010.

[14] J. F. V. de Souza J. Kurniawan, A. T. Dang, G-Yu Liu, and T. L. Kuhl. Preparation and characterization of solid-supported lipid bilayers formed by langmuir - blodgett deposition : A tutorial. *Langmuir*, 35:15622–15639, 2019.

[15] K. L. Weirich, J. N. Isearlachvili, and D. K. Fygensen. Bilayer edge catalyse supported lipid bilayer formation. *Biophys. J.*, 98:85–92, 2010.

[16] E. Reimhut, F. H o ok, and B. Kasemo. Intact vesicle adsorption and supported biomembrane formation from vesicles in solution: Influence of surface chemistry, vesicle size, temperature and osmotic pressure. *Langmuir*, 19:1681–1691, 2003.

[17] Md. M. Rahman Y-H Kim, Z-L. Zhang, N. Misawa, R. Tero, and T. Vrisu. Supported lipid bilayer formation by giant vesicle fusion induced by vesicle-surface electrostatic attractive interaction. *Chem. Phys. Lett*, 420:569–573, 2006.

[18] C. Kataoka-Hamai and T. Yamazaki. Induced rupture of vesicles adsorbed on glass by pore formation at the surface-bilayer membrane. *Langmuir*, 31:1312–1319, 2015.

[19] J. Andersson and I. K oper. Tethered and polymer supported bilayer lipid membranes. *Membranes(Basal)*, 6:30, 2016.

[20] W. Knoll, C. W. Frank, and C. Heibel et al. Functional tethered lipid bilayers. *J. Biotechnol.*, 74(3):137–158, 2000.

[21] C. Cranfield, S. Carne, B. Martinac, and B. Cornell. *The Assembly and Use of Tethered Bilayer Lipid Membranes (tBLMs). In: Owen D. (eds) Methods in Membrane Lipids.*, volume 1232. Humana Press, New York, NY, 2015.

[22] R. Tero. Substrate effects on formation process, structure and physiochemical properties of supported lipid bilayers. *Materials (Basal)*, 5(12):2658–2680, 2012.

[23] C. Kataoka-Hamai and K. Kawakami. Interaction mechanisms of giant unilamellar vesicles with hydrophobic glass surfaces and silicone oil-water interfaces. *Langmuir*, 35:16136–16145, 2019.

[24] A. Charrier and F. Thibaudau. Main phase transitions in supported lipid single bilayer. *Biophys J.*, 89:1094–1101, 2005.

[25] H. M. Seeger, G. Marino, A. Alassandrini, and P. Facci. Effect of physical parameters on the main phase transition of supported lipid bilayers. *Biophys J.*, 97(4):1067–1076, 2009.

Chapter 5

Effect of the interaction of acetic acid on PC lipids

5.1 Introduction

Under atmospheric pressure in excess water conditions, the phase behavior of a lipid bilayer is solely decided by its intrinsic parameters such as the nature of the head group region, degree of unsaturation, and length of the hydrocarbon chain region [1]. It has been observed that the phase behavior, especially the main transition temperature (gel to fluid phase) and formation of ripple phase in saturated PC lipids are affected by many external factors including hydration, pressure, solvent pH and the presence of salts [2]. High pressure and low pH increases the fluid to gel transition temperature of PC bilayers, as indicated by different experiments and simulations [3, 1, 4, 5]. Above a certain concentration, different alkali chloride salts increase the main transition temperature of PC lipids [5]. In addition to these environmental effects, the interaction of certain small amphiphilic molecules such as cholesterol, ethanol, and dimethyl sulphoxide (DMSO) can also alter the phase behavior of lipids [6, 5]. DMSO has multiple uses in a biological system as an adjuvant cryoprotectant, free radical scavenger, membrane fusogen, membrane permeabilizer, and inducer of cell differentiation. The presence of an S-O group in DMSO allows it to form multiple hydrogen bonds with water, and hence it is highly water-soluble. Synchrotron studies on the interaction of DMSO with a PC lipid have shown that DMSO destabilizes the fluid phase and favors the gel phase [7]. Ethanol is found to show a biphasic effect on the main transition temperature of DPPC multilayers. At low concentrations < 50 mg/ml, ethanol decreases the transition temperature and at high concentrations > 50 mg/ml, it increases the transition temperature. At higher concentrations of ethanol, below 42°C (main transition temperature of pure DPPC), DPPC forms an

interdigitated phase [5]. Another example is the incorporation of cholesterol and cholesterol derivatives, which affect the chain ordering and lowers the main transition temperature [8]. In general, any molecule which disrupts chain ordering favors the fluid phase and reduces the main transition temperature and molecules which reduce head group repulsion, favors the gel phase and increases the main transition temperature.

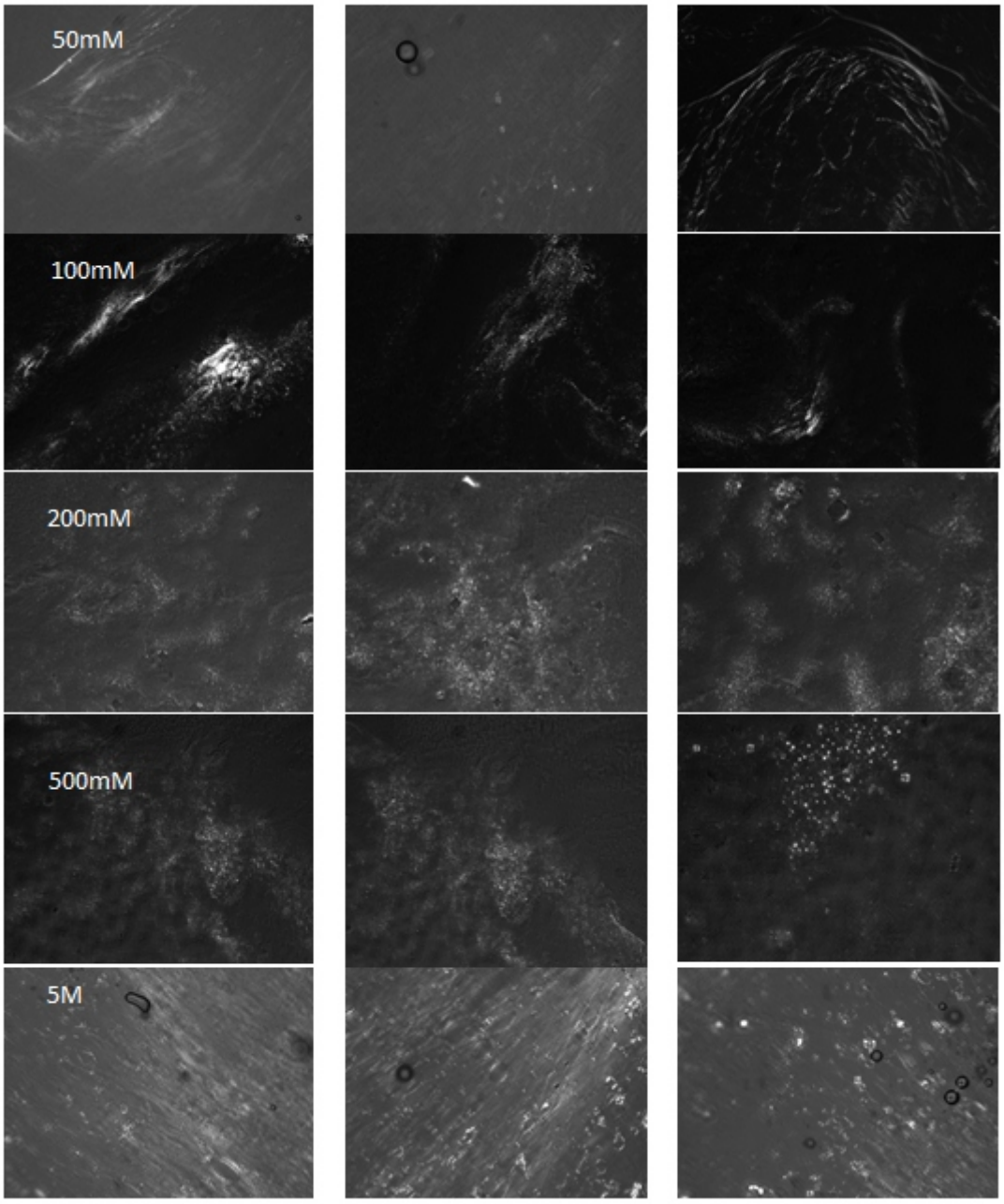

Figure 5.1: POM images of DMPC:AA samples showing birefringence.

Acetic acid is the simplest form of carboxylic acid found in mammalian cells [9]. The acetyl group derived from acetic acid is fundamental to many biological processes. By binding to

coenzyme A, it plays a central role in the metabolism of carbohydrates and fat [9]. In bacilllus subtilis bacterium, acetic acid acts as a signal to stimulate the formation of structurally complex biofilms [10]. Apart from biological interest, acetic acid also finds applications in medicinal and industrial fields, especially as a food additive and preservative. It is not well established as to how acetic acid interacts with the cell membrane. Most of the studies on model membrane systems have focused on the permeation of acetic acid molecules through the lipid membrane [11, 12]. These studies also propose the use of acetic acid as a molecular probe to study the passive permeation of small molecules through the membrane. However, certain simulations have shown that acetic acid has a preferential interaction with the lipid head group region [13]. This preferential interaction of acetic acid can have a significant impact on the phase behavior of lipid bilayers.

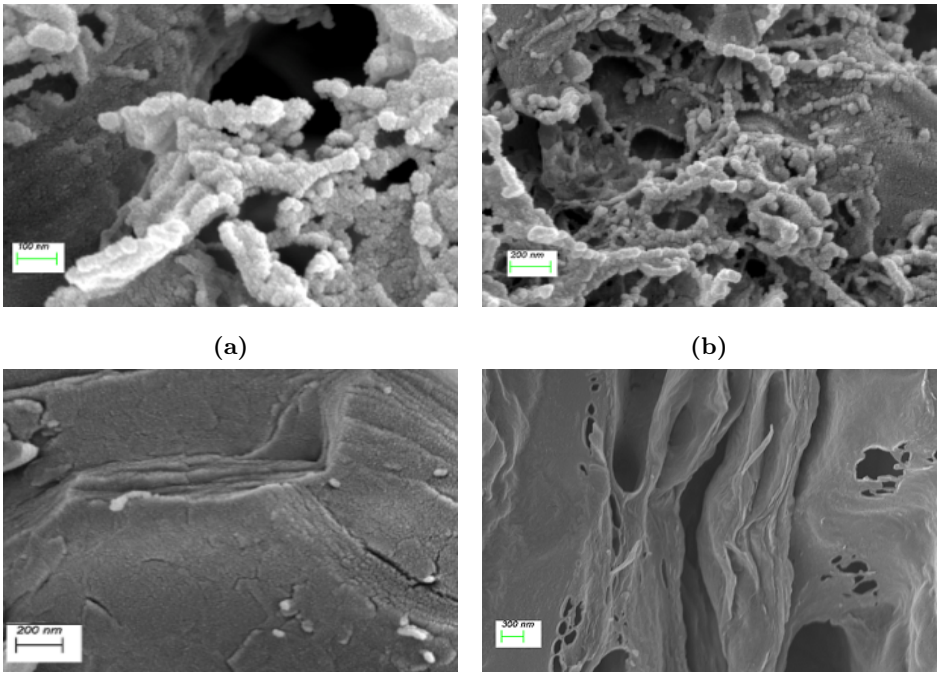

Figure 5.2: Cryo-SEM images of DMPC:AA (10wt%) after 5 days of preparation for (a) 50 mM (scale bar-100 nm) (b) 500 mM (scale bar-300 nm) (c) 1 M (scale bar-200 nm) (d) 5 M (scale bar-200 nm) acetic acid concentrations in the solution. Note that (a) & (b) have more vesicular structures compared to (c) & (d)

This chapter focuses on the interaction of acetic acid molecules with PC lipid bilayers and the effect of this interaction on the structure and phase behavior of PC bilayers.

DMPC lipid samples were prepared with varying concentrations of acetic acid solution in Milli-Q water. The lipid weight percentage in the solution was kept at 10 wt% for most of the studies, except for the studies on the effect of hydration on lipid - acetic acid binary system.

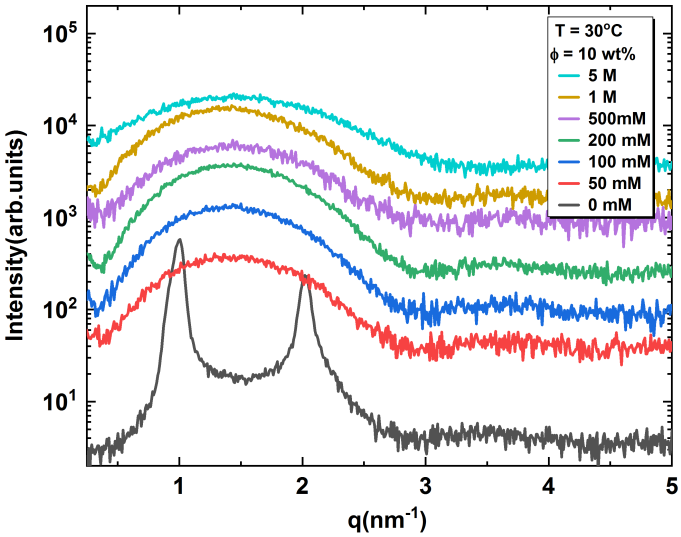

Figure 5.3: SAXS data of DMPC lipid (10 wt%) as a function of acetic acid concentrations at 30°C

5.2 Results

5.2.1 Cryo-SEM and SAXS studies

Acetic acid is found to interact with PC bilayers. Similar to the case of UMP, acetic acid induces a charge on the membrane, which results in the formation of a swollen lamellar phase. Just after preparation, the turbidity of the samples changed with acetic acid concentration. The sample with the least concentration of acetic acid (50 mM) was a uniformly turbid solution to start with, whereas 5M sample was only slightly turbid. Correspondingly, samples were birefringent under a polarizing optical microscope (POM), unlike a ULV solution that appears dark under POM (fig.5.1). With incubation time, the turbidity of the samples reduces, and all the samples became clear after incubation of 5 days at 30°C. Cryo-SEM images of these samples showed the presence of mostly small vesicular structures coexisting with the lamellar phase for acetic acid concentrations of 500 mM and below. For 1 M and 5 M acetic acid, the samples showed only lamellar morphology (fig.5.2). But all the samples showed broad diffraction patterns corresponding to the form factor of the bilayer (fig.5.3). This indicates that although 1M and 5M samples showed lamellar morphology with cryo-SEM, the measurement of periodicity was limited by the maximum d-spacing our SAXS setup can measure. The diffraction patterns obtained were fitted to the bilayer form factor, and the electron density profiles were obtained. The electron density profiles obtained from DMPC samples (10 wt%) at different acetic acid (AA) concentrations as a function of temperature

Conc. of AA	Z_h (nm)	
	30°C	60°C
100 mM	1.97	1.63
200 mM	1.99	1.63
500 mM	1.88	1.57
1 M	1.93	1.56
5 M	1.50	1.43

Table 5.1: Table showing the Z_h values of DMPC with different acetic acid concentrations at 30°C and 60°C. The bilayer thickness is defined as $2Z_h$.

are shown in fig.5.4.

The bilayer thickness calculated from the form factor is tabulated in table.5.1. Similar to the case of UMP, the bilayer thickness is significantly reduced in the presence of acetic acid in a concentration-dependent manner at 60°C. The DMPC sample with 5 M AA showed most thinning of the bilayer. On cooling as well as on heating, similar to DMPC: UMP system, DMPC: AA system also showed an abrupt change in bilayer thickness near 30°C. The bilayer thickness increased at 30°C for all samples except the 5 M AA sample. This behavior of DMPC in 5 M acetic acid solution is confirmed using WAXS and DSC measurements, and discussed in the latter parts of this chapter. The abrupt change in bilayer thickness at 30°C indicates the formation of a gel phase above T_m of pure DMPC.

For 20 wt% lipid samples, peaks corresponding to the swollen lamellar phase are present in their SAXS patterns. Fig.5.5 shows the appearance of peaks corresponding to the swollen lamellar phase for 20 wt% samples at 60°C. The d-spacings of swollen lamellar phases obtained are 16 nm and 15.7 nm, respectively, for DMPC: 1 M AA and DMPC: 100 mM AA samples. This means that the lamellar periodicity is limited by the water content in the sample. Also, the bilayers are better correlated in the case of 1 M acetic acid since the peaks are sharper. The pH of 100 mM acetic acid solution is 2.88, whereas that of a 1 M acetic acid solution is 2.38. The pKa of the PC head group region is around 1. Hence the possible charging of the bilayer due to the reduction of pH of the solution can be ruled out. We conclude that the binding of dissociated acetic acid molecules to the membrane leads to the charging of the bilayers and formation of the swollen lamellar phase.

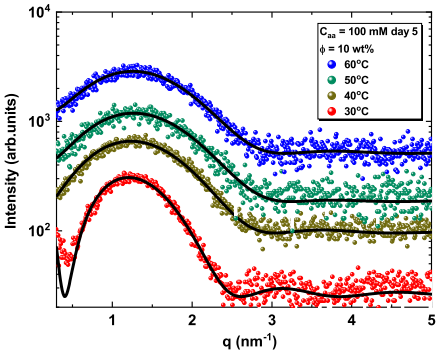

(a)

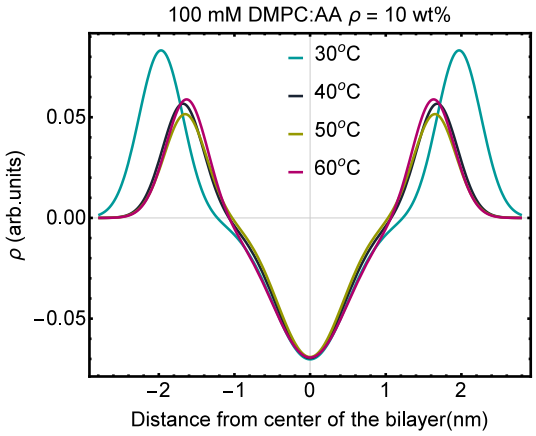

(b)

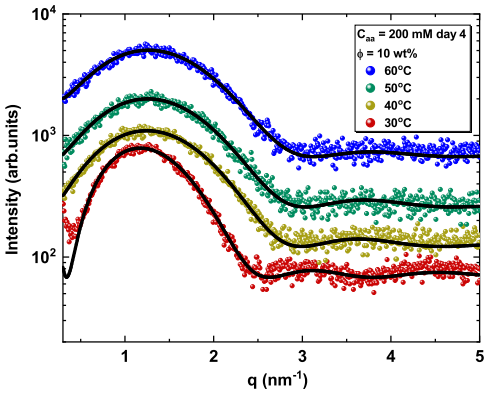

(c)

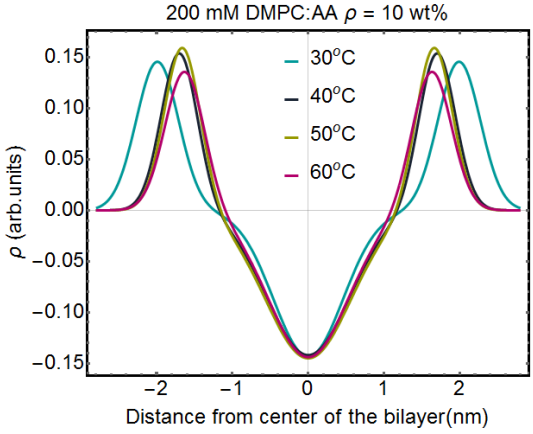

(d)

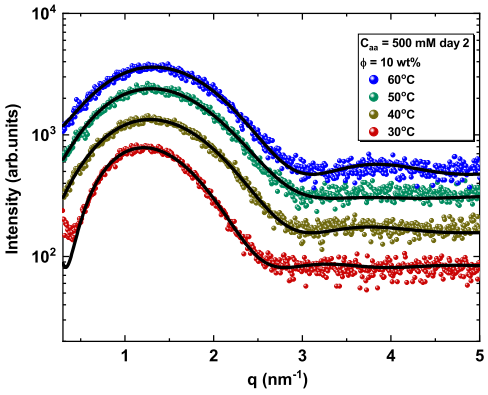

(e)

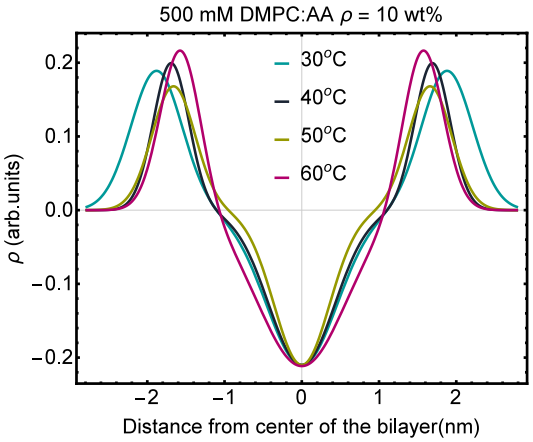

(f)

Effect of incubation on the phase behavior of PC bilayers with AA

Effect of the interaction of acetic acid on the phase behavior of PC bilayers was studied as a function of incubation time and temperature. Compared to UMP, the kinetics of phase change in the presence of acetic acid is found to be slower. Hence the samples were only incubated at 55°C for further SAXS and WAXS studies. With incubation, all the samples (1 M AA and

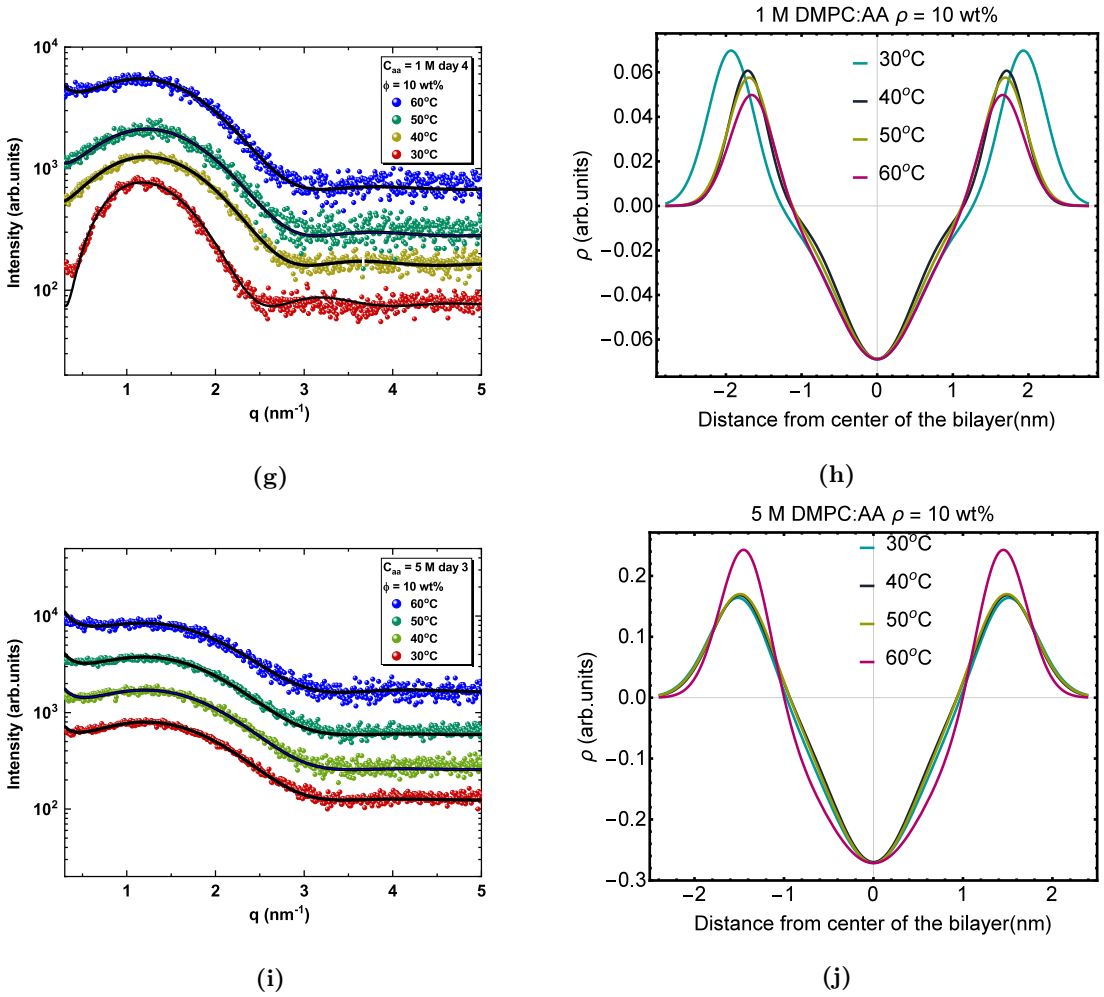

Figure 5.4: SAXS patterns (left) and corresponding EDPs (right) obtained for DMPC:AA (10 wt%) samples with AA concentrations of (a) 100 mM (c) 200 mM (e) 500 mM (g) 1 M (i) 5 M. The solid lines in the saxs profiles are the fits to the expression for the bilayer form factor.

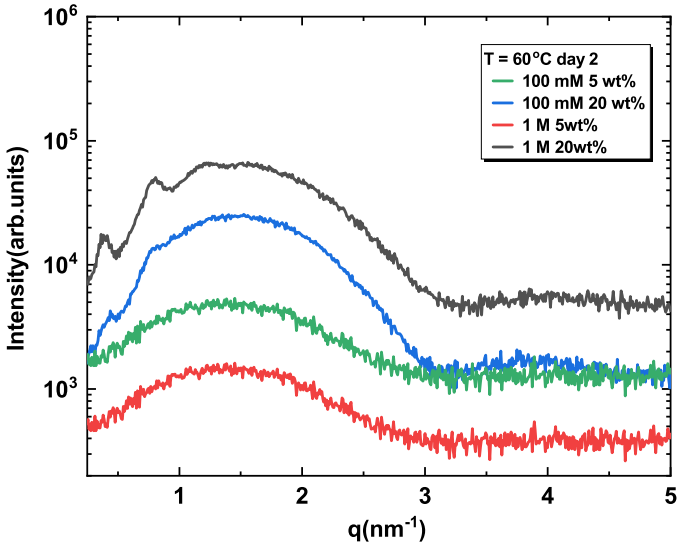

Figure 5.5: SAXS data of DMPC with 100 mM and 1 M AA at 60°C at two different lipid weight percentages (5 wt% and 20 wt%). Note that 20 wt% samples show peaks corresponding to swollen lamellar phase with d-spacing of 16 nm (100 mM AA) and 15.7 nm (1 M AA)

below) showed the formation of the gel phase, which melts at 42°C on heating. Samples with higher acetic acid concentration showed the formation of an interdigitated phase, which melts above 50°C. WAXS and DSC studies confirmed this phase behavior observed using SAXS. To avoid the possible evaporation of the solvent and hence the change in AA concentration in the sample over the long incubation time involved, all the DSC samples were incubated only at room temperature. This problem is not present in the case of sealed capillaries used for SAXS and WAXS studies.

5.2.2 SAXS studies

SAXS data obtained for samples incubated at 55°C showed the formation of swollen lamellar phase with high d-spacing (fig.5.6). This phase is induced by the adsorption of charged acetic acid molecules to the membrane. On further incubation, both 200 mM and 1 M samples form a gel phase (note that the patterns show 5 orders of lamellar peaks), which melts above 40°C (fig.5.7). The d-spacings obtained from DMPC : AA(10 wt%) samples at different AA concentrations (200 mM and 1 M) after 10 and 12 days of incubation at 55°C are tabulated below (table.5.2). The d-spacing of this gel phase is 6.8 nm, which is only 0.5 nm more than that of pure DMPC in the gel phase. Therefore the electrostatic repulsion and hence the charge on the bilayer are negligible in this phase.

One possible explanation is that at this stage, all the charged acetic acid molecules ad-

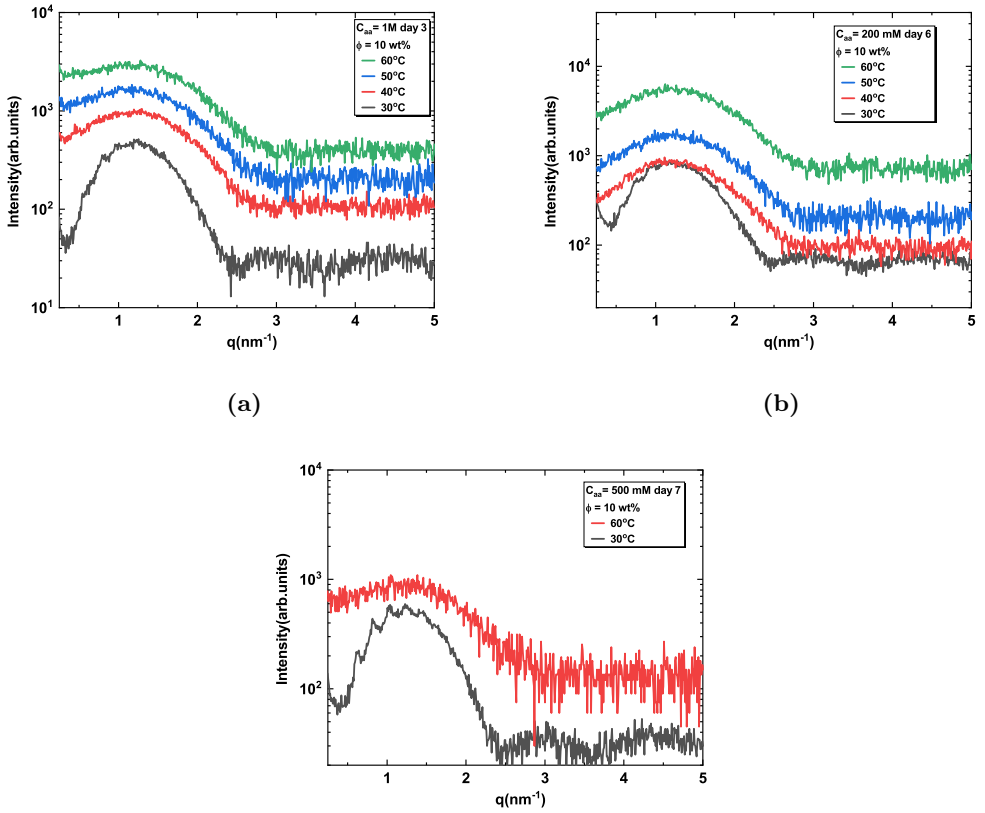

Figure 5.6: SAXS data of (a) DMPC: 1M AA (b) DMPC: 200 mM AA (c) DMPC: 500 mM AA (10 wt%) after 3 , 7 & 6 days of incubation at 55°C. The d-spacing is ≈ 30 nm at 30°C.

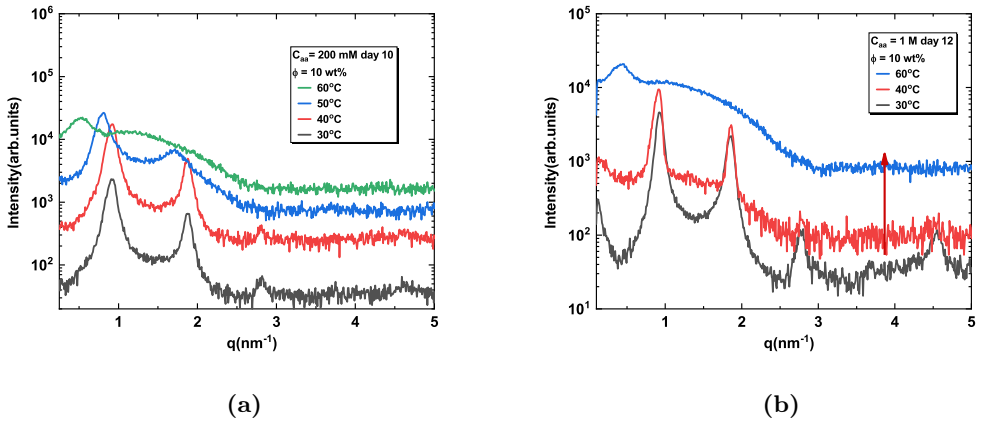

Figure 5.7: SAXS profiles of DMPC: AA samples at (a) 200 mM (after 10 days) and (b) 1 M (after 12 days) incubated at 55°C as a function of temperature.

sorbed on the membranes get replaced with undissociated acetic acid molecules in the solution. The electron density profiles (EDP) obtained from the SAXS patterns using the Fourier reconstruction method [14] showed a region of low electron density between the bilayer and

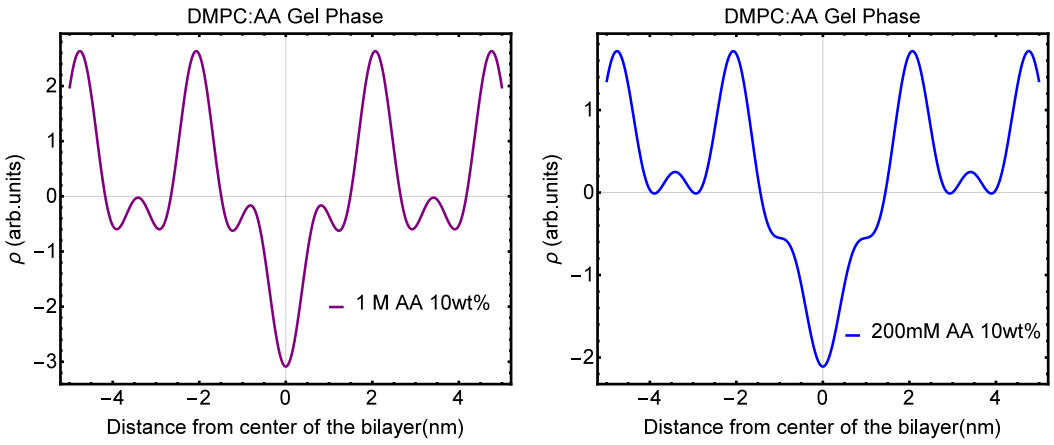

(a) **(b)**

Figure 5.8: Electron density profiles of DMPC bilayer in the gel phase at 30°C in 1M and 200 mM acetic acid solutions incubated at 55°C for 12 & 10 days

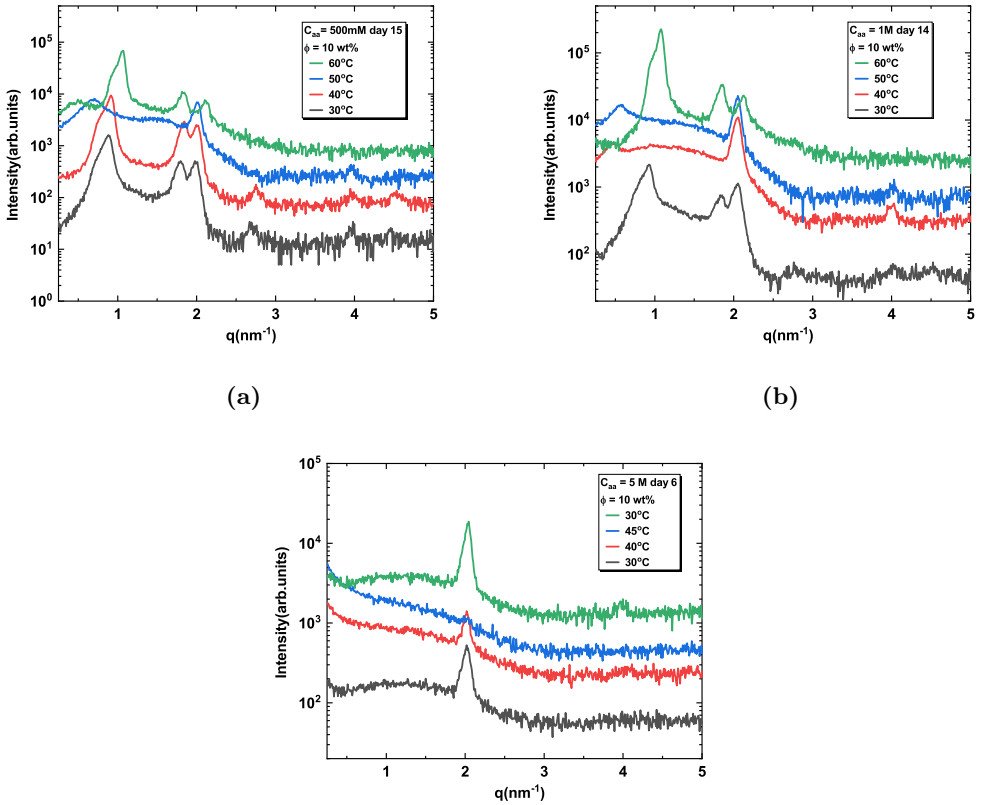

(a) **(b)**

(c)

Figure 5.9: SAXS profiles of DMPC : AA samples at (a) 500 mM (after 15 days) and (b) 1 M (after 14 days) showing coexistence of lamellar gel phase and interdigitated phase (c) 5 M (after 6 days) showing peaks corresponding to the interdigitated phase along with a form factor background

water phase, which suggests the possible adsorption of acetic acid molecules at the interface (fig.5.8). Since the acetic acid molecule has a lower electron density in comparison to the

C_{aa}	T	Phase	d-spacing
200 mM	30°C	L_β	6.85 nm
	40°C	L_β	6.85 nm
	50°C	L_α	8.00 nm
	60°C	L_α	12.37 nm
1 M	30°C	L_β	6.80 nm
	40°C	L_β	6.86 nm
	60°C	L_α	14.75 nm

Table 5.2: Table showing d-spacings obtained for 200 mM and 1M AA DMPC samples on incubating over 10 and 12 days at 55°C. L_β-lamellar gel phase, L_α-lamellar fluid phase.

PC headgroup region and water, the adsorption of acetic acid at the interface creates a low electron density region between the headgroup and water. This can be easily seen in the EDP obtained. However, on heating, the samples showed a higher d-spacing of 8 nm and 15 nm, respectively, at 50°C and 60°C for 200 mM AA: DMPC sample. The peak observed is very broad, which suggests the reduction in correlation length or number of correlated bilayers, which is not expected for an electrostatically stabilized phase (fig.5.7). Therefore the high d-spacing obtained is mostly due to the increased undulation repulsion between the bilayers as a result of the adsorption induced thinning of the bilayer. But more experiments are needed to interpret this behavior clearly. Similar to the 200 mM AA sample, a 1M AA sample showed a d-spacing of 15 nm at 60 °C on heating.

With further incubation, samples with high concentrations (500 mM and above) of acetic acid form an interdigitated phase, whereas samples with low acetic acid concentration do not show the formation of interdigitated phase even after incubation for 30 days (fig.5.9 and table.5.3). The formation of the interdigitated phase in 5 M AA samples was found to be faster in comparison to 1 M and 500 mM AA samples. The interdigitated phase melts above 50°C and forms a hexagonal phase in the case of 500 mM and 1 M samples and an isotropic phase in the case of the 5 M sample (fig.5.9). The edps obtained from interdigitated and hexagonal phases are shown in fig.5.10. The phase behavior of DMPC: AA system thus is found to be much similar to that of the DMPC: UMP system.

The hexagonal phase formed on the melting of the interdigitated phase is believed to be an inverted phase rather than a direct phase due to the following reason. Since 5:1 DMPC: UMP samples over a very wide range of hydration levels show the melting of the interdigitated phase to a hexagonal phase, a similar behavior can be expected with acetic acid. A direct

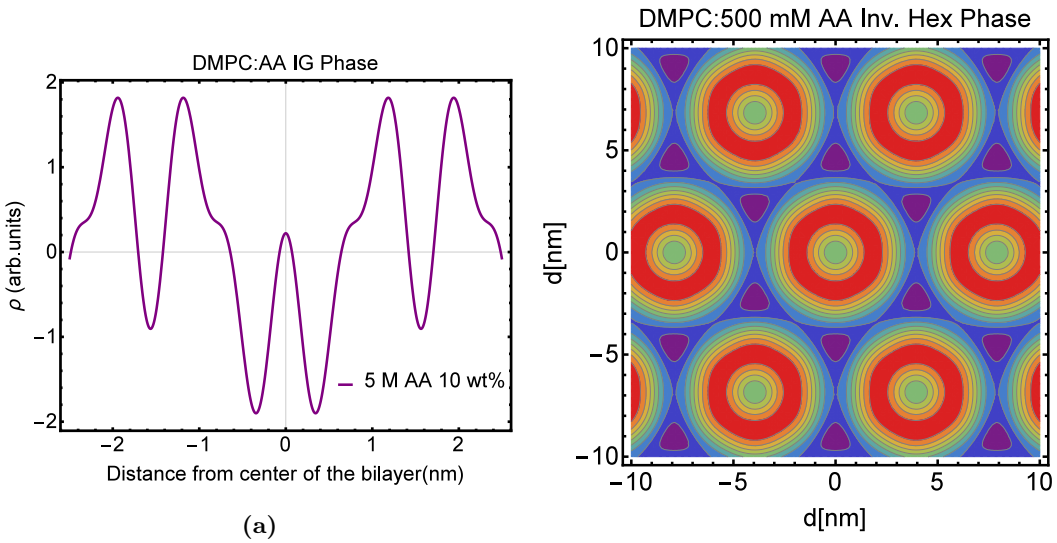

Figure 5.10: Electron density profiles of interdigitated bilayer (5M AA) at 30°C and inverted hexagonal phase of 500 mM acetic acid sample at 60°C

hexagonal phase is usually observed at sufficiently high hydration levels [15]. The presence of the hexagonal phase over such extended hydration levels indicates that the phase formed is an inverted hexagonal phase rather than a direct hexagonal phase [16].

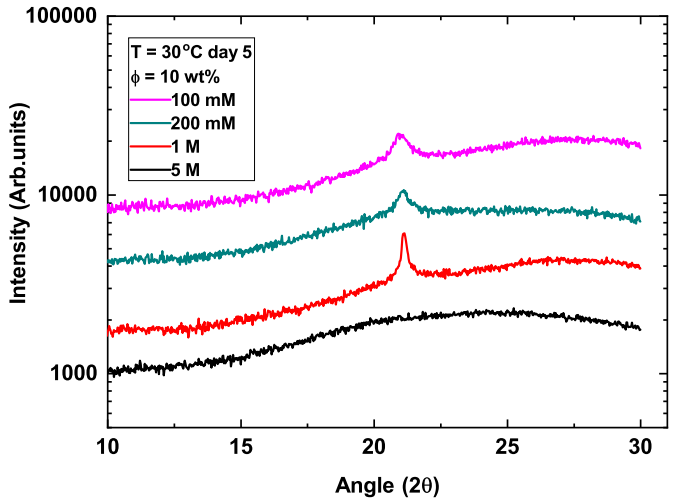

Figure 5.11: WAXS data of DMPC (10 wt%) as a function of acetic acid concentration at 30°C. Note that sample 5 M AA didn't show any wide angle peak for incubation of 2 days at 55°C

C_{aa}	T	Phase	d-spacing
500 mM Day15	30°C	L_β	7.08 nm
		L_I	3.16 nm
	40°C	L_β	6.90 nm
		L_I	3.16 nm
	50°C	L_α	8.09 nm
		L_I	3.12 nm
	60°C	L_α	12.93 nm
		H	5.91 nm
1 M Day 14	30°C	L_β	6.80 nm
		L_I	3.06 nm
	40°C	L_α	13.75 nm
		L_I	3.06 nm
	50°C	L_α	11.09 nm
		L_I	3.06 nm
	60°C	I	5.87 nm
5 M Day 16	30°C	I	6.30 nm
		L_I	3.12 nm
	40°C	I	8.23 nm
		L_I	3.12 nm
	45°C	I	7.71 nm
		L_I	3.12 nm
	50°C	I	8.07 nm
		L_I	3.12 nm
	60°C	L_I	8.07 nm

Table 5.3: Table showing d-spacings of different phases of DMPC obtained for different concentrations of acetic acid incubated at 55°C. L_β- lamellar gel phase, L_α-lamellar fluid phase,L_{IG}-Interdigitated phase,I-Isotropic phase, H- Hexagonal phase

5.2.3 WAXS studies

WAXS data obtained at 30°C for various acetic acid concentrations showed that all the samples except DMPC with 5M AA are in the gel phase (fig.5.11). This indicates that the pH of the solution is not playing any active role in the elevation of the transition temperature. In other words, if the elevation of transition temperature is merely due to the effect of reduction

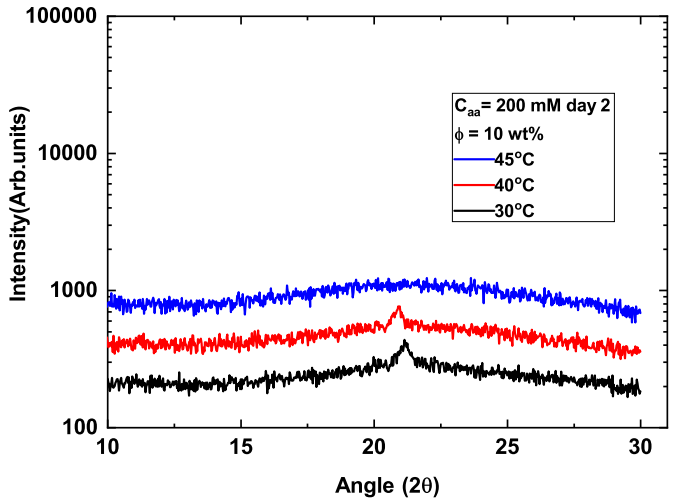

(a)

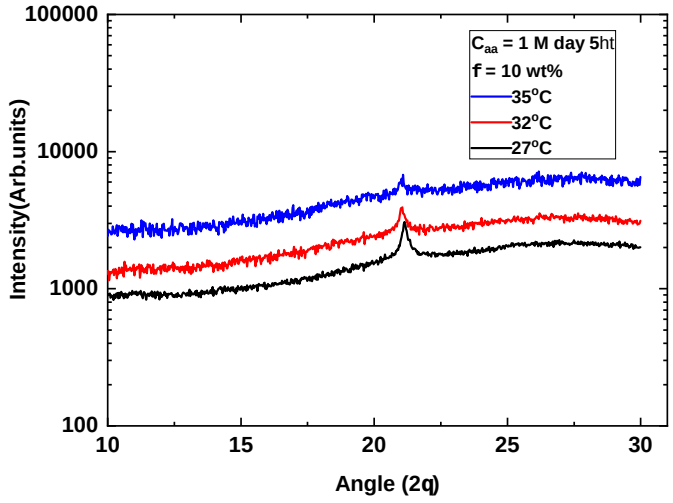

(b)

Figure 5.12: WAXS profiles of DMPC : AA samples at (a) 200 mM after 2 days and (b) 1 M after 5 days of incubation at 55°C

in the pH, then 5 M acetic acid, which has the least pH (2.01), should show a significant change in the transition temperature. Also, the single symmetric peak at 0.42 nm (fig.5.12) is similar to that of the gel phase induced by UMP, suggests that the chains are untilted in this gel phase. Hence we assume similar to the case of UMP, the adsorption-induced head group conformational changes could be one possible reason for the elevation of the transition temperature.

The non-monotonic shift in the gel-fluid transition temperature of DMPC with acetic acid concentration can be explained by invoking two simultaneous processes involved. The first

C_{aa}	T	d-spacing
100 mM (Day10)	25°C	0.418 nm
	30°C	0.420 nm
	35°C	0.421 nm
	40°C	0.425 nm
200 mM (Day10)	31°C	0.42 nm
	38°C	0.423 nm
	42°C	0.425 nm
500 mM (Day 14)	28°C	0.419 nm
		0.411 nm
		0.369 nm
	35°C	0.422 nm
		0.412 nm
		0.370 nm
	40°C	0.424 nm
		0.412 nm
		0.372 nm
	45°C	0.412 nm
		0.374 nm
	50°C	0.412 nm
		0.376 nm
5 M (Day 6)	30°C	0.411 nm
		0.369 nm
	35°C	0.411 nm
		0.370 nm
	40°C	0.412 nm
		0.372 nm

Table 5.4: Table showing wide peaks observed for gel phase and interdigitated phase formed by DMPC:AA samples

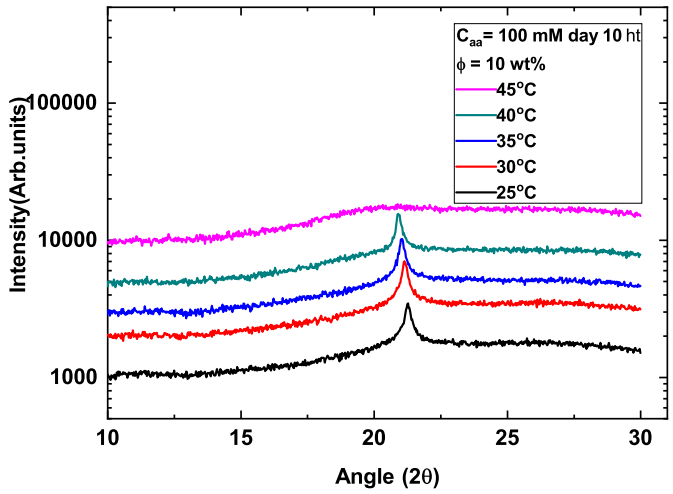

(a)

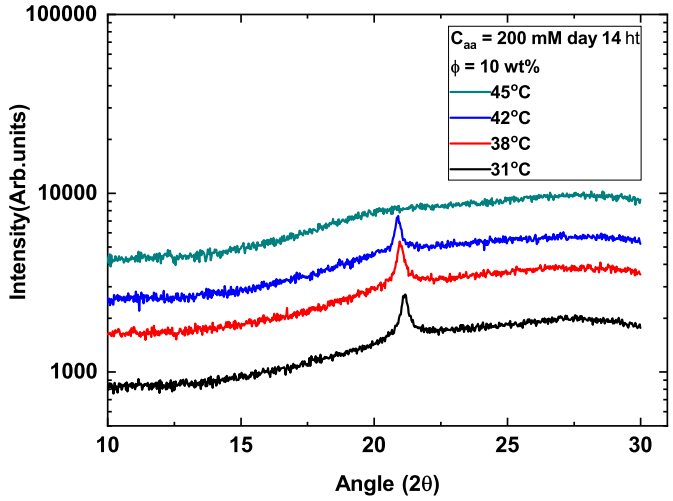

(b)

effect is the adsorption induced change in head group conformation. The second effect is the increased chain disordering and reduction in bilayer thickness with the adsorption of acetic acid. The competition between these two opposing effects decides the transition temperature of the phase. In the case of 5M acetic acid, the reduction in bilayer thickness is the largest (table.5.1) compared to the samples with lower AA concentrations.

The samples with AA concentration 500 mM and above showed the formation of the interdigitated phase and corresponding peaks in the wide-angle region (fig.5.13 and table.5.4). The melting transition temperature of the interdigitated phase induced by 5 M AA samples was found to change with incubation time. With 6 days of incubation, the sample showed a transition temperature below 45°C, whereas with further time, the transition shifts and

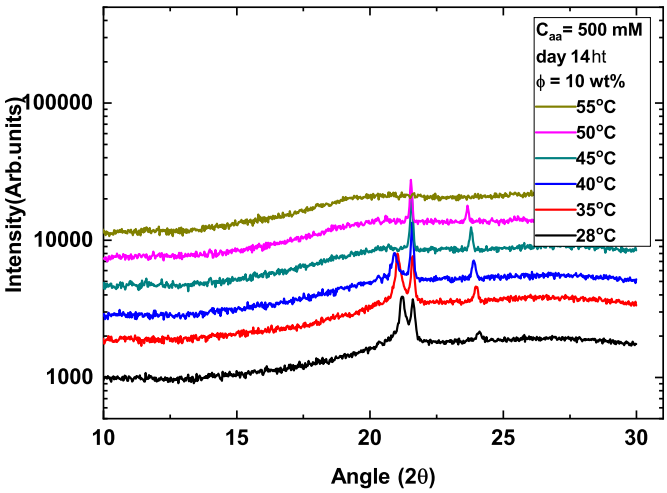

(c)

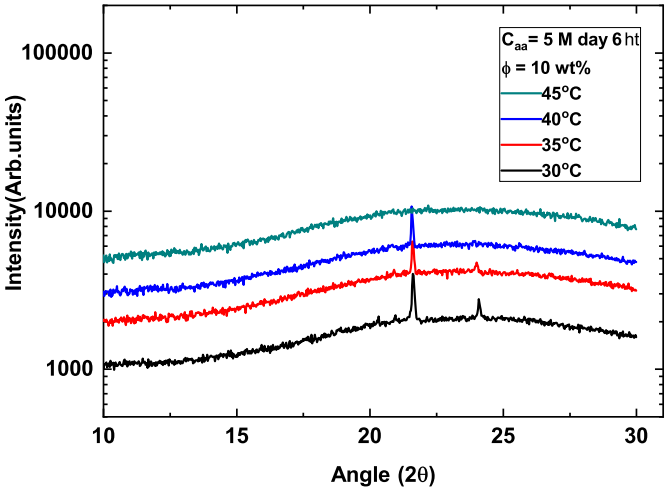

(d)

Figure 5.13: WAXS profiles of DMPC : AA samples at (a) 100 mM after 10 days and (b) 200 mM after 14 days (c) 500 mM after 14 days (d) 5 M after 6 days of incubation at 55°C

saturates 50°C. This effect is probably due to the long relaxation time scales needed for the sample to reach the equilibrium state. Once the system reaches the equilibrium the melting transition temperature of interdigitated phase is independent of AA concentration.

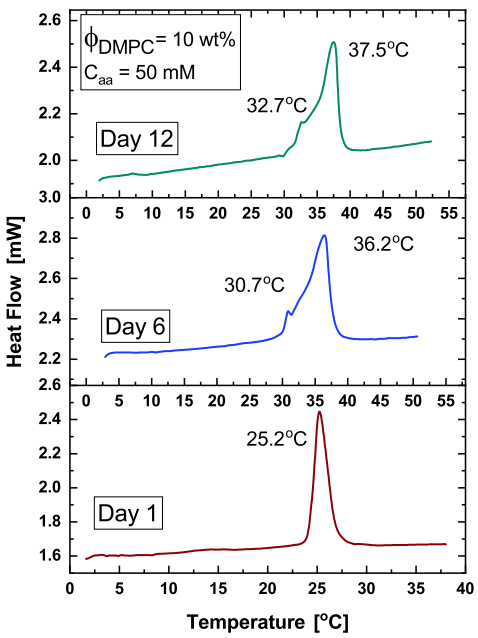

(a)

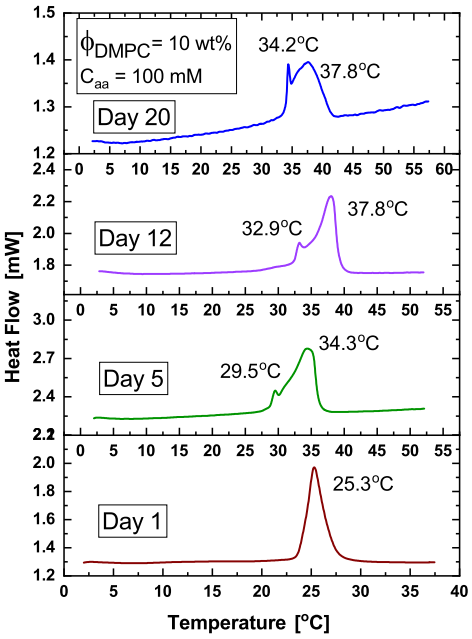

(b)

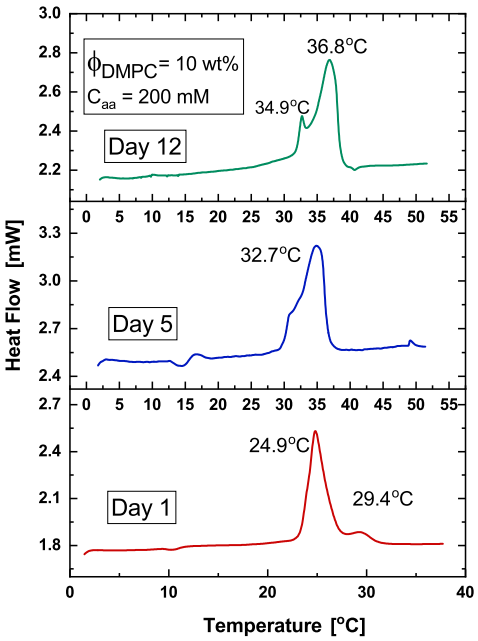

(c)

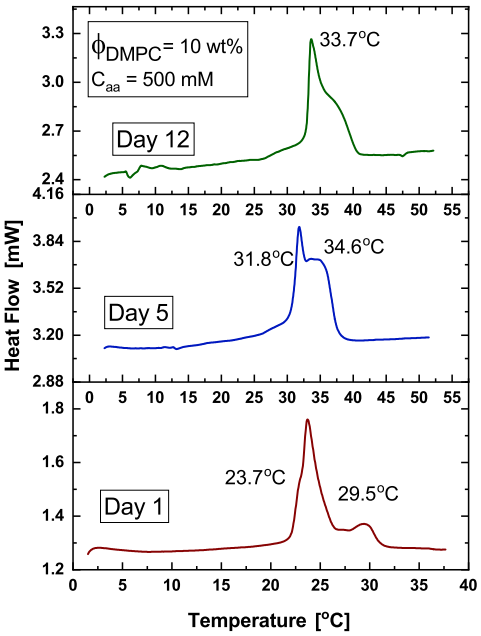

(d)

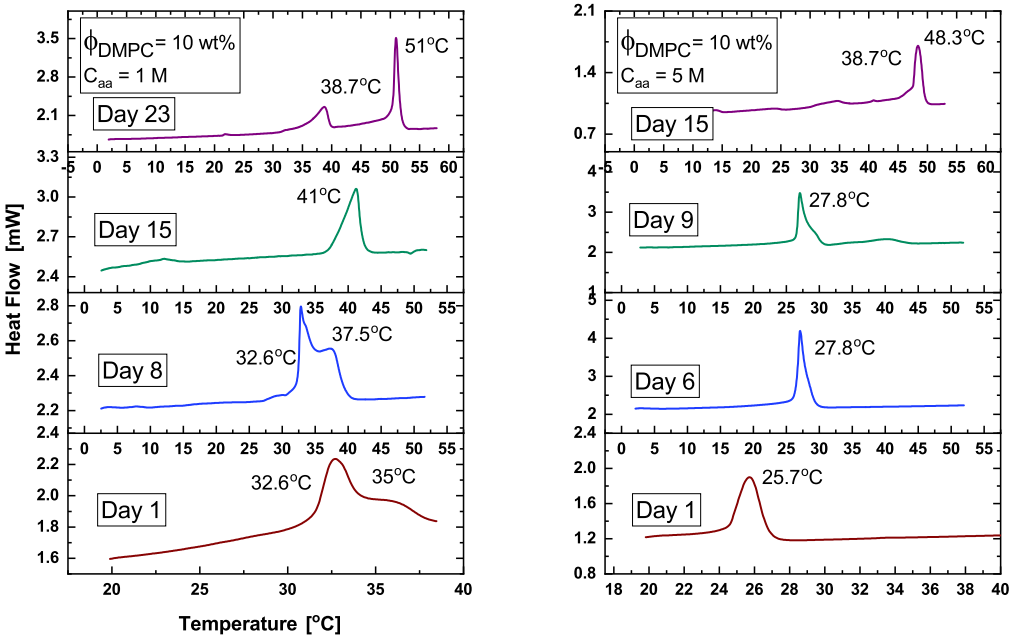

(e) (f)

Figure 5.14: DSC profiles of DMPC : AA samples (a) 50 mM (b) 100 mM (c) 200 mM (d) 500 mM (e) 1 M (f) 5M incubated at room temperature.

5.2.4 DSC studies

DSC studies were carried out only on samples incubated at room temperature. This is to avoid evaporation of the solvent when incubated at 55°C for long incubation times. The DSC curves obtained for samples with different acetic acid concentrations and for different incubation times are shown in fig.5.14. These results are in agreement with the WAXS data. The samples with lower AA concentration (50 mM and 100 mM) for short incubation time (Day1) do not show much change from pure DMPC in the main transition temperature, although the pre-transition is found to be absent. But 200 mM , 500 mM and 1 M AA samples showed a shift in gel phase transition temperature in the DSC thermogram from the first day of incubation . This difference in phase behavior between lower and higher AA samples is probably due to the low adsorption rate and the difference in number of acetic acid molecules in the solution. This behavior is consistent with the observation that lower AA concentration samples took a few days(2-6 days depending on the sample concentration) to become completely clear. With time, all the samples showed a shift in the main transition temperature. For a day of incubation, 1 M samples showed the maximum change in transition temperature. Similar to the behavior observed in SAXS and WAXS studies, 5 M sample shows not much change in the main transition temperature. Lower acetic acid samples were

only evaluated for 2 weeks since these samples do not show the formation of the interdigitated phase. With incubation of 9 days, the 5M AA sample showed the melting of the interdigitated phase at 40°C. With further incubation, this transition is shifted to 48°C. 1 M AA sample showed elevation of gel to the fluid phase transition to 41°C upon incubation of 15 days. With incubation of 23 days, the sample showed two transitions: one corresponding to the fluid to gel phase transition at 38°C and the other one corresponding to the melting of the interdigitated phase at 51°C , which suggests that these two phases coexist at low temperatures.

5.2.5 Raman Spectroscopy studies

Raman spectroscopy studies were done to probe the head group conformations in different phases. The spectra were collected over a range from 600 cm^{-1} to 3000 cm^{-1}. For the convenience of discussion, it is split up into three ranges. Assignment of Raman vibration bands of head group and chain regions of the lipid can be found in refs. [17, 18, 19, 20], and are also tabulated in chapter 2. The measurements were carried out on the gel phase of 1 M samples and the interdigitated phase of 5 M sample. The detailed analysis is described below.

Comparison of 1 M AA sample with pure DMPC

Raman spectra were taken at 32°C for both the samples. The 1 M AA sample was incubated at room temperature for 12 days and shows a gel to fluid transition temperature of 38°C. Pure DMPC is in the fluid phase at 32°C (fig.5.15).

1) 600- 1000 cm^{-1} region.

In the case of pure DMPC, at 32°C, a peak at 716 cm^{-1} corresponding to the gauche conformation of the O-C-C-N^+ in the headgroup region is observed [19]. In the case of 1 M AA samples, the adsorption of acetic acid induces a conformational change from gauche to trans and correspondingly a peak at 890 cm^{-1} is observed [19]. This indicates that an increase in acetic acid concentration increases the fraction of lipid molecules having trans conformation of the head group. Pure acetic acid shows two prominent bands in this range [21]. The more intense one is at 2940 cm^{-1} and the other at 890 cm^{-1}. The observed band at 890 cm^{-1} can have contributions both from pure AA and from the fraction of the O-C-C-N^+ group in the trans conformation. A comparison of the intensities of the observed peaks at 890 cm^{-1} and 2940 cm^{-1} in the spectra of DMPC-1MAA samples indicates that AA alone is not sufficient to account for the intensity of the sharp peak observed at 890 cm^{-1}. Hence there is a significant contribution from the trans isomers of the O-C-C-N^+ moiety in the headgroup. Also, the presence of the peak at 2940 cm^{-1} can be considered as a signature of acetic acid

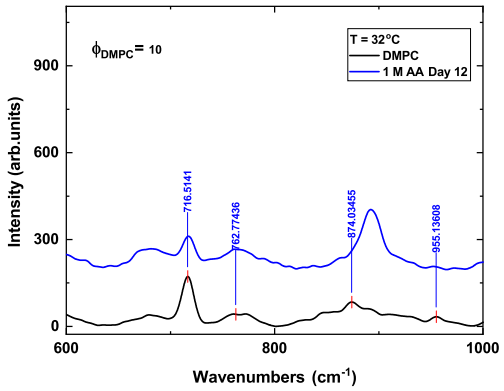

(a)

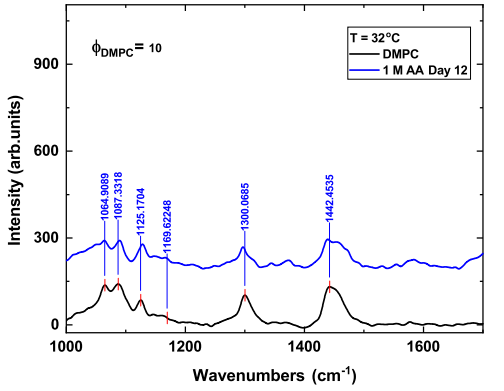

(b)

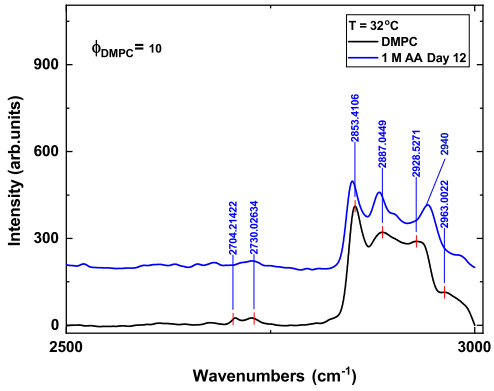

(c)

Figure 5.15: Comparison of Raman spectra of pure DMPC with samples having 1 M AA concentration at 32°C. The concentration of lipid in the solution is 10wt%.

in the complex [21].

2) 1000-1750 cm^{-1} region.

As mentioned before, in chapter2-Part2, 1000-1200 cm^{-1} bands correspond to the C-C

bond stretching vibrations. The bands at 1063 and 1128 cm^{-1} are assigned to the trans mode of C-C stretching, and the band at 1090 cm^{-1} indicate the gauche conformation of C-C bond stretching. The relative ratio between the trans to gauche conformations increases abruptly at the fluid to gel phase transition. The relative increase in the peak intensity of 1128 cm^{-1} band in 50 mM and 1 M AA samples indicates that both 50 mM and 1M AA samples are in the gel phase at this temperature.

Another important feature of the spectra found at 1736 cm^{-1} is assigned to the C=O vibration band of the glycerol backbone. In the case of lipid samples with acetic acid, there is a small shift in the peak position to lower values (1709 cm^{-1}), indicating the interaction of acetic acid with C=O bonds in the lipid [22]. The intensity of this band also increases with acetic acid concentration. The shift in the peak position would probably corresponds to increased hydrogen bonding of C=O groups of lipids either among themselves or with acetic acid. There are FTIR measurements that showed a shift in C=O vibrations corresponding to an increase in hydrogen bond interactions between the lipids [22]. But further experiments are needed to confirm this conclusion. The carbonyl stretching vibrations of acetic acid are centered around 1664 cm^{-1}.

3) 2500 cm^{-1} to 3000 cm^{-1} region.

Gel to the fluid phase transition temperature of the lipid can be detected from the methylene stretching bands at 2500 to 3100 cm^{-1} region. From the (fig.5.15), it can be seen that for pure DMPC, the bands at 2887 cm^{-1} and 2923 cm^{-1} are broader compared to those of 1M AA sample and which indicate that the DMPC bilayers are in the fluid phase in the absence of AA. The peak at 2940 cm^{-1} is assigned to methyl stretching vibrations of acetic acid.

Thermal phase behavior 1 M AA sample

Raman spectra of 1M DMPC samples incubated for 5 days at 55°C, were collected at three different temperatures is shown in fig.5.16. The transition temperature of this sample measured by the WAXS technique is around 37°C. At 35°C, the sample is in the gel phase, and at 46°C and 55°C the sample is the in the fluid phase. Raman spectra collected in this case are described below.

1) 600-1000 cm^{-1} region.

The O-C-C-N^+ bonds have more trans conformation compared to gauche conformation at all the temperatures. This indicates a change in head group conformation due to the adsorption of acetic acid.

2) 1000-1750 cm^{-1} region.

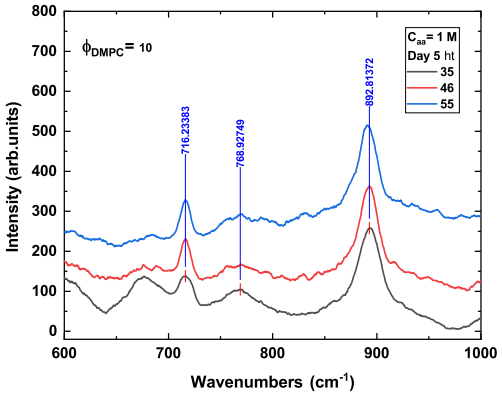

(a)

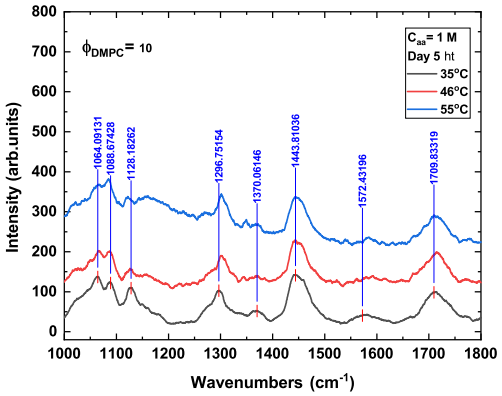

(b)

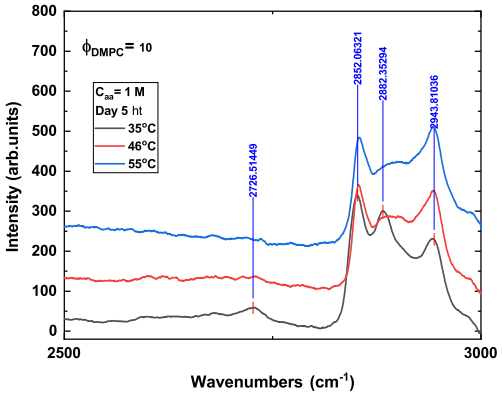

(c)

Figure 5.16: Raman spectra of DMPC:1M AA incubated for 5 days at 55°C) as a function of temperature

Bands in the 1000-1200 cm^{-1} range show a decrease in the trans to gauche conformation ratio of C-C bonds at 45°C and 55°C in comparison to 35°C. The peak at 1736 cm^{-1} corresponding to the C=O vibrational band has shifted to 1709 cm^{-1}. Hence with incubation

time as well as acetic acid concentration, the hydrogen bonding increases between acetic acid and lipids or between lipids, and these H-bonds are present even at higher temperatures in the fluid phase.

3) 2500-3000 cm^{-1} region.

Changes in spectral features in the 2500-3000 cm^{-1} bands at 45°C or 55°C indicate the formation of the fluid phase from the gel phase. The one extra sharp peak observed at 2943 cm^{-1} at all temperatures is assigned to the asymmetric stretching vibration of CH_2 groups of acetic acid.

Thermal phase behavior of the interdigitated phase of 5 M AA sample

The 5 M acetic acid sample incubated at 55°C for 15 days showed the interdigitated phase, which was confirmed by WAXS and SAXS studies. The melting temperature of the interdigitated phase is found to be around 55°C. Fig.5.17 shows the Raman spectra obtained this sample.

1) 600-1000 cm^{-1} region.

In the interdigitated phase of the 5M AA sample, O-C-C-N^+ groups showed a very strong peak at 890 cm^{-1}, corresponding to its trans configuration. The intensity of the band increases with increase in temperature below the melting transition of the interdigitated phase.

2) 1000-1750 cm^{-1} region.

The C-C stretching bands of the chain region at 1000-1200 cm^{-1} change only above 55°C and correspondingly represent the melting transition of the interdigitated phase. The band at 1297 cm^{-1} is sharper in the interdigitated phase and becomes broader in the fluid phase. The band at 1487 cm^{-1}, which is associated with the scissoring and twisting modes of methylene groups in the chain, represent the crystallinity of the interdigitated phase [23]. The relative intensity of shifted C=O vibrations is found to increase with temperature. There is a sudden increase in the intensity of this peak at 45°C, which is the melting transition of the coexisting gel phase.

3) 2500-3000 cm^{-1} region.

Intensities of bands at 2700-3000 cm^{-1} range changed abruptly at the transition of interdigitated gel to isotropic phase transition on heating at 55°C. The intensity of the band at 2940 cm^{-1} (represents the asymmetric stretching vibration of CH_2 groups of acetic acid)changes from 45°C on wards on heating.

Raman spectroscopy studies show that in the presence of acetic acid, the head group conformation changes as indicated by the shift in vibrations of O-C-C-N^+ group. In the

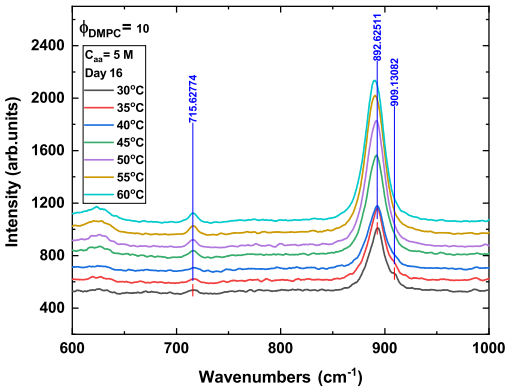

(a)

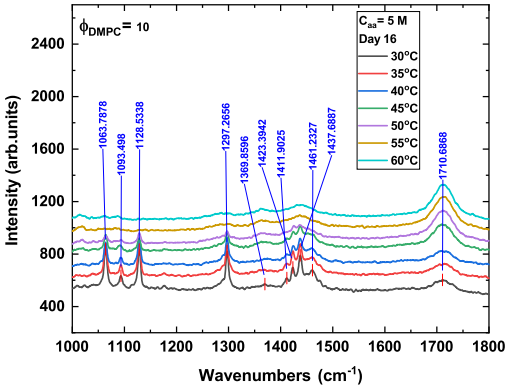

(b)

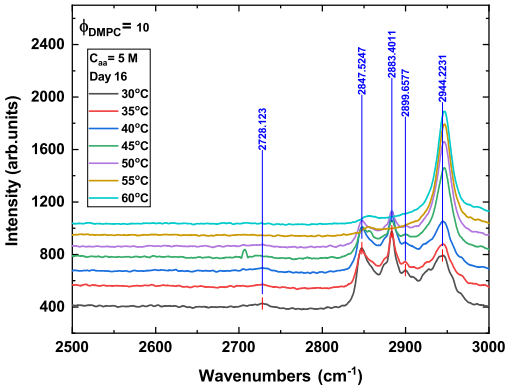

(c)

Figure 5.17: Raman spectra of DMPC:5M AA incubated for 15 days at 55°C as a function of temperature

presence of acetic acid, the carbonyl stretching vibrations of the glycerol backbone changes, which probably indicate the presence of increased hydrogen bonding between the head groups or interaction between acetic acid and the head group region.

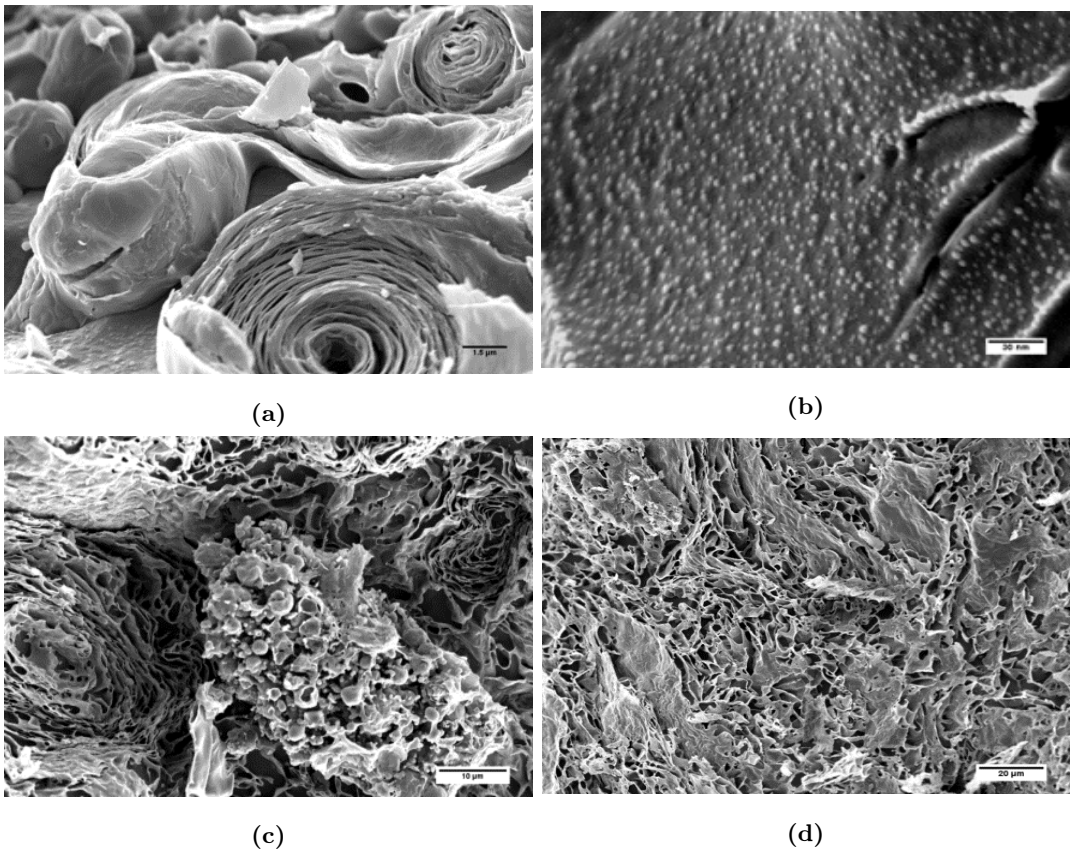

Figure 5.18: Cryo-SEM images obtained for DPPC in the presence of (a) 0 mM (scale bar 1.5 μm) and (b) 200 mM (scale bar 30 nm) (c) 500 mM (scale bar 10 μm) (d) 2M (20 μm) acetic acid solutions after a week of sample preparation.

5.3 Effect of acetic acid on phase behavior of DPPC

We have also studied the influence of acetic acid on DPPC (1,2-dipalmitoyl-sn-glycero-3-phosphocholine), which differs from DMPC in having two, 16 carbon saturated chains using cryo-SEM, SAXS, and WAXS. It is observed that even in the case of DPPC, the incorporation of acetic acid shifts the gel phase transition temperature. With long incubation, all the samples showed the formation of the interdigitated phase. Similar to the case of DMPC, 5M acetic acid has less effect on the transition temperature compared to 100 mM. In the presence of AA, the main transition temperature of DPPC phase was shifted to 55°C with incubation at 55°C. The interdigitated phase formed over incubation is found to melt at 60°C.

5.3.1 SAXS and Cryo-SEM studies

In contrast to DMPC, even in the case of 100 mM AA, DPPC readily forms a clear solution upon hydration, indicating that the adsorption of acetic acid on the bilayer. Cryo-SEM images taken showed the presence of small vesicular structures along with the lamellar phase. Lower

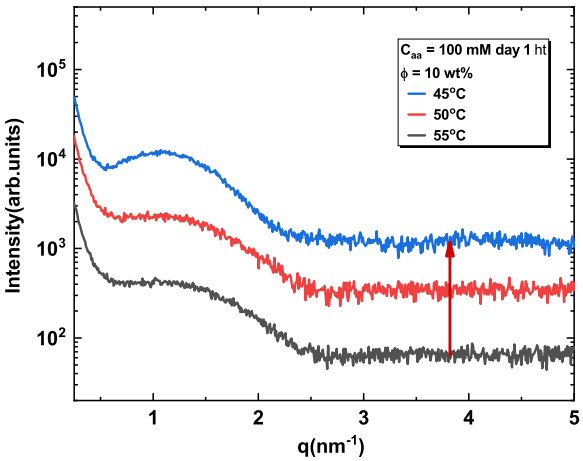

(a)

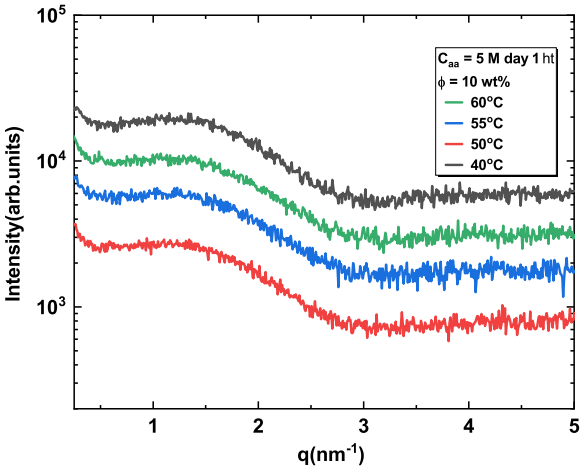

(b)

Figure 5.19: SAXS patterns of DPPC lipid at (a) 100 mM and (b) 5 M acetic acid concentrations after 1 day of sample preparation. These patterns correspond to the form factor of the bilayer. Also 100 mM AA sample showed a change in diffraction pattern at 45°C on heating whereas 5 M AA sample showed no change.

concentration of (200 mM) AA showed a significant fraction of small vesicular structures (fig.5.18). Initially, the SAXS profile of samples showed a diffraction pattern corresponding to the form factor of the bilayer. Fig.5.19 shows diffraction patterns obtained for DPPC with 100 mM AA and 5 M AA for a few temperatures. Similar to the case of DMPC, 100 mM AA showed a change in the diffraction pattern at 45°C. The transition temperature of pure DPPC is 42°C. But 5 M AA: DPPC shows no change in diffraction pattern even at 40°C, which indicates a lowering of the transition temperature. The samples incubated at 55°C showed the presence of a swollen lamellar phase below the corresponding transition temperatures

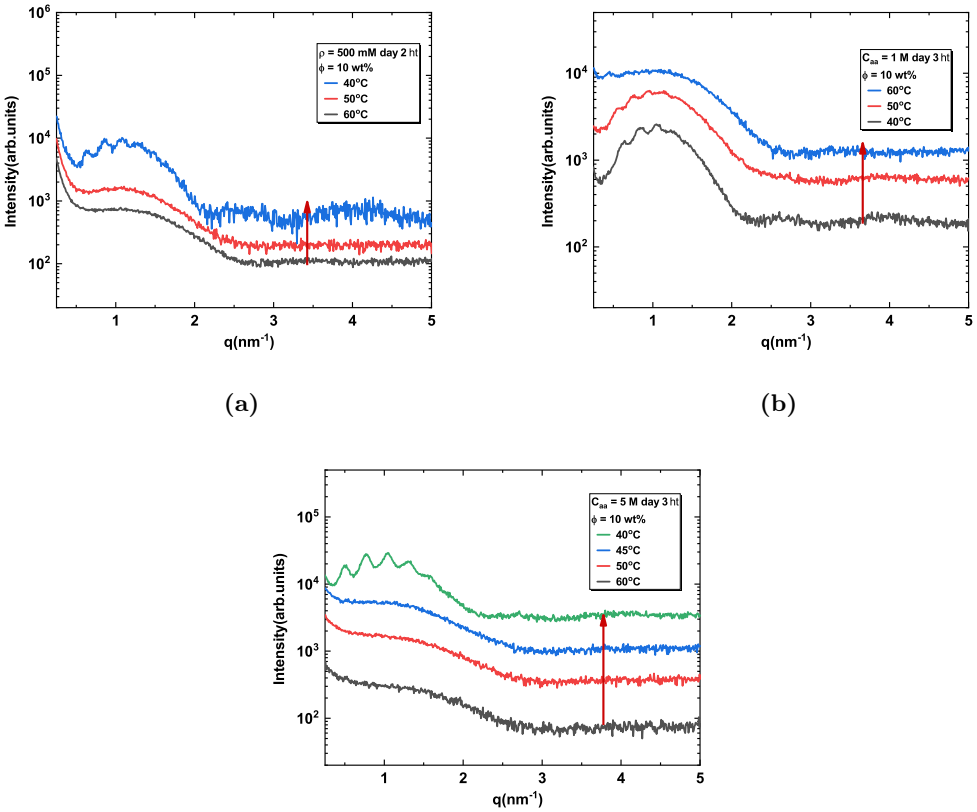

Figure 5.20: SAXS patterns of DPPC lipid at (a) 500 mM and (b) 1 M (c) 5 M acetic acid concentrations after 2-3 days of sample preparation, on incubation at 55°C showing swollen lamellar phase. The red arrow in the figure indicates the direction of temperature change.

of samples, which depends on the incubation period. The presence of multiple orders of diffraction peaks in the SAXS pattern indicates the electrostatically stabilized lamellar phase. On day 3 of incubation, 5 M AA also showed the presence of a swollen lamellar phase at 40°C. The d-spacings of 1 M and 5 M samples respectively are 30.6 nm and 23.2 nm (fig.5.20).

5.3.2 WAXS studies

The WAXS patterns obtained for DPPC: AA samples incubated for different periods of time are shown in fig.5.21. Compared to the DPPC gel phase wide-angle peaks, DPPC: AA samples showed sharper symmetric peaks similar to those found in DMPC: UMP and DMPC: AA samples. Although in the case of the 1M sample, the peak is very clean and sharp, lower concentrations showed more complex peak profiles. Hence it is not clear from the current data set whether the samples are forming a completely untilted gel phase. But in the case of a 1M sample, the gel phase is clearly untitled because of the sharp symmetric wide-angle peak

centered at 0.423 nm. 5 M acetic acid showed the presence of two sharp peaks in the wide-angle. A weak peak at 0.423 nm and a much stronger peak at 0.415 nm. This might indicate the coexistence of gel and interdigitated phases since the first peak of the interdigitated phase appears at 0.41 nm. The SAXS and WAXS patterns of 1M AA sample incubated for 20 days show the formation of the interdigitated phase with a d-spacing of 3.6 nm (fig.5.22 and table.5.5). The slight increase in the d-spacing of the interdigitated phase compared to that of DMPC is due to the increased chain length of DPPC. The wide-angle peaks could not be indexed to any lattice due to the presence of extra weak peaks at 0.436 nm and 0.421 nm.

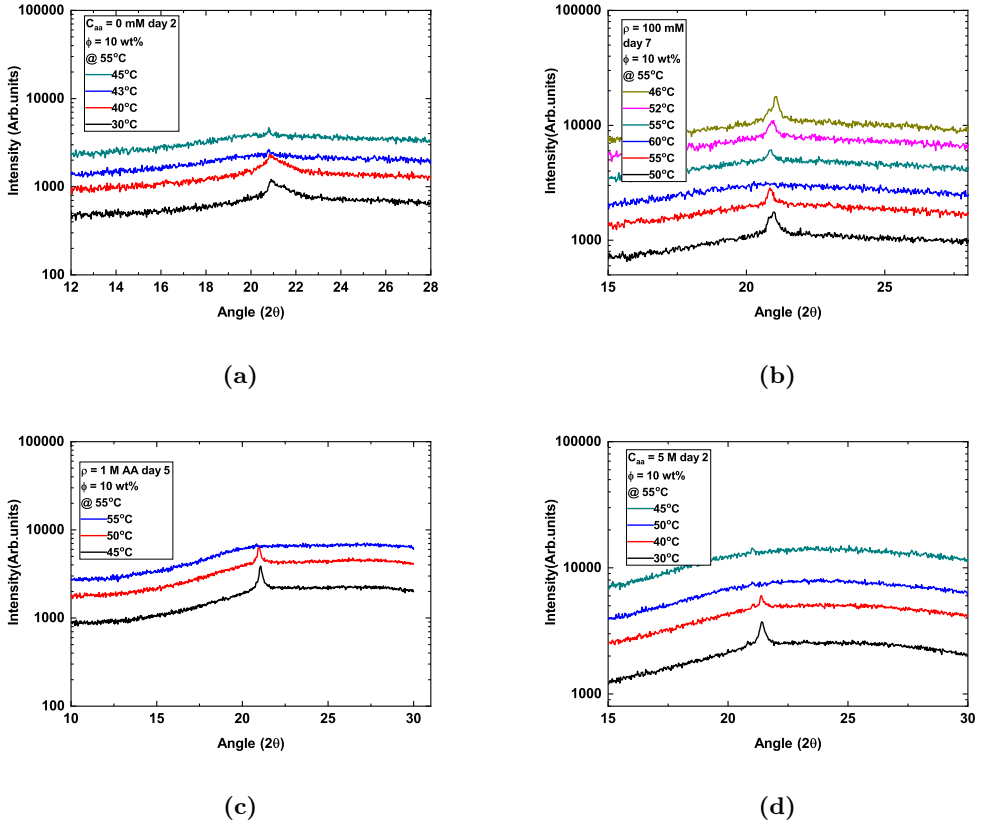

Figure 5.21: WAXS patterns of DPPC lipid at (a) 0 mM (Pure DPPC) and (b) 100 mM (c) 1 M (d) 5 M acetic acid concentrations incubated at 55°C.

Wide-angle x-ray scattering was done on aligned multilayer stacks of DPPC with 1M AA (fig.5.23). The interdigitated phase formed in the sample vial after incubation for 14 days, was coated on the glass substrate and hydrated for a day. The wide-angle features obtained were very similar to the case of DMPC: UMP system, as discussed in chapter 2. Multilayers showed the coexistence of the gel phase with an interdigitated phase at 45°C. Wide-angle peaks observed are therefore corresponding to an untitled gel phase and tilted interdigitated phase. The presence of many wide-angle peaks, as well as their tiny spot like nature observed

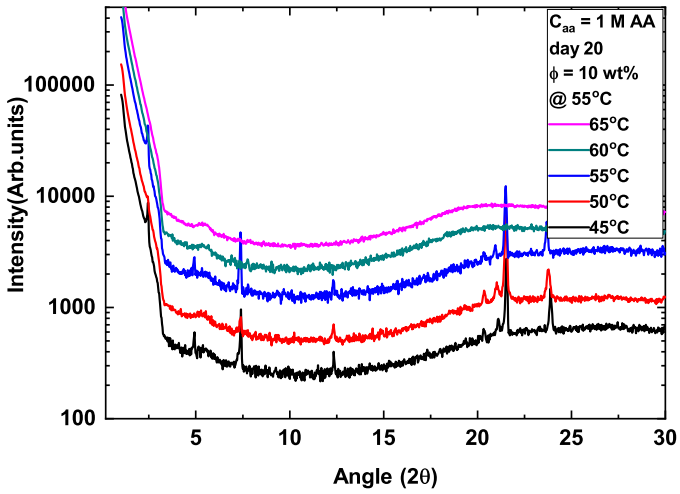

Figure 5.22: XRD pattern obtained for DPPC: 1M AA sample incubated at 55°C for 20 days showing formation interdigitated phase.

T (°C)	d spacing/ lattice parameter (nm)	
	SA	WA
45	3.59	0.41, 0.37 (0.436, .0421)
50	3.59	0.41, 0.37 (0.436, 0.42)
55	3.59	0.41,0.37 (0.436, .042)

Table 5.5: Small angle and wide angle peak positions obtained for 1 M AA samples incubated for 20 days. 0.41 nm and 0.37 nm represent the two major peaks from the interdigitated phase (peaks at 0.436 nm and 0.421 nm represent weakly intense peaks from the interdigitated phase).

in the aligned sample, suggests a 3D crystalline nature of the interdigitated state.

5.4 Discussions

Effect of the interaction of AA on the structure and phase behavior of PC lipid bilayers were studied using different experimental techniques. In the presence of AA, in the fluid phase, DMPC lipid bilayers showed thinning of the membrane in an AA concentration-dependent manner. 5 M AA samples showed the most thinning of the bilayer. All the samples except 5 M AA, showed a large change in the main transition temperature initially. This means that the pH is not playing any role in the elevation of the main transition temperature. WAXS and DSC studies confirm the stabilization of the gel phase above the T_m of pure DMPC. All the samples showed the presence of a swollen lamellar phase initially resulting from the

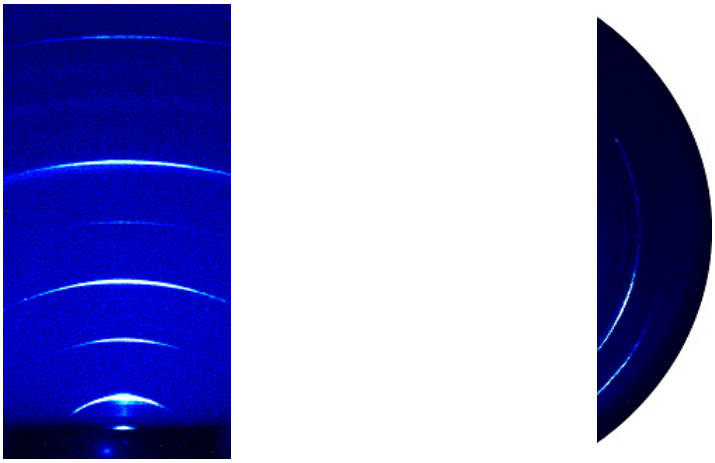

(a) **(b)**

Figure 5.23: Aligned x-ray diffraction data of DPPC:1 M AA at interdigitated phase (a) SAXS region showing peaks corresponding to a lamellar interdigitated phase with d-spacing 3.6 nm and (b) WAXS region showing two off-axis peaks arising from tilted chains of interdigitated phase

charging of the membranes due to the adsorption of dissociated AA molecules. With further incubation (200mM as well as 1M AA samples), the d-spacing of the gel phase comes down to 6.85 nm, which is only 0.5 nm more than that of DMPC in the gel phase. In this phase, the charge on the bilayer is negligible. We presume that in this phase, all the dissociated acetic acid molecules on the membrane are replaced by undissociated acetic acid molecules from the solution. The EDPs obtained from the gel phase confirms the presence of AA molecules at the bilayer interface. This gel phase melts into a fluid phase above 40°C. The fluid phase has a periodicity of 15 nm at 60°C. The presence of just one or two peaks and their relatively large widths indicate that this swollen phase is not electrostatically stabilized but is undulation stabilized. With further incubation over two weeks, 500 mM and 1M AA samples showed the formation of the interdigitated phase. 200 mM sample showed the formation of the interdigitated phase after incubation for 28 days. Still lower concentrations do not show the formation of the interdigitated phase within 30 days. The 5 M AA samples readily form the interdigitated phase on incubation for a week at 55 °C. It was seen that the melting temperature of interdigitated phase changes with incubation time initially and saturates at 50°C. The interdigitated phase melts into an isotropic phase in the case of 5 M AA and hexagonal phase in the case of 1 M and 500 mM AA samples, similar to the cases of 1:1 and 5:1 DMPC: UMP samples, respectively. In the case of 5:1 DMPC: UMP sample, the hexagonal phase was found at different levels of hydrations, i.e., from excess water to the

aligned sample, which suggests that this phase is inverted.

Acetic acid-induced changes in the phase behavior are also observed in the case of DPPC lipid bilayers. The samples showed the formation of a swollen lamellar phase to start with indicating the adsorption of charged acetic acid molecules. WAXS studies showed a shift in the gel phase transition temperature of DPPC to 55°C with incubation over a week for 100 mM AA concentration. 5 M AA induces interdigitation of DPPC samples readily on incubation for 3-4 days. The WAXS peaks from the interdigitated phase could not be were not indexed into any lattice. WAXS studies done on aligned multilayer stacks of DPPC: 1 M AA showed coexistence of tilted interdigitated phase with an untilted gel phase similar to the case observed with UMP. The interdigitated gel phase in the aligned XRD pattern showed two off-axis peaks in the wide-angle region.

Raman spectroscopy studies done on DMPC: AA samples showed a change in head group conformation with AA concentration. The O-C-C-N^+ bond was found to change from trans to gauche in the presence of AA. This corresponds to a change in the head group conformation from being parallel to the bilayer plane to a perpendicular configuration. Similar to the case found with UMP, this change in head group conformation results in a reduction in the head group area, thereby an increased van der Waals interaction between the chains, which resulted in the observed elevation of the gel phase transition temperature. The interdigitated phase formed by the DMPC: AA is found to be similar to that of DMPC with UMP. The formation of the interdigitated phase is most probably stabilized by dipole-dipole interaction between adjacent lipid head groups from two nearby bilayers. Further work is needed to characterize the structure of this phase completely.

5.5 Conclusion

Acetic acid is found to adsorb to PC lipid bilayers. This modifies the structure and phase of the behavior of PC bilayers. In the presence of higher concentrations of acetic acid, bilayers readily form an interdigitated phase upon incubation, which melts into a hexagonal phase on heating.

Bibliography

[1] H. Matsuki, M. Goto, K. Tadai, and N. Tamai. Thermotropic and barotropic phase behavior of phosphatidylcholine bilayers. *Int. J. Mol. Sci*, 14(2):2282–2302, 2013.

[2] J. N. Israelachvilli. *Intermolecular and surface forces*. Elsevier, third edition, 2014.

[3] M. Goto, M. Kusube, N. Tamai, H. Matsuki, and S. Kaneshina. Effect of hydrostatic pressure on the bilayer phase behavior of symmetric and asymmetric phospholipids with same total chainlength. *Biochem. Biophys. Acta*, 1778(4):1067–1078, 2008.

[4] K. Lai, B. Wang, Y. Zhang, and Y. Zhang. Md simulations showed that transition temperature of dppc increases with pressure. *Phys. Chem. Chem. Phys.*, 14:5744–5752, 2012.

[5] R. Koynova and M. Caffrey. Phase and phase transitions of phosphatidylcholines. *Biochem. et. Biophys. Acta*, 1376:91–145, 1998.

[6] Z. W. Yu and P. T. T. Quinn. The modulation of membrane strucutre and stability by dimethyl sulphoxide (review). *Mol. Membr. Biol.*, 15:59–68, 1998.

[7] Z. W. Yu and P. J. Quinn. Phase stability of phosphatidylcholine in dimethylsulfoxide solutions. *Biophys. J.*, 69:1456–1463, 1995.

[8] R. N. Lewis R. N. McElhaney M. G. Benesch, D. A. Mannock. A calorimetric and spectroscopic comparison of the effects of lathosterol and cholesterol on the thermotropic phase behavior and organization of dipalmitoylphosphatidylcholine bilayer membranes. *Biochemistry*, 50(46):9982–9997, 2011.

[9] L.Lindahl, S. Genheden, L. A. Eriksson, L. Olsson, and M. Bettiga. Sphingolipids contribute to acetic acid resistance in zygosaccharomyces bailii. *Biotechnol. Bioeng.*, 113(4):744–753, 2016.

[10] Y. Chen, K. Gozzi, F. Yan, and Y. Chai. Acetic acid acts as a volatile signal to stimulate bacterial biofilm formation. *mBio*, 6:e00392–15, 2015.

[11] T. X. Xiang and B. D. Anderson. Permeability of acetic acid across gel and liqqid crystalline lipid bilayers conforms to free-surface area theory. *Biophys. J*, 72(1):223–237, 1997.

[12] T. X. Xiang and B. D. Anderson. Phospholipid surface density determines the partitioning and permeability of acetic acid in dmpc:cholesterol bilayers. *J. Membr. Biol.*, 148(2):157–167, 1995.

[13] M. Orsi, W. E. Sanderson, and J. W. Essec. Permeability of small molecules through a lipid. *J. Phys. Chem. B*, 113(4):744–753, 2016.

[14] S.T-Nagle, Y. Liu, J. Legleiter, and J. F. Nagle. Structure of gel phase dmpc determined by x-ray diffraction. *Biophys. J*, 83:3324–3335, 2002.

[15] R. Krishnaswamy, S. K. Ghosh, S. Lakshmanan, V. A. Raghunathan, and A. K. Sood. Phase behavior of concentrated aqueous solutions of cetyltrimethylammonium bromide (ctab) and sodium hydroxy naphthoate (shn). *Langmuir*, 23:10439–10443, 2005.

[16] R. Koynova and B. Tenchov. *Encyclopedia of Biophysics : Chapter -Phase Transitions and Phase Behavior of Lipids*. Springer Science and Business Media, 2008.

[17] K. Czamara, K. Majzner, M. Z. Pacia, K. Kochan, A. Kaczor, and M. Baranska. Raman spectroscopy of lipids: a review. *J. Raman Spectrosc.*, 83(6):4–20, 2014.

[18] B. Maherani, E. Arab-Tehrany, E. Rogalska, B. Korchowiec, A. Kheirolomoom, and Michel Linder. Vibrational, calorimetric, and molecular conformational study on calcein interaction with model lipid membrane. *J Nanopart. Res.*, 15(1792):1–17, 2013.

[19] A. Fasanellaa, K. Cosentinob, A. Beneducib, G. Chidichimob, E. Cazzanellia, R.C. Barberia, and M. Castriota. Thermal structural evolutions of dmpc-water biomimetic systems investigated by raman spectroscopy. *Biochim. Biophys. Acta*, 1860:1253–1258, 2018.

[20] H. Akutsu. Direct determination by raman scattering of the conformation of the choline group in phospholipid bilayers. *Biochemistry*, 20:7359–7366, 1981.

[21] F. Wan, L. Du, W.Chen, P. Wang, J. Wang, and H. Shi. A novel method to directly analyze dissolved acetic acid in transformer oil without extraction using raman spectroscopy. *Energies.*, 10(7):967–990, 2017.

[22] D.J. Siminovitch, P. T. T Wong, and H. H. Mantsch. Effect of cis and trans unsaturation on the structure of phospholipid bilayers : A high pressure infrared spectroscopic study. *Biochemistry*, 26:3277–3287, 1987.

[23] D.J. Siminovitch, P. T. T Wong, and H. H. Mantsch. High pressure infrared spectroscopy of ether and ester linked phosphatidylcholine aqueous dispersions. *Biophys. J.*, 51:465–473, 1987.

Chapter 6

Direct imaging of rippled structures of lipid-cholesterol membranes using Cryo-SEM and AFM

6.1 Introduction

Lipids in a eukaryotic cell are classified into three major categories: glycerophospholipids, sphingolipids, and cholesterol [1]. Depending on the head group regions, glycerophospholipids are categorized again into phosphoethanolamine, phosphatidylcholine, and phosphorylserine groups. The hydrophilic headgroup regions of these molecules are connected via an ester linkage to two hydrophobic alkyl chains of varying length (16-20 carbons), one of which usually is unsaturated. Sphingolipids have a more complex structure formed from a sphingosine based backbone, which is linked to a second fatty acid chain through an amide bond. Both of the acyl chains are usually saturated and can contain a maximum of 24 carbons. The head group region usually contains ethanolamine or serine or choline groups. The third category, which forms 30-40% of total lipid concentration in almost all cell types of vertebrates, is cholesterol fig.(6.1). It belongs to the family of aromatic polycyclic molecules called sterols. Cholesterol has a planar rigid aromatic core with an iso-octyl chain that forms the hydrophobic part and an OH group at the other end that forms a small hydrophilic head group. Unlike other lipids, cholesterol does not form any self-assembled structures. Most of the cholesterol content in our body is present in various cell membranes at different concentration levels. Being one of the main constituents of cell membranes, the major biological functions of cholesterol has to do with the activities of the membrane itself.

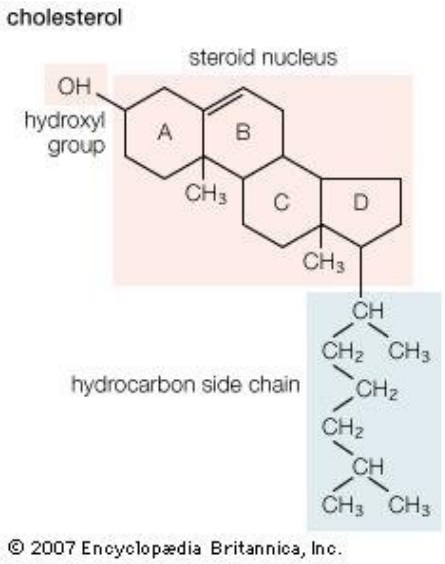

Figure 6.1: Structure of cholesterol

A lot of studies that explored the interaction of cholesterol with a lipid membrane have indeed shown that cholesterol plays significant role in maintaining rigidity and permeability of the membranes [5, 6]. In this context the influence of cholesterol on the phase behaviour of model bilayer systems made up of different lipids has been a subject of numerous studies [6, 7, 8, 9, 10, 11, 12, 13]. DSC studies showed that the incorporation of cholesterol to different PC lipid membranes leads to the broadening and eventual disappearance of the gel to fluid phase transition [8]. It was also found that the effect of cholesterol on the thermotropic behaviour of different lipids mainly depends on the phospholipid polar head group and unsaturation in the chain region [1]. In fluid bilayers, the affinity of cholesterol to interact with different lipids vary in the order sphingomyelin > PC > PE. Cholesterol is also found to discriminate the acyl chain region of lipids as well [14]. The unsaturated lipids are found to have lesser interaction with cholesterol in comparison to saturated ones. At lower concentrations(<20 mol%), cholesterol significantly affects the ripple phase behavior of saturated lipid.

When incorporated in both fluid and gel phases of PC lipids, above certain threshold concentration, cholesterol was found to induce liquid-ordered phase(L_o) which is characterised by orientational order, lateral mobility, rigidity and permeability in between the two phases whereas rotational diffusion same as that in the fluid phase [1]. This can be considered as the reason for the overall phase homogeneity of cell membranes despite being a mixture of higher melting sphingolipids (T_m = 37°C) and lower melting unsaturated glycerophospholipids. In fact removal of cholesterol from cell membranes results in the formation of phase-separated micro-domains similar to fluid(L_α or L_d) and gel(L_β) phase [15]. Cholesterol in a way sup-

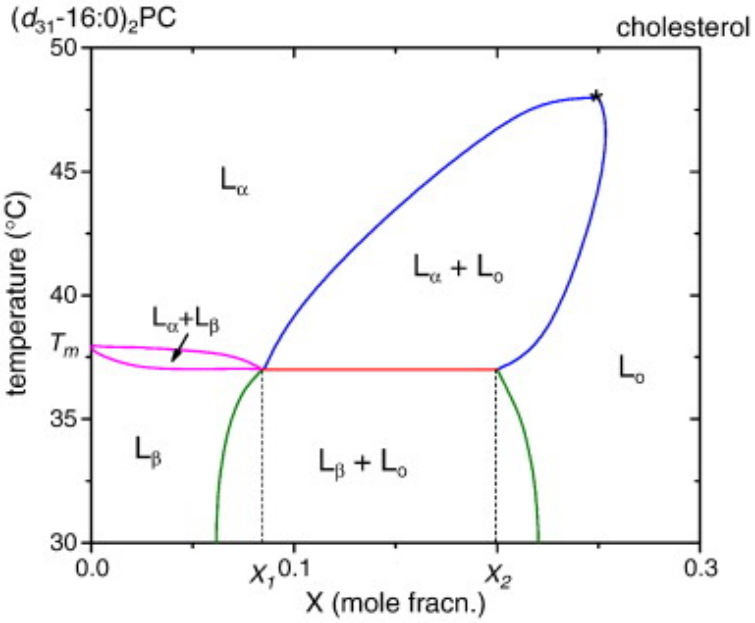

Figure 6.2: Generic phase diagram for binary mixtures of a single lipid with cholesterol dispersed in excess water. Phase boundaries are those for chain-perdeuterated dipalmitoylphosphatidylcholine, (d31-16:0)2PC [2, 3]. L_β, gel phase; L_α, fluid (disordered) phase; Lo, liquid-ordered phase. Single-phase regions (L_α, L_β, L_o) and two-phase regions (L_β +L_α, L_β + L_o, L_α + L_o) are indicated. Reproduced from [4]

press the L_α-L_β phase separation and promote L_o-L_d two fluid phase coexistence [1].

The liquid-ordered phase induced by cholesterol in different lipids has aroused huge interest among biophysicists due to their intrinsic features similar to the heterogeneities called rafts in cell membranes. Rafts are compositional heterogeneities embedded in the pool of lipids in cell membranes. They have increased cholesterol and sphingomyelin concentrations compared to the rest of the membrane. These heterogeneities are speculated to act as signaling junctions for various biochemical processes, including GPI anchored protein involved signal transduction and intercellular signalling [16, 17]. The liquid-ordered phase is found to have area per lipid less than that of the fluid phase and hence is thicker than the latter [10, 18]. In addition to the higher concentration of cholesterol and sphingolipid, these differences are also assumed to help certain membrane activities. Since none of the fluorescence experiments on cell membranes revealed raft-like structures, the formation and functions of rafts remain disputed despite the existence of several unambiguous evidences for the induction of the liquid-ordered phase by cholesterol and similar sterols in PC bilayers.

6.1.1 Phase behavior of lipid bilayers in the presence of cholesterol

The structural features of embedding biomolecules play major roles in the resulting phase behaviour of lipid bilayers. The effect of cholesterol on the phase behavior of single and mixed lipid bilayers has been the subject of different experimental studies. NMR and spectroscopic studies done on binary mixtures of lipid with cholesterol have shown fluid-fluid phase coexistence fig(6.2) above the main-transition temperature, T_m of the lipid for cholesterol concentration above 5 mol% [2, 19]. Below T_m, L_o, and L_β phases are found to coexist. Below 5 mol %, cholesterol has a very minor effect on the thermotropic transitions of the lipid. But several studies have shown that cholesterol significantly affects the ripple phase behaviour of saturated lipids. Above 20-25 mol% of cholesterol concentration, the main transition is completely abolished, and the liquid-ordered state is stabilized. These results showed the possibility of two-phase coexistence in a binary system. But direct observational tools like fluorescence microscopy and x-ray or neutron diffraction [20, 21, 10, 22] did not show phase separation in binary mixtures above T_m of the lipid. Ternary mixtures consisting of a saturated and an unsaturated lipid and cholesterol showed fluid-fluid coexistence below T_m of the higher melting lipid [23, 24]. Although the phase diagrams obtained from different techniques do not agree well with each other, all the experiments do show the formation of liquid-ordered phase, and the abolishing of the fluid to gel transition at high concentration of cholesterol.

The condensing and thickening of bilayers in the L_α phase to form the L_o phase in the presence of cholesterol is largely accounted for by the structure of cholesterol, which consists of a planar rigid core and a small hydrophilic head group region. The preferred configuration of cholesterol in lipid bilayers is side by side arrangement near to a lipid parallel to the layer normal, which significantly alters the lipid chain configuration.

6.1.2 Previous studies on ripple phase of PC bilayer

Phosphatidylcholines (PC) are by far the most widely studied class of lipids, due to their prevalence in many biological membranes [25]. PCs with saturated chains generally exhibit three different bilayer phases as a function of temperature at high hydrations [26]. The fluid (L_α) phase occurs above T_m and is characterized by a large head group area, high lateral diffusion, and high chain flexibility. T_m is also known as the chain-melting transition temperature. Below the pre-transition temperature T_p, the gel ($L_{\beta'}$) phase is formed, where the chains order on a two-dimensional crystalline lattice [27]. In the case of PC lipids with saturated chains, the long-axis of the chains is tilted with respect to the bilayer normal, due

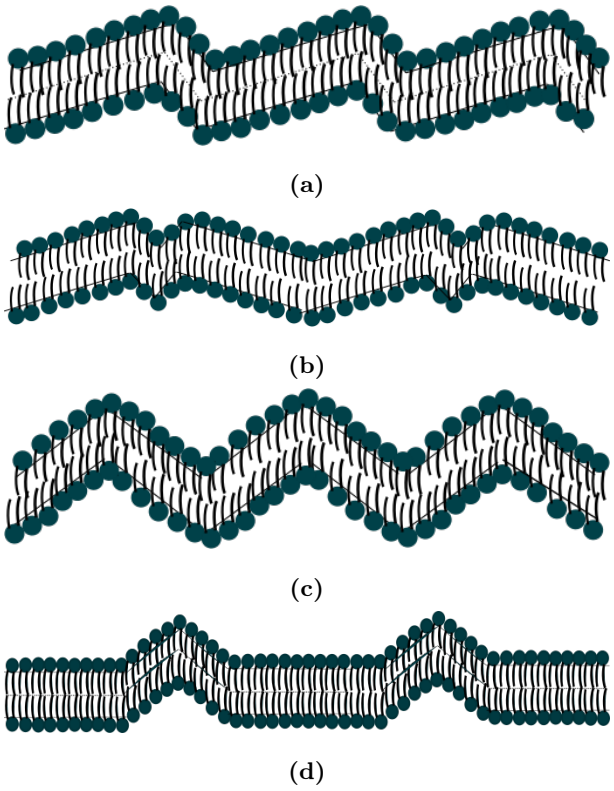

Figure 6.3: Schematic of different ripple structures reported in the literature. (a) asymmetric ripples with saw-tooth height profile ($\Lambda/2$ ripples), (b) symmetric metastable ripples with twice the wavelength of the former, observed on cooling from the fluid phase (Λ ripples), (c) symmetric ripples with shorter wavelength observed in lipid-cholesterol membranes and (d) long-wavelength ripples observed in lipid-cholesterol membranes.

to the larger cross-sectional area of the headgroup compared to the chains. In between T_p and T_m, a modulated phase, called the ripple ($P_{\beta'}$) phase, is observed. This phase is characterized by one-dimensional height and thickness modulations of the bilayer.

The first systematic x-ray diffraction study of the ripple phase was carried out by Tardiau et al. [28]. This phase is found to be characterized by a two-dimensional oblique lattice. Electron density maps (EDM) of this phase determined from the diffraction data show that the bilayers have a sawtooth-like height profile, with a wavelength of about 15 nm and an amplitude of about 1.5 nm. Subsequent diffraction studies drew attention to the thickness modulation of the bilayers accompanying their height modulation [29, 30, 31]. It is found that the minor arm of the ripple is thinner than its major arm. In the major arm, the chains are more ordered as in the gel phase, whereas in the minor arm, they are disordered akin to the fluid phase. In conformity with these results, Nuclear magnetic resonance (NMR) studies show the presence of two different molecular conformations in the ripple phase, similar to those in the fluid and gel phases [32]. Diffusion experiments reveal two values of the diffusion

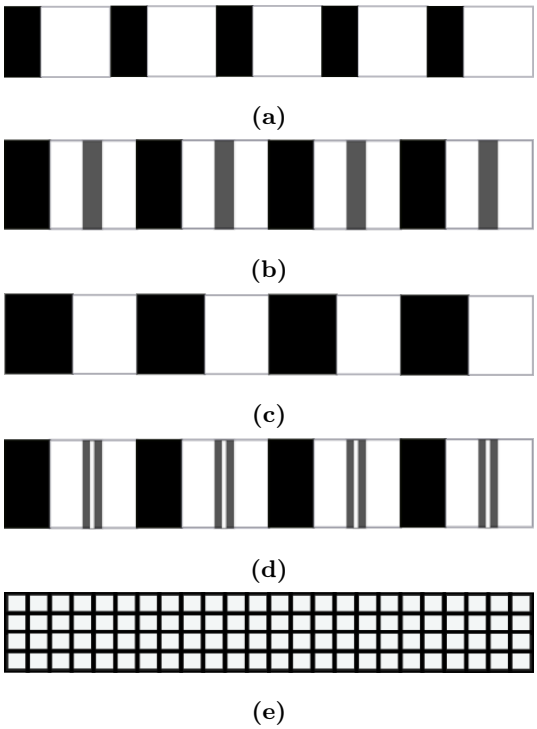

Figure 6.4: Schematic of different ripple structures reported in the literature. (a) asymmetric ripples with saw-tooth height profile in pure lipids ($\mu/2$ ripples), (b) symmetric metastable ripples with twice the wavelength of the former, observed in pure lipids on cooling from the fluid phase (Λ ripples), (c) symmetric ripples with shorter wavelength in lipid-sterol membranes below the pre-transition and (d) long-wavelength ripples in lipid-cholesterol membranes above the pre-transition.(e) Two dimensional lattice found in the case DPPC: Cholesterol sample.

coefficient that can be correlated to the fluid and gel components in the ripple phase [33].

In addition to the widely observed asymmetric ripple phase described above, there have been some reports of a metastable symmetric ripple phase observed on cooling from the fluid phase [34, 35, 36]. The modulation wavelength in this phase is almost twice that in the coexisting asymmetric ripple phase. Bilayers in this phase are believed to consist of a sequence of 'M'-shaped segments [37, 38]. There has also been one report of a two-dimensionally modulated ripple phase in PC bilayers under moderate hydration [39].

Most of the direct imaging studies of the ripple phase have been carried out using freeze-fracture transmission electron microscopy (FF-TEM) [40, 41, 42, 43, 44]. In this technique, a thin layer of the sample is first quenched rapidly from the temperature of interest to about -150°C in order to preserve the structure of the phase under study. It is then fractured under vacuum, and the fracture plane is known to follow the bilayer mid-plane preferentially. A replica of the fractured surface is created by depositing platinum at an angle on the fractured surface. Thus topographical features of the surface are mapped on to thickness variations of

the platinum layer. After reinforcing the replica with a layer of carbon, the sample is dissolved away using a suitable solvent. The replica is then imaged using TEM to obtain information about the topography of the fractured surface. It is not straight forward to determine the amplitude of the height modulation of the bilayers from the TEM images, although the shape (saw-tooth vs. triangular) can be directly inferred from the relative widths of the dark and bright stripes corresponding to the two arms of the ripple [37]. Scanning tunneling microscopy (STM) has also been employed to image the replica and obtain quantitative information on bilayer height modulations in the ripple phase [45]. The results of these studies are in agreement with those of the diffraction experiments and show the formation of the asymmetric (saw-tooth) ripple phase and the metastable ripple phase with almost twice the periodicity. In addition, these experiments reveal the presence of an underlying hexagonal symmetry in the ripple phase that extends over μm-sized regions, which remains unexplored. Further, they also show the formation of ripples having a periodicity of the order of a few 100 nm in samples cooled from the gel phase. These structures usually have a short correlation length, which might explain why they do not give rise to noticeable peaks in diffraction patterns.

Besides FF-TEM and FF-STM, the ripple phase has also been studied in supported bilayers using another direct imaging technique, namely atomic force microscopy (AFM). Although the values of the observed amplitude of rippling are different from those obtained from scattering and FF experiments, these AFM measurements confirm that inter-bilayer interactions do not play any role in the formation of the ripple phase [46, 47].

The incorporation of different biomolecules, particularly cholesterol, can significantly affect the ripple phase behavior of saturated lipids. In the ripple phase, FF-TEM experiments show that the ripple wavelength increases with cholesterol concentration and diverges near 20 mol% [41, 48, 49, 50]. X-ray scattering experiments show that the melting of the gel phase with cholesterol concentration occurs via a modulated phase consisting of alternating cholesterol-rich and cholesterol-poor stripes [51]. In this modulated phase, the bilayers have a symmetric (triangular) height modulation, with a wavelength of about 7 nm and an amplitude of about 0.2 nm. Rather surprisingly, although this phase has been observed in many binary PC-sterol membranes using x-ray scattering [52], it has not to be observed using any of the direct imaging techniques. Different types of rippled structures reported in the literature in pure lipid membranes and in lipid-cholesterol membranes are schematically shown in fig.6.3.

This chapter discusses the effect of cholesterol on the rippling of DPPC bilayers using AFM and cryo-SEM.The following section demonstrates that the much simpler cryo-scanning electron microscopy technique, where the fractured surface is imaged directly using SEM can

provide comparable information on the ripple phases of phospholipid bilayers. In addition to reproducing earlier results of FF-TEM studies on DPPC and DPPC-cholesterol membranes, there is evidence for the formation of two novel rippled structures of DPPC-cholesterol membranes. Using AFM imaging the symmetric ripple of DPPC-cholesterol is also observed.

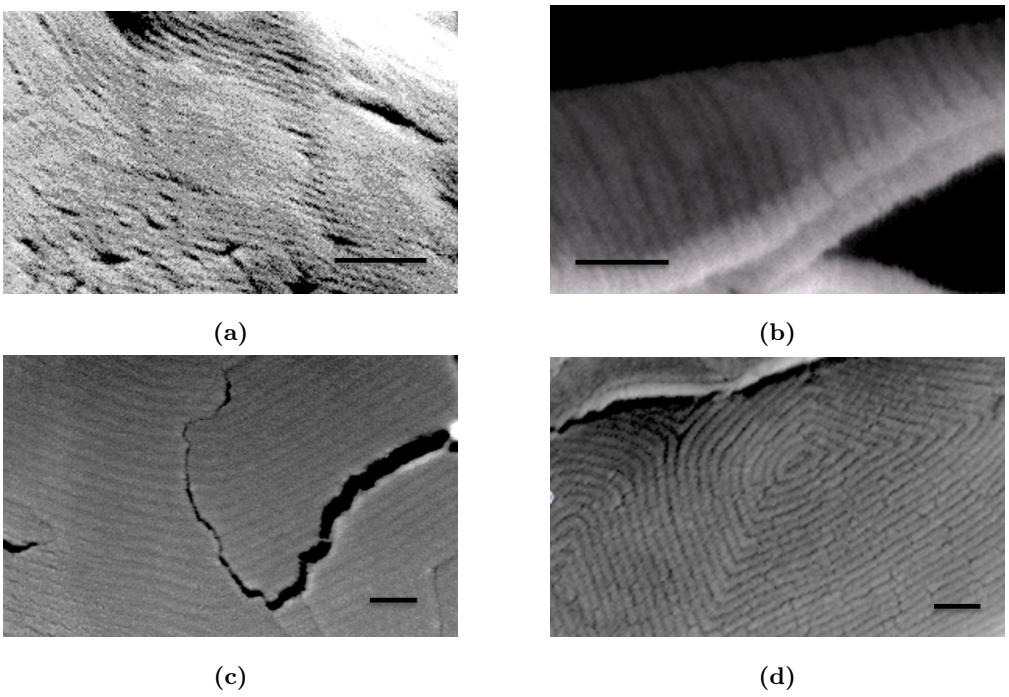

Figure 6.5: Ripple structures observed in DPPC bilayers quenched from 37° C. (a) $\Lambda/2$ ripples with asymmetric profile ($\lambda \approx 13$ nm), (b) Λ ripples with 'M-shaped' segments ($\lambda \approx 22$ nm), (c) Λ ripples with no groove ($\lambda \approx 22$ nm), (d) Long-wavelength asymmetric ripples ($\lambda \approx 17$ nm).Scalebar - 50 nm

6.1.3 Contrast in SEM images

The image in a SEM is produced by scanning a focussed electron beam on the specimen surface in a raster pattern [53]. Interaction of the electron beam with the specimen produces various signals that contain information about the topography and composition of the sample. In the present study, the signal corresponds to the number of secondary electrons emitted by the sample that is collected by the secondary electron detector, which provides information about surface topography. The intensity of each pixel in the image is proportional to the strength of the signal from the corresponding point on the sample surface. Due to their relatively low energies, only the secondary electrons emitted from within a few nm thick layer near the surface can escape from the sample and contribute to the observed signal. In the case of organic samples, such as the ones studied here, the secondary electrons arise essentially from the thin platinum layer deposited on the surface. The number of emitted

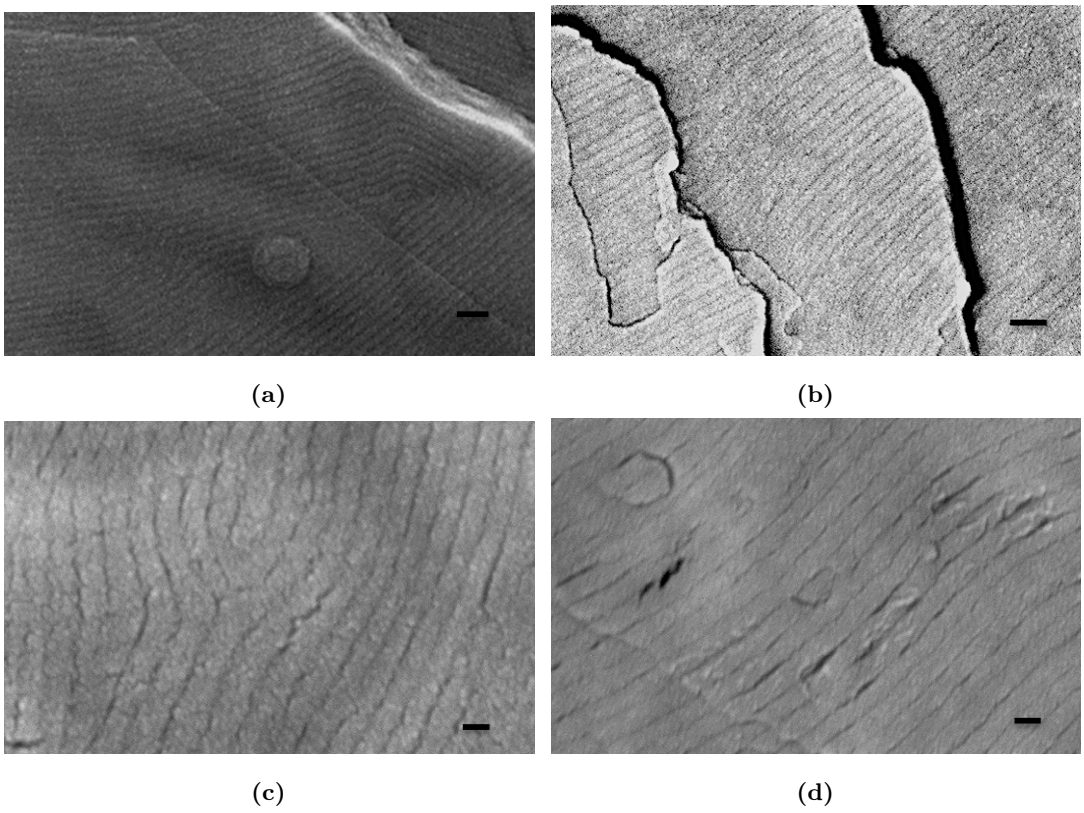

Figure 6.6: Rippled structures observed in DPPC-cholesterol membranes quenched from 31°C for cholesterol concentrations of 5 mol% ($\lambda \approx 28$ nm) (a), 10 mol% ($\lambda \approx 27$ nm) (b), 15 mol% ($\lambda \approx 34$ nm) (c) and 20 mol% ($\lambda \approx 51$ nm) (d). Scalebar - 50 nm

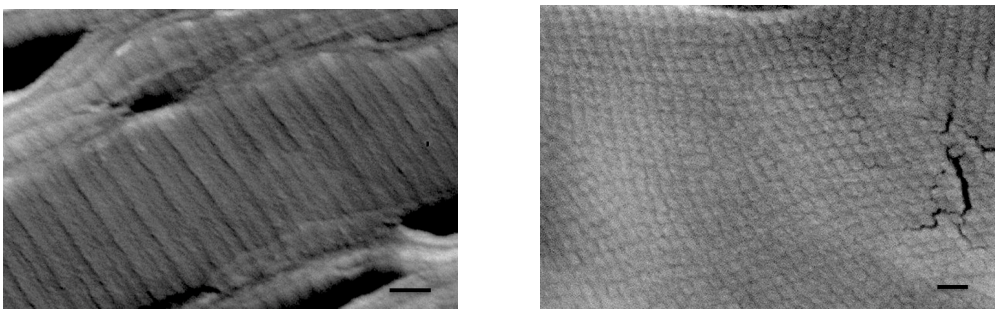

Figure 6.7: Novel rippled structures observed in DPPC-cholesterol membranes quenched from 31°C. (a) 2-groove ripples with $\lambda \approx 57$ nm in a 5 mol% cholesterol sample. (b) Two-dimensional lattice with $\lambda \sim 30$ nm in a 10 mol% cholesterol sample incubated for one week. Scalebar - 50 nm

secondary electrons increases with the angle between the direction of the incident electron beam and the local surface normal. Hence steep surfaces and edges appear brighter than flat surfaces, which in turn are brighter than deep recesses. A schematic of different patterns observed in the present study is given in fig.6.4. Although the intensity distribution in an

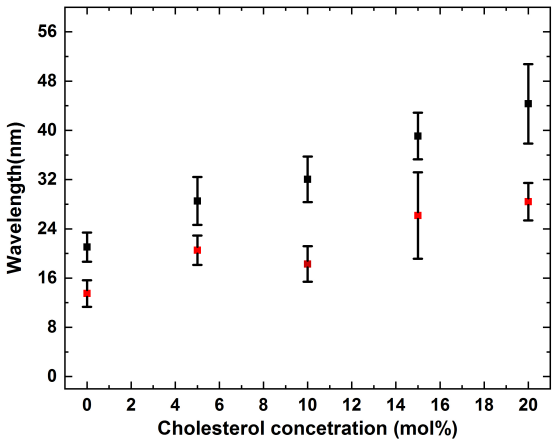

Figure 6.8: Variation of ripple wavelength with cholesterol concentration at 37 °C. Black and red symbols refer to co-existing Λ and $\Lambda/2$ ripples, respectively.

image is directly related to the topography of the surface, it is not possible to completely determine the latter from the former. Since the structures encountered in the present study are spatially periodic, it is possible to determine their wavelength very accurately, but their amplitudes cannot be estimated. As mentioned earlier, the bright and dark bands in FF-TEM images arise as a result of a shadowing effect, since platinum is deposited at an angle to the average surface normal. Hence patches of the surface whose normals are oriented towards the deposition direction appear bright, and those whose normals are oriented away appear dark. The contrast between the dark and bright bands decreases as the amplitude of the height modulation decreases. The dark and bright bands in cryo-SEM images do not correspond to regions of different orientations of the surface. Instead, as mentioned above, they correspond to regions of low and high secondary electron emission, respectively, which can be associated with the troughs and crests of the surface height modulation. It is difficult to infer the detailed shape of the ripples (saw-tooth or triangular) from the relative widths of the dark and bright bands, unlike in the case of FF-TEM images. However, from a knowledge of the patterns corresponding to the known bilayer height profiles, it is possible to infer many features of the profiles responsible for the other observed patterns.

6.2 Results and Discussion

6.2.1 Rippled structures of pure DPPC membranes

T_p and T_m of DPPC bilayers in excess water conditions are 35.0°C and 41.5°C, respectively [54]. Cryo-SEM images of DPPC multilamellar liposomes quenched from 37°C in the ripple

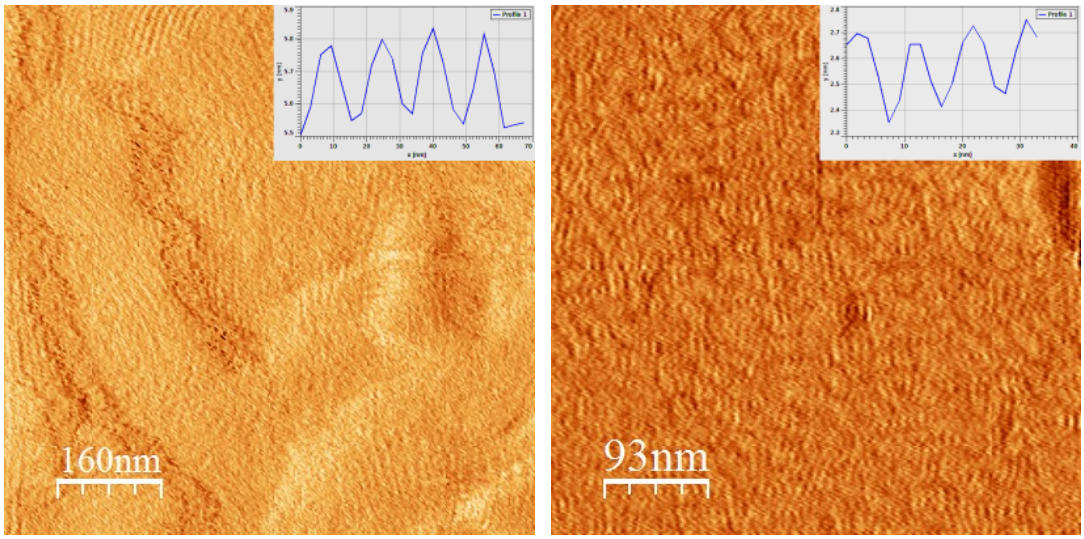

(a) **(b)**

Figure 6.9: Deflection mode AFM images of (a) DPPC- 10 mol% cholesterol supported membrane showing ripples with $\lambda \approx 15$ nm and (b) DPPC-15 mol% cholesterol supported membrane showing $P_{\beta'}$ phase ripples with $\lambda \approx 8$ nm. The insets show intensity variation along a direction normal to the ripples.

phase show four different types of patterns (fig.6.5). Parts of the sample show an asymmetric pattern (fig.6.5(a)), schematically shown in fig.6.4(a), with a wavelength of about 13 nm. Based on the results of earlier studies, this can be identified as the $\Lambda/2$ ripples of the stable ripple ($P_{\beta'}$) phase of DPPC bilayers (fig.6.3(a)). Some areas of the sample show a structure corresponding to fig.6.4(b), with a wavelength of around 22 nm (fig.6.5(b)). Since the wavelength of this structure is about 1.7 $\times$ that of the $P_{\beta'}$ phase, it can be identified as the metastable Λ ripples observed in many earlier studies using both FF-TEM and x-ray scattering. The observed pattern is consistent with the M-shaped profile proposed for this structure (fig.6.3(b)).

In addition to these two well-known structures, we observed two more structures in some parts of the sample. Both are asymmetric patterns (fig.6.4(a)), one having a wavelength of 22 nm (fig.6.5(c)) and the other having a wavelength of 17.5 nm (fig.6.5(d)). The former has the same wavelength as the Λ ripples, but the central groove of the M-like profile is absent. The latter structure was observed only in a few areas of the sample, whereas the former was much more widespread.

No ripple structures were found in samples quenched from 31°C in the gel phase. This is in contrast to some of the earlier FF-TEM studies where long-wavelength ripples with short correlation length were observed in this phase [55]. The reason for this discrepancy is not clear at present, but we might note that such ripples have not been detected in any of the

scattering experiments in the gel phase.

6.2.2 Rippled structures of DPPC-cholesterol membranes

Cryo-SEM images of DPPC multilayer liposomes with varying cholesterol concentration, quenched from 31°C, are shown in fig.6.6. Samples quenched from 37°C show very similar patterns that are correlated over shorter length scales. Both $\Lambda/2$ and Λ ripples are seen in these two sets of samples at all cholesterol concentrations up to 20 mol%. Wavelengths of both these structures are found to increase with increasing cholesterol concentration (fig.6.8), in agreement with the results of earlier FF-TEM studies. The contrast between the bright and dark regions is significantly reduced as cholesterol concentration is increased. This suggests a reduction in the amplitude of the ripples with increasing cholesterol concentration, as previously reported [56].

Samples quenched from 31°C exhibit, in addition, two novel structures that have not been reported earlier (fig.6.7). One of them shows two thin dark stripes (fig.6.7a), schematically shown in fig.6.4c, instead of one as in the case of Λ ripples. This suggests that the profile has two thin grooves near the crest, instead of one as in the case of M-shaped Λ ripples. The second is a two-dimensionally modulated structure with a wavelength of about 30 nm (fig.6.7(b)), schematically shown in fig.6.4(d). These 2D patterns were observed mainly in 10 % cholesterol samples, which were incubated for about a week at 31°C.

Landau theories of phase transitions in lipid bilayers have predicted the possible existence of a variety of ripple phases of different symmetries [57, 58]. These include symmetric triangular ripples, asymmetric saw-tooth ripples, and 2-D ripples. It is possible that their energies are not significantly different, so that small variations in local conditions, such as temperature and hydration, could stabilize different structures in different parts of the sample. Further, it is also possible that the fast quenching occurring during sample preparation traps the system in some metastable states, as is the case with the Λ ripples. Such scenarios can account for a large number of structures observed in the present study.

6.2.3 AFM imaging of DPPC-cholesterol membranes

As mentioned in the introduction, x-ray scattering experiments on DPPC-cholesterol membranes have reported the formation of a symmetric ripple phase with a much shorter wavelength than the asymmetric $\Lambda/2$ ripples [51, 59]. In addition to cholesterol, this P_β phase has also been observed with a variety of other sterols [52]. The wavelength of the ripples in the P_β phase is around 7 nm and decreases with increasing sterol concentration. The amplitude

of these ripples estimated from scattering data is about 0.2 nm, which is much less than that of the $\Lambda/2$ ripples. As mentioned earlier, the contrast between bright and dark regions in FF-TEM, as well as in cryo-SEM is very sensitive to the amplitude of the height modulations. Probably because of their low amplitude, these ripples have not been observed in any of the FF-TEM studies on PC-cholesterol membranes. We also do not find any signature of the P_β phase in our cryo-SEM images of DPPC-cholesterol membranes. Since AFM does not suffer from this limitation, we have used this technique to image different ripple phases in supported DPPC-cholesterol bilayers at ambient temperature. AFM images of DPPC multilayers containing 5% cholesterol show ripples with a wavelength of 16 nm and amplitude of 0.3 nm (fig.6.9(a)). It may be noted here that whereas the measured value of the wavelength is very accurate, that of the amplitude is not, since the radius of curvature of the AFM tip is comparable to the wavelength of the ripples. Hence it cannot descend into the troughs of the height modulation, resulting in a lower estimate of the amplitude. The wavelength of these ripples is comparable to that observed in samples of similar composition using cryo-SEM (fig.6.8). In the case of 15 mol% cholesterol samples, ripples with a periodicity of 8 nm is observed at 25 °C (fig.6.9(b)). The amplitude measured is about 0.3 nm. According to the DPPC-cholesterol phase diagram determined from scattering data, the P_β is expected to occur at this composition and temperature [59]. Further, the measured value of the wavelength agrees very well with that determined from diffraction data. Thus we can be certain that this image indeed corresponds to the P_β phase.

6.3 Conclusion

Cryo-SEM and AFM experiments were carried out on the modulated phases exhibited by DPPC and DPPC-cholesterol membranes below the chain melting transition temperature. All the ripple structures observed in these systems in earlier studies were reproduced. In addition to the earlier ripple structures, two novel modulated structures were found in these systems. AFM imaging was carried out on the symmetric ripple phase of DPPC-cholesterol system explored previously only through small-angle x-ray scattering studies. These results show that the cryo-SEM technique can provide information on these systems comparable to that obtained using the much more demanding FF-TEM technique, which has been widely used to study membrane systems.

Bibliography

[1] T. P. W. MacMullen, R. N. A. H. Lewis, and R. N. McElhaney. Cholesterol-phospholipid interactions, the liquid ordered phase and lipid rafts in model and biological membranes. *Curr. Opi.Colliod and Interface Sci*, 8:459–468, 2004.

[2] M. R. Vist and J. H. Davis. Phase equilibria of cholesterol/dipalmitoylphosphatidylcholine mixtures: deuterium nuclear magnetic resonance and differential scanning calorimetry. *Biochemistry*, 29:451–464, 1990.

[3] J. H. Davis, J. J. Clair, and J. Juhasz. Phase equilibria of DOPC/DPPC-d_{62}/Cholesterol mixtures. *Biophys. J.*, 96:521–539, 2009.

[4] D. Marsh. Liquid ordered phase induced by cholesterol: A compendium of binary phase diagram. *Biochim. Biophys. Acta*, 1798:688–699, 2010.

[5] E.M. L. Bastiaanse, K. M.H öld, and A. V. der Laarse. The effect of membrane choelsterol content on ion transport processes in plasma membranes. 33:272–283, 1997.

[6] W. K. Subczynski, M. Pasekiewicz-Gierula, J. Widomska, L. Mainali, and M. Raguz. High cholesterol/low cholesterol: Effects in biological membranes : A review. *Cell BioChem. and Biophys.*, 75:369–385, 2017.

[7] L. Redondo-Morata, M. I.Gianna, and F. Sanz. Influence of choelsterol on the phase transitons of lipid bilayers: A tmeperature controlled force spectroscopy study. *Langmuir*, 28:12851–12860, 2012.

[8] D. A. Mannock, R. N. A. H. Lewis, and R. N. McElhaney. Comparative calorimetric and spectroscopic studies of the effects of lanosterol and cholesterol on thermotropic phase behavior and organization of dipalmitoyl phosphatidyl choline bilayer membranes. *Biophys. J*, 91(9):3327–3340, 2006.

[9] S. L. Veatch and S. L. Keller. Organization in lipid membranes containing cholesterol. *Phys. Rev. Lett*, 89:26–23, 2002.

[10] T. J. McIntosh. The effect of cholesterol on the structure of phosphatidylcholine bilayers. *Biochim. Biophys. Acta*, 513(1):43–58, 1978.

[11] J. Pan, T. T. Mills, S. Tristram-Nagle, and J. F. Nagle. Cholesterol perturbs lipid bilayers non universally. *Phys. Rev. Lett.*, 100:16–19, 2008.

[12] R. N. McElhaney. The use of differential scanning calorimetry and differential thermal analysis of model and biological membrane. *Chem. Phys. Lipids*, 30(2-3):229–259, 1982.

[13] O. G. Mourtisen and J. Martin. What's so special about cholesterol? *Lipids*, 39:1101–1113, 2004.

[14] J. R. Silvius. Role of cholesterol in lipid raft formation: lessons from lipid model systems. *Biophys. Biochim. Acta*, 1610:174–183, 2003.

[15] M. Hao, S. Mukherjee, and F. R. Maxfield. Cholesterol depletion induces large scale domain segregation in living cell membranes. *Proc. Natl. Acad. Sci. U. S. A*, 98:13072–13077, 2001.

[16] K. Simons and E. Ikonen. Functional rafts in cell membrane. *Nature*, 387:569–572.

[17] K. Simons and W. L. Vaz. Model systems, lipid rafts, and cell membranes. *Annu. Rev. Biophys. Biomol. Struct.*, 33:269–295, 2004.

[18] J. B. Leathes. Role of fats in vital phenomena. *Lanchet*, 1:853–856, 1925.

[19] D. J. Recktenwald and H. M. McConnell. Lateral phase separations in binary-mixtures of phosphatidylcholine and cholesterol. *Biochim. Biophys. Acta*, 33:A191, 1981.

[20] S. Karmakar, B. R. Sarangi, and V. A. Raghunathan. Phase behavior of lipid - cholesterol membranes. *Solid State Commun.*, 139:630–634, 2006.

[21] K. Mortensen, W. Pfeiffer, E. Sackmann, and W. Knoll. Structural properties of a phosphatidylcholine- cholesterol system as studied by small-angle neutron scattering - ripple structure and phase diagram. *Biochim. Biophys. Acta*, 945:221–245, 1988.

[22] D. Needham, T. J. McIntosh, and E. Evans. Thermomechanical and transition properties of dimyristoylphophatidylcholine/cholesterol bilayers. *Biochemistry*, 27:4668–4673, 1988.

[23] G. W. Feigenson and J. T. Buboltz. Ternary phase diagram of dipalmitoyl - pc/ dilauroyl - pc / cholesterol: nanoscopic domain formation deriven by cholesterol. *Biophys. J.*, 80:2775–2788, 2001.

[24] J. Zhao, J. Wu, F. A. Heberle, T. T. Mills, P. Klawitter, G. Huang, G. Constanza, and G. W. Feigenson. Phase studies of model biomembranes : Complex behavior of dspc/dopc/choelsterol. *Biochim. Biophys. Acta*, 1788:2114–2123, 2009.

[25] M. J. Janiak, D. M. Small, and G. G. Shipley. Temperature and compositional dependence of the structure of hydrated dimyristoyl lecithin. *J. Biol. Chem.*, 254:6068–6078, 1979.

[26] A. M. Seddon, D. Casey, R. V. Law, A. Gee, R. H. Templera, and O. Cesab. Drug interactions with lipid membranes. *Chem. Soc. Rev.*, 38:2509–2519, 2009.

[27] S. Tristram-Nagle, Y. Liu, J. Legleiter, and J. F. Nagle. Structure of gel phase dmpc determined by x-ray diffraction. *Biophys. J.*, 83:3324–3335, 2002.

[28] A. Tardieu, V. Luzzati, and F. C. Reman. Structure and polymorphism of the hydrocarbon chains of the lipids: a study of lecithin-water phases. *J. Mol. Biol*, 75:711–733, 1973.

[29] W. J. Sun, S. Tristram-Nagle, R. M. Suter, and J. F. Nagle. Structure of the ripple phase in lecithin bilayers. *Proc. Natl. Acad. Sci. U.S.A*, 93:7008–12, 1996.

[30] K. Sengupta, V. A. Raghunathan, and J. Katsaras. Novel structural features of the ripple phase of phospholipids. *Europhys. Lett.*, 49:722–728, 2000.

[31] K. Akabori and J. F. Nagle. Structure of the dmpc lipid bilayer ripple phase. *Soft Matter*, 11:918–926, 2015.

[32] R. Witthort, C. Schmidt, and R. Griffin. Solid-state carbon-13 nuclear magnetic resonance of lecithin gel to liquid crystalline phase transitions. *Biochemistry*, 20(14):4223–4228, 1981.

[33] M. B. Scheider, W. K. Chan, and W. W. Webb. Fast diffusion along defects and corrugations in phospholipids pβ' liquid crystals. *Biophys. J.*, 43(2):157–165, 1983.

[34] H. Yao, S. Matuoka, B. Tenchov, and I. Hatta. Metastable ripple phase of fully hydrated dipalmitoylphosphatidylcholine as studied by small angle x-ray scattering. *Biophys. J.*, 59:252–255, 1991.

[35] J. A. N. Zasadzinski and M. B. Schneider. Ripple wavelength, amplitude, and configuration in lyotropic liquid crystals as a function of effective headgroup size. *J. Phys. (France)*, 48:2001–2011, 1987.

[36] J. Katsaras, S. Tristram-Nagle, Y. Liu, R. L. Headrick, E. Fontes, P. C. Mason, and J. F. Nagle. Clarification of the ripple phase of lecithin bilayers using fully hydrated, aligned samples. *Phys. Rev. E*, 61:5668–5677, 2000.

[37] E. Sackmann, D. Ruppel, and C. Gebhardt. Defect structure and texture of isolated bilayers of phospholipids and phospholipid mixtures. In W. Helfrich and G. Heppke, editors, *Liquid Crystals of One- and Two-dimensional Order*. Springer-Verlag, Berlin, 1980.

[38] K. Sengupta, V. A. Raghunathan, and J. Katsaras. Structure of the ripple phase of phospholipid multibilayers. *Phys. Rev. E*, 68:031710, 2003.

[39] L. Yang and M. Fukuto. Modulated phase of phospholipids with a two-dimensional square lattice. *Phys. Rev. E*, 72:010901(1–4), 2005.

[40] P. P. da Silva. Freeze-fracture of dipalmitoyl lecithin vesicles. *J. Microsc.*, 12:185–192, 1971.

[41] A. J. Verkleij, P. H. J. Th. Ververgaert, L. L. M. Van Deenen, and P. F. Elbers. Phase transitions of phospholipid bilayers and membranes of *Acholeplasma Iaidlawaii B* visualized by freeze fracturing electron microscopy. *Biochim. Biophys. Acta*, 288:326–332, 1972.

[42] P. H. J. Th. Ververgaert, A. J. Verkleij, P. F. Elbers, and L. L. M. Van Deenen. Analysis of the crystallization process in lecithin liposomes: A freeze-etch study. *Biochim. Biophys. Acta*, 311:320–329, 1973.

[43] H. W. Meyer and W. Richter. Freeze fracture studies on lipids and membranes. *Micron*, 32:615–644, 2001.

[44] J. A. Zasadinski, J. Schneir, and J. Gurley. Scanning tunneling microscopy of freeze-fracture replicas of biomembranes. *Science*, 239:1013–1015, 1988.

[45] J. T. Woodward IV and J. A. Zasadzinski. High-resolution scanning tunneling microscopy of fully hydrated ripple-phase bilayers. *Biophys. J.*, 72:964–976, 1997.

[46] C. Leidy, T. Kaasgard, J. H. Crowe, O. G. Mouristen, and K. Jørgenson. Ripples and the formation of anisotrpic lipid domains:imaging two component double bilayers by atomic force microscopy. *Biophys. J.*, 83:2625–2633, 2002.

[47] Y. Fang and J. Yang. Role of the bilayer- bilayer interaction on the ripple structure of supported bilayer in solution. *J. Phys. Chem.*, 100:15614–15619, 1996.

[48] E. J. Luna and H. M. McConnell. Intermediate monoclinic phase of phosphatidyl cholines. *Biochim. Biophys. Acta*, 466:381–392, 1977.

[49] M. A. Singer A. Hocks, M. Dinda. The ripple phase of phosphatidylcholines: Effect of chain length and cholesterol. *Biochim. Biophys. Acta*, 903:177–183, 1987.

[50] B. R. Copeland and H. M. McConnel. The rippled structure in bilayer membranes of phophatidylcholine and binary mixtures of phosphaidylcholine and cholesterol. *Biochim. Biophys. Acta*, 559:95–109, 1980.

[51] S. Karmakar and V. A. Raghunathan. Cholesterol-induced modulated phase in phospholipid membranes. *Phys. Rev. Lett.*, 91:98–102, 2003.

[52] Md. Arif Kamal and V. A. Raghunathan. Phase behaviour of phospholipid - phytosterol membranes. *Soft Matter*, 8:8952, 2012.

[53] J. J. Bozzola and L. D. Russell. *Electron Microscopy: Principles and Techniques for Biologists*. Jones and Bartlett, Boston, second edition, 1999.

[54] D. M. Small. *The physical chemistry of lipids*. Springer, first edition, 1986.

[55] H.W. Meyer and W. Ritcher. Freeze fracture studies on lipids and membranes. *Micron*, 32:615–644, 2001.

[56] J. T. Woodward and J. A. Zasadzinski. Amplitude, wave form, and temperature dependence of bilayer ripples in the $P_{\beta'}$ phase. *Phys. Rev. E*, 53:3044–3047, 1996.

[57] C.-M. Chen, T.C. Lubensky, and F.C. MacKintosh. Phase transitions and modulated phases in lipid bilayers. *Phys. Rev. E*, 51(1):504–513, 1995.

[58] K. Sengupta, V. A. Raghunathan, and Y. Hatwalne. Role of tilt order in the asymmetric ripple phase of phospholipid bilayers. *Phys. Rev. Lett.*, 87:055705, 2001.

[59] S. Karmakar and V. A. Raghunathan. Structure of phospholipid-cholesterol membranes: An x-ray diffraction study. *Phys. Rev. E*, 71:061924, 2005.

Chapter 7

AFM imaging of fluid-fluid phase coexistence in binary PC lipid-hydroxycholesterol system

7.1 Introduction

The structure of cholesterol is shown in fig.7.1. The rigid core of the cholesterol molecule is formed out of 4 trans-fused aromatic rings. To one end of this core, a polar hydroxyl group and to the other end, a hydrocarbon chain are attached, giving cholesterol an amphiphilic nature. A diverse variety of biomolecules such as bile acid salts, certain steroid hormones, vitamin D, etc. are formed by biochemical modifications of cholesterol. Apart from these molecules, certain side-chain derivatives of cholesterol are produced during its metabolic pathway or during the synthesis of bile acids (fig.7.1). These derivatives which are formed *in vivo* enzymatically regulates cholesterol homeostasis and primarily serve as cellular signals for excess cholesterol

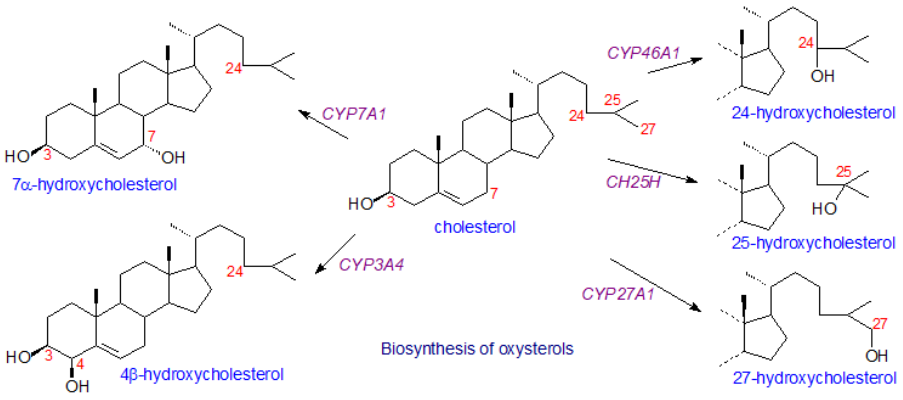

Figure 7.1: Derivatives of cholesterol formed by enzymatic synthesis [1]

(a) **(b)**

Figure 7.2: Structure of 25-hydroxycholesterol and 27-hydroxycholesterol [2]

[2]. Although cholesterol is one of the major component of the eukaryotic cell membrane, its oxygenated derivatives- oxysterols is only present in minor amounts in the membrane [3]. Oxysterols are broadly classified into two categories [1]. The derivatives produced by oxygenation of the steroid ring at 7 positions such as 7-ketocholesterol, 7-α cholesterol, 7-α hydroxycholesterol, and 7-β hydroxycholesterol form the first group. These molecules are synthesised either via reactive free radicals or enzymatically. The molecules which are synthesised by oxygenation of cholesterol at iso-octyl tail region fall into the second group which includes 25- hydroxycholesterol (fig.7.2a) and 27-hydroxycholesterol (fig.7.2b) and 24 S- hydroxycholesterol. These are produced only through enzymatic synthesis.

Features such as low concentration levels in the cell membrane [5] larger transfer rate between the membranes (almost 50 times more than cholesterol) [6, 7] and much shorter life

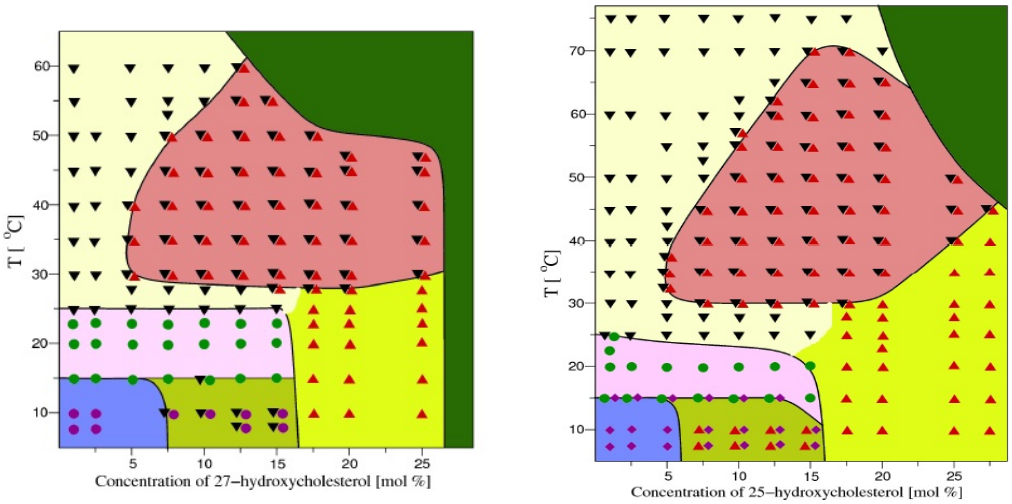

(a) **(b)**

Figure 7.3: Partial phase diagrams obtained from x-ray scattering studies of (a)DMPC: 25-hydroxycholesterol system (b)DMPC: 27-hydroxycholesterol system from ref.[4]. The pink shaded region represent the fluid- fluid coexistence region. black inverted triangles and red upright triangles represent the two fluid phases, green circles represent the ripple phase and purple circle represent the gel phase.

span, of oxysterols in comparison to cholesterol make them ideal candidates in cellular signaling pathways [8]. In the metabolic pathway of cholesterol, excess cholesterol in cellular organelles like macrophages is converted into 27-hydroxycholesterol and cholestenoic acid for excretion while in the brain, excess cholesterol gets converted into 24S- hydroxycholesterol to pass through the blood-brain barrier [9]. Some studies have shown that hydroxycholesterol crosses the brain-blood barrier more easily compared to cholesterol [10, 11]. These results suggest that the effect of oxysterol in lipid membranes will be different from that of cholesterol. There are many experimental studies and a few simulation studies which have looked into details of the influence of hydroxycholesterol on the structure and phase behavior of model lipid membranes [12, 13, 14].

Oxysterols perturb membrane properties differently compared to cholesterol, mainly because of their increased orientational possibilities in the membrane due to the presence of the extra oxygen [15, 12]. Effect of the incorporation of cholesterol and its derivatives on the phase behaviour of lipid monolayers was studied by Theunissen et al. [12]. It was found that the orientations of 7-ketocholesterol and 25-hydroxycholesterol were similar to cholesterol in the bilayer. But 7-α and 7-β hydroxycholesterol take tilted configurations with respect to the bilayer normal. The effect of 7-α and 7-β hydroxycholesterol on the membrane was found to be similar to that of cholesterol in the sense that they induce condensing effect on the membrane, reduce membrane permeability while increasing bilayer thickness. 25- hydroxycholesterol, on the other hand, increases glucose permeability while acting as a spacer molecule which disrupts the hydrocarbon packing rather than condensing the chain.

In the case of the binary system made from POPC: 25-hydroxycholesterol, angle-resolved fluorescence depolarization microscopy, and electron spin resonance showed that till 5 mol% concentration 25-hydroxycholesterol behaves similar to cholesterol [13]. A simulation study [14] has shown that the induction of 25- hydroxycholesterol to the membrane instead of cholesterol changes the overall energy landscape for sterol orientations in the membrane. The presence of polar groups at both ends of the molecule in the case of 25-hydroxycholesterol increases the configurational possibilities of hydroxycholesterol in the bilayer. In the case of membranes containing cholesterol the introduction of 25-hydroxycholesterol to the membrane disrupts the position and orientation of cholesterol, increasing its solvent accessibility [14]. The following section details previous x-ray scattering studies on the interaction of different PC lipids with 25 and 27-hydroxycholesterols.

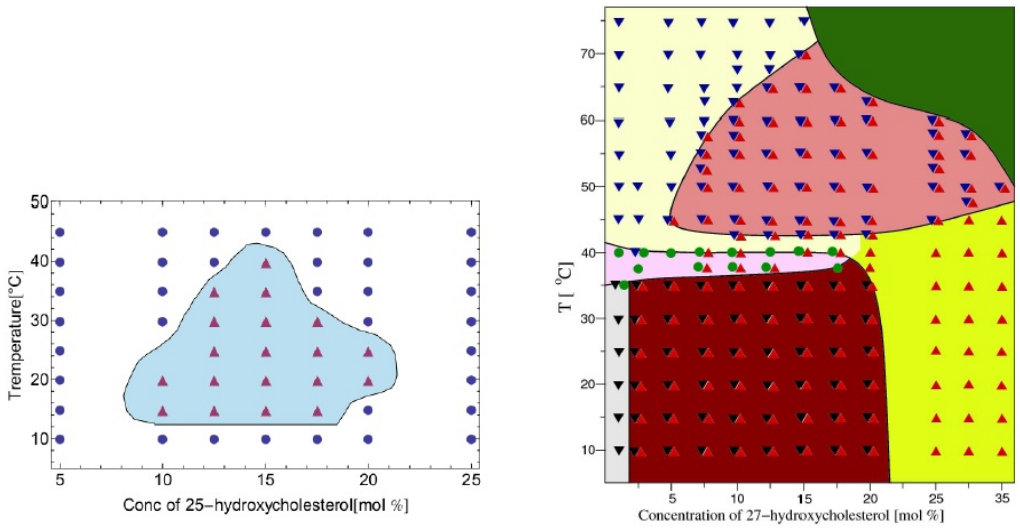

(a) **(b)**

Figure 7.4: Partial phase diagram from x-ray scattering studies of (a) DLPC (1,2-dilauroyl-sn-glycero-3-phosphocholine): 25-hydroxycholesterol system deduced from ref.[16]. Blue circles in the image represent single phase region and purple upright triangle indicate two phase region (b) DPPC: 27-hydroxycholesterol system deduced from ref.[4]. Pink shaded region represents two fluid phase coexistence region. In the image, black inverted triangles and red upright triangles represent the two fluid phases, green circles represent the ripple phase and purple circle represent the gel phase.

7.2 Previous studies

Systematic x-ray diffraction studies were done on aligned multilayer stacks of PC lipids with varying hydroxycholesterol concentrations. These studies clearly showed that the phase behavior of these lipids is different in the presence of hydroxycholesterol. Hydroxycholesterol is found to induce fluid-fluid coexistence above T_m of the lipid over a range of temperature and concentration. An overview of these studies reported in refs.[4, 16, 17]is given below.

7.2.1 Phase behavior of DMPC bilayers in the presence of 25 and 27 - hydroxycholesterol

The most striking feature of these phase diagrams is the closed loop fluid-fluid immiscibility region observed above the main transition temperature of the lipid (figs.7.3). This phase coexistence was found to span a wide range of temperatures and concentrations. In the case of DMPC, both 25- hydroxycholesterol and 27- hydroxycholesterol are found to induce fluid-fluid phase coexistence above the main transition temperature of DMPC [4]. The effect of hydroxycholesterol on the phase behaviour of DMPC below the main phase transition

temperature is found to be similar to that of cholesterol.

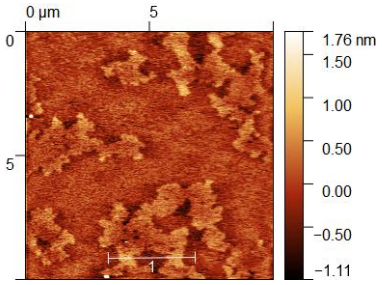

(a) DOPC:DMPC(1:1 molar ratio) at 22°C

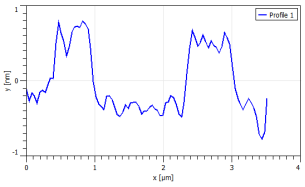

(b) Height profile of (a)

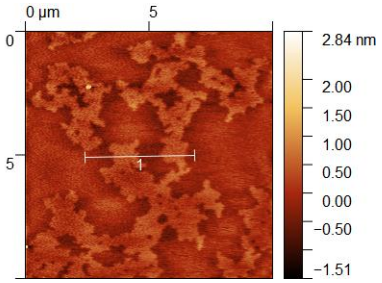

(c) DOPC:DMPC(1:1 molar ratio) at 22°C

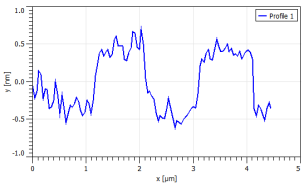

(d) Height profile of (c)

Figure 7.5: AFM images of supported bilayers formed from DOPC:DMPC(1:1) lipid mixtures, taken at room temperature. Height profiles along the lines drawn in (a) and (c) are shown in (b) and (d), respectively.

At concentrations < 2.5 mol%, 27-hydroxycholesterol (fig.7.3(a)) does not show any effect on the phase behavior of DMPC. Both the main transition (T_m) and pre-transition (T_p) temperatures remain the same till 15 mol% of sterol concentration. Beyond 15 mol%, T_m falls off sharply and vanishes at around 17.5 mol%. T_p does not fall off sharply, but also vanishes at around 17.5 mol%. Ripple wavelength gradually increases with increasing sterol content in the bilayer. Below 15°C up to 5 mol% of 27-hydroxycholesterol concentration, the gel phase of DMPC exists. Above 5 mol% sterol concentration and below 15°C, a coexistence of the gel phase with a sterol-rich fluid phase is observed. Above T_m, between 5 mol% and 25 mol%, two fluid phases are found to coexist over a range of temperatures. One fluid phase has almost the same d-spacing as that of a single fluid phase observed for lower hydroxycholesterol concentrations ($<$ 5 mol%) [4]. The second fluid phase has a d-spacing similar to the single fluid phase observed at higher concentrations of sterol ($>$25 mol%). The difference in d-spacing (0.4-0.6 nm) between these two fluid phases do not depend on the temperature. Above certain temperature, the coexistence vanishes, and a single fluid phase is observed. This transition temperature increases with oxysterol conncentration until 15 mol%, above which the oxysterol crystallizes out. Hence the upper critical solution temperature (UCST), which corresponds to the maximum of this phase boundary is not accessible for this system. Apart from a few

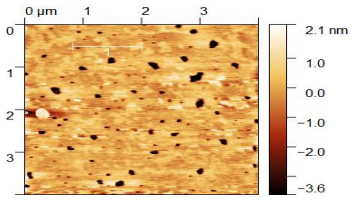

(a) DMPC:25H(7mol%) at 27°C

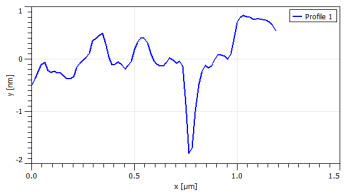

(b) Height profile of (a)

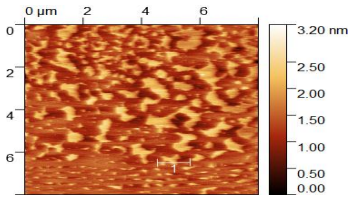

(c) DMPC:25H(10mol%) at 27°C

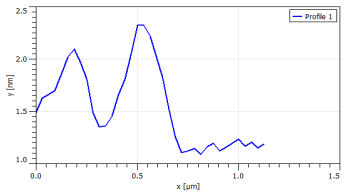

(d) Height profile of (c)

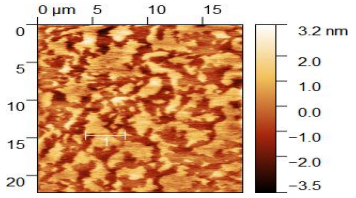

(e) DMPC:25H(15mol%) at 27°C

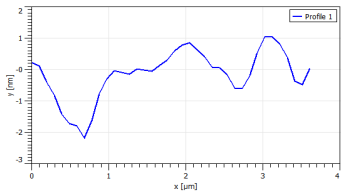

(f) Height profile of (e)

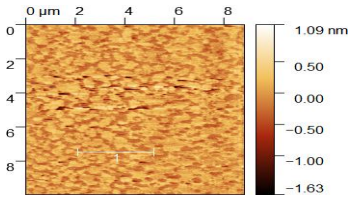

(g) DMPC:25H(20mol%) at 27°C

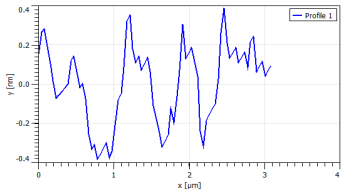

(h) Height profile of (g)

Figure 7.6: (Left) AFM images of a supported bilayer made from a binary mixture of DMPC lipid containing 25-hydroxycholesterol at room temperature for different concentrations. The images show domains due to phase separation.(Right) Corresponding height profiles.

features such as variation of ripple phase wavelength with hydroxycholesterol concentration, the qualitative phase behavior of DMPC with 25-hydroxycholesterol (fig.7.3(b)) is the same as that with 27-hydroxycholesterol.

7.2.2 Phase behavior of DLPC and DPPC bilayers in the presence of 25 and 27-hydroxycholesterol

Similar to the case of DMPC, at a low concentration of 25-hydroxycholesterol (< 5 mol%), the phase behavior of shorter chained DLPC (1,2-dilauroyl-sn-glycero-3-phosphocholine) is not affected by the presence of sterol [16]. Above 10 mol% of 25-hydroxycholesterol, fluid-fluid phase coexistence was observed (fig.7.4). Electron density profiles obtained from x-ray scattering data showed that the phase rich in sterol has a higher bilayer thickness(3.6 nm) compared to the sterol-poor phase(3.1 nm). The extent of two-phase coexistence increases

with sterol concentration till 15 mol% above, which it decreases and slowly disappears at 22 mol% of sterol concentration. Above 22 mol%, a single fluid phase was observed. 27-hydroxycholesterol does not induce any phase coexistence in DLPC bilayers above T_m. The phase behavior of DPPC in the presence of 27-hydroxycholesterol (fig.7.4) is found to be much similar to the case of DMPC: 27 hydroxycholesterol and the system showed fluid-fluid phase coexistence above the main transition temperature of DPPC [4]. But 25-hydroxycholesterol does not induce fluid-fluid phase coexistence in DPPC bilayers [17]. In the case of unsaturated lipid such as POPC, both 25-hydroxycholesterol, as well as 27-hydroxycholesterol, did not induce any phase separation [16].

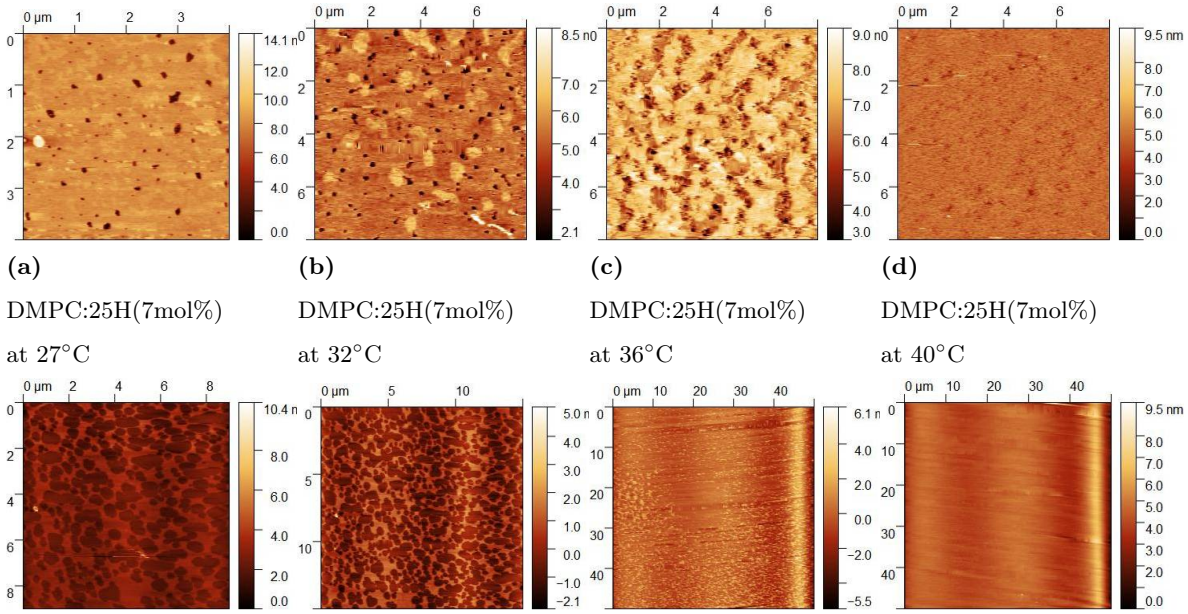

Figure 7.7: AFM images of a supported bilayer made from a binary mixture DMPC lipid containing 25-hydroxycholesterol at 7 mol% and 10 mol% at various temperatures

The general observations from x-ray scattering studies on binary mixtures of 25 and 27-hydroxycholesterol with saturated PC lipids are:

1) Hydroxycholesterol induces a closed loop fluid-fluid coexistence above the T_m of the lipid over a range of temperatures, defined by an upper and a lower critical solution temperatures (UCST and LCST)

2) Similar to the case with cholesterol the gel phase of lipids is destabilized by hydroxycholesterol

3) 25-hydroxycholesterol as well as 27-hydroxycholesterol are found to induce fluid phase coex-

istence in different lipids depending on the chain length. 25-hydroxycholesterol induces phase separation in shorter chain lipids whereas, 27-hydroxycholesterol induces phase coexistence in longer chain lipids. For intermediate chain length, both 25 and 27-hydroxycholesterol induce fluid-fluid coexistence.
4) The two coexisting fluid phases showed a difference in the bilayer thickness of 0.4-0.6 nm. The sterol rich phase was found to be thicker compared to the sterol-poor phase.

In this chapter, we study the influence of hydroxycholesterols on the phase behavior of PC bilayers using AFM. Atomic force microscopy (AFM) gives a topographical resolution of 0.1 nm. This makes it a suitable tool to study phase coexistence in lipid bilayers. Solid supported lipid bilayers were obtained by the SUV fusion method or GUV rupturing method (described in chapter 4) and used as the model system for studying the phase behavior of DMPC and DLPC bilayers in the presence of 25 and 27-hydroxycholesterol.

7.3 Results and Discussions

7.3.1 Calibration of AFM using DOPC-DMPC binary system

DOPC is an unsaturated lipid which has a main transition temperature of -16.5°C. DMPC is a saturated phospholipid with two 14 carbon alkyl chains and has a main transition temperature of 24°C. At room temperature, DMPC is in the gel phase and DOPC is in the fluid phase. Hence binary mixtures formed out of these two show gel-fluid phase coexistence at room temperature. Using AFM, we have observed this two-phase coexistence, and the values of bilayer parameters obtained were compared with those obtained from other studies. AFM images (figs.(7.5a & 7.5c)) clearly show two different regions having different thickness. The thicker region shows irregular morphology suggesting gel-like features, whereas the thinner region forms the uniform background, which is in the fluid phase. The difference in heights between the domains is 1-1.2 nm. This value matches with the observed difference found for fluid - gel coexistence using AFM [18].

7.3.2 AFM imaging of DMPC: 25-hydroxycholesterol binary system

Partial phase diagrams obtained from systematic x-ray scattering studies on aligned samples showed the presence of coexistence of two fluid phases above the chain melting transition temperature (T_m) of different lipids, namely DMPC, DPPC, and DLPC. The AFM studies were done as a function of temperature for DMPC: 25-hydroxycholesterol, DMPC: 27-hydroxyterol,

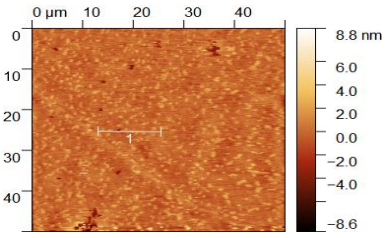

(a) DMPC:27H(4mol%) at 27°C

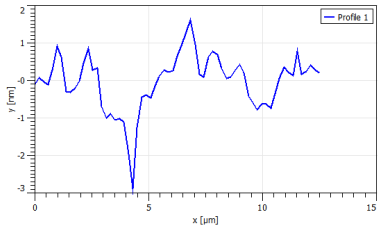

(b) Height profile of (a)

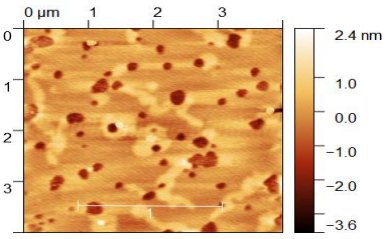

(c) DMPC:27H(10mol%) at 30°C

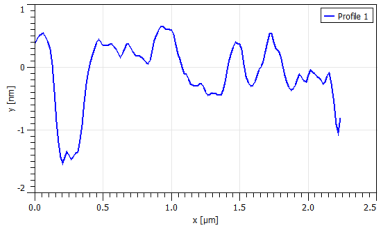

(d) Height profile of (b)

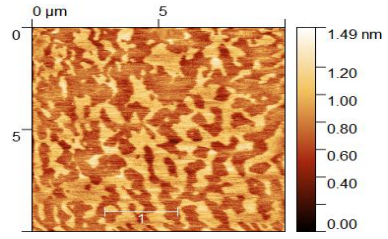

(e) DMPC:27H(15mol%) at 27°C

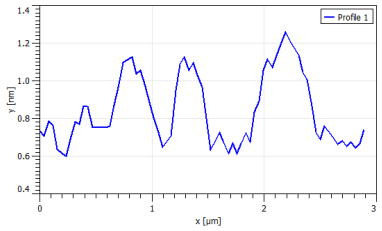

(f) Height profile of (e)

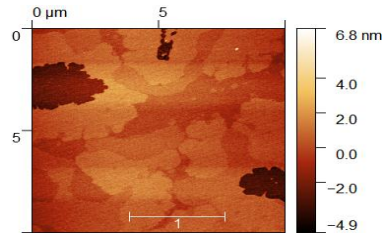

(g) DMPC:27H(20mol%) at 28°C

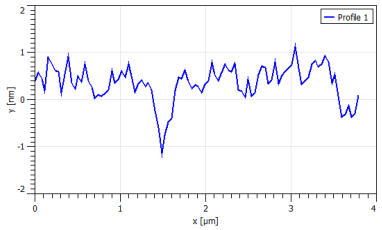

(h) Height profile of (g)

Figure 7.8: AFM images of a supported bilayer made from a binary mixture DMPC lipid with 27-hydroxycholesterol for different concentrations. The corresponding height profiles along the lines drawn in the images are given on the right.

and DLPC: 25-hydroxycholesterol systems. At higher temperatures (> 40°C), the cantilever showed an increased thermal noise, which led to poor quality of images. Hence DPPC-27 hydroxycholesterol samples, which show phase coexistence only above 40 °C, were not studied.

Temperature controlled AFM imaging was done over a range of temperatures and concentrations where the system exhibits two-phase coexistence. Thickness measured from the images give additional information about the different coexisting phases. Also, since the supported bilayers are made up of single bilayers, results of these experiments can be com-

pared with the fluid-fluid coexistence observed in fluorescence imaging of Giant Unilamellar Vesicles(GUVs) composed of binary mixture of lipids with hydroxycholesterol.

Partial phase diagram obtained from detailed x-ray experiments on DMPC: 25-hydroxycholesterol has shown that above 5 mol% of 25-hydroxycholesterol two fluid phases coexist. The lower critical solution temperature of the two-phase region is around 28°C. This temperature is higher than T_m of DMPC, which is around 24°C. The temperature controller used in these experiments allows the sample to only reach a temperature of 2-3°C above room temperature while cooling from high temperatures. So, on cooling, the AFM images were taken only till 27°C. The temperature range of domain formation is found to be similar to the range observed in x-ray scattering studies. The slight offset observed in the temperature range of phase co-existence can be related to the effect of the substrate on the transition temperature of the lipids. It has been shown that the sample-substrate interaction can broaden the transition temperature of the lipids in SLBs [19, 20]. We infer this to be the reason for the observed offsets in the upper and lower critical solution temperatures in comparison to the boundary defined by x-ray scattering studies.

In the AFM images (fig.7.6), three different color regions corresponding to different heights can be clearly observed. The dark brown color indicates holes in the bilayer and therefore

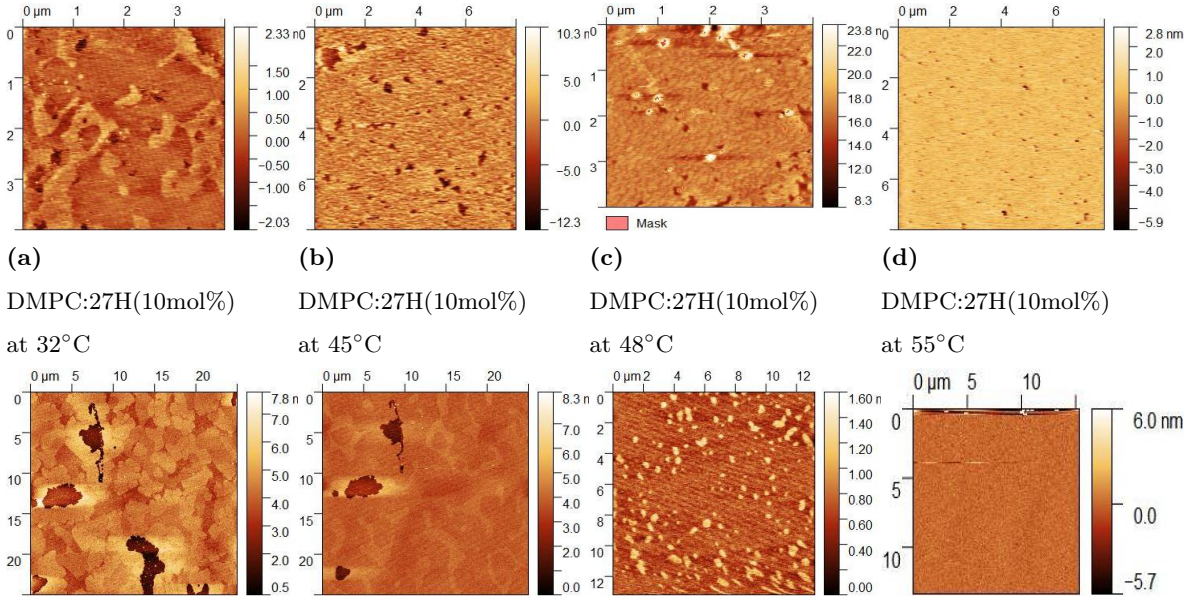

(a) DMPC:27H(10mol%) at 32°C

(b) DMPC:27H(10mol%) at 45°C

(c) DMPC:27H(10mol%) at 48°C

(d) DMPC:27H(10mol%) at 55°C

(e) DMPC:27H(20mol%) at 27°C

(f) DMPC:27H(20mol%) at 32°C

(g) DMPC:27H(20mol%) at 40°C

(h) DMPC:27H(20mol%) at 48°C

Figure 7.9: AFM images of binary mixture of DMPC lipid with 27-hydroxycholesterol at 10 mol% and 20 mol% concentrations at various temperatures.

corresponds to the substrate regions. The variation in color within the bilayer patches correspond to regions of different thickness and hence to phase coexistence. The amount of thicker domain was found to increase with the increase in hydroxycholesterol concentration. The fluid domains are characterised by regular shape with smooth edges due to line tension. On GUVs, fluid-phase domains of the same kind can easily fuse with each other. But in the case of bilayers formed on a substrate the fusion of domains may take long time due to the substrate interaction. Although we have not seen any fusion of domains at a given temperature, the shape of the domains as well as inter-domain connections, observed in the AFM images, suggest that observed phase coexistence is a fluid-fluid phase coexistence than a gel- fluid phase coexistence. The difference in bilayer thickness of coexisting phases observed is around 0.8-1 nm. The domains disappear and a uniform bilayer is obtained at high temperatures (fig.7.7).

7.3.3 AFM imaging of DMPC:27-hydroxycholesterol binary system

The qualitative features of phase behavior observed for DMPC: 27-hydroxycholesterol is the same as that found for DMPC: 25-hydroxycholesterol. As the concentration of hydroxycholesterol increases, the fraction of the thicker domain is found to increase (fig.7.8). This behavior is also seen for samples with 25-hydroxycholesterol. The difference in thickness between the two phases is found to range between 0.6 nm to 1 nm (fig.7.9).

7.3.4 Phase behavior of DLPC: 25-hydroxycholesterol binary system

DLPC contains two saturated alkyl chains, each of which consists of 12 carbons and has a transition temperature of -2°C. From the partial phase diagram obtained for DLPC:25-hydroxycholesterol, it was observed that the two-phase coexistence appears at 10 mol% sterol concentration over a small temperature range (13°C to 26°C) (fig.7.4). As the concentration of sterol increases, the temperature range of two-phase coexistence increases until 15 mol% and thereafter reduces. One characteristic feature of this phase diagram is that it has a single-phase at both higher and lower sterol concentrations (22 mol% and 7mol%, respectively) (fig.7.10). AFM images did not show any phase coexistence for samples with 22 mol% , 4 mol%, and 7.5 mol% of 25-hydroxycholesterol. Hence the AFM results correlate well with x-ray studies. Similar to binary mixtures of DMPC with 25 and 27-hydroxycholesterol, the fraction of thicker domains increases with increase in sterol concentration at a given temperature (fig.7.10). This suggests that the thicker domains are sterol-rich compared to thinner domains. The difference in thickness is found to be around 0.8 nm. At high temperatures a single fluid phase is observed is all compositions studied (fig.7.11).

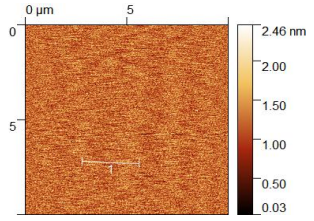

(a) DLPC:25H(4mol%) at 27°C

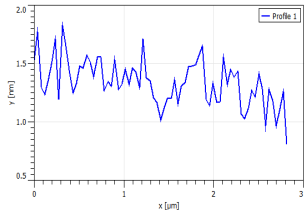

(b) Height profile of (a)

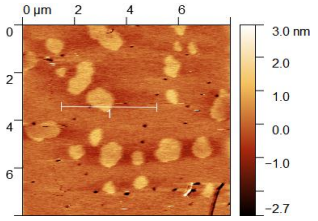

(c) DLPC:25H(10mol%) at 27°C

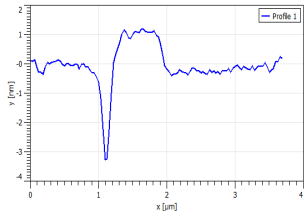

(d) Height profile of (c)

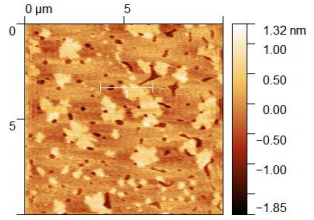

(e) DLPC:25H(15mol%) at 28°C

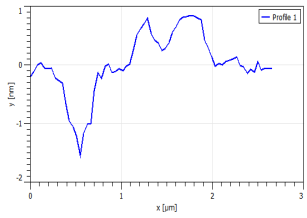

(f) Height profile of (e)

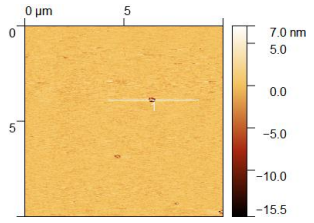

(g) DLPC:25H(22mol%) at 27°C

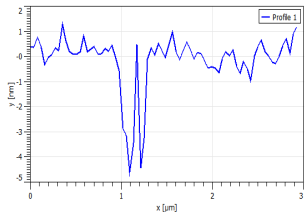

(h) Height profile of (g)

Figure 7.10: AFM images of a supported bilayer made from a binary mixture DLPC lipid containing 25-hydroxycholesterol at room temperature for 4mol%, 7.5mol%, 10mol%, 15mol% and 22mol% concentrations. The corresponding height profiles are given on the right.

7.4 Conclusion

Phase coexistence in binary hydroxycholesterol-lipid systems was probed using AFM. The phase coexistence region in temperature and concentration obtained match with that from x-ray scattering studies. The domain height differences measured is similar to the values obtained from x-ray diffraction. The fraction of thicker domains is found to increase with sterol concentration. This suggests that the fluid phase with higher thickness is richer in sterol content.

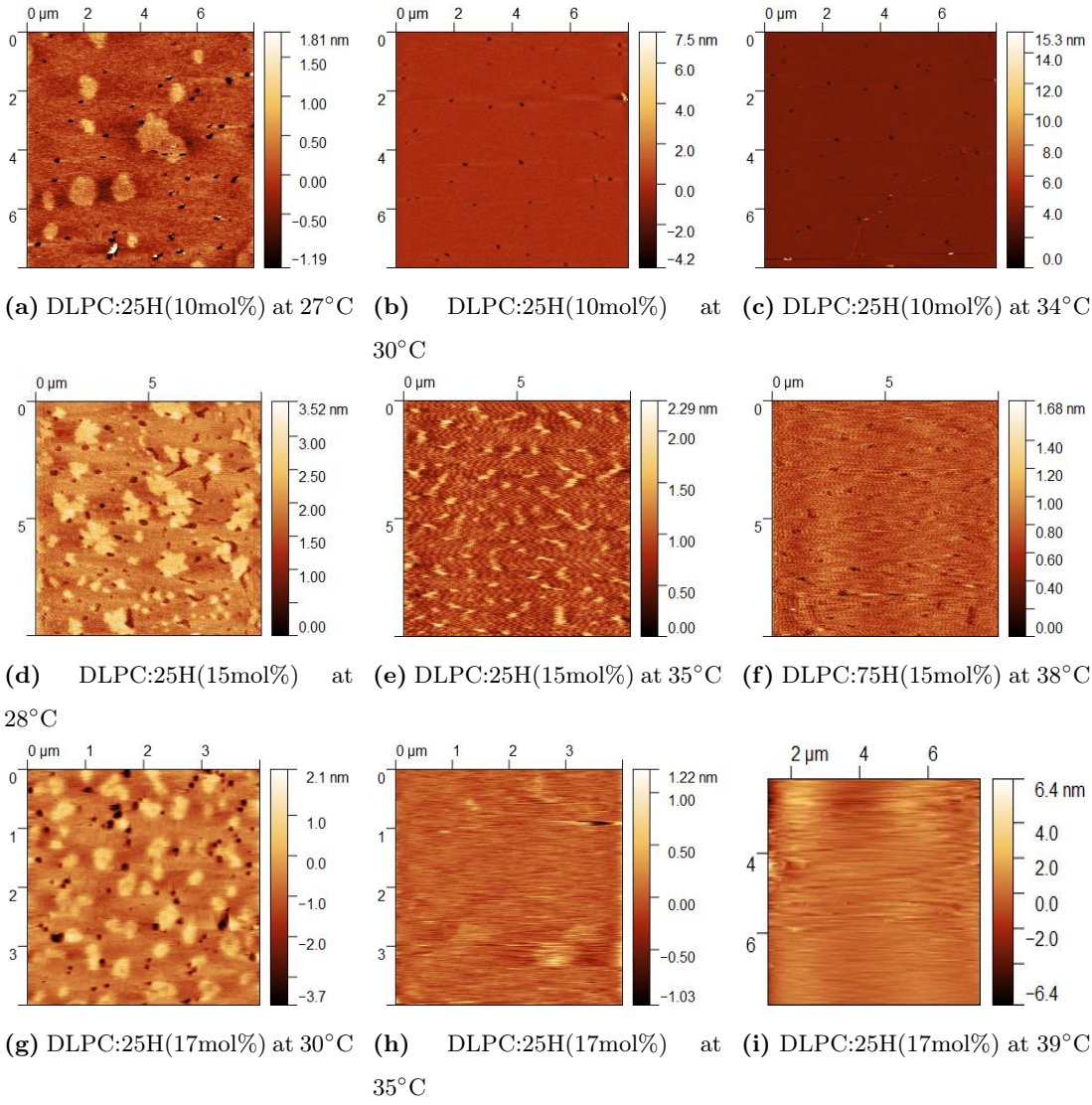

(a) DLPC:25H(10mol%) at 27°C **(b)** DLPC:25H(10mol%) at 30°C **(c)** DLPC:25H(10mol%) at 34°C

(d) DLPC:25H(15mol%) at 28°C **(e)** DLPC:25H(15mol%) at 35°C **(f)** DLPC:75H(15mol%) at 38°C

(g) DLPC:25H(17mol%) at 30°C **(h)** DLPC:25H(17mol%) at 35°C **(i)** DLPC:25H(17mol%) at 39°C

Figure 7.11: AFM images of a supported bilayer made from a binary mixture DLPC lipid containing 25-hydroxycholesterol for 10mol%, 15mol% and 17mol% concentrations at various temperatures.

Bibliography

[1] A. J. Brown and W. Jessup. Oxysterols: Sources, cellular storage and metabolism, and new insights into their roles in cholesterol homeostasis. *Molecular Aspects of Medicine*, 30:111–22, 2009.

[2] B. N. Olsen, P. H. Sclesinger, D. S. Ory, and N. A. Baker. Side-chain oxysterols: From cells to membranes to molecules. *Biochim. Biophys. Acta*, 1818:330–336, 2012.

[3] B. N. Olsen, P. H. Sclesinger, and N. A. Baker. Perturbations of membrane structure by cholesterol and cholesterol derivatives are determined by sterol orientation. *J. Am. Chem. Soc.*, 131:4854–4865, 2012.

[4] M. A. Kamal. *Influence of some membraneactive biomolecules on the phase behavior of model lipid membranes.* Phd. thesis, 2012.

[5] K. D. Roberts, L. Bandy, and S. Lieberman. The occurrence and metabolism of 20-hydroxycholesterol in bovine adrenal preparations. *Biochemistry*, 8:1259–1270, 1969.

[6] Y. Lange, J. Ye, and F. Strebel. Movement of 25-hydroxycholesterol from the plasma membrane to the rough endoplasmic reticulum in cultured hepatoma cells. *J. Lipid Res.*, 36:1092–1097, 1995.

[7] S. Meaney, K. Bodin, U. Diczfalusy, and I. Björkhem. On the rate of translocation in vitro and kinetics in vivo of the major oxysterols in human circulation: Critical importance of the position of the oxygen function. *J. Lipid Res.*, 43:2130–2135, 2002.

[8] S. M. Peyrot, S. Nachtergaele, G. Luchetti, and L. K. M-Mcgrane et. al. Tracking the subcellular fate of 20(s)- hydroxycholesterol with click chemistry reveals a transport pathway to the golgi. *J. Biol. Chem.*, 289:11095–11110, 2014.

[9] I. Björkhem. Are side-chain oxidized oxysterols regulators also in vivo? *J. Lipid Res.*, 50:Suppl:S213–8, 2009.

[10] M. Hilsch, I. Haralampiev, P. M′uller, D. Huster, and H. A. Scheidt. Membrane properties of hydroxycholesterols related to the brain cholesterol metabolism. *Beilstein. J. Org. Chem.*, 13:721–727, 2017.

[11] D. Lütjohann, O. Breuer, G. Ahlborg, I. Nennesmo, A. Sidén, U. Diczfalusy, and I. Björkhem. Evidence for an age-dependent flux of 24s-hydroxycholesterol from the brain into the circulation. *Proc. Natl. Acad. Sci. U.S.A.*, 93:9799–9804, 1996.

[12] J. J. H. Theunissen, R. L. Jackson, H. J. M. Kempen, and R. A. Demel. Membrane properties of oxysterols, interfacial orientation,influence of membrane permeability and redistribution between membranes. *Biochim. Biophys. Acta*, 860:66–74, 1986.

[13] J. C. Verhagen, P. T. Braåke, J. Teunissen, G. Van Ginkel, and A. Sevanian. Physical effects of biologically formed cholesterol oxidation products on lipid membranes investigated with florescence depolarization spectroscopy and electron spin resonance. *J. Lipid Res.*, 37:1488–1502, 1996.

[14] B. N. Olsen, P. H. Schlesinger, D. S. Ory, and N. A. Baker. 25- hydroxysterol increases the availability of cholesterol in phospholipid membranes. *Biophys. J*, 100:948–956, 2011.

[15] A. Wnetrzak, K. Makyla-Juzak, A. Filizkowska, W. Kulig, and Volume =250 Pages=553-564 year =2017 P. Dynarrwicz-Ĺ title=Oxysterol versus cholesterol in model nueronal membrane:1. The case of 7-Ketocholesterol. The Langmuir monolayer study, Journal=J. Membr. Biol.

[16] Madhukar S. *Influence of some sterols and nucleotides on the structure of self-assembled amphiphilic systems.* Phd. thesis, 2017.

[17] Bibhuranjan Sarangi. *Organization of sterols in model lipid membranes.* Phd. thesis, 2010.

[18] J. T. Marquês, A. S. Viana, and R. F. M. De Almeida. Ethanol effects on binary and ternary supported lipid bialyers with gel/fluid domains and lipid rafts. *Biochim. Biophys. Acta*, 1808:405–414, 2011.

[19] H. L. Wu, Y. Tong, Q. Peng, N. Li, and S. Ye. Phase transition behaviors of the supported dppc bilayer investigated by sum frequency generation (SFG) vibrational spectroscopy and atomic force microscopy (AFM). *Phys. Chem. Chem. Phys.*, 3:1411–1421, 2016.

[20] Y. Gerelli. Ethanol effects on binary and ternary supported lipid bialyers with gel/fluid domains and lipid rafts. *Biochim. Biophys. Acta*, 1808:405–414, 2011.

Chapter 8

Conclusion

In this thesis, we have studied the interaction of different bioactive molecules such as uridine 5'- monophosphate (UMP), acetic acid, and cholesterol and its derivatives with model lipid membranes. The aim of this study is to understand how these water-soluble molecules adsorb on the PC bilayer and alter the structure and phase behavior of PC lipids. These experimental investigations were carried out using a variety of techniques, including SAXS, WAXS, fluorescence microscopy, AFM and DSC. Main results obtained from these studies are summarized below and some directions for further studies are indicated.

Chapter 2 discusses the effect of the interaction of UMP on the structure and phase behavior of DMPC bilayers. These studies showed that in the fluid phase of DMPC, UMP preferentially adsorbs to the bilayer leading to a change in the bilayer thickness. With time the adsorption of UMP is found to change the phase behavior of the lipid. Samples with two different molar ratios (1:1 and 5:1) were studied. UMP is doubly charged at neutral pH, and the adsorption of charged UMP molecules onto the head group region leads to the formation of electrostatically stabilised swollen lamellar phase. This swollen lamellar phase has a higher main transition temperature (42°C) compared to that of the DMPC lipid. WAXS, DSC, fluorescence microscopy experiments confirm the formation of the gel phase. 2D-XRD studies showed that in the gel phase the chains are not tilted with respect to the bilayer normal. Raman spectroscopy studies showed that the head group conformations changes in the presence of UMP, which probably leads to a reduction in the head group area and increase the main transition temperature. With further incubation, the samples showed the formation of the interdigitated phase, which melts into an inverted hexagonal phase at higher temperatures (55°C). The formation of the interdigitated phase requires a large head group area, and the gel phase initially has a reduced head group area compared to DMPC. The wide angle region of the 2D-XRD patterns showed that the chains are tilted in the interdigitated

phase. The formation of the tilted interdigitated phase, as well as its melting into an inverted hexagonal phase, is rather surprising since the formation of an inverted hexagonal phase requires a smaller headgroup area. This system has to be further explored systematically.

Chapter 3 discusses the hydrotropic aggregation of UMP and UMPDSS molecules. This chapter explores the effect of counterions on the aggregation behavior of UMP molecules. These studies were motivated by the differences in the interaction of these species with the lipid membrane, discussed in chapter 2. The hydrotropic action of these molecules was probed using different experimental techniques such as FDA solubility measurements and ANS fluorescence measurements, pyrene fluorescence measurements, and DLS and SEM. UMPDSS is found to be a better hydrotrope in comparison to UMP molecules. The biological significance of these results is not clear at present.

Chapter 4 introduces a novel method of formation of solid-supported lipid bilayers using AA-induced rupture of Giant Unilamellar Vesicles (GUVs). AA was found to induce a pore in the bilayer, which resulted in the formation of the supported lipid bilayers. Also, acetic acid was able to induce fusion of GUVs to the already formed bilayer patches, which can be used to form extended supported bilayer patches. Hence this method is a much easier way of preparation of supported bilayers on any given substrate. The fluidity of the supported bilayer formed is analysed by FRAP measurements. Although experiments provide a qualitative picture of the rupture of GUVs and bilayer patch formation, detailed calculations can throw further insights into these processes. There are well established theoretical calculations on the dynamics of pore formation in GUVs suspended in buffer solutions under various conditions. To study the rupture of GUVs on the substrate, these calculations need to be extended with incorporating interaction energy of bilayer with the substrate.

Chapter 5 describes studies on the structure and phase behavior of PC lipids in the presence of AA. The phase behavior observed is surprisingly identical to that observed in the presence of UMP. Many questions remain currently unanswered, including the formation of the interdigitated phase with tilted chains and melting of the interdigitated phase into an inverted hexagonal phase. Such a melting behaviour has not been reported in the literature. Further studies are needed to explain the phase behavior observed. Since acetic acid and UMP both are weakly acidic in nature and their influence on phase behavior lipid membranes are similar, the effect of pH on the phase behavior of lipid membranes can be analysed.

Chapter 6 focuses on cryo-SEM imaging of the ripple structures formed by lipid membranes. Studies presented here show that cryo-SEM images can reveal many details of the structure of ripple phases, which are otherwise obtained using the much more tedious FF-

TEM. The outcome of this study is that cryo-SEM can provide as detailed information on the ripple phases as FF-TEM. This fact is not much appreciated in the literature.

The presence of oxysterols on the phase behavior of PC lipids were analysed by AFM imaging techniques. These studies are described in chapter 7. These systems show a closed-loop two fluid phase coexistence region above the main transition temperature of the lipid. Using AFM, we are able to show that the sterol-rich phase is thicker compared to the sterol poor phase. This behavior is similar to what is seen in the case of cholesterol. But cholesterol does not induce a fluid-fluid coexistence in PC bilayer. The ability of oxysterol molecules to take different orientations in the bilayer seems to be the reason for this phase behavior. Further experiments are required to confirm this hypothesis.